

UC Berkeley

UC Berkeley Electronic Theses and Dissertations

Title

Seismic Response Assessment of Thin Boundary Elements of Special Concrete Shear Walls

Permalink

<https://escholarship.org/uc/item/3r46v8qh>

Author

Arteta, Carlos Alberto

Publication Date

2015

Peer reviewed|Thesis/dissertation

Seismic Response Assessment of Thin Boundary Elements of Special Concrete Shear Walls

by

Carlos Alberto Arteta

A dissertation submitted in partial satisfaction of the
requirements for the degree of

Doctor of Philosophy

in

Engineering – Civil and Environmental Engineering

in the

Graduate Division

of the

University of California, Berkeley

Committee in charge:

Professor Jack P. Moehle, Chair

Professor Khalid M. Mosalam

Professor David R. Brillinger

Fall 2015

Seismic Response Assessment of Thin Boundary Elements of Special Concrete Shear Walls

Copyright 2015
By
Carlos Alberto Arteta

Abstract

Seismic Response Assessment of Thin Boundary Elements of Special Concrete Shear Walls

by

Carlos Alberto Arteta

Doctor of Philosophy

in

Engineering – Civil and Environmental Engineering

University of California, Berkeley

Professor Jack P. Moehle, Chair

Damage observed near the base of shear walls of reinforced concrete buildings after the Chile (2010) and New Zealand (2011) earthquakes are signs of shortcomings in the design of walls that need to be addressed. This investigation presents results of an experimental test program on ten reinforced concrete rectangular prisms representative of the flexural compression zone of flanged shear walls. The tested elements have transverse reinforcement detailing that matches or exceeds modern code requirements for special boundary elements. The main test variables were the amount and spacing (both vertical and horizontal) of the hoop and crosstie reinforcement. The elements were subjected to monotonically increasing axial compression until failure. Effects of strain gradient (both through the wall length and along the wall height) and effects of wall shear are not represented in the present tests. Nonetheless, the axial compression tests provide insights into the behavioral characteristics of actual wall boundaries. The global force shortening behavior of the specimens was commanded by a thin core which integrity was heavily compromised due to cover spalling, rebar buckling and out-of-plane instability. Measured load-displacement relations did not exhibit an acceptable ductile behavior suggesting that current building code requirements for special boundary elements do not necessarily achieve effective confinement to be protected against brittle axial failure. Enhanced detailing (increasing the volumetric ratio of confinement reinforcement and decreasing its horizontal spacing) improved behavior but did not produce ductile response in all cases. Reported damage extension concentrated over length corresponding to two-and-half times the thickness of the specimens. Compressive strain limits for stable behavior are proposed to be function of the gage length over which they are measured.

Bar buckling reduced the load carrying capacity of the reinforced concrete prisms because of the strength loss suffered by the longitudinal reinforcement, but also because it prevented the effective confinement of the concrete core. An experimental campaign comprising 48 analytical specimens allowed studying the relationship between tie spacing and stiffness, and the diameter of the longitudinal bars, that influenced their response when undergoing lateral instability (inelastic buckling). The behavior of tied bars undergoing lateral instability in the inelastic range is highly influenced by the relative restrictive tie spacing over which bar buckling is forced into, and the relative stiffness of the transverse ties and the longitudinal bar. The

experiments assume a rigid contact between the bar and the tie, therefore hook opening is not modeled. For the range of tie stiffness and bar geometries tested, the results indicate that the tie spacing has to be smaller than 4.5 times the bar diameter to prevent bar buckling over a large range of plastic axial strains.

Empirical core stress strain curves, accounting for bar buckling, are reported for point wise strain measurements, as well as for average axial strains recorded within the damaged region. The results show that usable strain limits, to guarantee a stable core response in pure compression, are between 1.1 and 2.0%. Average empirical core stress strain curves are proposed for modeling purposes. Implication of the compressive strain limits observed are evaluated in a hazard-consistent manner by means of the Conditional Scenario Spectra (CSS). The CSS is a set of realistic earthquake spectra with assigned rates of occurrence that reproduce the hazard at a site. Structural responses are obtained by means of numerical analysis of a multistory shear wall under the seismic demand of more than eight-hundred ground motions consistent with the CSS. The case study allows estimating risk curves to evaluate the likelihood of exceeding certain threshold compressive strains in the boundary of the cross section. The single case numerical model showed that the limited strain capacity of these elements is only likely to negatively impact the behavior of the wall system at risk levels beyond the code-based expectations of good behavior.

To Roci,

For caring so much, and giving away her time to me.

Acknowledgments

First and foremost, I want to thank my wife Rocío for all those hours waiting for me to finish something, willing to cheer me up when the horizon was not that clear. Thanks for the patience, and for taking care of everything else, especially of Tomás. Thanks for crossing with me every small goal that lead to finishing this dissertation. Thanks for being a mother, a student, and wife at the same time, for me to focus on this project. Tomás' innocence really provided a unique environment where no worries could enter. Thanks dear son for those much needed breaks.

I am truly grateful with Professor Jack Moehle who thought me the enjoyment of understanding the mechanics principles of the reinforced concrete. Professor Moehle has been a generous mentor, who guided me while pursuing my research interests. I want to take this opportunity to express the gratitude of my family for all his generous support during our stay in the US. It has been a wonderful opportunity to work under his guidance, being able to understand his point of view on so many topics of my interest. I am especially appreciative of his support when pursuing other research interests, which will be very useful when I come back to Colombia.

Several other professors at the University of California at Berkeley have instilled in me, their enthusiasm about their subject of expertise. I want to specially thank Professor Norm Abrahamson, for always making sure I understood the basics, and the complexities of the probabilistic seismic hazard analysis. Part of Chapter 5 of this dissertation was conceived under his generous guidance. Thanks to Professor Filip Filippou, for teaching me structural analysis, and for his willingness and enjoyment when discussing the development of Chapter 3 with me.

I want to dedicate the work done during this investigation to my Father, a man of exemplary warm human qualities. This is the second one his missing, but I know he would have enjoyed it much. This dissertation is also dedicated to my dear friend Pedro Therán, a life mentor, who thought me humbleness, perseverance, and respect for the others. Thanks for being a close example of life achievements, and for opening your wings to me when I returned home, and my professional partner was not there anymore.

I want to thanks our relatives in Colombia for taking care of business in our absence. Special thanks to my sisters Claudia and Margarita, my mother Yolanda, and my mother in law Maria T. for so much help in the daily details of life in Barranquilla.

My dear friends Ibbi and Lindsey Almufti, Chris and Colleen Cagurangan, Roberto Gutierrez, and the wonderful Judy Kahn, made us always feel among family in this foreign lands. Thanks for celebrating with us, and showing us the Northern Californian culture with intimacy.

The support from Graduate Student Daniela Martínez and Jorge Archbold was really needed in the laboratory while developing the first set of experiments, but mostly outside of it, when Tomás required entertainment beyond my exhausted energy. The support from Undergraduate Students Angela Tarng, Itria Licitra, Isaac Williams, Anthony Campana, Lin Zhu and Kenzo Horiuchi is acknowledged with great appreciation. I want to acknowledge the support of the laboratory staff in Davis Hall and at RSF. Thanks for teaching me the details to succeed in my future laboratory experiences.

I would like to thank Universidad del Norte and Departamento Administrativo de Ciencia, Tecnología e Innovación, Colciencias, for providing necessary financial funding to pursue my doctoral studies in the U.S. I would also like to thank LASPAU for their support in administering my scholarship. The financial support of the University of California, Berkeley, is greatly appreciated as well.

Two rebar fabricators supported this research: ERICO (LENTON) and CMC Rebar Fabricators provided part of the reinforcing steel used in the laboratory specimens; their support is acknowledged with gratitude.

The research presented in this dissertation has been supported in part by the National Institute of Standards and Technology through the ATC 94 project and by the National Science Foundation under award number 1208192. Opinions, findings, conclusions and recommendations in this document are those of the author and do not necessarily represent those of the sponsors.

Table of Contents

Introduction.....	xviii
Scope	xviii
Objectives.....	xviii
Organization	xix
Research Significance	xix
Chapter 1 - Field Observations and Motivation	1
1.1 Problem Contextualization.....	2
1.2 Reported Core Compressive Strains in the Literature.....	5
1.3 Recent Studies on Thin Walls	7
1.4 Cyclic Test on Rectangular Reinforced Concrete Specimens.....	9
Chapter 2 - Experimental Investigation	12
2.1 Test Specimens.....	12
2.2 Design.....	12
2.3 Materials.....	14
2.4 Variables of Investigation	14
2.5 Instrumentation and Test Setup.....	16
2.6 Test Results	18
2.6.1 <i>General global response</i>	18
2.6.2 <i>Response of specimen W14: onset of bar buckling</i>	19
2.6.3 <i>Response of specimens W3, W5, W6 and W7: effect of the confining window size and crosstie hooks</i>	23
2.6.4 <i>Analysis of the post peak response (specimens W8 and W9): global lateral instability and rebar buckling</i>	25
2.6.5 <i>Response of specimens W10, W11 and W12: cross sections with all bars tied</i>	29
2.7 Implications of the Results.....	31
2.7.1 <i>Usable strain limits</i>	31
2.7.2 <i>Global displacement and local strains relationship</i>	32
2.8 Further Research	36

2.9	Final Comments	36
Chapter 3 - Analytical Investigation Part I: Buckling Models		39
3.1	Previous Studies on Reinforcing Bar Buckling.....	39
3.2	Experimental Observation of Longitudinal Steel Buckling	41
3.3	Inelastic Buckling Model of Isolated Bars	41
3.3.1	<i>Force-based beam-column element formulation</i>	<i>42</i>
3.3.2	<i>Force-based and displacement-based beam-column element formulation comparison</i>	<i>44</i>
3.3.3	<i>Force-based and displacement-based element state determination</i>	<i>44</i>
3.3.4	<i>Quadrature rule for distributed plasticity beam-column elements.....</i>	<i>46</i>
3.3.5	<i>Nonlinear geometric formulation</i>	<i>47</i>
3.3.6	<i>Nonlinear incremental analysis</i>	<i>49</i>
3.4	Modeling Inelastic Buckling of Tied Longitudinal Bars Embedded in Concrete.....	54
3.4.1	<i>Typical response</i>	<i>57</i>
3.4.2	<i>Inelastic buckling model of tied bars</i>	<i>65</i>
3.5	Final Comments	75
Chapter 4 - Analytical Investigation Part II: R/C Sections		78
4.1	Confined Concrete Models in the Literature.....	78
4.2	Equilibrium Requirements for Ductile Behavior in Compression	81
4.3	Parallel Model for Prediction of Responses.....	84
4.3.1	<i>Geometry and materials constitutive description</i>	<i>84</i>
4.3.2	<i>Parallel spring model description and state determination</i>	<i>85</i>
4.3.3	<i>Force-shortening response prediction.....</i>	<i>86</i>
4.4	Local Force-Shortening Relationship Estimation	89
4.4.1	<i>Force-shortening relationship within the damage zone</i>	<i>89</i>
4.4.2	<i>Point wise force-average shortening relationship.....</i>	<i>91</i>
4.5	Empirical Core Stress-strain Curves	93
4.5.1	<i>Confined concrete response in the damage zone.....</i>	<i>93</i>
4.5.2	<i>Statistics of the empirical confined core stress-strain relationship in the damage zone (DZ).....</i>	<i>96</i>
4.5.3	<i>Statistics of pointwise empirical confined core stress strain relationships</i>	<i>97</i>

4.5.4	<i>Confined concrete stress strain relationships for modeling</i>	98
4.6	Final Comments	100
Chapter 5	- Implications of Results	101
5.1	Engineering Demand Parameter (EDP) Risk	101
5.1.1	<i>Seismic hazard estimation</i>	102
5.1.2	<i>EDP risk per PEER PBEE framework</i>	104
5.1.3	<i>Conditional scenario spectra (CSS) for EDP risk estimation</i>	105
5.2	Risk-based Implications of Limited Strain Capacity in Boundary Elements.....	111
5.2.1	<i>Prototype analysis and design</i>	111
5.2.2	<i>Inelastic modeling</i>	112
5.2.3	<i>Hazard-consistent structural response assessment with the CSS methodology</i> ...	121
5.3	Final Comments	129
Chapter 6	– Summary and Conclusion	130
References	134
Appendix A	- Digital Image Correlation	140
A.1	Brief Summary of DIC Basic Principles	140
A.2	Displacement Field Estimation	141
A.3	Strain Field Estimation and Maximum Error	144
A.4	Instrumentation and Data Set Description.....	144
A.5	DIC-strains and Out-of-plane Correction.....	147
A.6	DIC-strains Error Estimation.....	149
A.7	An Attempt to Correct for DIC-errors.....	150
A.8	Conclusions	153
A.9	Acknowledgments	153
Appendix B	- Inelastic bar buckling	154
B.1	Average Response, Tangent Modulus Evolution, Displaced Shape, Tie Demand and Axial Strain Distribution	155
B.2	Strain Field Evolution and Tangent Modulus Distribution	162
B.3	Stress-strain Evolution of the Discrete Fiber.....	169
B.4	Response of the Analytical Specimens of Bar Buckling Under Tie Setup 1 and 2.....	171
B.5	Algorithm for Estimating ε_b , m_h or $f_r(\varepsilon_p)$ given s/d_b and $(d_{bt}^2/l_t)/(d_{bt}^2/L_o)$	173

Appendix C - Grading Ground Motion Modification Procedures for Structural Analysis Based on Conditional Scenario Spectra	180
C.1 Motivation	180
C.2 Structural Design and Inelastic Modeling	181
C.3 Ground Motion Selection and Modification Procedures	183
C.4 Structural Responses.....	184
C.5 EDP risk curves from CSS	185
C.6 Final comments.....	187
Appendix D - Conditional Scenario Spectra Metadata.....	188
D.1 CSS Metadata.....	188

Table of Figures

Figure 1.1 - Observed damage in multistory reinforced concrete shear wall buildings during the 2010 Maule Earthquake in Chile [center: 10-story building in Viña del Mar (photo by Patricio Bonelli); right: 19-story building in Santiago (left and right photos by Jack Moehle)].....	1
Figure 1.2 - Plastic hinge model relating global to local demand parameters on test specimens...	2
Figure 1.3 - Moment-curvature relations of the cross section and corresponding strain profile for roof drift ratio of 1.5% and flange in tension.....	3
Figure 1.4 - Approximate relationships between axial load, steel reinforcement at the boundaries, neutral axis depth of the compression zone, and roof drift of cantilever walls. (a) approximate neutral axis depth (adapted from (Moehle et al., 2011)); (b) approximate roof drift values that trigger SBE detailing requirements. Note: the values in the chart were estimated for $f'_c = 4$ ksi [28MPa] and $f_y = 60$ ksi [420MPa].....	4
Figure 1.5 - Strain at fracture of transverse steel. (Data source, (Mander et al., 1988a; Moehle & Cavanagh, 1985; B. D. Scott et al., 1982), after Moehle (2014)).....	7
Figure 1.6 - Force versus average strain on identical specimens reported by two different authors. (Data source, (Mander et al., 1988a; B. D. Scott et al., 1982)). (Note: 1 mm = 0.0394 in; 1 MN = 224.8 kips).....	7
Figure 2.1 - Specimens global geometry (a), global view of test setup for specimen W5 (b), and cross section geometry and variables of interest (c). [Note: 1 in. = 25.4 mm].	13
Figure 2.2 – Material properties: (a) unconfined concrete strength versus corresponding strain at the day of test; (b) experimental stress-strain curve for an A706 #7 longitudinal bar.....	14
Figure 2.3 - Transverse reinforcement in wall specimens: (a) plan view of transverse reinforcement layer; (b) geometry of the “window” bounded by h_x and s	15
Figure 2.4 - Instrumentation setup.....	17
Figure 2.5 - Response evolution of Wall 7: (a) load-axial shortening relationship; (b) cover concrete axial strains evolution; (c) specimen damage evolution.	19
Figure 2.6 - Damage localization on the West (left hand side of each pair) and East face of the specimens.....	20
Figure 2.7 - Test evolution of specimen W14: (a) force versus average strain relationship and failure sequence of the damage zone; (b) details of the damaged zone.....	21
Figure 2.8 - Tensile tie strains of specimen W14: (a) tie strain distribution along the height of the reduced section zone at three instance of the test evolution; (b) critical ties strain versus average vertical strain in the reduced section zone.....	22
Figure 2.9 - Compressive strain evolution in longitudinal reinforcement on the East face of specimen W14: (a) tied bar strain distribution along the height; (b) tied bar longitudinal	

strain along the buckling length, versus average strain of damage zone; (c) non-tied bar strain distribution along the height; (d) non-tied bar longitudinal strain along the buckling length, versus average strain of damage zone.....	23
Figure 2.10 - Normalized force versus average strain relation for all specimens (gage length = 72 in. [1829 mm]).	24
Figure 2.11 - Spread of plasticity.....	25
Figure 2.12 - Out-of-plane response of specimen W9: (a) normalized out-of-plane displacement profile; (b) Axial force – moment interaction relationship during the test evolution of specimen.	27
Figure 2.13 - Strain evolution in a buckled bar in specimens W8 and W9.	28
Figure 2.14 - Force versus core deformation response at various levels along the length of the specimen	30
Figure 2.15 - Usable strain limits versus normalized gage length for specimens W8, W9, W11 and W12.	31
Figure 2.16 - Plastic hinge model: (a) wall under lateral and vertical loading; (b) wall global and local deformation profiles; (c) idealized elastic and plastic curvature distribution; (d) plastic hinge model.	33
Figure 2.17 - Limiting normalized roof drift ratio versus selected plastic hinge length.	34
Figure 2.18 - Two-dimensional plastic hinge model (adapted from Takahashi et al. (2013)).	35
Figure 2.19 - Comparison between estimated and observed plastic flexural drift.....	36
Figure 3.1 - Buckling of different diameter bars appearance.	42
Figure 3.2 - (a) Element basic force system; (b) basic deformation system; (c) forces at the section level	42
Figure 3.3 - Fiber section geometry, deformations and material constitutive model parameters.	43
Figure 3.4 - Curvature distribution comparison between a force-based and a displacement-based beam-column element.	45
Figure 3.5 - Displacement-based element state determination flow chart.....	46
Figure 3.6 - Force-based element state determination flow chart.....	46
Figure 3.7 - Integration points locations and weights for the Gauss-Lobatto quadrature rule.	47
Figure 3.8 - Frame element nonlinear statics under corotational formulation (adapted from (Filippou, 2014)).	48
Figure 3.9 - Basic axial force acting on the deformed shaped of the members of a buckled bar: (a) for a two-node discretization; (b) for a six-node discretization.	49
Figure 3.10 - Finite element model to simulate inelastic bar buckling.....	50
Figure 3.11 - Fiber configuration sensitivity analysis.	51

Figure 3.12 - Buckling response comparison for different element discretization and two different steel materials: (a) bilinear steel material; (b) trilinear steel material with yield plateau.....	52
Figure 3.13 - Global and local response of the select model (<i>N6C20R10</i>). (a) Normalized applied axial load versus average shortening of the bar; (b) deformed shape; (c) normal strain distribution at the centroid.	53
Figure 3.14 - Response at the fiber level at midspan: (a) extreme fiber under compression only; (b) centroidal fiber; (c) extreme fiber under strain reversal after buckling initiates [Note: 1 ksi = 6.9 MPa].....	54
Figure 3.15 - Response comparison with (Monti & Nuti, 1992).....	55
Figure 3.16 – Inelastic buckling models of tied embedded bars.....	56
Figure 3.17 - Buckling response of Test 29 ($d_b = 7/8$ in. , Tie Setup 2, $d_{bt} = 1/4$ in.): (a) average stress versus average axial strain relationship; (b) normalized tangent moduli evolution with average axial strain; (c) deformed shape; (d) stress strain relationship of the tie adjacent to mid height.	58
Figure 3.18 - Strains in the midspan cross section at different levels of average axial strain (Test29).....	59
Figure 3.19 - Normalized tangent moduli distribution within the critical cross section at different levels of average axial strain (Test 29)	60
Figure 3.20 – Evolution of the stress-strain relationship of the fibers in the critical section of Test 29.....	60
Figure 3.21- Response of Test 28 close to the onset of buckling ($d_b = 7/8$ in. [22 mm], Tie Setup 2, $d_{bt} = 0$): (a) average stress versus average axial strain relationship; (b) normalized section flexural stiffness evolution with average axial strain; (c) strain field evolution of the critical section; (d) tangent modulus distribution.	62
Figure 3.22 – Deformed shape and local strains of Test 29: (a) normalized lateral displacement at $U/L_o = 10\varepsilon_y$; (b) distribution of element axial strains at $U/L_o = 10\varepsilon_y$; (c) element axial strain versus average axial strain relationship for three elements (16, 17 and 18) within the buckling length of the bar.	63
Figure 3.23 – Buckling response variation with transverse tie diameter (from left to right, Test 28, 30 & 33).....	64
Figure 3.24 – Model describing the average axial stress – strain response of tied bars undergoing inelastic buckling.	66
Figure 3.25 - Response of Tests 11 to 15 (Tie Setup 1) and Tests 35 to 41 (Tie Setup 2) ($d_b = 1$ in. [25mm]).	67
Figure 3.26 – Post buckling response in terms of f_r and ε_p for: (a) Tie Setup 1 and (b) Tie Setup 2.....	67
Figure 3.27 – Normalized buckling strain in terms of s/d_b and $(d_{bt}^2/l_t)/(d_{bt}^2/L_o)$. (Note: 1 in. [25mm]).	68

Figure 3.28 - Post yield slope coefficient in terms of s/d_b and $(d_{bt}^2/l_t)/(d_{bt}^2/L_o)$. (Note: 1 in. [25mm]).	69
Figure 3.29 - Post buckling relative strength f_r at $\epsilon_p=0.02$ in terms of s/d_b and $(d_{bt}^2/l_t)/(d_{bt}^2/L_o)$. (Note: 1 in. [25mm]).	69
Figure 3.30 - Model prediction versus analytical experiment.	74
Figure 3.31 - Estimated versus observed values of ϵ_b and m_h .	75
Figure 3.32 - Analysis of residuals for ϵ_b and m_h .	76
Figure 4.1 – Comparison of the (Mander et al., 1988b) and (Saatcioglu & Razvi, 1992) confined concrete models for the geometry of specimen W7.	81
Figure 4.2 Stresses and forces acting on the critical cross section: (a) non-buckling rebar case; (b) case of partial buckling in rebar of the confined core.	83
Figure 4.3 Parallel model geometry and materials definition.	84
Figure 4.4 Example of the state determination of the springs-in-parallel model. (a) given strains and corresponding stresses of each spring; (b) resisting force-average strain relation of each spring and the system.	87
Figure 4.5 Experimental and “blind” prediction of axial load versus average strain relations. (Note: gage length for the experimental curves is 72 in. [1828 mm]).	88
Figure 4.6 - Model to estimate the force-shortening response of the most damage zone:(a) spring in series representation of the specimen; (b) force-shortening relationship of the different portions of the wall; (b) force-average strain relationships (Note: average strains of the DZ spring are estimated using gage length L_{DZ} equal to the average spalling lengths in Figure 2.11).	90
Figure 4.7 Semi-empirical and prediction of axial load versus average strain relations for the damage zone (DZ). (Note: average strains of the DZ curves are estimated using gage length L_{DZ} equal to the average spalling lengths in Table 4.3).	91
Figure 4.8 Experimental and predictive model of axial load versus average strain relations for different gage lengths. (Note: average strains gage lengths are: 72 in. [1828 mm] for the Global curves; L_{DZ} equal to the average spalling lengths in Table 4.3 for the DZ curves; and 2.2 in. [60mm] for the core strain gages CO _{SG} curves).	92
Figure 4.9 - Core empirical stress-strain relationship estimation for the DZ: (a) constitutive model for the steel and cover (unconfined) concrete; (b) recovered force-average shortening relation for the confined core; (c) recovered confined core stress-average strain relationship for the DZ. (Note: average strains gage length is equal to L_{DZ} in Table 4.3 for specimen W7).	93
Figure 4.10 Empirical stress-strain relations of the confined core from the damaged zone of specimens W3 and W12.	95
Figure 4.11 Strain demand distribution in ties of specimens W9 and W12: (a) normalized force versus average axial strain in the DZ; (b) transverse strain demand on the central tie of specimen W9 and W12 at three stages of the force-shortening relationship.	96

Figure 4.12 Model and empirical core strength comparison.	96
Figure 4.13 Confined core strains at different levels of strength loss. (a) scatter of recorded values of strain and corresponding damage zone length for specimens W3 to W12; (b) box plots comparing the dispersion of the empirical data and models for different confinement strain measures.	97
Figure 4.14 Confined core strength for two strain gage lengths.	98
Figure 4.15 Mean confined core strains at different levels of strength loss for specimens W8, W9, W11 and W12 (Note: gage length for the 1CO _{SG} and 2CO _{SG} are $0.2t_w = 2.4$ in. [60 mm] and $1.2 t_w = 14.4$ in. [366 mm], respectively; mean gage length for the DZ series is $2.5t_w = 30$ in. [762 mm]).	98
Figure 4.16 - Proposed confined concrete stress-strain relationships for different gage lengths. (Note: gage length for the 1CO _{SG} and 2CO _{SG} are $0.2t_w = 2.4$ in. [60 mm] and $1.2 t_w = 14.4$ in. [366 mm], respectively; mean gage length for the DZ series is $2.5t_w = 30$ in. [762 mm]).	99
Figure 5.1 – Seismic hazard: (a) hazard curves for several structural periods for the Yerba Buena Island site; (b) uniform hazard spectrum for 2,500 years return period and code-based response spectra (5% damped).	103
Figure 5.2 - Deaggregation of the seismic hazard for PE 2 % / 50yrs.	104
Figure 5.3 - IDA results and corresponding fragility curve estimation (adapted from (Haindl et al., 2015))	105
Figure 5.4 - Magnitude-distance pairs for selected seed ground motions (unique scenario spectra).	106
Figure 5.5 – Target UHS spectra for different hazard levels.	107
Figure 5.6 – CMS construction.	108
Figure 5.7 – Scenario spectra for hazard levels 2×10^{-3} , 1×10^{-3} and 2.5×10^{-4}	108
Figure 5.8 - Scenario spectra: (a) 402 scenario spectra (5% damped); (b) assigned rate of occurrence for each spectrum of the CSS	109
Figure 5.9 - Hazard curves at different periods recovered from the conditional scenario spectra.	109
Figure 5.10 – Global EDPs from CSS runs of models in Appendix C: (a) maximum roof drift ratio (RDR) versus spectral displacement S_d ; (b) maximum base shear versus spectral acceleration S_a	110
Figure 5.11 – Structural responses (EDP) risk curves example.	111
Figure 5.12 – Geometry, reinforcement and model of the T-wall studied.	112
Figure 5.13 – Compression quadrant of the concrete models for nonlinear analysis.	114

Figure 5.14 – Cyclic “pushover” analysis results for the SoM model: (a) base shear versus roof drift; (b) force versus average strain in the stem boundary element; (c) cyclic response of the steel model; (d) force versus average shortening in the stem boundary element.	115
Figure 5.15 – Cyclic “pushover” analysis results for the DuM model: (a) base shear versus roof drift; (b) force versus average strain in the stem boundary element; (c) cyclic response of the steel model; (d) force versus average shortening in the stem boundary element.	116
Figure 5.16 – Cyclic moment-curvature relationships at the integration point locations of the first story element.	117
Figure 5.17 – Seismic demand corresponding to three different hazard level, for nonlinear dynamic analyses purpose (Note: the spectra are constructed for a 5% damping ratio).	118
Figure 5.18 – Roof drift ratio response comparison.	119
Figure 5.19 – Base shear response comparison.	120
Figure 5.20 – Strain response history in the centroid of the flange.	120
Figure 5.21 – Strain response history in the centroid of the SBE of the stem.	120
Figure 5.22 – Compressive strain response history in the centroid of the SBE of the stem.	121
Figure 5.23 – Individual record spectra, variability and comparison with code-based response spectra.	122
Figure 5.24 – Roof drift ratio versus spectral acceleration relationships: (a) scattergram of RDR_{max} and $S_a(T)$; (b) fragility curves for different levels of RDR_{max}	123
Figure 5.25 – Relationships of roof drift ratio, tensile and compressive strains in the centroid of the SBE at the edge of the stem: (a) scattergram of maximum tensile strains $\epsilon_{t,max}$ and RDR_{max} ; (b) scattergram of maximum compressive strains $\epsilon_{c,max}$ and RDR_{max} ; (c) $\epsilon_{t,max}$ versus $\epsilon_{c,max}$ relationship.	124
Figure 5.26 – Lognormal fragility curves of $\epsilon_{c,max}$ in terms of RDR_{max}	125
Figure 5.27 – Rate versus EDP level: (a) rates of occurrence for maximum roof drift ratio; (b) rates of occurrence for maximum compressive strain in the stem SBE; (c) rates of occurrence for maximum tensile strain in the stem SBE.	126
Figure 5.28 – Maximum SBE tensile strain risk for the SoM and DuM models.	127
Figure 5.29 – Maximum SBE compressive strain risk for the SoM and DuM models.	128
Figure 5.30 – Maximum roof drift ratio risk for the SoM and DuM models.	129
Figure A.1.1 - Evolution of a speckle pattern with loading: (a) prismatic specimen under pure compression prior to loading; (b) evolution of a speckle pattern with increasing compressive loading.	141
Figure A.2.1 - Subset gray-level intensities, discretization and polynomial fit (adapted from (Chu et al., 1985)).	142

Figure A.2.2 - Reference subset before and after deformation ((a) adapted from Chu et al. (1985); (b) adapted from Pan et al. (2009)).	143
Figure A.4.1 - Instrumentation setup for DIC.	145
Figure A.4.2 - Test evolution and comparison of axial strains (ε_{yy}) from displacement transducers, concrete strain gages and DIC.	146
Figure A.4.3 - Load-strain relations for the PDT-strain data set (left) and the SGC-strain data set (right) (in this figures, positive strains are compression).	147
Figure A.5.1 – Out-of-plane evolution of specimen W7. (a) out-of-plane displacement at different loading values; (b) strain correction due to out-of-plane displacement.	148
Figure A.5.2 - Comparison of DIC-strains before and after out-of-plane corrections.	148
Figure A.6.1 - DIC error estimation.	149
Figure A.6.2 - DIC relative error estimation.	150
Figure A.6.3 - Median relative error evolution with average shortening of the specimen.	150
Figure A.7.1 - Strain errors correction estimates.	151
Figure A.7.2 - Comparison of original DIC-strain, corrected DIC-strains and CSG-strains.	152
Figure A.7.3 - Median relative error evolution (after correction) with average shortening of the specimen.	153
Figure B.1.1 – Test 28: (a) average response; (b) section stiffness evolution; (c) displaced shape. Distribution at $U/L_o = 30\varepsilon_y$ of: (e) lateral displacement; (f) axial stress; (g) moment; and (h) axial strain.	155
Figure B.1.2 – Test 30: (a) average response; (b) section stiffness evolution; (c) displaced shape; (d) tie response close to mid span. Distribution at $U/L_o = 30\varepsilon_y$ of: (e) lateral displacement; (f) axial stress; (g) moment; and (h) axial strain.	156
Figure B.1.3 – Test 31: (a) average response; (b) section stiffness evolution; (c) displaced shape; (d) tie response close to mid span. Distribution at $U/L_o = 30\varepsilon_y$ of: (e) lateral displacement; (f) axial stress; (g) moment; and (h) axial strain.	157
Figure B.1.4 – Test 32: (a) average response; (b) section stiffness evolution; (c) displaced shape; (d) tie response close to mid span. Distribution at $U/L_o = 30\varepsilon_y$ of: (e) lateral displacement; (f) axial stress; (g) moment; and (h) axial strain.	158
Figure B.1.5 – Test 33: (a) average response; (b) section stiffness evolution; (c) displaced shape; (d) tie response close to mid span. Distribution at $U/L_o = 30\varepsilon_y$ of: (e) lateral displacement; (f) axial stress; (g) moment; and (h) axial strain.	159
Figure B.1.6 – Test 34: (a) average response; (b) section stiffness evolution; (c) displaced shape; (d) tie response close to mid span. Distribution at $U/L_o = 30\varepsilon_y$ of: (e) lateral displacement; (f) axial stress; (g) moment; and (h) axial strain.	160

Figure B.1.7 – Test 35: (a) average response; (b) section stiffness evolution; (c) displaced shape; (d) tie response close to mid span. Distribution at $U/L_o = 30\varepsilon_y$ of: (e) lateral displacement; (f) axial stress; (g) moment; and (h) axial strain.....	161
Figure B.2.1 – Test 28: (a) strain field evolution; (b) tangent modulus distribution evolution.	162
Figure B.2.2 – Test 29: (a) strain field evolution; (b) tangent modulus distribution evolution.	163
Figure B.2.3 – Test 30: (a) strain field evolution; (b) tangent modulus distribution evolution.	164
Figure B.2.4 – Test 31: (a) strain field evolution; (b) tangent modulus distribution evolution.	165
Figure B.2.5 – Test 32: (a) strain field evolution; (b) tangent modulus distribution evolution.	166
Figure B.2.6 – Test 33: (a) strain field evolution; (b) tangent modulus distribution evolution.	167
Figure B.2.7 – Test 34: (a) strain field evolution; (b) tangent modulus distribution evolution.	168
Figure B.3.1 – Tests 28 to 31: history of the fibers stress-strain relationship at the critical section, for different tie diameters.....	169
Figure B.3.2 – Tests 32 to 34: history of the fibers stress-strain relationship at the critical section, for different tie diameters.....	170
Figure B.4.1 – Response of Tests 1 to 5 and 21 to 27 ($d_b = 3/4$ in. [19 mm]).	171
Figure B.4.2 – Response of Tests 6 to 10 and 28 to 34 ($d_b = 7/8$ in. [22 mm]).	171
Figure B.4.3 – Response of Tests 11 to 15 and 35 to 41 ($d_b = 1$ in. [25 mm]).	172
Figure B.4.4 – Response of Tests 16 to 20 and 42 to 48 ($d_b = 1\ 1/4$ in. [32 mm]).	172
Figure C.2.1 – General layout of structural elements: (a) plan; (b) elevation of Frame 1.....	182
Figure C.2.2 – Pushover curves.	183
Figure C.3.1 – Selected ground motion set and their variability: (a) LM set, with variability around the median; (b) TM set, without much variability; (c) variability (in log units) of the LM and TM sets for different periods.....	184
Figure C.4.1 – Structural response under each set of ground motions: (a) maximum roof drift ratio versus elastic spectral displacement at the fundamental period; (b) normalized maximum base shear versus spectral acceleration at the fundamental period.....	185
Figure C.4.2 – Boxplots of the structural responses.	185
Figure C.5.1 – Engineering demand parameter response from CS runs on the NLC model: (a) maximum roof drift ratio versus elastic spectral displacement at the fundamental period; (b) normalized maximum base shear versus spectral acceleration at the fundamental period.	186
Figure C.5.2 – Hazard curves for maximum roof drift ratio: (a) with responses from the TM set; (b) with responses from the LM set; (c) interpolated rates for median values from runs with the TM and LM set.	186

Figure C.5.3 – Hazard curves for normalized base shear: (a) with responses from the TM set; (b) with responses from the LM set; (c) interpolated rates for median values from runs with the TM and LM set. 187

Figure D.1.1 – Rate versus EDP level, DuM model: (a) rates of occurrence for maximum roof drift ratio; (b) rates of occurrence for maximum compressive strain in the stem SBE; (c) rates of occurrence for maximum tensile strain in the stem SBE. 198

Table of Tables

Table 2.1 - As tested material properties and reinforcement detailing	16
Table 2.2 - Regression coefficients for strain limits calculations	32
Table 2.3 - Selected specimens and input variables for estimating plastic flexural drift R_p	35
Table 3.1 - Tie and hoop diameter requirements for specimens W5 to W12 according to Bresler and Gilbert (1961). [Note: 1 in. = 25.4 mm].....	41
Table 3.2 – Inelastic buckling analytical experiment matrix [Note: 1 in. = 25.4 mm].....	56
Table 3.3 - Buckling strain ε_b normalized to yield strain.	70
Table 3.4 – Post yield slope m_h	70
Table 3.5 – Post buckling strength coefficients f_r for $e_p = 0.001, 0.0025, 0.005, 0.0075$	71
Table 3.6 – Post buckling strength coefficients f_r for $e_p = 0.01, 0.015, 0.02, 0.025$	72
Table 3.7 – Post buckling strength coefficients f_r for $e_p = 0.03, 0.04, 0.05, 0.06$	73
Table 3.8 – Tests selected [Note: 1 in. = 25.4 mm].....	75
Table 4.1 - Parameter substitution for modeling unconfined concrete.....	80
Table 4.2 - Spring parameter for modeling of specimen W7.	86
Table 4.3 – Confined concrete model parameters.	89
Table 4.4 – Confined concrete stress-strain model parameters.	100
Table D.1.1 – Metadata of Conditional Scenario Spectra set.....	188

Introduction

Reinforced concrete shear walls are widely used in earthquake-resistant building construction because, in addition to being economical, they are capable of providing required stiffness, strength, and ductility capacity to protect building systems against strong earthquake shaking. Where earthquake shaking will result in inelastic response including compressive yielding of the boundary elements of the wall, special boundary elements are required. Such boundary elements generally have closely spaced transverse reinforcement to confine the core concrete and provide lateral support for longitudinal reinforcement. The intent is to provide a capability for stable compressive yielding. Building codes around the world prescribe reinforcing steel detailing requirements with the purpose of enabling the boundary element to achieve the anticipated performance. As wall boundary element geometries have evolved over past decades, however, questions have arisen about the effectiveness of some of these building codes to achieve the desired performance. Recent field and laboratory experiences have demonstrated that certain wall geometries are prone to failure of their flexural compression zone at intermediate level of seismic shaking. This dissertation presents laboratory test results, along with mathematical models, and a seismic hazard-consistent methodology to evaluate the response in compression of boundary elements of code-compliant multistory thin walls.

Scope

This research discusses the subject of limited compressive strain capacity and damage localization of thin reinforced concrete boundary elements, with the aim of having a better understanding of its causes and implications. The discussion is opened with recent field observations of damaged wall boundaries of multistory reinforced concrete building, and ends with a risk-based assessment of their expected behavior. The discussion is fed by a comprehensive experimental campaign, complemented with structural modeling. The intent is to provide the engineering community with a set of tools to analyze and design special boundary elements of thin wall with updated information.

Objectives

The general objective of this investigation is to assess the effectiveness of different transverse reinforcement layouts to achieve ductile behavior of relatively thin wall boundaries under pure compression. Three specific objectives are: (i) to evaluate the adequacy of ACI 318 provisions for special boundary elements; (ii) to estimate confined concrete empirical constitutive relations consistent with the response of modern thin wall boundaries; and (iii) to investigate the implications of the ductility capacity of special boundary elements in the response of multistory shear walls.

Organization

The dissertation comprises five chapters describing recent field and laboratory observations of the response of thin reinforced concrete walls subjected to seismic shaking. It presents new laboratory results on the response of thin reinforced concrete prisms under pure compression, and introduces a methodology to assess the implications of the experimental findings in a hazard-consistent manner.

Chapter 1 provides observed evidence of structural wall damage during a recent earthquake, along with a contextualization on the mechanics describing wall deformations at the local and at the critical section levels. It also presents a literature review on reported ultimate strains of reinforced concrete prism in compression, recent studies on thin walls under lateral loading, as well as cyclic response of rectangular reinforced concrete prisms with intermediate and special detailing.

Chapter 2 presents a laboratory experimental campaign on ten reinforced concrete prisms. The specimens can be considered to approximately represent the extreme flexural compression zone of the stem of a flanged wall, having transverse reinforcement detailing that matches or exceeds current code requirements for special boundary elements. The specimens were subjected to monotonically increasing axial compression until failure. The axial compression tests provide insights into the behavioral characteristics of actual wall boundaries. Usable compressive strain limits for the type of elements tested are proposed as a function of different gage lengths over which the strains are measured.

Chapter 3 provides results from analytical experiments evaluating the inelastic buckling of bars restrained by evenly spaced ties. The experiment, comprising 48 analytical specimens allows the development of a simple empirical model that offers the complete average axial stress-strain curve of tied longitudinal bars undergoing lateral instability (buckling), in terms of a few input parameters such as the tie spacing, and the diameter of the longitudinal and transverse bars.

Chapter 4 presents the empirical stress-strain relationships of the confined concrete of the specimens tested, including bar buckling. Average monotonic confined concrete stress-strain curves, representative of the materials tested are proposed for various gage lengths.

Chapter 5 presents a methodology to assess the experimental results of the previous chapters with a hazard-consistent basis. The Conditional Scenario Spectra concept is introduced to estimate the risk of structural responses. A numerical evaluation of a reinforced concrete wall model, with constitutive materials and expected plastic zone geometry as those observed in the field, helps understand the implication of the results.

Finally, **Chapter 6** summarizes the investigation and provides additional concluding remarks.

Research Significance

The tests reported here comprise full-scale reinforced concrete rectangular prism in compression which are scarce in the literature. They significantly increase the number of available data points for large cross section aspect ratio. The test results provide insight on the expected spread of the plasticity in rectangular prisms with large height-to-thickness ratio. Instrumentation of the

specimens allowed estimating the level of strain at which longitudinal bar buckling is triggered; and the loading and relaxation patterns along the specimens length.

Chapter 1 - Field Observations and Motivation

Damage observed near the base of shear walls of reinforced concrete buildings after the Chile (2010) and New Zealand (2011) earthquakes are signs of shortcomings in the design of walls that need to be addressed (**Figure 1.1**). Of particular interest is the damage at the edges (boundary elements) of the cross sections, which is characterized by longitudinal bar buckling, hoops opening, and large volumetric reduction of the concrete cores (Sritharan et al., 2014; Wallace et al., 2012). The appearance of the crushed boundaries and the observation that the damage extended over short distances along the wall height suggest that these failures were relatively brittle. Wallace et al. (2012) report the damage height to be one to three times the wall thickness for buildings damaged during the Chile 2010 earthquake. The occurrence of brittle failure can be explained, in part, by the sparse and poorly detailed transverse reinforcement in the buildings. An open question that still remains is whether thin walls with improved boundary element detailing would behave in a more ductile manner.



Figure 1.1 - Observed damage in multistory reinforced concrete shear wall buildings during the 2010 Maule Earthquake in Chile [center: 10-story building in Viña del Mar (photo by Patricio Bonelli); right: 19-story building in Santiago (left and right photos by Jack Moehle)]

To answer this question, a series of laboratory tests was carried out and reported here. The laboratory test program comprised ten prismatic reinforced concrete specimens that were subjected to monotonically increasing axial compression until failure. The test specimens can be considered to approximately represent the extreme flexural compression zone of the stem of a flanged wall (for example, a T-, L- or U-shaped wall). That region of a structural wall is subjected to high axial compressive strains due to combined axial force and moment. Effects of strain gradient (both through the wall length and along the wall height) and effects of wall shear are not represented by the tests. Nonetheless, the axial compression tests provide insights into the behavioral characteristics of actual wall boundaries. The general objective of the experimental campaign was to assess the effectiveness of different transverse reinforcement layouts to achieve ductile behavior of relatively thin wall boundaries under pure compression. Specific objectives were: (i) to evaluate the adequacy of ACI 318 (2011, 2014) provisions for special boundary

elements (SBE); (ii) to evaluate the effect of crosstie spacing (both vertical and horizontal); (iii) to assess the relative effectiveness of 135-degree seismic hooks versus 90-degree standard hooks as the method for anchoring crossties; and (iv) to estimate the spread of plastic deformation in slender rectangular prisms under compressive loading. The effects of these variations are reported, with an aim of better understanding the detailing requirements necessary to achieve ductile response.

1.1 Problem Contextualization

Figure 1.2 shows a plastic hinge model of a T-shaped reinforced concrete shear wall cantilever. The kinematics of the simple model assumes all the roof lateral displacement is due to plastic rotation at the plastic hinge, neglecting any elastic contribution outside the plastic hinge. In this manner, demand parameters at a local level, such as the curvature at the base cross section, can be related to global demand parameters such as the roof displacement with relatively simple expressions. The tip displacement of the wall, pivoting at the base, is given by

$$\delta_u = \theta_{p,u} H_w \quad (1.1)$$

where $\theta_{p,u}$ is the plastic rotation at the hinge and H_w is the height of the wall. Assuming a uniform curvature distribution along the expected plastic hinge length ($L_w/2$), the plastic rotation in terms of the curvature ϕ_u of the cross section and the maximum fiber compressive strain ϵ_{cu} is

$$\theta_{p,u} = \phi_u \left(\frac{L_w}{2} \right) = \left(\frac{\epsilon_{cu}}{c} \right) \left(\frac{L_w}{2} \right) \quad (1.2)$$

where L_w is the length of the wall and c is the neutral axis depth from the maximum fiber in compression.

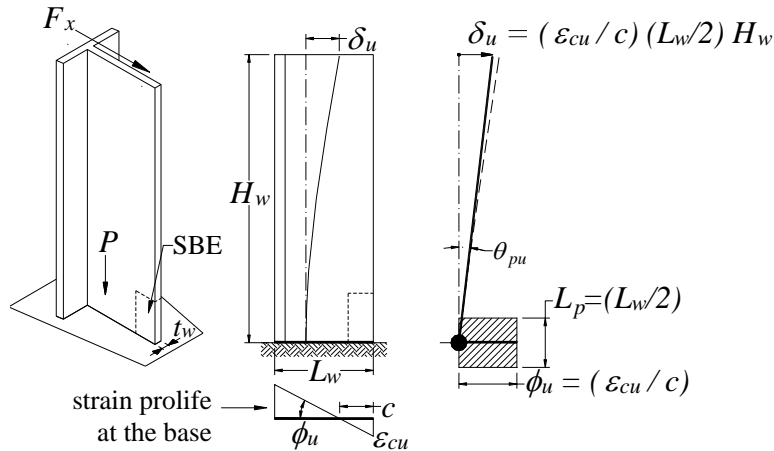


Figure 1.2 - Plastic hinge model relating global to local demand parameters on test specimens.

Combining **Equations (1.1)** and **(1.2)** allows estimating the demand imposed at the cross section level by a given roof drift ratio δ_u/H_w as

$$\phi_u = \left(\frac{\delta_u}{H_w} \right) \left(\frac{2}{L_w} \right) \quad (1.3)$$

Figure 1.3a shows moment-curvature relations of the wall cross section at its base. Two curves shown are for moments either compressing the flange or the stem of the wall. Moment capacities for the direction compressing the narrow stem are larger because of the large area of steel yielding in the flange. This direction of loading produces a relatively deep neutral axis because the thin compression zone requires extending further into the wall to equilibrate the large tensile force in the longitudinal steel of the flange. The deeper neutral axis results in relatively large concrete compressive strains for a given curvature, such that the curvature capacity is exhausted at relatively lower values. The strain profile shown in **Figure 1.3b** depicts the axial strain demand on the boundary element of the wall for a relatively low axial load ($0.1A_gf'_c$), where A_g is the gross cross section area of the wall and f'_c is the unconfined concrete strength), and for a roof drift ratio of 1.5% (a value that might be expected under strong earthquake ground motion) in the direction that compresses the stem. Even though a gradient of strains is apparent, for this example, the average strain demand on the boundary element is higher than the crushing strain of the concrete, enough as to require concrete confinement to ensure a ductile behavior of the concrete in compression. This strain demand could become higher if the axial load demand on the wall is increased (which is not uncommon due to architectural planning and construction practices in many countries around the world).

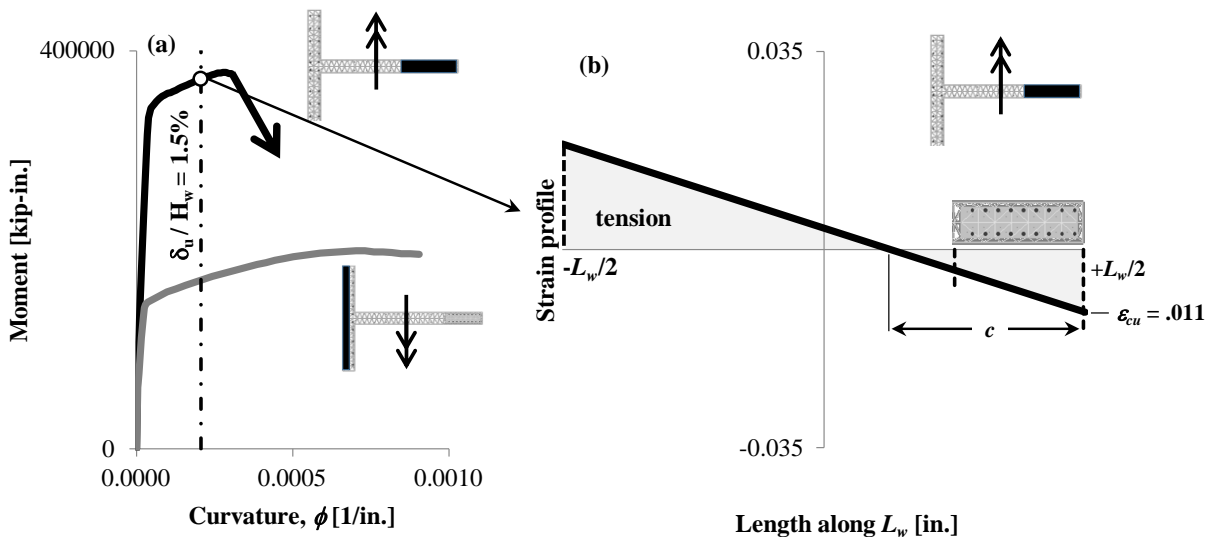


Figure 1.3 - Moment-curvature relations of the cross section and corresponding strain profile for roof drift ratio of 1.5% and flange in tension.

In ACI-318-11, one of two provisions defining the need for SBE follows a displacement-based approach stating that the compression zone of special structural walls requires SBE detailing if

$$c \geq \frac{L_w}{600 \left[\left(\frac{\delta_u}{H_w} \right) \right]} \quad (1.4)$$

where δ_u/H_w is the design roof drift consistent with the direction compressing the wall edge under evaluation. This expression is based on the plastic hinge model in **Figure 1.2** and is

derived by combining **Equations (1.1)** and **(1.2)**, and by selecting a limiting compressive strain ϵ_{cu} equal to 0.3% (with additional number rounding).

Figure 1.4a is adapted from (Moehle et al., 2011) and presents approximate values of the neutral axis depth for rectangular cantilever walls, accounting for different levels of ultimate axial load. Walls with C-, L-, or T-shapes under lateral demand that compresses the stem can be represented by the positive values of the horizontal axis in this figure. Values to the right hand side of the figure indicate that the longitudinal reinforcement ratio of the compression zone ($A'_s/(L_w b)$) is smaller than the opposite site (the flange) in tension. The neutral axis depth grows with increments in the tension steel and with increasing axial load. This is consistent with the description above regarding the correlation of high axial loads with larger expected uniaxial deformation of the extreme fiber in compression. Given the relatively shallow slopes of the curves presented, the neutral axis depth scales more with small variations of axial load than with large differences between the tension and compression steel ratios. The relations in **Figure 1.4b** are estimated by combining the curves in **Figure 1.4a** with the expression for c/L_w in **Equation (1.4)**. These are approximate relations between axial load, provided longitudinal steel reinforcement area, and minimum roof drift ratios that trigger the requirement for SBE detailing at the edges of the walls. High values of axial load (for example $P_u = 0.3A_g f'_c$), make the drift demand that triggers the SBE requisite invariant to the longitudinal reinforcement provided (flat bottom curve). This is because of the large pre-compression under pure axial load, prior to any additional flexural-compression demand associated to lateral shaking. It is also apparent that under the same level of axial load demand, C-,L-, or T-shaped walls would require SBE detailing under smaller roof drift ratios, as compared to rectangular symmetric cross sections (for example, $A_s - A'_s = 0$).

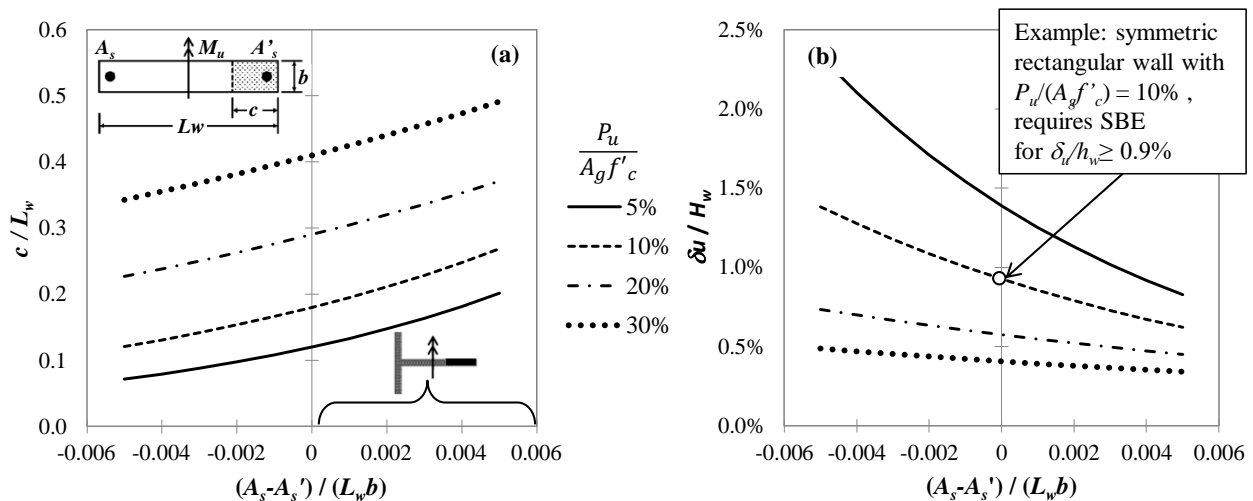


Figure 1.4 - Approximate relationships between axial load, steel reinforcement at the boundaries, neutral axis depth of the compression zone, and roof drift of cantilever walls. (a) approximate neutral axis depth (adapted from (Moehle et al., 2011)); (b) approximate roof drift values that trigger SBE detailing requirements. Note: the values in the chart were estimated for $f'_c = 4$ ksi [28MPa] and $f_y = 60$ ksi [420MPa].

From the latter discussions it is concluded that a good design practice accounts for all the tension steel in the flange of wall with composite cross section. This is specifically specified in ACI 318-14§18.10.5 which contains seismic provisions for the design of special structural walls. The examples described above are idealizations of some common cases in which the geometric

characteristic of the cross section, combined with intermediate flexural and axial demand, results in exacerbated compressive demand at the edges of a reinforced concrete shear wall. The research reported here is designed to evaluate whether thin wall boundary elements are able to perform in a ductile manner under pure compressive loads, to ensure a global stable response of special reinforced concrete shear walls.

1.2 Reported Core Compressive Strains in the Literature

Laboratory tests of full-scale rectangular prisms in compression are scarce in the literature. Reported experiments of reinforced concrete prisms in compression (Mander et al., 1988a; Moehle & Cavanagh, 1985; B. D. Scott et al., 1982; Sheikh & Uzumeri, 1980) mainly focus on testing confinement effectiveness of different layouts of longitudinal and transverse reinforcement. These experiments provide stress-strain relationships of confined concrete with strains estimated over a predefined length where damage is expected.

While circular and square cross sections are typical for these studies, Mander et al. (1988a) report tests on 16 one half-scale rectangular wall units, with cross section 5.9 x 27.6 in. [150 x 700 mm] and aspect ratio (height-to-thickness ratio) of 8. These tests represent the behavior of the flanges of prototype hollow columns under seismic action; hence, they were laterally restrained at the edges to avoid out-of-plane displacement. Some of the tested specimens are considered heavily reinforced, with transverse reinforcement ratio¹ ranging from 0.68% to 2.92%, in the through-thickness direction of the cross section (ρ_v). The ratio between transverse reinforcement spacing (s) and the longitudinal bar diameter (d_b) was in the range $1.6 \leq s/d_b \leq 6.0$. Core strains reported in this study are inferred from displacements measured over 15.7 in. [400 mm] (2.7 times the wall thickness) of length within a predefined damaged zone monitored with several displacement transducers. Measuring the shortening of this plastic zone proved to be challenging due to the formation of inclined failure planes. For this reason, after the peak load was attained, a critical transducer was identified to estimate the strains in the descending branch of the force-shortening relationship. This critical transducer had to fully cover the damage zone and its measured displacement had to approximately coincide with the stroke displacement. Reported ultimate confined core stains (at first hoop fracture) are in the range 2.5% to 5.5%.

Most compression tests reported for rectangular columns have been configured such that all longitudinal bars are engaged by a hoop leg or a crosstie. Moehle and Cavanagh (1985) performed compression tests on 8 one-half scale reinforced concrete prisms of square cross sections (12 x 12 in. [305 x 305 mm]). Two of these specimens are of particular interest because their internal longitudinal bars are only restrained by the flexural stiffness of the perimeter hoops. Their response showed poor ductility because they were not able to regain strength after the onset of concrete cover spalling. This behavior could be attributed to the combination of unsupported longitudinal bars and poorer confinement effectiveness due to use of only a perimeter hoop without crossties. For all specimens, s/d_b was 2.0 and the transverse steel ratio in one direction ranged from 0.61 to 1.04%. Analogous to what Vallenias et al. (1977) reported, plastic post-peak-load strains were estimated indirectly, and not from direct shortening measurements of the testing region. Core strains were inferred from overall shortening

¹ For a given direction, the transverse reinforcement ratio is defined as the area of transverse steel divided by the area bounded by the core width and the spacing between adjacent layers of transverse reinforcement.

measurements, assuming that beyond the strain at peak load, all the plastic displacement is accommodated within a damage zone length of 15 in. [381 mm] (1.25 time the depth of the cross section). Ultimate strains at first hoop fracture were in the range 4.8 to 9.5%.

B. D. Scott et al. (1982) reported on the response of 20 full-scale 17.7 x 17.7 in. (450 x 450 mm) reinforced concrete columns, having two different layouts of longitudinal and transverse steel. One had eight longitudinal bars tied by squared perimeter hoops and diamond-shape internal hoops. The other had had twelve longitudinal bars tied by a squared perimeter hoops and octagonal internal hoops. Transverse reinforcement ratio in one direction was between 0.67 and 1.55% and s/d_b ranged from 2.7 to 4.9. For these tests, strains were also estimated from shortening of a region where damage was constrained by adding additional transverse reinforcement outside that region. The gauge length for this strain estimation was 15.7 in. (400 mm) (approximately equal to the core width) and was monitored by four displacement transducers, one on each face. Average concrete strains at first hoop rupture were in the range 1.7% to 3.8%.

The post-peak strain softening nature of reinforced concrete prisms in compression requires that estimated plastic strains have an associated gage length over which they are measured. This is required because the strain distribution is not uniform along the specimen length due to damage localization (Markeset & Hillerborg, 1995). The limiting core strains reported in the literature are calculated from displacement measurements over a wide range of gage lengths. These gage lengths are usually associated to the extent of a monitored area where damaged is constrained to occur. For the aforementioned tests, the monitoring length ranged between 1 and 2.7 times the smallest cross section dimension. As described before, direct measurement of the shortening of this damage zone is challenging because interaction between the specimen and the instrumentation is unavoidable. This is especially true close to the most heavily deformed portions of the specimen where concrete spalls-off, diagonal cracks form, bar bucking and tie opening takes place, and deformation of the rods, where the transducer are mounted, may occur. The tests described report maximum core compressive strain capacity at first hoop rupture between 1.7 and 9.5%. Values in this wide range are mainly controlled by the layout and amount of transverse reinforcement provided, but it should be recognized that they are also associated to the specific gage length over which they were measured (Bazant, 1989; Shah & Sankar, 1987).

A similar data set as the one described above is summarized in **Figure 1.5**. The figure shows strain ϵ_{cu} at first transverse steel fracture for column under monotonic compressive loading, as a function of the minimum confining stress, normalized by the unconfined concrete strength ($f_{le,min}/f'_c$). The data was collected by (Moehle, 2014) from tests by (Mander et al., 1988a; Moehle & Cavanagh, 1985; B. D. Scott et al., 1982) on columns under concentric or moderately eccentric loading. As an example, diamond markers correspond to Series B containing results of similar cross sections gathered by two different authors (Moehle & Cavanagh, 1985; B. D. Scott et al., 1982). For this case, scatter in the domain of ϵ_{cu} is apparent over the short range $0.07 \leq f_{le,min}/f'_c \leq 0.09$, where minimum and maximum ϵ_{cu} differ by factor 3.3.

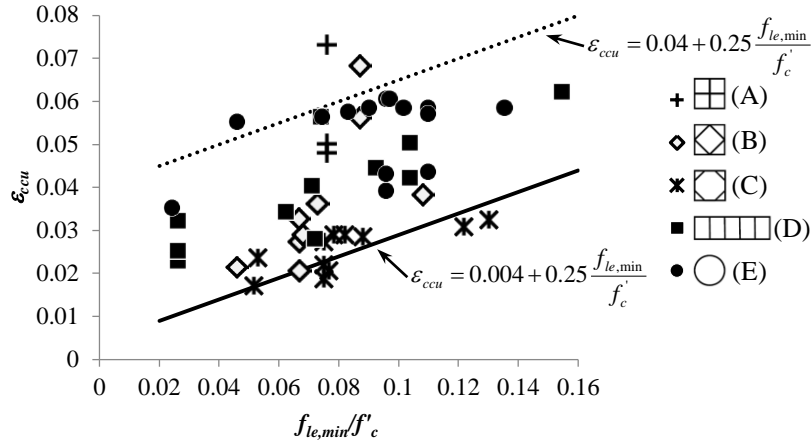


Figure 1.5 - Strain at fracture of transverse steel. (Data source, (Mander et al., 1988a; Moehle & Cavanagh, 1985; B. D. Scott et al., 1982), after Moehle (2014))

An example of inconsistent post peak response for identical specimens is presented in **Figure 1.6**. B. D. Scott et al. (1982) and Mander et al. (1988a) independently reported force versus average strain response of the test on Units 6 and 13 performed by (B. D. Scott et al., 1982). Both authors report strains from displacements measured over the same gauge length. As described before, while Mander et al. (1988a) used the critical transducer to ensure measurements within the most damage zone, B. D. Scott et al. (1982) reports average strain of transducers on the four faces of the columns. Differences in the post peak response reported are apparent, with first hoop rupture strain differing by factor 1.7.

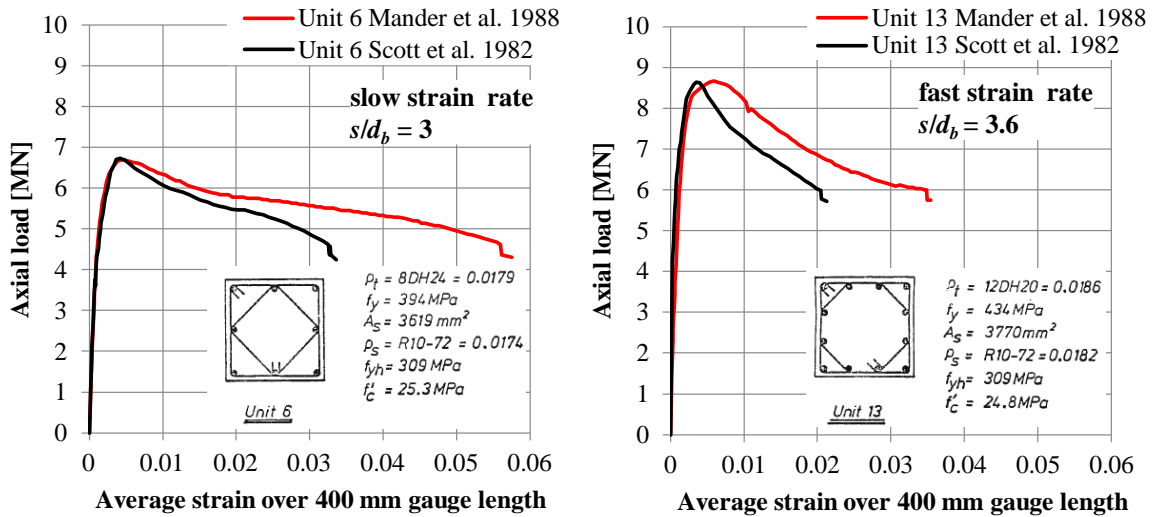


Figure 1.6 - Force versus average strain on identical specimens reported by two different authors. (Data source, (Mander et al., 1988a; B. D. Scott et al., 1982)). (Note: 1 mm = 0.0394 in; 1 MN = 224.8 kips)

1.3 Recent Studies on Thin Walls

The large M_w 8.8, 2010 Chile Earthquake, exposed problems in multistory reinforced concrete shear wall buildings, triggering the initiation of several research projects to study the response of thin walls under earthquake loading. Hube et al. (2014) and Alarcon et al. (2014) studied the response of nine one-half scale specimens, representative of prototype slender thin walls with

thicknesses of 5.9 in. [150 mm] and 7.9 in. [200 mm]. The specimens were designed following typical Chilean practice, using distributed longitudinal web reinforcement with additional boundary steel at the edges. The objective of this set of tests was to replicate the behavior of walls damaged during the 2010 Chile earthquake. One of the specimens had crossties restraining the web distributed steel, and another had enhanced boundary transverse reinforcement comprising closed hoops at the edges of the wall. For this specimen, ratio of hoop spacing to bar diameter, s/d_b , was 9 for the longitudinal bars in the boundary. The specimens were tested under different levels of axial load, ranging from typically $0.15f'_cA_g$ up to $0.35f'_cA_g$, where A_g is the gross area of the concrete section and f'_c is the specified unconfined concrete compressive strength. The specimens lost their load-carrying capacity due to flexural compression failure, followed by lateral instability of the bottom portion, along the entire length of the specimen. Overall, the force-displacement response was similar among the specimens with the thicker web, with small differences in their displacement ductility capacity promoted by the variation of the testing variables. The maximum drift ratio capacity, sustained in two consecutive cycles without loss of lateral load resistance, ranged from approximately 1.2 to 2.0%. The specimen with crossties along the web length and with boundary elements at the edges showed a slightly improved ductility capacity with respect to the rest of the specimens. Additionally, the inclusion of closed hoop at the edges reduced the out-of-plane instability after boundary crushing. On the other hand, the wall with the thinnest web showed a limited displacement capacity as compared to the rest of the specimens. The authors attributed this to the largest cover-to-core thickness ratio, which resulted in larger compressive stress on the core after concrete cover spalls off. It is also reported, that ductility capacity of the specimens decreased with increasing axial load. The vertical extent of damage was measured as the vertical extent of concrete cover spalling, with a reported mean value of 2.63 times the wall thickness (t_w). It is believed that the small thickness of the specimens is the main variable dominating the response.

Takahashi et al. (2013) discuss the drift capacity of structural walls with poor detailing at the wall boundaries. The objective of that paper was to propose displacement predictive equation based on plastic hinge length equal to $2.5t_w$. For this purpose, ten reinforced concrete wall specimens with asymmetric cross section, comprising a boundary column at one end, and either a thin rectangular boundary element or an L-shaped boundary element on the opposite side. This design ensures high compressive strain demand on the weaker edge (opposite to the column) under ultimate lateral force. Web thickness of the specimens ranged from 3.5 in. [90 mm] to 5.5 in. [140 mm]; ratios of the neutral axis depth to the wall thickness were in the range $2 \leq c/t_w \leq 6$; and the neutral axis depth to wall length ratio were in the range $0.1 \leq c/l_w \leq 0.35$. Transverse reinforcement of the weaker boundaries is not compliant with ACI 318-08 (2008) seismic requirement, and comprised various layouts of crossties to restrain the longitudinal bars. The typical crosstie layout includes a checkerboard pattern, where each bar in the boundary is tied at every other layer of transverse reinforcement (for example, every 2.8 in. [70 mm]). Other specimens had all the longitudinal bars tied at every layer of transverse reinforcement (every 1.4 in. [35 mm]), while one of the specimens did not have crossties. The longitudinal bar diameter in the boundary of all specimens was the same; therefore, ratio s/d_b was either 3.5 or 7. The extent of the boundary element transverse reinforcement along the length of the web was larger than half the neutral axis depth in most cases. The specimens were tested under different levels of axial load, ranging from $0.03f'_cA_g$ to $0.08f'_cA_g$. The flexural drift capacity reported, measured at the instant when the lateral strength drops to 80% of the peak (for example at $0.8V_{max}$), was in the range 0.4 to 1.05%. This drift capacity is measured in the direction that compresses the weak

boundary, and does not include contribution to the displacement from shear deformations and/or horizontal slip along flexural cracks. The ultimate compressive strain in the extreme fiber in compression at $0.8V_{max}$ was in the range 0.66 to 0.84%. This strain was measured at the bottom of the specimens over gage length extending between 2.9 and 4.0 times the wall thickness. Damage in the weak boundary extended over height equal to $2.5t_w$. This value is used as the plastic hinge length in a two-dimensional model proposed to estimate the plastic flexural drift of walls dominated by flexural compression, offering good correlation with the experimental results. This model is explained further in **Chapter 2**.

Lowes et al. (2012) tested four one-third scale reinforced concrete wall models, representative of a 10-story prototype of modern construction in the Western United States. The prototype wall length was 30 ft [9.1 m], with thickness of 18 in. [460 mm] and height of 100 ft [30 m]. The specimens were tested under relatively large shear demand, as compared with their capacities, with moderate axial load ranging from $0.095f'_cA_g$ to $0.13f'_cA_g$. Three of the specimens had longitudinal reinforcement splices at the base. For these specimens, the limiting drift capacity at the effective height of the model ranged from 0.75 to 1.9%. The following discussion focuses on the fourth specimen, which is one of particular interest because it did not have splices of the longitudinal steel, and resulted in flexural-compression failure at relatively low displacements. This specimen was detailed with distributed vertical and transverse steel, and had edge boundary elements that were compliant with seismic detailing of ACI-318-11. The boundary element transverse reinforcement ratio in the through-thickness direction, was $\rho_y = 0.88\%$, with s/d_b equal to 4 and longitudinal steel ratio equal to 3.4%. The following damage states are reported, along with corresponding effective drift ratio: (i) appearance of horizontal and diagonal cracks occurred at 0.10%; (ii) compression yielding occurred at approximately 0.30%; (iii) cover spalling was observed at 0.64% and concentrated over a small height of approximately 1 wall thickness (actual spread of damage is not reported); (iv) bar exposure and onset of core crushing occurred at 0.88%; (v) bar buckling occurred at 0.91%. At larger drift, the damage extended over the whole length of the boundary element, resulting in loss of lateral load resisting capacity. It is reported that compressive damage of boundary elements is the most commonly observed damage following earthquakes, and this is confirmed by 60% of the specimens in a database of rectangular wall tests presented. According to the authors, the set of experimental results presented evidence of the low drift capacity of modern code compliant slender structural walls subjected to high seismic shear demand.

Although it is convenient to relate wall damage states to global engineering demand parameters, such as drift demand, it is important to recognize that the drift ratio definition is not consistent among the tests summarized above, nor is the pattern of the applied seismic load, which results in different gradients of moment demand along the tested specimens. This is believed to add scatter in the results presented, and even produce some “false positive” acceptable responses.

1.4 Cyclic Test on Rectangular Reinforced Concrete Specimens

Experimental test on reinforced concrete rectangular prisms subjected to axial tensile strain excursions, prior to compression, have been reported by (Acevedo et al., 2010; Chai & Elayer, 1999; Creagh et al., 2010; Welt et al., 2016). Chai and Elayer (1999) report on axial reversed cyclic tension and compression tests on fourteen slender reinforced concrete prisms,

representative of the end regions of a ductile multistory shear wall. The specimens have cross section 4 x 8 in. [102 x 203 mm], width of 8 in [203 mm] and height-to-thickness ratio ranging from 11.75 to 17.75. Longitudinal reinforcement ratio of the specimens was 2.1 or 3.8%, and transverse reinforcement spacing was such that $s/d_b = 6$. The main objective of the test program was to get an understanding of the mechanism involved in the lateral instability of the plastic hinge region of a wall when subjected to large-amplitude tension and compression cycles. The testing protocol comprised half cycles of axial tensile strain, followed by a half cycle in compression to a target of 1/5 or 1/7 of the previous tensile strain. In subsequent cycles, the tensile and corresponding target compressive strains were increased until a large out-of-plane displacement was detected. An important variable of the test program was the largest tensile strain (ϵ_{sm}) under which the specimen was still stable. This value corresponds to the maximum tensile strain recorded one cycle prior to the one in which lateral instability in compression (global buckling) occurred. Recorded maximum tensile strain reduces with increasing height-to-thickness ratio, with approximate reported average values of $\epsilon_{sm,ave} = 1.00\%$, 1.20%, and 1.90% (corresponding to 5.2, 5.9 and 9.7 times the yield strain) for specimens with height-to-thickness ratio of 17.75, 14.75 and 11.75, respectively. These values are considered conservative because of two main reasons: (i) they were obtained under a uniform strain field along the element length, which does not represent the actual strain gradient along the height of boundary elements in the critical section of multistory shear wall; additionally, (ii) the restraint of the web along the length of the wall is not represented in the test, nor are the boundary conditions at the extremes of the tested specimens, which were pinned.

Following the 2010 Chile Earthquake, Acevedo et al. (2010) and Creagh et al. (2010), each tested two reinforced concrete prisms, constructed following ACI 318-08 (2008) provisions for ordinary (OBE) and special boundary (SBE) elements, respectively. The specimens represent the end region of the critical section of a shear wall, and were 6 x 12 in. [152 x 305 mm] rectangular in cross section, with height-to-thickness ratio of 6. Longitudinal reinforcement ratio of the specimens was 3.7%, and transverse reinforcement spacing was such that ratio s/d_b was 10.7 for the OBEs and 2.7 for the SBEs. For each detail, one of the specimens was tested under pure compression, while the other was pulled to a tensile strain of 4%, and then subjected to compressive loading. The compression-only test resulted in sudden loss of load carrying capacity after the peak load was attained, just after the onset of concrete cover spalling. This sudden failure was unexpected for the SBE, given the large volumetric transverse reinforcement ratio provided. In the other tests, cracked planes developed perpendicular to the specimen axis during the tensile excursion, with some crack closure due to relaxation when the specimens were unloaded, before proceeding to the compression phase. Failure due to lateral instability of the specimens was observed during the subsequent compression cycle, at approximately 20% (for the OBE) and 33% (for the SBE) of the maximum load attained by the specimens that were tested only in compression. For each specimen global buckling occurred while the prisms were still elongated but under compressive stress. This is attributed to the asymmetric nature of the crack-closure process, in which at low compressive loads, only the two curtains of longitudinal steel (which have previously yielded in tension) contribute to the internal resistance of the cross section. As expected, each curtain is not equidistant from the axis of the applied load, resulting in a moment acting out of the plane of the test specimen, causing out-of-plane lateral displacement. As the out-of-plane moment exceeded the moment capacity, lateral instability failure occurred.

Also motivated by field observations of crushed boundaries in multistory reinforced concrete walls following the 2010 Chile Earthquake, Welt et al. (2016) conducted two independent test programs on 33 rectangular prisms, with the main focus of assessing the impact of different transverse reinforcement layouts on the response of boundary elements under cyclic axial loading. The specimens are classified according to their compliance with ACI 318-14 for boundary elements as: non-compliant (NBE), ordinary boundary elements (OBE), special boundary elements (SBE), and enhanced special boundary elements (xSBE). Specimens with various geometries were tested at two different sites: the first set of specimens, tested at the University of Chile (UoC) had length equal to 11.8 in. [300 mm] with thicknesses of 5.1 in. [130 mm], 7.1 in. [180 mm] and 9.8 in. [250 mm], and resulting height-to-thickness ratios ranging from 4 to 8.9; the second set was tested at the U.S. Army Corps of Engineers Construction Engineering Research Laboratory (CERL), and comprised specimens with rectangular cross section of 7.9 x 15.0 in. [200 x 380 mm], with height-to-thickness ratio of 5.0. Longitudinal reinforcement ratio of the specimens ranged from 2.0 to 3.9%, with some specimens having no longitudinal reinforcement. Transverse reinforcement spacing was such that ratio s/d_b ranged between 4.0 and 8.3. Transverse reinforcement ratio in the through-thickness direction of the specimens was in the range $0.34 \leq \rho_y \leq 1.76\%$. Of special interest are the SBE and the xSBE specimens because of the expected large compressive strain demand they would see under seismic action. The SBE set comprised 8 specimens with $s/d_b = 4.0$, transverse reinforcement ratio in the range $0.88 \leq \rho_y \leq 1.76\%$, with every other internal longitudinal bar restrained by a hoop leg or a crosstie. The xSBE set comprised 5 specimens with $s/d_b = 4.0$, transverse reinforcement ratio in the range $1.47 \leq \rho_y \leq 1.76\%$, with all internal bars tied by either overlapping closed hoops and/or crossties with seismic hooks. It is reported from the compression tests that only the xSBE specimens were able to sustain the peak load over increasing compressive strains, with limiting average strain capacity, at 30% strength loss, of approximately 3.5%. Additionally, longitudinal bar buckling was found to be a trigger for rapid loss of axial load carrying capacity. Reported average strain at which this occurred was approximately 2.0 and 3.5% for an SBE and xSBE specimen, respectively. For the SBE specimens, tensile strain excursions of 0.5, 2.0, and 5.0%, prior to compression, resulted in a reduction of the confined concrete strength of 5, 20, and 50%, with respect to specimens under monotonic compression. It was concluded that crossties do not provide significant restraint against longitudinal bar buckling and do not contribute sufficiently to achieving ductile behavior in compression. Hoops and crossties might not be interchangeable for providing restraint against lateral instability of the longitudinal bars.

The set of tests summarized above lead to the conclusion that specimens that meet the minimum requirements for OBE and SBE per ACI-318-14 do not necessarily achieve the intended deformation capacities in compression. The investigation presented in the following chapters explores some of the causes of this behavior.

Chapter 2 - Experimental Investigation

This chapter presents laboratory test results of the response of thin boundary element test specimens subjected to pure compression. The tested elements have transverse reinforcement detailing that matches or exceeds modern code requirements for special boundary elements. The test program comprised ten prismatic reinforced concrete specimens that were subjected to monotonically increasing axial compression until failure. The specimens can be considered to approximately represent the extreme flexural compression zone of the stem of a flanged wall. That region of a structural wall is subjected to high axial compressive strains due to combined axial force and moment. Effects of strain gradient (both through the wall length and along the wall height) and effects of wall shear are not represented in the present tests. Nonetheless, the axial compression tests are expected to provide insights into the behavioral characteristics of actual wall boundaries.

2.1 Test Specimens

A set of ten rectangular prismatic reinforced concrete specimens with aspect ratio (height-to-thickness ratio) of 6 were tested at the *nees@berkeley* laboratory. **Figure 2.1** depicts general geometric characteristics of the specimens. The set comprises specimens with cross section of dimensions 12.0 x 36.0 in. [305 x 914 mm] and clear height $h_w = 72.0$ in. [1,830 mm]. The specimens are considered full-scale and the cover thickness, measured to the outside edges of the perimeter hoop, was fixed at 1.5 in. [38 mm]. This thickness is larger than the 3/4 in. [19 mm] required as a minimum by ACI-318 (2014) for walls that are not exposed to weather or in contact with the ground, but is considered typical in practice because it avoids constructability issues that may arise when smaller cover thickness values are adopted. To more closely study the force-shortening response of the core, one of the specimens had a reduced cross section of 9 x 33 in. [229 x 838 mm], with no cover, located at mid height, with length equal to 30 in. [762 mm] (which corresponds to 2.5 times the thickness of the other specimens).

2.2 Design

The test program was conceived while the ACI-318-11 code was the latest approved version of ACI 318, but after field observations following the Chile (2010) earthquake showed that response of poorly detailed reinforced concrete wall boundaries was not satisfactory. To test the adequacy of the code provisions in use at that time, the transverse reinforcement of the specimens was detailed following ACI-318-11 provisions for special boundary elements (SBEs).

The need for SBEs at the edge of walls with aspect ratio (quotient of the wall height and its length) of at least 2, is defined in ACI-318 using two separate set of provisions: one uses a displacement-based approach, while the other uses a limiting stress-based approach. The first alternative applies to walls that are effectively continuous from the base to the top of the structure, with a single critical section for flexure and axial load. The compression zone of these elements require SBE detailing if

$$c \geq \frac{L_w}{600 \left[\gamma \left(\frac{\delta_u}{H_w} \right) \right]} \quad (2.1)$$

where c is the neutral axis depth, estimated under nominal moment strength and factored axial loads in the direction of the design displacement δ_u ; coefficient γ is 1.0 in ACI-318-11 and 1.5 in ACI-318-14; L_w and H_w are the length and height of the wall, respectively. The second alternative requires SBE-type of detailing in walls where the stress demand in the extreme fiber in compression exceeds 20% of the nominal compressive strength of the concrete (for example, $\sigma_u \geq 0.2f'_c$). This stress demand is estimated by means of a linear elastic model, using load combinations that include earthquake effects, and using gross cross section properties.

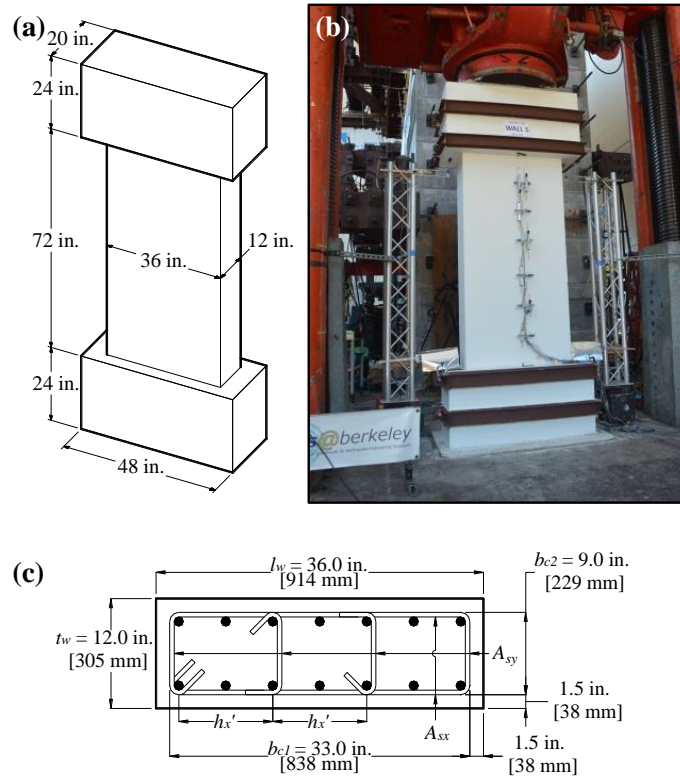


Figure 2.1 - Specimens global geometry (a), global view of test setup for specimen W5 (b), and cross section geometry and variables of interest (c). [Note: 1 in. = 25.4 mm].

Equations (2.2) and **(2.3)**, correspond to equations 21-4 and 21-5 of ACI 318-11 respectively, and define the minimum amount of transverse reinforcement required in the two orthogonal directions of a confined concrete column cross section.

$$\frac{A_{sh}}{sb_c} \geq 0.3 \frac{f'_c}{f_{yt}} \left(\frac{A_g}{A_{ch}} - 1 \right) \quad (2.2)$$

$$\frac{A_{sh}}{sb_c} \geq 0.09 \frac{f'_c}{f_{yt}} \quad (2.3)$$

where s [in.] is the center-to-center spacing of transverse reinforcement; b_c [in.] is the cross-sectional dimension of the core measured to the outside edges of the transverse reinforcement; A_{sh} [in.²] is the total provided cross-sectional area of transverse reinforcement within spacing s , and perpendicular to dimension b_c ; A_g is the gross area of the concrete section; A_{ch} is the cross-sectional area of the core measured to the outside edge of the perimeter hoop; f'_c is the specified unconfined concrete compressive strength; and f_{yt} is the specified yield strength of the transverse reinforcement. For special wall boundary elements, ACI 318-11 requires compliance with both, **Equation (2.3)**, while ACI 318-14 requires compliance with both, **Equations (2.2)** and **(2.3)**. **Equation (2.3)** can be understood as a lower limit to **Equation (2.2)**, to prevent having under reinforced cross sections whenever quotient A_g/A_{ch} tends to 1. This is likely for a cross section with a small cover thickness relative to outer dimensions of the boundary element.

2.3 Materials

Design nominal concrete strength was 4.0 ksi [28 MPa] at 28 days and reinforcing steel yield strength was 60.0 ksi [414 MPa] for all specimens. Actual unconfined concrete strength at the day of the test was estimated as the average strength of three 6 x 12 in. [152 x 304 mm] cylinders tested under standard ASTM-C39/C39M-12a (2012). All reinforcing steel is compliant with standard ASTM-A706/A706M-9b (2009). **Table 2.1** contains the material properties of the specimens as tested. Additionally, stress strain curves were obtained experimentally for some of the cylinders at the day of the test. **Figure 2.2a** contains a scattergram relating concrete strength f'_c with corresponding strain $\overline{\varepsilon}_{co}$, measured over an 8 in. [203 mm] gauge length. Mean concrete strain at peak strength was $\overline{\varepsilon}_{co} = 0.0030$ with coefficient of variation $COV = 5.3\%$. **Figure 2.2b** depicts typical stress strain curve for a 7/8 in. [22 mm] diameter longitudinal bar.

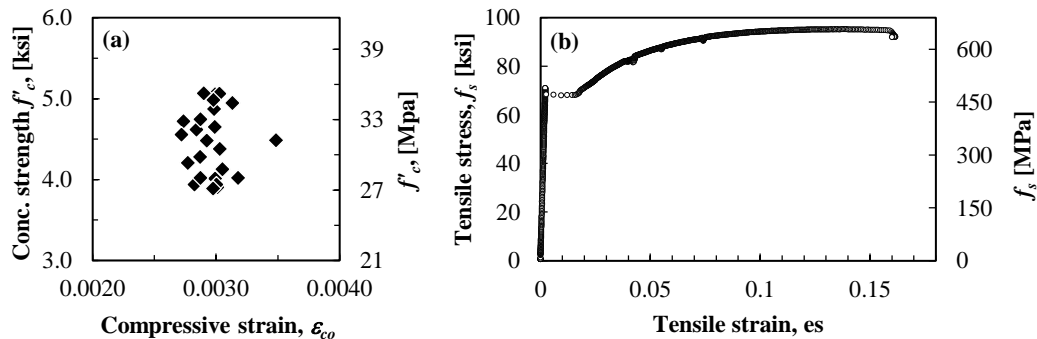


Figure 2.2 – Material properties: (a) unconfined concrete strength versus corresponding strain at the day of test; (b) experimental stress-strain curve for an A706 #7 longitudinal bar.

2.4 Variables of Investigation

It was of interest to validate whether compliance with either of the above equations have positive repercussions in the ductile behavior of boundary elements under pure compression.; hence, the design of specimens W3 through W14 complied with **Equation (2.3)** and specimens W9 and W12 also complied with **Equation (2.2)**. To study the impact of the distance between longitudinal bars engaged by crossties, the variable (h_x 's) is also studied. This variable represents the area of the “window” bounded vertically by the distance s between sets of hoops and crossties, and horizontally by the distance h_x' between longitudinal bars that are supported by

hoops and crossties (**Figure 2.3**). ACI-318-11 allows the maximum center-to-center distance between crossties or hoop legs of the boundary elements to be as large as 14 in. [356 mm], while ACI 318-14 allows the lesser of 14 in. [356 mm] and $2/3 t_w$. It was hypothesized that the ratio $h_x' s / A_{ch}$ in some code-compliant designs is too large to achieve effective confinement. Therefore, in this project the largest distance h_x' (measured center-to-center of tied bars) selected for the design of any of the specimens was 10.3 in. [262 mm] (approximately $0.85t_w$), while the shortest selected value for h_x' was 7.7 in. [196 mm] (approximately $0.65t_w$). This distance was selected as a minimum because it is believed that smaller values might hinder the concrete placement process in practice. Specimens W6 through W14 were designed using this value.

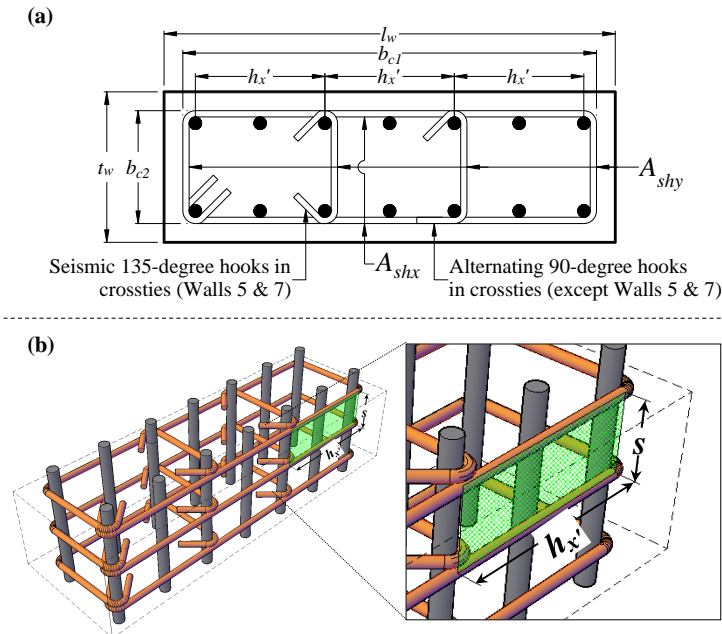
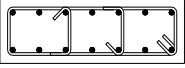
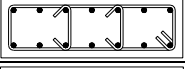


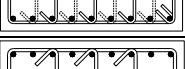
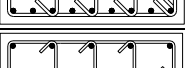
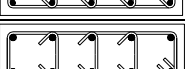
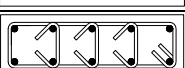
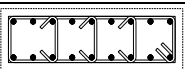
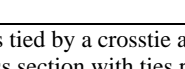


Figure 2.3 - Transverse reinforcement in wall specimens: (a) plan view of transverse reinforcement layer; (b) geometry of the “window” bounded by h_x' and s .

To review the relative capability of 90-degree hooks and 135-degree hooks to restrain longitudinal bars adequately, two pairs of specimens were constructed with identical transverse and longitudinal steel configuration, differing only in the configuration of their crossties: (i) W3 with W5 and (ii) W6 with W7. Specimens W3 and W6 had alternating 90- and 135-degree hooks at the crosstie ends, while specimens W5 and W7 only had 135-degree crosstie hooks.

The layout of ties along the height of specimen W8 was different from the rest of the specimens. This specimen has the same longitudinal reinforcement layout and nominal material properties as those of specimen W7, but a checkerboard pattern for the location of the crossties in plan and elevation was employed. With this design, each internal bar in the cross section is restrained by a tie at every other layer of transverse reinforcement. This can be contrasted with the design of specimens W3 through W7 and specimen W9, in which every other internal bar in the cross section is only restrained by the longer leg of the perimeter hoops. **Table 2.1** contains a summary of the characteristics mentioned above for all the specimens.

Table 2.1 - As tested material properties and reinforcement detailing

ID	Cross section	f'_c ksi (MPa)	f_y ksi (MPa)	f_{yt} ksi (MPa)	d_b in. (mm)	ρ %	s in. (mm)	s/d_b	h'_x in. (mm)	d_{bt} in. (mm)	ρ_x %	ρ_y %	$\rho_{x,ACI1}$ %	$\rho_{x,ACI2}$ %
3		3.8 (26)	68.8 (474)	72.2 (498)	1 (25)	2.6	4.0 (102)	4.0	10.3 (262)	1/2 (13)	1.10	0.60	0.71	0.47
5		4.0 (28)	69.6 (480)	65.0 (448)	1 (25)	2.6	4.0 (102)	4.0	10.3 (262)	1/2 (13)	1.10	0.60	0.85	0.56
6		4.2 (29)	67.9 (468)	65.0 (448)	7/8 (22)	2.5	4.0 (102)	4.6	7.7 (196)	1/2 (13)	1.10	0.75	0.89	0.58
7		4.4 (30)	67.9 (468)	65.0 (448)	7/8 (22)	2.5	4.0 (102)	4.6	7.7 (196)	1/2 (13)	1.10	0.75	0.91	0.60
8†		4.4 (30)	76.4 (527)	71.5 (493)	7/8 (22)	2.5	4.0 (102)	4.6 9.2+	7.7 (196)	1/2 (13)	1.10	0.82 ⁺⁺	0.84	0.56
9		4.6 (32)	76.4 (527)	70.3 (485)	7/8 (22)	2.5	4.0 (102)	4.6	7.7 (196)	5/8 (16)	1.70	1.16	0.90	0.59
10		4.7 (32)	76.4 (527)	71.5 (493)	7/8 (22)	1.4	4.0 (102)	4.6	7.7 (196)	1/2 (13)	1.10	0.75	0.90	0.59
11		5.1 (35)	77.6 (535)	71.5 (493)	1 1/4 (32)	2.9	4.0 (102)	3.2	7.7 (196)	1/2 (13)	1.10	0.75	0.97	0.64
12		4.4 (30)	77.6 (535)	70.3 (485)	1 1/4 (32)	2.9	4.0 (102)	3.2	7.7 (196)	5/8 (16)	1.70	1.16	0.85	0.56
14*		4.7 (32)	69.3 (478)	74.8 (516)	7/8 (22)	2.5	4.0 (102)	4.6	7.7 (196)	1/2 (13)	1.10	0.75	**	0.57

+ Bars tied by a crosstie are restrained at every other layer of transverse reinforcement.
 †Cross section with ties placed on a checkerboard pattern.
 ++ Average of two adjacent layers due to the checkerboard pattern used for laying out the ties.
 *Calculated values are for the reduced section portion of the specimen where $A_g = A_{ch}$.
 ** Does not apply because $(A_g / A_{ch} - 1) = 0$.
 A_{shx} : total cross-sectional area of transverse reinforcement within spacing s , in the long direction of the section.
 A_{shy} : total cross-sectional area of transverse reinforcement within spacing s , in the short direction of the section.
 b_{c1} : dimension of the long direction of the section core.
 b_{c2} : dimension of the short direction of the section core.
 h'_x : center-to-center horizontal spacing of tied bars in the long direction of the section.
 $\rho_x = A_{shx}/(b_{c2} \cdot s)$ and $\rho_y = A_{shy}/(b_{c1} \cdot s)$ are the provided transverse reinforcement ratios in the two principal directions of the cross section.
 $\rho_{x,ACI1} = 0.3f'_c / f_{yt} (A_g / A_{ch} - 1)$ and $\rho_{x,ACI2} = 0.09 f'_c / f_{yt}$ are estimated using “as tested” materials properties.

2.5 Instrumentation and Test Setup

Tests were performed using the Southwark-Emery Universal Testing Machine of the Pacific Earthquake Engineering Research Center (PEER). This machine, capable of applying monotonic load up to 4,000 kips [17,778 kN] in compression, is part of the *nees@berkeley* laboratory facility of the University of California, Berkeley. The load is applied by a variable axial piston pumping unit, which is able to control the load rate. **Figure 2.4** shows instrumentation and test setup of the experiments. Axial load was applied monotonically at a rate of 150,000 to 200,000 lb/min [667 to 890 kN/min]. Tests were terminated when the applied load dropped below approximately 30% of the maximum applied force. Applied load was measured by a built-in pressure capsule (PC) on top of the loading yoke. Average shortening of the specimen was

measured by the relative displacement of the top and bottom head using potentiometric displacement transducers (PDT) in the North and South sides of the specimens. String potentiometric displacement transducers (“*wirepots*”) were mounted on a distant reference wall to measure out-of-plane displacement at each load increment.

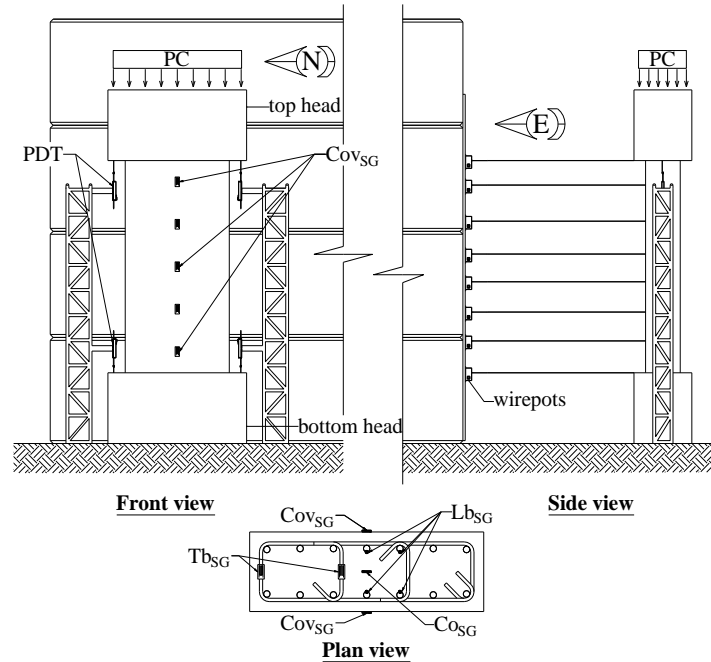


Figure 2.4 - Instrumentation setup.

For specimens W3 reinforcement strains were measured at specimen mid height, with one gauge on a longitudinal bar (Lb_{SG}), one on a hoop short leg, and one on a crosstie (Tb_{SG}). Specimens W5 through W7 had strain gages (Lb_{SG}) glued at mid height of the four corner longitudinal bars. These specimens also had strain gages in one tie and one hoop short leg (Tb_{SG}) at three different locations along the height. Wire strain gauges for the concrete surface (Cov_{SG}) were used to measure cover deformations in the vertical direction at various locations along the height of specimens W5 through W14.

To detect the onset of longitudinal bar buckling and the strain distribution in the bars, specimens W8 through W14 had strain gages (Lb_{SG}) glued at discrete locations (every 5 in. [127 mm]) along longitudinal bars on the West and East faces. Strain gages were also glued in one tie (Tb_{SG}) at every other layer of transverse reinforcement to measure transverse deformations in the through-thickness direction of the specimens. Additionally, to measure longitudinal strains (in the vertical direction) of the core of specimens W8 through W14, plastic strain gages (Co_{SG}) were embedded in the middle of the cross section at six discrete locations along the height. Gauge length for concrete (Cov_{SG} and Co_{SG}) and steel (Lb_{SG} and Tb_{SG}) strain gauges was 2.4 in. [60 mm] and 0.2 in. [5 mm], respectively. For all specimens, except W5, digital images were taken during the evolution of the test using a high resolution camera facing the West surface of the specimen. This side of the element had a random speckle pattern which changed with the evolution of the loading. This variation on the pattern is correlated to a corresponding displacement and strain field by means of the digital image correlation (DIC) technique (Chu et

al., 1985). **Appendix A** contains a description of the DIC technique and presents its application for the estimation of the strain field of specimen W7.

2.6 Test Results

2.6.1 General global response

The maximum initial load that a specimen can attain is limited by concrete cover spalling. A typical load-displacement relation, along with evolution of strains at discrete portions of the concrete cover, as well as damage evolution of the West face of specimen W7, is shown in **Figure 2.5**. Three instances of the test evolution are highlighted: (i) at peak load, (ii) at the onset of concrete cover spalling, and (iii) when the load carrying capacity drops to 30% of the maximum attained load, close to the test conclusion. **Figure 2.5a** shows the applied load versus shortening relation of the specimen. The initial theoretical stiffness is shown as well, and is estimated using the actual material properties at the moment of the test as

$K_0 = 1/h_w [E_c (A_g - A_s) + E_s A_s]$, where E_c is the concrete modulus of elasticity ($E_c = 57,000\sqrt{f'_c}$, psi). The parabolic nature of the ascending branch of the force-shortening relation shows an apparent deviation from the linear behavior at load levels close to 60% of the maximum load. The maximum load is limited by the onset of concrete cover crushing, after which there is an instantaneous small drop in load carrying capacity. For larger shortening values, the load carrying capacity of the specimen follows a steep descending branch, because plastic demand starts developing in a localized region of the length of the specimen. The localization of damage is explained by the occurrence of several fragile phenomena such as longitudinal bar buckling, tie hook opening and expulsion of core concrete. Out-of-plane displacement of the specimen also takes places due to the asymmetric nature of concrete cover spalling, which is facilitated by the large aspect ratio (height-to-thickness quotient) of the specimen. To further study the initiation of the cover spalling phenomenon, **Figure 2.5b** shows the axial strain distribution of the concrete cover of the West face, where the first sign of cover spalling was detected. The limiting strain of unconfined concrete is approximately 0.3% (**Figure 2.2a**), which coincides with the maximum strain values recorded by the lower two cover strain gages. Picture (ii) in **Figure 2.5c**, confirms that cover concrete crushing starts within the bottom third of the specimen and spreads upward with the evolution of the force-shortening relationship. After the first observed concrete crushing, the cover strains unload in different manners, depending on their location within the localized damaged zone. In the particular case of specimen W7, the strains in the gage at mid height reduce to zero because of the complete detachment of the cover at that location, which corresponds to the area of concentrated plastic deformation where bar buckling took place (**Figure 2.6**). The strain demand reduction in the upper two strain gages is explained by the relaxation of the undamaged portion of the specimen, which expands over the region of concentrated damage. It is worth mentioning that the bottom two strain gages are showing some compressive strains because threaded rods placed in the trough-thickness direction of the specimen prevented the large cover pieces from falling free and away. Therefore, they did not fully relax after their detachment from the core.

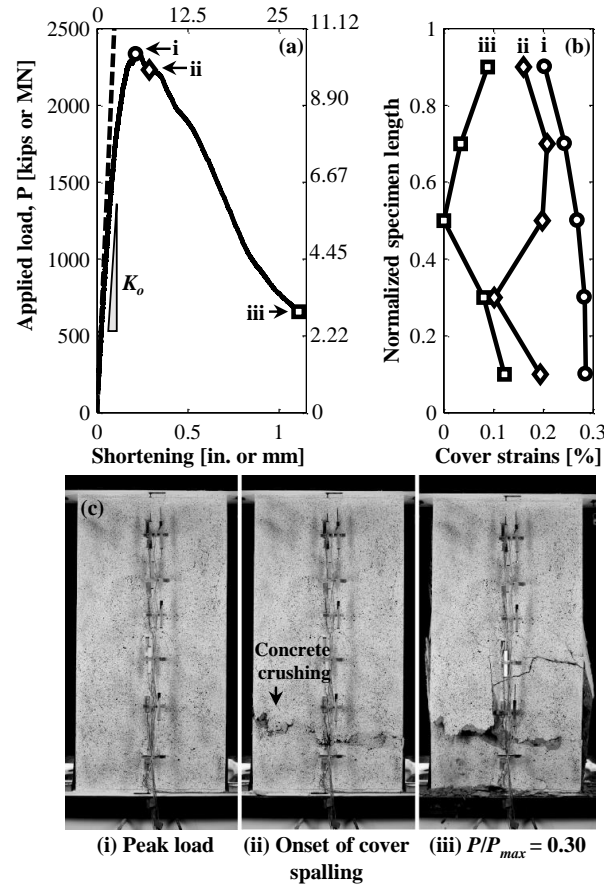


Figure 2.5 - Response evolution of Wall 7: (a) load-axial shortening relationship; (b) cover concrete axial strains evolution; (c) specimen damage evolution.

Figure 2.6 shows pictures of all specimens after each test was concluded and the specimens were cleaned up by removal of loose concrete. For all specimens, damage concentrated over a length of around two to three wall thicknesses along their height. Due to asymmetric concrete cover crushing and resulting out-of-plane displacements, the length over which spalling extended is different for the East and the West faces. This is expected because the eccentricity between the applied axial load and the centroid of the spalled-off cross section generates an over-turning moment that forces additional compressive stresses over one of the faces. The spalled-off zone includes a smaller portion of length equal to four hoops spacing (16 in. [406 mm]) approximately, over which bar buckling develops.

2.6.2 Response of specimen W14: onset of bar buckling

Specimen W14 was tested to study the force-shortening relationship of the confined core of the specimens. To force the damage to occur over a predefined zone, the specimen was constructed with no cover over a length of 30 in. [762 mm] centered at mid height. This selected length is equal to 2.5 times the thickness of the other specimens (W3 through W12) and approximately corresponds to damaged lengths observed in walls in the field after the 2010 Chile Earthquake (Wallace et al., 2012), as well as in laboratory tests on thin wall specimen that replicate the Chilean construction typology (Hube et al., 2014).

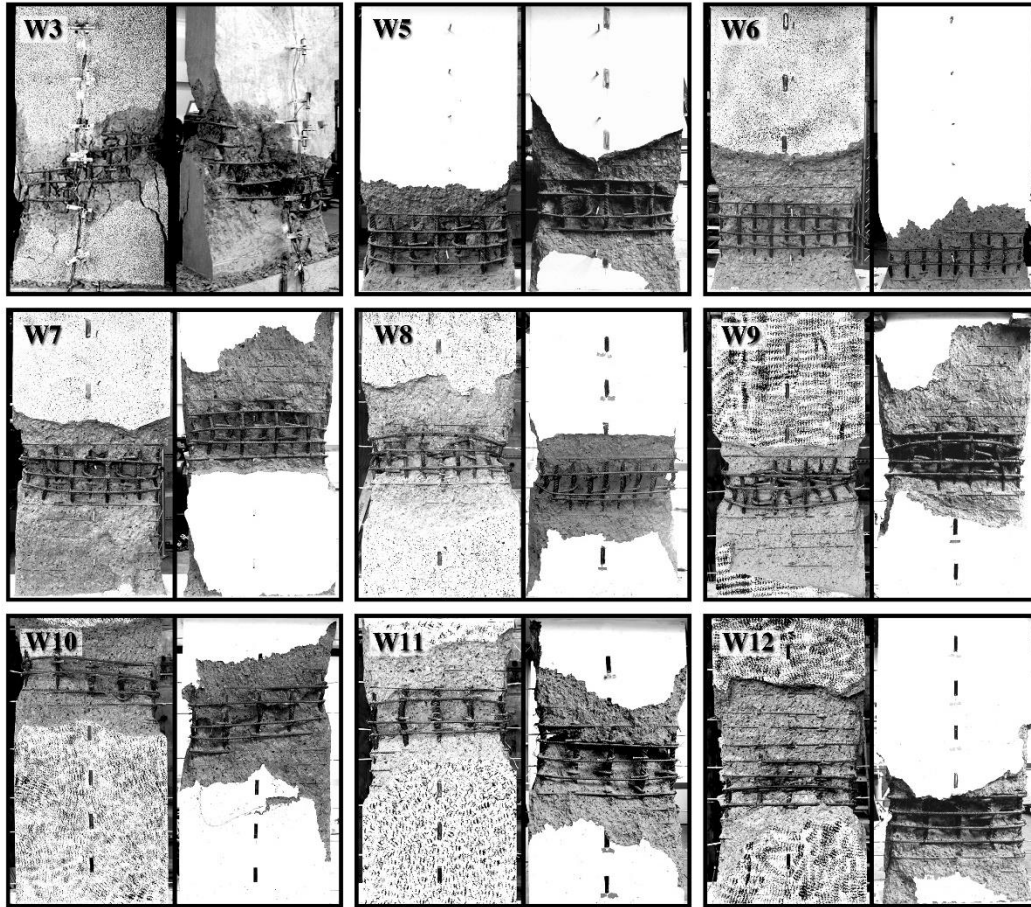


Figure 2.6 - Damage localization on the West (left hand side of each pair) and East face of the specimens.

Figure 2.7a shows the axial force versus average strain in the damage zone of specimen W14. The force is normalized by the nominal maximum load² $P_o = f'_c (A_g - A_s) + f_y A_s$ and the average compressive strain is estimated with two concrete strain gages placed in the middle of the cross section at one-thirds and two-thirds of the length of the reduced section zone. The onset of longitudinal and transverse bars yielding is marked at average axial strains of 0.0021 and 0.0045, respectively. The onset of tie yielding is related to expansion of the cross section and demarcates the start of a gentle softening slope after the peak load is attained. Yielding of the transverse reinforcement, in the absence of significant strain-hardening, can generally be expected to result in softening because, as the “plastic concrete” material expands outward it will become progressively less stable unless the out-of-plane resistance increases, which cannot occur for yielding transverse reinforcement. Horizontal cracks in the thin skin that covers the reinforcement are evidence of flexural deformations of the perimeter hoops, which is also associated with lateral instability of the longitudinal reinforcement. The failure sequence was recorded every 1/15 of a second and shows sudden expulsion of core concrete, which is triggered

² In the estimation of P_o , the concrete capacity is typically reduced by factor 0.85, to account for differences between standard cylinder and in-situ strength. This difference arises mainly due to water migration promoted by capillarity action in the early hardening stages of the concrete. This increases the water-to-cement ratio of the upper parts of the specimens, which results in reduced compressive strength of those areas. The specimens of this research were casted horizontally (West or East face facing down), therefore factor 0.85 is not used in the estimation of P_o throughout this investigation.

by the onset of bar buckling at an average compressive strain of 0.0086. The test was concluded when the rapid loss of load carrying capacity was detected. This allowed studying the geometry and states of the material immediately after the onset of failure, avoiding excessive crushing of the core and additional deformation of the buckled bars. Concrete expulsion resulted in a reduction of the core cross-sectional area. The evaluation of the damage zone after the test conclusion shows evidence of bar buckling of non-tied as well as tied bars (**Figure 2.7b**). For the former, observed buckling length is three to four hoops spacing ($14d_b$ to $18d_b$), depending on the location of the bar along the perimeter. The larger buckling length is for those bars closer to the center of the long hoop leg where its flexural stiffness offers less resistance against lateral displacement. Buckling length for the tied bars was approximately two tie spacings ($9d_b$), and included the opening of the 135-degree hook of the restraining tie.

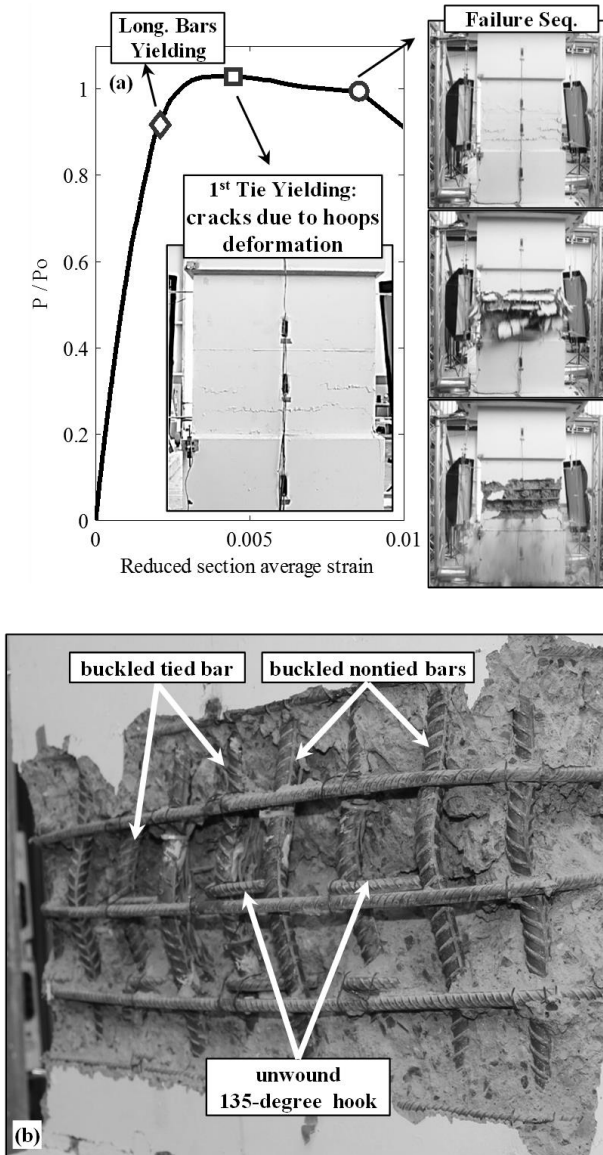


Figure 2.7 - Test evolution of specimen W14: (a) force versus average strain relationship and failure sequence of the damage zone; (b) details of the damaged zone.

Tensile strains in ties along the height of the reduced section are shown in **Figure 2.8a** at three different stages of the response of specimen W14: (i) at the first observed longitudinal bar yielding (diamond markers); (ii) at the first measured tie yielding (square markers); and (iii) at the onset of the sudden loss of load carrying capacity (circular markers). Tensile tie strain versus average compressive strain of the reduce section is depicted in **Figure 2.8b** for the two most demanded ties (Tb_{SG6} y Tb_{SG7}) located above mid-height of the reduced section zone. Location of the critical tie (Tb_{SG6}) approximately coincides with the top portion of the buckling length of a bar in the East face, and the bottom portion of a juxtaposed buckled bar on the West face. Before transverse reinforcement yielding, the transverse-to-average-axial strain ratio is approximately 0.55. This is larger than typical values of Poisson ratio for plain concrete but it is comparable to values reported by Mander (1984) for Wall 11, which was reinforced with ties and had a similar transverse reinforcement ratio in the through-thickness direction of the specimen. After yielding, the transverse-to-average-axial strain ratio further increases due to lateral expansion of the core and lateral displacement of the longitudinal bars. The onset of failure occurs for strains in the critical tie of approximately 1.5%.

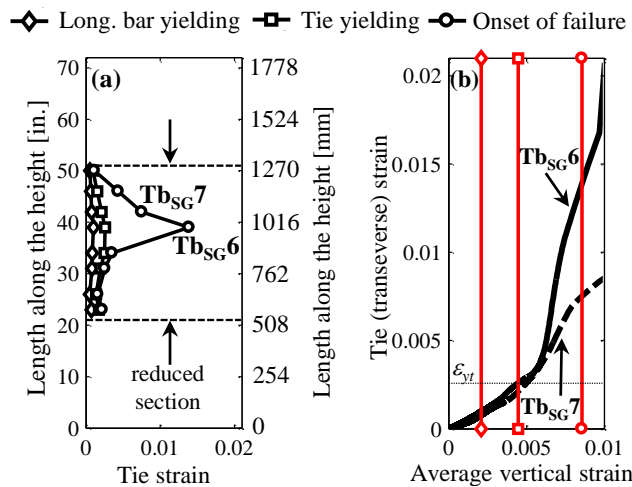


Figure 2.8 - Tensile tie strains of specimen W14: (a) tie strain distribution along the height of the reduced section zone at three instance of the test evolution; (b) critical ties strain versus average vertical strain in the reduced section zone.

Onset of loss of load carrying capacity of specimen W14 was triggered by lateral instability of the longitudinal reinforcement. **Figure 2.9a** and **Figure 2.9c** show the strain distribution along the height of both a tied and a non-tied bar on the East face of the specimen. The plots depict the same three stages of the response described for the ties above (that is, at first longitudinal bar yielding, at first tie yielding and at the onset of failure). It is observed that up to longitudinal bar yielding, the strain distribution is uniform along the entire length of the bars. After the first tie yielding, and up to the onset of failure, strains concentration is observed over three critical stain gages (Lb_{SG6}, Lb_{SG7} y Tb_{SG8}) on the tied bar and four critical gages (Lb_{SG5}, Lb_{SG6}, Lb_{SG7} y Tb_{SG8}) on the non-tied bar. To further understand the strain evolution, close and within the buckling length of the longitudinal bars, **Figure 2.9b** and **Figure 2.9d** show bar compressive strains at discrete locations versus the average compressive strain of the reduced section. Prior to first longitudinal bar yielding, the longitudinal bar-to-average-strain ratio is close to 1.0. This ratio increases for larger strains of the reduced section until strains in some portions of the bars start plateauing at different instants, depending on their location along the

buckling length. This is explained by the fact that strain gages are adhered facing the core, and outward lateral displacement of the bars will exacerbate their compressive strains until, due to bar buckling, three distinct plastic hinges form at the top, at the bottom, and at mid height of the buckling length (Dhakal & Maekawa, 2002). Once these concentrated plasticity zones develop, compressive strains in the gages closer to mid height of the buckling length will further increase while strains in other locations will relax. It is worth noticing, that prior to buckling, bar axial compressive strain rate increases at lower core average strains for the non-tied bars as compared to the tied bar.

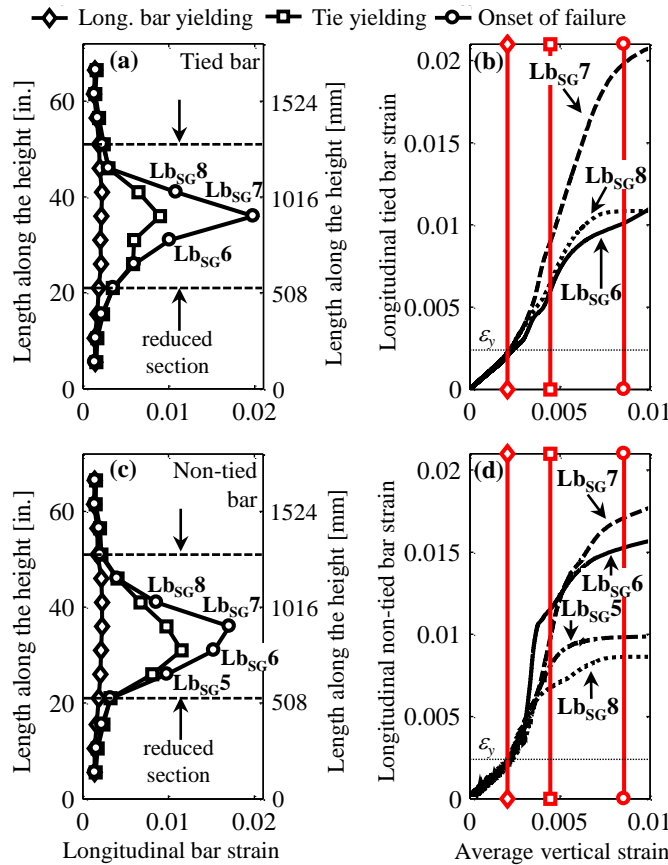


Figure 2.9 - Compressive strain evolution in longitudinal reinforcement on the East face of specimen W14: (a) tied bar strain distribution along the height; (b) tied bar longitudinal strain along the buckling length, versus average strain of damage zone; (c) non-tied bar strain distribution along the height; (d) non-tied bar longitudinal strain along the buckling length, versus average strain of damage zone.

2.6.3 Response of specimens W3, W5, W6 and W7: effect of the confining window size and crosstie hooks

Four specimens are considered to test the influence of the distance h_x' between tied bars, on the behavior of the prismatic elements. Specimens W6 and W7 had the same nominal material properties, gross geometry, separation s between transverse reinforcement layers and similar area of longitudinal reinforcement as W3 and W5, but the distance h_x' is 25% shorter (resulting in a 25% increase in the transverse steel ratio in the through-thickness direction, ρ_{ty}). In order to review the relative capability of 90-degree hooks and 135-degree hooks to restrain longitudinal bars adequately, the responses of specimens W3 and W6 are contrasted with that of specimens

W5 and W7, respectively. Specimens W3 and W6 had alternating ties with 90-degree hooks at one end and 135-degree hooks at the other, while ties on specimens W5 and W7 had two 135-degree hooks anchored into the core at both ends.

During the test, specimens W3, W5 and W6 experienced sudden drop of load-carrying capacity after very small plastic deformation was sustained past the peak applied force. This reduction of force occurred when the specimens achieved average strains in the order of 0.3%, after which loss of cover concrete occurred in an abrupt manner. **Figure 2.10a** shows force-displacement relations for these four specimens. Average strains were calculated as the ratio between the shortening of the wall (calculated from the relative displacements of the top and bottom heads) and its original clear height between heads. The applied load is normalized to the maximum nominal load P_o . It is observed that the response of the specimens was similar in terms of load carrying capacity and average plastic deformation. Even though specimen W7 did not suffer a sudden decrease in load carrying capacity after spalling, and its post-test inspection showed evidence of larger spread of plasticity, the slope of the softening branch for this specimen is very similar to that of the rest of test specimens.

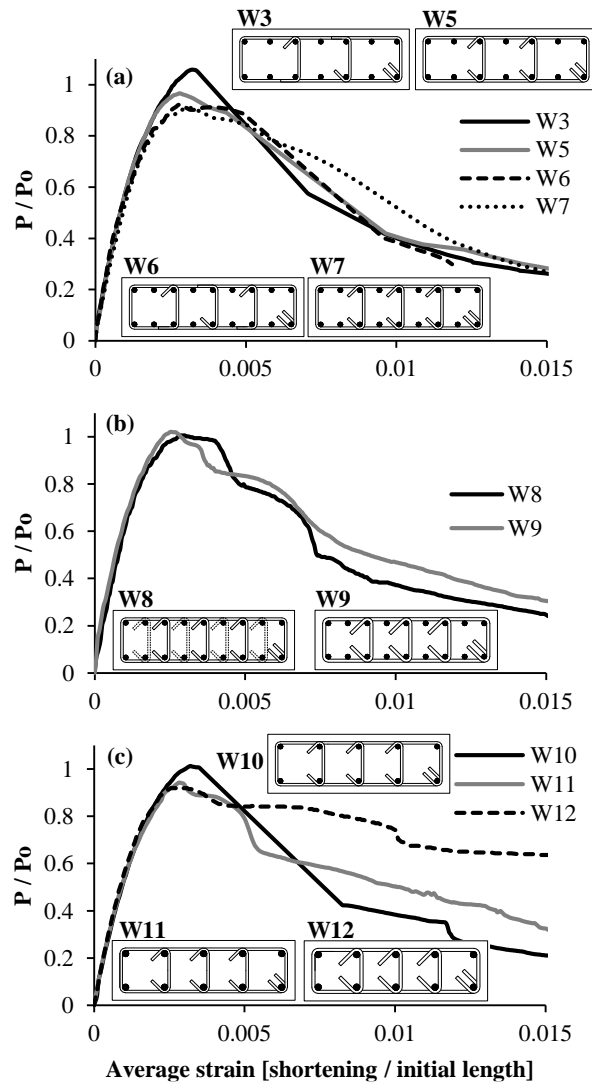


Figure 2.10 - Normalized force versus average strain relation for all specimens (gage length = 72 in. [1829 mm]).

To analyze the spread of plasticity along the length of the specimens, damage was measured in two ways: (i) as the length of the spalled-off portion on the face where the first sign of concrete crushing was; and (ii) as the average of the spalled-off length of the East and West faces of the specimens. **Figure 2.11** summarizes these values normalized by thickness, t_w , for all specimens. For specimens W3, W4, W5, and W7, the plastic deformations concentrated over portions comprising 24 to 56% of the clear height (h_w), corresponding to 1.4 to 3.3 times the specimen thickness. Results show that there is a slight improvement, in terms of the average spread of plasticity, promoted by the use of 135-degree seismic hooks in specimens W5 and W7 as compared to W3 and W6, respectively. Additionally, the smallest confining window size, $h_x's$, in specimens W6 and W7 as compared to W3 and W5, improved the spread of plasticity in the face where additional compression took place due to out-of-plane actions. All specimens with the smaller confining window show a slight improvement in spread of plasticity with respect to specimens W3 and W5. This is also explained in part by the larger amount of transverse reinforcement ratio in the through-thickness direction and by tighter mesh of vertical and horizontal reinforcement, which may tend to hold the concrete core concrete together.

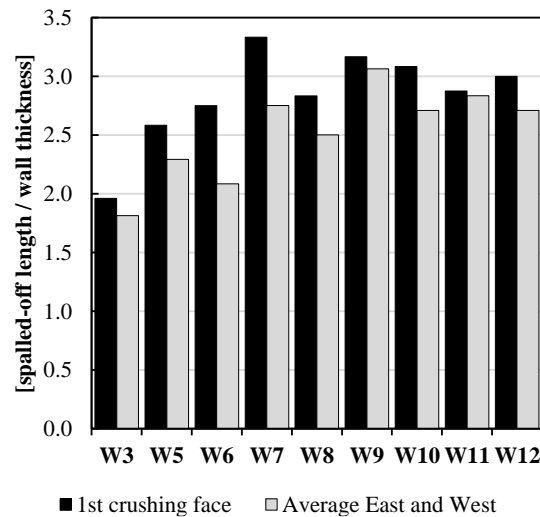


Figure 2.11 - Spread of plasticity.

2.6.4 Analysis of the post peak response (specimens W8 and W9): global lateral instability and rebar buckling

Specimen W7 showed a slight improvement in response when compared to specimens W3 to W6 because it did not exhibit a sudden loss of load carrying capacity, and the average length over which plastic deformation spread was about 20% longer than the aforementioned set. Albeit the improved behavior, the specimen was not able to sustain the maximum applied load after the onset of concrete cover spalling and it was hypothesized that the out-of-plane moment triggered early buckling of the longitudinal non-tied steel, hence preventing effective confinement of the concrete core. With this in mind, specimen W8 was conceived with the same geometry, nominal material properties and longitudinal reinforcement as specimen W7, but a change in the design was introduced by alternating the position of the ties, in a checkerboard pattern between adjacent layers of transverse reinforcement. The average transverse reinforcement steel ratio (calculated over the height of two adjacent layers of transverse steel) in the through-thickness-direction (ρ_{ty}) of specimen W8 is approximately 9% bigger than that of specimen W7. Excluding the four

longitudinal bars in the corners, a major difference introduced with the checkerboard pattern is that the ratio s/d_b is 9.2 for all internal bars in specimen W8. On the other hand, for specimen W7, this ratio is 4.6 for the tied bars, while the rest of the bars are only restrained by the flexural stiffness of the longer legs of the perimeter hoops.

Specimen W9 also had the same geometry, nominal material properties, and vertical and horizontal reinforcement layouts as specimen W7 but the diameter of the transverse steel bars was increased from $d_{bt} = 1/2$ in. [12.7 mm] to $5/8$ in. [15.9 mm]. With this variation, the specimen transverse reinforcement ratio increases by 55% with respect to specimen W7 and, additionally, the long hoop leg that provides restraint against lateral displacement of the non-tied longitudinal bars has bigger flexural stiffness. With the larger transverse reinforcement ratio, specimen W9 complies with the requirements of **Equations (2.2) and (2.3)** above. **Figure 2.10b** presents the normalized force versus average shortening relationship for specimens W8 and W9. Their force-average shortening response is similar to that of specimen W7, showing very limited ductility capacity after the peak load is attained. The average spread of plasticity of specimen W9 was approximately equal to three wall thicknesses ($3t_w$), while that of specimen W8 was close to $2.5t_w$.

To help understand the reason of the load resisting capacity reduction after the peak load is attained, **Figure 2.12a** depicts out of plane displacement profiles of specimen W9, normalized by its thickness, t_w . Out-of-plane response of specimens W3 to W8 is similar to that of specimen W9 but is not shown for the sake of brevity. Three instances of the response are highlighted: (i) at maximum load, which coincides with the onset of concrete cover crushing, (ii) at 90 percent of maximum load after the peak load is attained, and (iii) at 80 percent of maximum load after the peak load is attained. Out-of-plane instability is triggered by the asymmetric nature of concrete cover spalling, in which one face of the specimen crushes before crushing occurs on the opposite side. This behavior promotes an out-of-plane moment generated by the eccentricity of the applied axial load and the migrated centroid of the cross section. The double-curvature deformed shape developed is consistent with the observed damage in the upper portion of the East face and bottom part of the West face of the specimen (**Figure 2.6**). A rapid increase of lateral displacement can be observed after the maximum load is attained, even for small decrements of load carrying capacity. The largest out-of-plane displacement is observed at the location of the third *wirepot* from the top (WP7), and is directed toward the West. This is identified as a critical section worthy of further analysis.

An empirical axial force – moment interaction diagram for the test evolution of specimen W9 is constructed and compared with the theoretical PM failure surfaces in **Figure 2.12b**. The PM interaction surfaces are constructed assuming actual material properties at the moment of the test for two cases of cross section geometry: the outer orbit assumes the full cross section is available to sustain flexural compression demands and the inner one assumes half of the concrete cover has spalled off. The moment in the empirical PM curve is approximated as the applied axial load times the out-of-plane displacement at the critical section. It is observed that the maximum axial load is attained with relatively small lateral displacement. After the onset of concrete cover spalling, the out-of-plane moment grows rapidly and the empirical PM curve transitions from the outer orbit to the inner one, before a pronounced drop in axial load carrying capacity occurs.

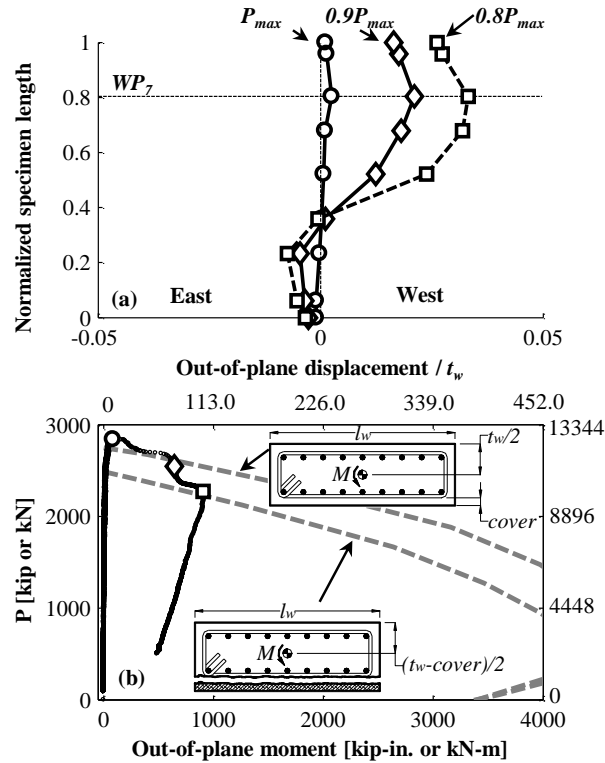


Figure 2.12 - Out-of-plane response of specimen W9: (a) normalized out-of-plane displacement profile; (b) Axial force – moment interaction relationship during the test evolution of specimen.

Longitudinal bar buckling leads to non-recoverable loss of strength and defines the usable limit strain of the specimens (Pantazopoulou, 1998). For specimen W9, buckling of tied longitudinal bars occurred over $4.5d_b$ and that of the non-tied bars occurred over $18d_b$ in average, corresponding to 1 and 4 tie spacings, respectively. On the other hand, internal bars in specimen W8 buckled over a length equal to $9d_b$, which corresponds to 2 tie spacings (due to the checkered board pattern used to layout the ties). **Figure 2.13** shows the influence of bar buckling on the post peak response of specimens W8 and W9. For this purpose, the force versus localized core axial strain response of each specimen is plotted along with the evolution of point wise strains of 7/8 in. [22.2 mm] longitudinal bars at three discrete locations within their buckling length. The local core strain response of each specimen is that of the core strain gauge (CO_{SG}) embedded within the region of concentrated plastic deformation, where rebar buckling occurred. The approximate buckling shape of a selected bar and the approximate relative location of the longitudinal bar strain gages (which face the concrete core) are also depicted. It is worth clarifying that, for specimen W8, the selected bar is laterally restrained by ties every 8 in. [203 mm], while for specimen W9, the selected bar is only restrained by the flexural stiffness of the long leg of the perimeter hoop every 4 in. [102 mm].

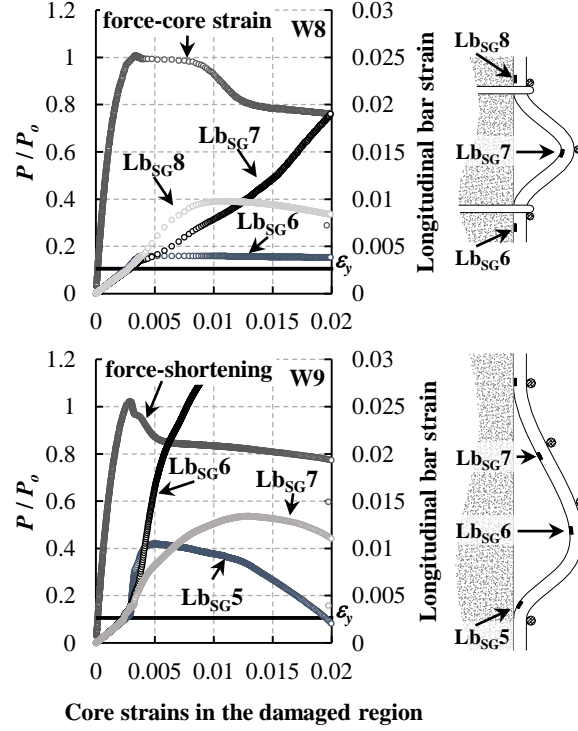


Figure 2.13 - Strain evolution in a buckled bar in specimens W8 and W9.

In both cases, the bar strains deviate from a linear behavior after the peak load is attained, and the bars have already yielded. At this point, cover spalling has initiated, removing some of the lateral restraint for the longitudinal bars to move outward. Analogous to the case of specimen W14, lateral instability of the longitudinal bars in the direction perpendicular to the East and West faces increases the compressive strain demand of those gages closer to mid span (central hinge) of the buckling length: these are identified as Lb_{sg7} for W8 and Lb_{sg6} for W9. Meanwhile, those gages away from the central hinge will relax as the lateral instability progresses. This relaxation occurs for localized bar strains (Lb_{sg8} for W8 and Lb_{sg7} for W9) between 1 to 1.5%, which is consistent with the observations for specimen W14.

An estimate of the relative load carrying capacity loss due to longitudinal bar buckling is given by **Equation (2.4)**:

$$\Delta P_b = (1 - \alpha) f_y A_{sb} \quad (2.4)$$

where A_{sb} is the area of those bars that buckle and α is a modifier of their yield strength. According to Monti and Nuti (1992), for the case of bars in the air under pure compression, a lower bound of the factor α can be estimated as:

$$\alpha \geq \frac{6}{\frac{L}{D}} \quad (2.5)$$

where L is the unsupported bar length and D its diameter. Unsupported length L can be approximated by the buckling length of the bars, which results in α factors of 0.65 for the internal bars of specimen W8 and 0.33 for the non-tied bars of specimen W9. Assuming an α

factor of 1 for the four corner bars of each specimen, which were adequately restrained by the short hoop legs, and 1 for the tied bars of specimen W9, which buckled over length $4.5d_b$, it is estimated that buckling of the internal bars of specimens W8 and W9 results in a 8.5% reduction in their theoretical maximum load carrying capacity (P_o). This is a small reduction that only explains in part the loss of axial force capacity observed after the peak load is attained, for local core strains on the order of 1.2% and 0.6% for specimens W8 and W9, respectively.

In addition to the loss in load carrying capacity, two other important effects of longitudinal bar buckling impact the post peak response of the specimens: (i) it reduce the effective confinement of the core, limiting its gain in strength, and (ii) it facilitates expulsion of concrete core material, thereby further reducing the effective available cross-sectional area.

2.6.5 Response of specimens W10, W11 and W12: cross sections with all bars tied

Specimen W10 was nominally identical to specimen W7, except the unsupported longitudinal bars of specimen W7 were not included in specimen W10. This resulted in a 56% reduction in the longitudinal steel ratio (ρ_l). This specimen was constructed to test the hypothesis that the non-tied bars in the cross section could have an unfavorable impact in the global response of the specimens due to their proclivity to buckle under low plastic strain demand. Specimens W11 and W12 had the same longitudinal reinforcement layout as specimen W10, but the longitudinal reinforcement ratio was increased to 2.9% by using 10/8 in. [32.3 mm] diameter bars. The resulting s/d_b ratio for these two specimens is 3.2. Nominal transverse reinforcement of specimens W11 and W12 was identical to that of specimens W7 and W9, respectively. **Figure 2.10c** and **Figure 2.11** depict normalized force versus average shortening relationships and extent of cover spalling for specimens W10, W11 and W12.

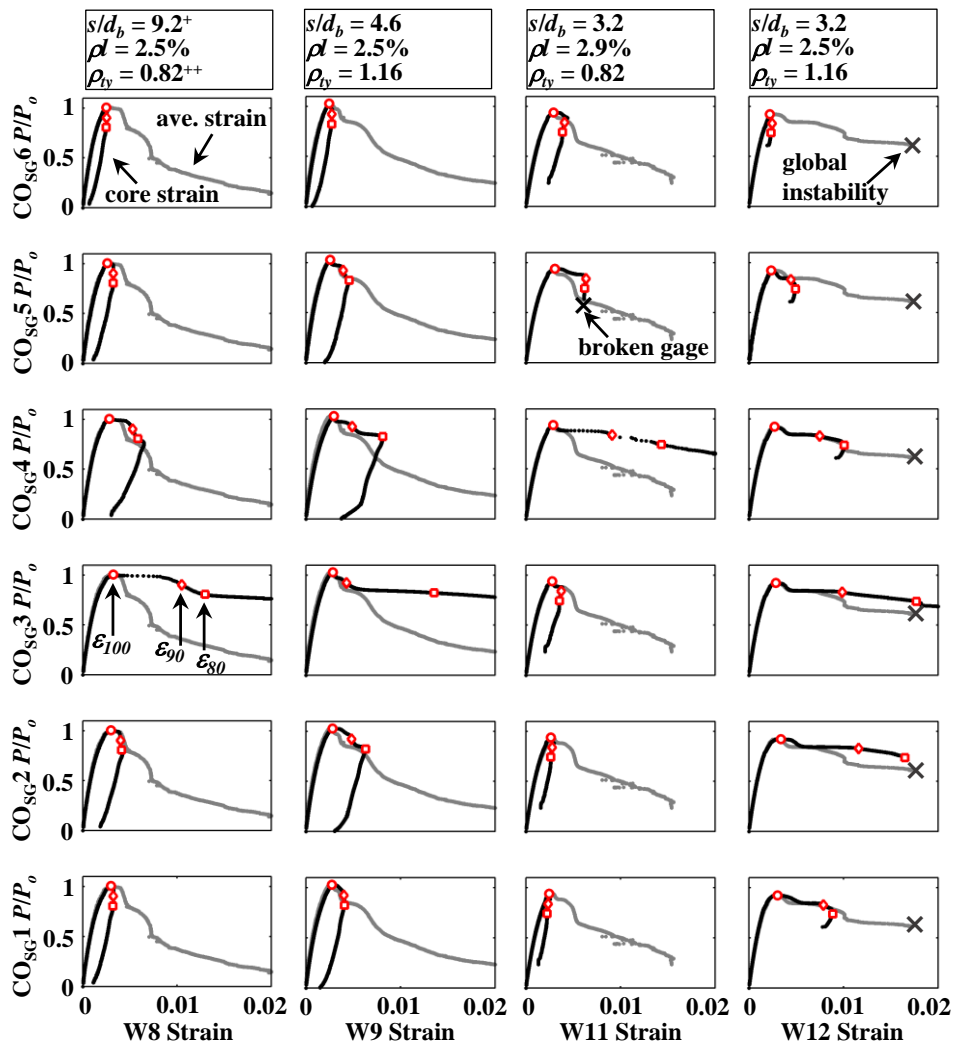
Specimen W10 suffered from an abrupt loss of load carrying capacity instants after the peak load was attained. Loss of cover area for this specimen did not progress gradually. On the contrary, a large cover slate of approximately 38% the specimen height detached from the core at average strain of around 0.3%, limiting the load carrying capacity of the specimen. The lower longitudinal steel ratio in this specimen resulted in reduced bending moment capacity, offering low resistance to the out-of-plane moment.

The force versus average shortening response of specimen W11 is similar to that of specimens W7, showing reduced average ductility capacity after the peak load is attained. Buckling of the internal longitudinal bars developed over 3 tie spacings (approximately $9.5d_b$) and forced the opening of the 135-degree hooks of two adjacent ties. Post-test analysis, however, showed limited lateral outward displacement of these buckled bars as compared to those in specimens W3 to W10. This is explained by the reduced s/d_b ratio resulting from the large diameter bars used as longitudinal reinforcement.

Specimen W12 showed an improved average force-shortening response with respect to the rest of the specimens. Longitudinal bar buckling was completely inhibited by the larger diameter bars used for the transverse reinforcement, as compared to specimen W11. The specimen failed due to global out-of-plane lateral instability at an average axial strain of approximately 1.8%.

To further study the post peak response of the specimens, **Figure 2.14** presents plots of normalized force versus axial core strains for specimens W8, W9, W11, and W12. These strains

were measured with the embedded plastic strain gages (CO_{SG}) at six discrete locations along the length of the prisms. Normalized force versus average axial strain relationships are also presented for the sake of comparing local and global deformation demand. Three instants of the response are highlighted and denoted ϵ_{100} (circular markers), ϵ_{90} (diamond markers), and ϵ_{80} (squared markers). These define, respectively, the local strain per level at which the peak load is attained, and the strains at which the load carrying capacity of the specimen dropped to 90% and 80% of the maximum. This facilitates understanding features related to the localization of strains, and relaxation response, and offers another perspective on the spread of plastic deformation. It is observed that as loading progresses past the peak load, a single gage is exposed to the largest compressive strain demands, while adjacent gages, and those farther apart, only develop some limited strains before unloading. In some locations, relaxation occurs with a slope close to the initial elastic stiffness, exactly after the peak load is reached.



Note: average strain gage length = 72 in. [1829 mm]; core strain gage length = 2.4 in. [60 mm]; +Bars tied by a crosstie are restrained at every other layer of transverse reinforcement; ++Average of two adjacent layers due to the checkerboard pattern used for laying out the ties.

Figure 2.14 - Force versus core deformation response at various levels along the length of the specimen

2.7 Implications of the Results

2.7.1 Usable strain limits

Axial strain limits of the prismatic elements tested are proposed next. Where flexural compression yielding is expected, these strain limits are useful for estimating usable curvature values of multistory shear walls, with comparable boundary elements at the extreme of their critical section. The proposed limits are based on strains measured at the ε_{90} and ε_{80} strength levels. The value ε_{80} is selected as an upper limit of strain capacity, because at larger strains, the reduction of load carrying capacity is associated to global lateral instability, longitudinal rebar buckling, and loss of core area, which might occur abruptly. Only data for specimens W8, W9, W11, and W12 are presented because those had embedded core strain gages, and did not suffer from sudden loss of load carrying capacity.

Axial strains must be associated to the gage length they are measured over. For this, the mean strain from contiguous gages is estimated taking into account 1 to 6 of the gage measurements at the various levels along the length of the wall. The span covered by the set of transducers involved in this estimation is assigned as gage length (GL). In order to specify maximum usable strain capacity associated with different gages lengths, **Figure 2.15** shows plots of ε_{90} and ε_{80} values versus gage length normalized by the wall thickness (GL/t_w). The Power regression curves shown are estimated according to

$$\varepsilon_{max} = \varepsilon_1 (GL / t_w)^{-\beta} \quad (2.6)$$

where ε_{max} is the maximum usable strain, and coefficients ε_1 and β , are summarized in **Table 2.2**.

The drop in load carrying capacity observed shortly after the peak load is attained in specimen W9 explains the lower limiting strain at the ε_{90} strength level. Strain limits at the ε_{80} strength level are similar among specimens W8, W9, and W11. Larger ultimate strain capacities are apparent for specimen W12 at both the ε_{90} and ε_{80} strength levels. Since point-wise strain tends to infinity in theory (for example, for zero gage length), a minimum gage length of one wall thickness is recommended, and to be consistent with the spread of plasticity data presented in **Figure 2.11**, a preferred range is between 2 and $3.5t_w$.

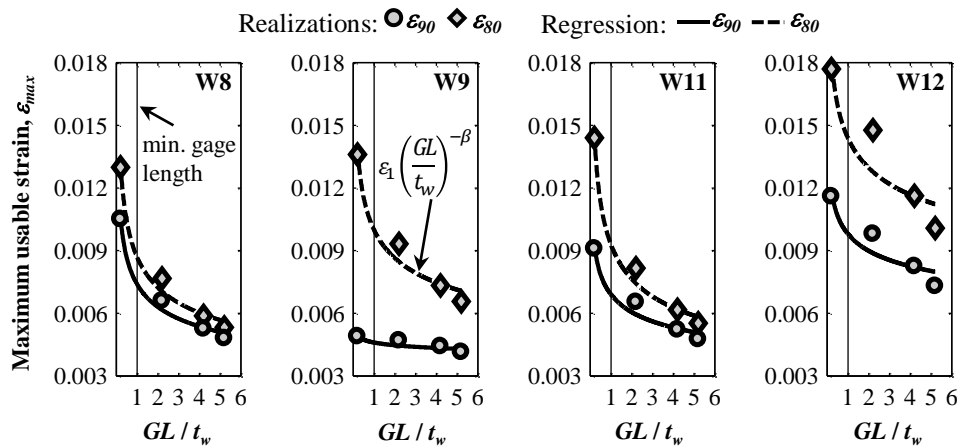


Figure 2.15 - Usable strain limits versus normalized gage length for specimens W8, W9, W11 and W12.

Table 2.2 - Regression coefficients for strain limits calculations

ID	$\epsilon_{1,90}$	β_{90}	$\epsilon_{1,80}$	β_{80}
W8	0.0074	0.231	0.0087	0.265
W9	0.0046	0.042	0.0100	0.210
W11	0.0069	0.188	0.0093	0.284
W12	0.0098	0.124	0.0144	0.151

2.7.2 Global displacement and local strains relationship

To contextualize the implications of the proposed strain limits in terms of a gage length, the lateral force resisting mechanism of the reinforced concrete shear wall presented in **Chapter 1** is repeated in the following for the sake of clarity. With the main objective of relating global displacement demand with local deformation capacity at the section level, **Figure 2.16** shows a four-stories T-shape structural wall with a single critical section at the base. The wall is subjected to lateral load F_x , at the roof, and axial load P , near the base. The prisms studied in this paper are also depicted in natural scale (1:1) for the sake of contextualizing their proportions. Under the action of lateral force F_x , the roof of the wall displaces laterally δ_u , pushing the system into the inelastic range of response. Under the action of this point load, the moment distribution along the height of the wall is linear. For adequately reinforced cross sections with typical yield-to-cracking moment ratio, the curvature distribution along the height of the wall can be approximate by an elasto-plastic model (M. J. N. Priestley & Park, 1987). This model decomposes the curvature distribution into an approximate linear elastic part, with yielding curvature ϕ_y , and another plastic portion with ultimate curvature ϕ_u (**Figure 2.16c**). It is common practice to assume that this ultimate curvature is uniform, equal to that of the critical section (for example, at the base), and that it extends a plastic hinge length equal to L_p . With this curvature distribution, the roof displacement can be estimated by the Principle of Virtual Work as:

$$\delta_u = \frac{\phi_y H_w^2}{3} + (\phi_u - \phi_y) L_p \left(H_w - \frac{L_p}{2} \right) \quad (2.7)$$

where H_w is the height of the wall. The first term of **Equation (2.7)** is the elastic contribution to the roof displacement, while the second term is the plastic contribution, which occurs as an additional rigid body rotation pivoting at mid height of the plastic hinge length. This model describes well the displacement due to the distribution of deformation along the element length, and with proper selection of length L_p , indirectly accounts for other mechanisms contributing to displacement such as bar slippage and tension shift (Moehle, 2014).

Alternatively, a simpler phenomenological plastic hinge model that allows direct estimation of roof displacement from ultimate plastic curvature capacity at the critical section is presented in **Figure 2.16d**. This model is useful to compare the impact of the strain limits proposed in this paper, by relating local level capacity such as limiting strains in the boundaries of a wall, and global level demand such as roof drift ratio (δ_u/h_w). This simple model has been extensively used in the literature (Moehle, 1992; M.J.N. Priestley et al., 2007; Wallace & Orakcal, 2002), and is the basis of provision in ACI-318-14§18.10.6.2, that evaluate the need for special boundary elements in structural walls with a single critical section at the base. The model assumes that the plastic hinge is centered at the base of the wall, and that the totality of the roof displacement is due to plastic rotation, θ_{pu} . This implies a rigid body motion of the cantilever wall, pivoting at the base, hence the roof displacement is given by:

$$\delta_u = \theta_{pu} H_w \quad (2.8)$$

Assuming the curvature is uniform along the selected plastic hinge length, it is possible to estimate the plastic rotation in terms of the ultimate unit deformation of the fiber under maximum compression, ε_{cu} :

$$\theta_{pu} = \phi_u L_p = \left(\frac{\varepsilon_{cu}}{c} \right) L_p \quad (2.9)$$

where ϕ_u is the ultimate curvature, and c is the depth of the neutral axis measured from the fiber under maximum compression. The impact of the results of the compression tests described above can be evaluated from a displacement-based perspective, by making plastic hinge length, L_p , equal to gage length, GL , and ultimate compressive strain, ε_{cu} , equal to ε_{max} (**Equation (2.6)**). Consequently, the plastic rotation in **Equation (2.9)** becomes:

$$\theta_{pu} = \left(\frac{\varepsilon_1}{c} \right) \left(\frac{L_p}{t_w} \right)^{-\beta} L_p \quad (2.10)$$

Combining **Equations (2.8)** and **(2.10)**, the roof drift ratio can be estimated in terms of a normalized plastic hinge length (L_p/t_w), the wall thickness t_w , and a set of coefficients associated to strain levels ε_{90} or ε_{80} :

$$\frac{\delta_u}{H_w} = \left(\frac{\varepsilon_1}{c} \right) \left(\frac{L_p}{t_w} \right)^{-\beta} L_p = \left(\frac{\varepsilon_1}{c} \right) \left(\frac{L_p}{t_w} \right)^{1-\beta} t_w \quad (2.11)$$

and coefficients ε_1 and β can be found in **Table 2.2**.

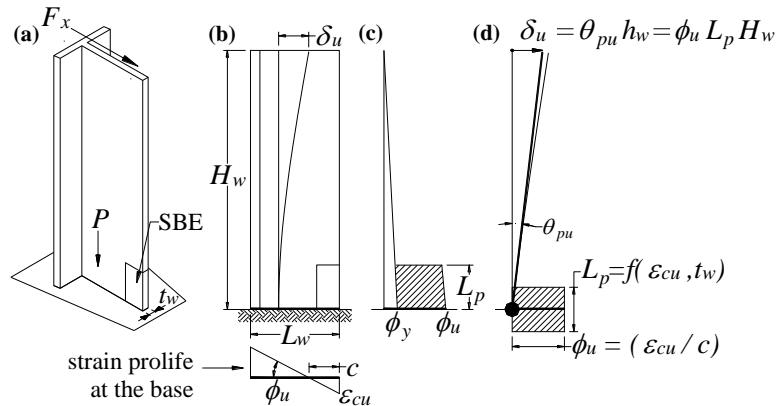


Figure 2.16 - Plastic hinge model: (a) wall under lateral and vertical loading; (b) wall global and local deformation profiles; (c) idealized elastic and plastic curvature distribution; (d) plastic hinge model.

Figure 2.17 compares the response of a hypothetical reinforced concrete wall of total height H_w , which boundary elements at the critical section have similar reinforcement characteristics, and assumed axial deformation capabilities, as those in specimens W8, W9 and W12. Response of specimen W11 is similar to that of specimen W8; therefore, its results are not presented for brevity. Given a selected plastic hinge length, the y-axis values in **Figure 16** are associated to a conservative roof drift ratio capacity because of the strain gradient present in

actual boundary element of walls subjected to lateral displacements, which was not accounted for in the experimental campaign presented here.

It is observed that although the maximum usable compressive strain, ε_{max} , decreases rapidly (in a Power fashion) with increasing plastic hinge length, the displacement capacity of the wall increases in an approximately linearly manner with increasing plastic hinge length.

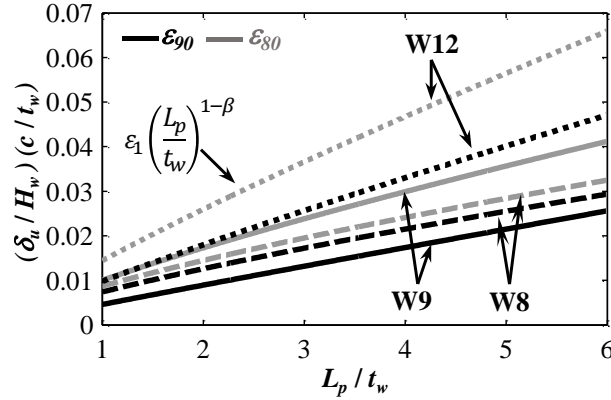


Figure 2.17 - Limiting normalized roof drift ratio versus selected plastic hinge length.

Another alternative to measure the implications of the proposed strain limits is based on the plastic hinge model presented by Takahashi et al. (2013) (**Figure 2.18**). As summarized in **Chapter 1** above, this model is based on the experimental data of ten reinforced concrete walls, designed to ensure flexural compression yielding of one of the boundaries. The model assumes that plastic compressive strain (ε_p) is uniform and concentrates near the bottom of the wall, over a small area bounded horizontally, by neutral axis depth c , and vertically, by plastic high length L_p . On the other hand, the area in tension is trapezoidal, extending over the whole height of the specimen. The remainder area is assumed to rotate as a rigid body, pivoting around the neutral axis (N.A.), on a plane located at L_p from the base. For loading direction compressing the weak boundary, the plastic component of the flexural drift (R_p) is defined as the rotation of this rigid area according to **Equation (2.12)**:

$$R_p = \frac{L_p}{c} \varepsilon_p \quad (2.12)$$

and the plastic strain (ε_p) of the compressed edge is the component of the ultimate strain (ε_{cu}), in addition to the strain at yield. For the specimens with ties at the boundaries, the strain at yield was estimated as 0.1%; therefore the plastic strain can be approximated as $\varepsilon_p = \varepsilon_{cu} - 0.001$.

To introduce the experimental results presented in this paper, the maximum compressive strain ε_{cu} is equated to ε_{max} from **Equation (2.6)**, and gage length GL is replaced by L_p , to estimate the plastic rotation R_p , in terms of a relative plastic hinge length as presented in **Equation (2.13)**.

$$R_p = \frac{t_w}{c} \left[\varepsilon_1 \left(\frac{L_p}{t_w} \right)^{1-\beta} - 0.001 \frac{L_p}{t_w} \right] \quad (2.13)$$

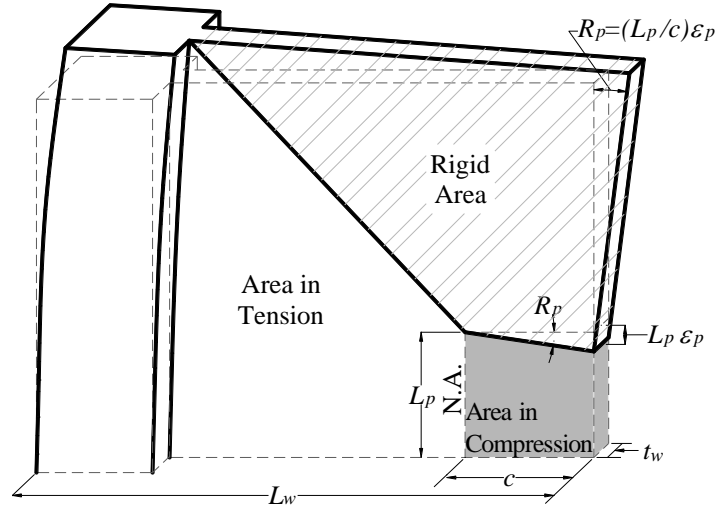


Figure 2.18 - Two-dimensional plastic hinge model (adapted from Takahashi et al. (2013)).

Eight of the specimens presented in (Takahashi et al., 2013) are selected, and their plastic flexural drift R_p is estimated (with **Equation (2.13)**) and contrasted with the experimental results. For this purpose, values for t_w/c are obtained from the experimental data of the aforementioned article. Coefficients $\epsilon_{l,80}$ and β are selected at the ϵ_{80} strength level from specimens W8 and W11 (of this study) to estimate, respectively, the maximum strain capacity of specimens with staggered ties and specimens with crossies restraining every bar at every layer of transverse reinforcement in the weak boundary. The specimen without crossies and another with very low axial load ($P < 0.03A_g f'_c$), which resulted in a shallow neutral axis depth, shorter than the extension of the boundary element, are not evaluated. **Table 2.3** contains the normalized axial load of each specimen and the set of variables required by **Equation (2.13)**. **Figure 2.19a** compares the experimental results with estimations of R_p using $L_p/t_w = 2.5$, as assumed by Takahashi et al. (2013), and $L_p/t_w = 3.5$, which is an upper limit observed in the experimental results presented above (**Figure 2.11**).

Table 2.3 - Selected specimens and input variables for estimating plastic flexural drift R_p .

Specimen ID	t_w/c	$P/A_g f'_c$	$\epsilon_{l,80}$	β_{80}
NM4	0.25	0.084	0.0093	0.284
NM5	0.20	0.062	0.0093	0.284
NS3 [†]	0.33	0.080	0.0087	0.265
NM3 [†]	0.33	0.054	0.0087	0.265
NM2 [†]	0.50	0.044	0.0087	0.265
PL6 [†]	0.17	0.059	0.0087	0.265
PM5 [†]	0.20	0.066	0.0087	0.265
PM3 [†]	0.33	0.049	0.0087	0.265

[†]Specimen with staggered ties

An acceptable representation of the experimental results is observed; the absolute value of the relative error for estimations using the shorter plastic hinge length $L_p/t_w = 2.5$, ranges from 1% to 35%, with mean error of 19% and coefficient of variation of 79%. For estimations using $L_p/t_w = 3.5$, the relative error ranges from 13 to 31%, with mean error equal to 19% and coefficient of variation of 34%. The residuals between the observed and the estimated data (δR_p

$= R_{p,observed} - R_{p,estimated}$) were compared with all the relevant variables of the experiment. A weak correlation with the applied load was observed, in which the residuals grow with increasing applied load. A correction factor of the form $\delta R_{p,c} = \theta_1(P/A_g f'_c) + \theta_2$ was applied to the estimations in **Figure 2.19a**, and the results are presented in **Figure 2.19b**. The parameters of the correction are $\theta_1 = 6$ and $\theta_2 = -0.33$, and the resulting mean relative error reduced to 15% for the two plastic hinge length used.

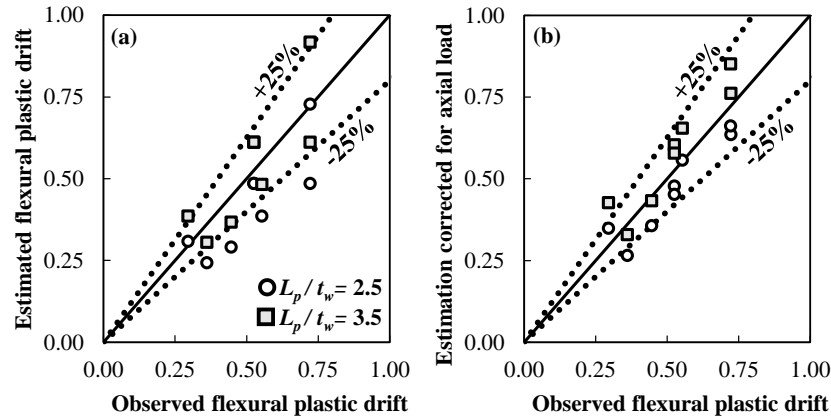


Figure 2.19 - Comparison between estimated and observed plastic flexural drift.

2.8 Further Research

In reinforced concrete thin cross sections, crossties might not adequately prevent lateral instability of longitudinal bars under relatively low plastic strain demand. Seismic hooks do not offer effective restraint to the longitudinal bars because the hooks open at the onset of lateral displacement of the bars. Future investigations should explore the effectiveness of hoops instead of crossties as internal transverse reinforcement. This will inhibit hook opening and will add additional flexural stiffness to restrain bar that are not engaged by a hoop leg (non-tied bars).

2.9 Final Comments

Results from compression tests of ten full-scale reinforced concrete prisms, representative of the boundaries of thin shear walls in seismic zones, were described. The specimens are compliant with ACI-318-11 and -14 seismic provisions for detailing of special boundary elements. Two main objectives of the tests were (i) to evaluate different layouts of transverse reinforcement using crossties to support longitudinal bars and confine the concrete core, and (ii) to estimate the axial deformation capabilities and associated spread of plasticity in slender rectangular prisms under compressive loading. Outcomes of this investigation suggest that current building code requirements for special boundary elements do not necessarily guarantee the achievement of effective confinement to protect their sections against brittle axial failure. The global force-shortening behavior of the specimens was controlled by a thin core whose integrity can be compromised due to cover spalling, longitudinal reinforcement buckling, and out-of-plane instability. Enhanced detailing (increasing the volumetric ratio of confinement reinforcement and decreasing its horizontal spacing) improved behavior but did not produce ductile response in all cases. Based on the experimental and analytical results, the following conclusions are obtained:

- i. Analysis of the deformation capacity of the confined core of specimen W14, with crossties only restraining every other internal longitudinal bar in the cross section, showed that the flexural stiffness of the long leg of rectangular hoops is insufficient to restrain longitudinal reinforcement from buckling. Recorded average strain of the confined core at the onset of bar buckling was approximately 0.9%. This value seemed limited by early lateral instability (buckling) of the non-tied longitudinal bars, which was triggered under small plastic deformation after yielding. Bar buckling was accompanied by expulsion of concrete core material, further reducing the resisting area, resulting in rapid loss of axial load carrying capacity.
- ii. The behavior of slender prismatic elements under pure compression is highly influenced by the asymmetric nature of concrete cover spalling. Asymmetric spalling leads to eccentricity between external forces and internal resistance, producing an out-of-plane moment that leads to additional out-of-plane displacement and, potentially, to instability in the through-thickness direction of the specimen. Walls with large cover-to-core thickness, as in the case of the test specimens, are especially prone to this type of behavior.
- iii. Cover spalling was observed over an average height comprising between 2 to 3 times the wall thickness. Additional damage localization occurred over lengths where bar buckling took place, which typically occurred over 3 to 4 hoop spacings (approximately 1 to 1.3 times the specimen thickness). This impacted the average strain ductility capacity of the specimens because portions of the prisms outside the damage zone did not develop plastic strain demand after the peak load was attained, but instead unloaded and relaxed with an unloading slope comparable to the initial elastic stiffness.
- iv. Buckling of the longitudinal reinforcement was observed at local plastic strains between 0.9 and 1.5%. This phenomenon had two consequences: (a) it reduced the post-spalling axial capacity of the longitudinal bars and (b) it reduced the post-spalling axial capacity of the confined core. These two effects led to post-spalling strength that was substantially less than the spalling load, such that plasticity did not spread along the test specimen height.
- v. Recorded buckling length for tied bars extended between 4.5 and 9.5 longitudinal bar diameters ($4.5 \leq d_b \leq 9.5$), and included, in most cases, the opening of the 90- and/or 135-degree hooks of the restraining crosstie. For non-tied bars, that is, those only restrained by the long leg of the perimeter hoop, buckling length extended between 14 and $18d_b$.
- vi. The measured average force-shortening relationship for specimens W3 through W11 was similar, developing a steep post peak descending branch at average strains ranging from 0.3 to approximately 0.5%. Response of specimen W12 showed an improved response with respect to the rest of the specimens. For this specimen longitudinal bar buckling was inhibited thanks to the larger diameter bars, the elimination of non-tied bars within the cross section, and the increase of volumetric ratio of confinement reinforcement. The specimen failed due to global out-of-plane lateral instability at an average axial strain of approximately 1.8%.
- vii. Acceptable concrete core axial strain ductility capacities only developed over small length of the specimen height due to damage localization. Usable strain limits are proposed to be a function of the gage lengths over which they are applicable, in the form $\varepsilon_{max} = \varepsilon_l (GL/t_w)^\beta$, where GL/t_w is the gage length normalized by the wall thickness and ε_l and β are Power regression coefficients. To ensure stability in compression, these limits are proposed at strength levels where the load carrying capacity has only dropped 10 or 20% (ε_{90} and ε_{80}).

strengths levels, respectively). For gage length of 2.5 times the wall thickness ($2.5t_w$), the usable strain capacities range from 0.68 to 1.25% at the ε_{80} strength level.

- viii. Although strain capacity decays rapidly with larger gage lengths, a simple plastic hinge model of a cantilever wall showed that longer hinge lengths are associated with larger global displacement capacities, albeit the reduction in usable strains. The dependence of the strain limits on gage length was introduced because of the softening nature of the response observed. For example, the deformation limiting the stable behavior of the specimens are set at strains values past that at peak strength, and lay on a softening branch (with negative slope) of the force-strain curves. Additionally, the strain limit versus gage length relationship proposed was used in the estimation of the plastic flexural drift of a set of eight reinforced concrete wall specimens found in the literature, obtaining good correlation with the observed data.

Chapter 3 - Analytical Investigation Part I: Buckling Models

Bar buckling reduces the load-carrying capacity of reinforced concrete prisms in compression in part because of the strength loss suffered by the longitudinal reinforcement but also because it reduced the effective confinement of the concrete core, which is prone to crushing. This chapter presents a modeling scheme with the purpose of understanding the mechanics of inelastic bar buckling, which affected the response of the specimens presented in **Chapter 2**. To mimic the results obtained in the laboratory, a model of longitudinal reinforcement buckling under monotonic axial compression is introduced and its response is contrasted against those found in the literature. An extension of this model is then presented to replicate the inelastic buckling of tied longitudinal bars, unilaterally restrained by concrete. An experiment comprising 48 analytical specimens allows the development of a simple empirical model that offers the complete average axial stress-strain curve of tied longitudinal bars undergoing lateral instability (buckling), given a few input parameters such as the tie spacing and the diameter of the longitudinal and transverse bars. This model will be used later in the document, as part of a more comprehensive model that estimates concrete core empirical stress strain relationships from the available data summarized above.

3.1 Previous Studies on Reinforcing Bar Buckling

Inelastic bar buckling has been studied by many authors in the laboratory (Bae et al., 2005; Bayrak & Sheikh, 2001; Mander, 1984; Monti & Nuti, 1992; Rodriguez et al., 1999). The laboratory experiments typically focus on testing bare reinforcing bars (in the air), with fixed boundary conditions to obtain average axial stress versus average axial strain relationships. Typical relevant variables of the experiments are the diameter of the bar (D), the unsupported length (L), the type of steel (defined by yield strength f_y), and initial imperfections. A main observation in these tests is that ductility and strength increase as the ratio L/D decreases. Inelastic buckling is delayed to strains larger than the yield strain only if the unsupported length is small compared to the bar diameter, and typically a value of around $L/D = 6$ is reported as a minimum to ensure stability. Given the laboratory setup, the buckling length is typically equal to the unsupported length in these experiments.

The analytical research has focused on different aspects of the inelastic bar buckling phenomena. Investigations by Gomes and Appleton (1997) and Kunnath et al. (2009) focus on formulating material constitutive models for cyclic stress-strain relationships of steel including buckling. These constitutive rules use the Menegotto-Pinto model as platform, with some modifications to include triggering and the post buckling response of longitudinal reinforcement. This type of model have been implemented in nonlinear analysis platforms such as OpenSees (McKenna et al., 2000), and is available for public use. Finite element formulation of the inelastic bar buckling problem is also part of the literature. Mau and Elmsout (1989) focused on the formulation, while Dhakal and Maekawa (2002) focused on the implementation of mathematical models comprising beam-columns elements to represent the buckling mechanism

of bare bars. The latter authors used displacement-based beam column elements with distributed fibers to simulate the results of Mander (1984) and Monti and Nuti (1992), offering good agreement with the laboratory test data. A main conclusion of Dhakal and Maekawa (2002) is that the average stress strain curve of bars undergoing lateral instability is solely dependent on the product of the slenderness ratio and the square root of the yield strength of the longitudinal bar ($L/D\sqrt{f_y}$).

One of the first works reporting the requirements for a stable response of tied longitudinal bars embedded in concrete was presented by Bresler and Gilbert (1961). The article reports on tie stiffness requirements to promote longitudinal bar buckling between two layers of transverse reinforcement. For moderate transverse reinforcement spacing, an important conclusion of this work is that the relative tie-to-longitudinal bar diameter required to provide effective transverse restraint is small. On the other hand, the restraint provided by the flexural stiffness of a hoop leg is relatively ineffective, unless impractically large hoop bar diameters are used. Two mathematical expressions used to support the aforementioned conclusion are rewritten as **Equation (3.1)** and **(3.2)**, in terms of the variables used in this document.

$$d_{bt} = \frac{d_b^2 \pi^2}{8} \sqrt{\frac{3l_t}{s^3}} \quad (3.1)$$

$$d_{bh} = \frac{d_b \pi}{4} \sqrt[4]{\frac{l_h^3}{s^3}} \quad (3.2)$$

Variables in **Equation (3.1)** are the diameter d_{bt} and length l_t of a tie; d_b for the longitudinal bar diameter; and s for the spacing between transverse reinforcement layers. Additional variables in **Equation (3.2)** are d_{bh} for the diameter and l_h for the length of the leg of a hoop, respectively. These two equations help investigating the axial tie and flexural hoop stiffness requirement for the experiments presented in **Chapter 2**. **Equation (3.1)** is used for the analysis of longitudinal bars engaged by a tie, assuming $l_t = 9$ in. [229 mm]. **Equation (3.2)** is used for the analysis of non-tied longitudinal bar, assuming $l_h = 33$ in. [838 mm]. For the first case, it is assumed that a single tie (of length l_t) per layer is restraining the longitudinal bar by means of its axial stiffness; and that hook unwinding (opening) is not likely. The second case is representative of an internal longitudinal bar located at midspan of the long leg of the perimeter hoop. Lateral displacement of this bar is restrained by the flexural stiffness of this leg (of length l_h), which is assumed to be fixed at both ends. **Table 3.1** compares provided (as built) versus required (per **Equation (3.1)** or **(3.2)**) tie or hoop diameter for the reinforced concrete prism experiments in **Chapter 2**. Given the tie spacing used in the laboratory specimens, two main observations are that (i) hoop diameter necessary to effectively restrain longitudinal bars against lateral instability are impractical, requiring $d_{bh} \geq 3.3$ in. [83.8 mm]; also, that (ii) only specimens W8 and W9 comply with the tie requirement, which is consistent with the reported buckling length of one tie spacing for their tied bar, as described in **Section 2.6**.

Table 3.1 - Tie and hoop diameter requirements for specimens W5 to W12 according to Bresler and Gilbert (1961). [Note: 1 in. = 25.4 mm].

Specimen ID	d_b [in.]	s [in.]	Provided d_{bt} and d_{bh} [in.]	Required d_{bt} [in.] [Eq. (3.1)]	Required d_{bh} [in.] [Eq.(3.2)]	$d_{bt,prov}/d_{bt,req}$	$d_{bh,prov}/d_{bh,req}$
W5	1.000	4	0.500	0.8	3.8	0.6	0.1
W7	0.875	4	0.500	0.6	3.3	0.8	0.1
W8	0.875	8	0.500	0.2	--	2.3	--
W9	0.875	4	0.625	0.6	3.3	1.0	0.2
W11	1.270	4	0.500	1.3	--	0.4	--
W12	1.270	4	0.625	1.3	--	0.5	--

More recently, other authors (Pantazopoulou, 1998; Papia & Russo, 1989; Papia et al., 1988) have also explored the stability of bars in reinforced concrete elements. Pantazopoulou (1998) presents an investigation showing that reinforcement stability depends on the interaction between the transverse reinforcement layout, core deformation capacity and bar diameters, and not only on the ratio between the restraining length and the longitudinal bar diameter. The idea that the layout and geometric properties of restraining ties play an important role in the response of longitudinal bar undergoing inelastic buckling is the main topic of this chapter, and is explored in detail by means of finite elements models in **Section 3.3** and **3.4** below.

3.2 Experimental Observation of Longitudinal Steel Buckling

Longitudinal steel buckling was observed in the damage zones of the specimens presented in **Chapter 2**. The damage zone observed had approximate length equal to 2 to 3 wall thicknesses, and included a smaller portion where additional plastic deformation concentrated, and where bar buckling developed. **Figure 3.1** presents a close-up view of specimens W5, W7 and W11 in the region where localization of damage took place. All other specimens experienced similar behavior, except specimen W12. Tied bar buckling length extended between 4.5 and 9.5 longitudinal bar diameters ($4.5 \leq d_b \leq 9.5$), and included, in most cases, the opening of the 90- and/or 135-degree hook of the restraining tie. Unrestrained bars buckled over approximately three to four hoop sets (for example, between 14 and $18d_b$). Corner bars buckled in higher modes, apparently because of the restraint and the force exerted by the perimeter hoops when elongating due to buckling of the internal bars.

3.3 Inelastic Buckling Model of Isolated Bars

In the following, a nonlinear bar buckling model under monotonic compressive loading is developed in the software package OpenSees (McKenna et al., 2000) and its results are contrasted with those of (Monti & Nuti, 1992). This model will serve as the basis for a more complex model, described later in this document, which includes lateral restraint by transverse ties and the core concrete.

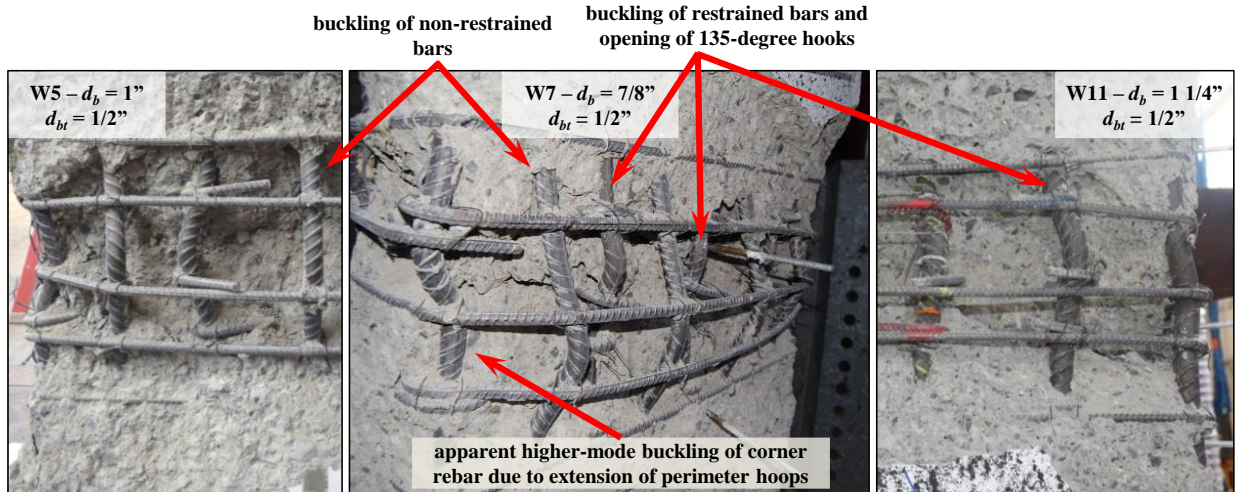


Figure 3.1 - Buckling of different diameter bars appearance.

3.3.1 Force-based beam-column element formulation

The basic force system of a two dimensional Bernoulli beam-column element is depicted in **Figure 3.2**. The basic force system, $\mathbf{q} = [q_1 \ q_2 \ q_3]^T$, comprises an axial load and two end moments. The shear forces in the basic system are dependent on the end moments and provide the required force balance to equilibrate the element in rotation and translation in the local y -direction. The basic deformations, $\mathbf{v} = [v_1 \ v_2 \ v_3]^T$, associated with the basic forces, comprise one axial deformation and two rotations of the end nodes. These flexural deformations are the result of the relative transverse displacement and rotation of the end nodes, and are measured relative to the chord joining them in the deformed configuration.

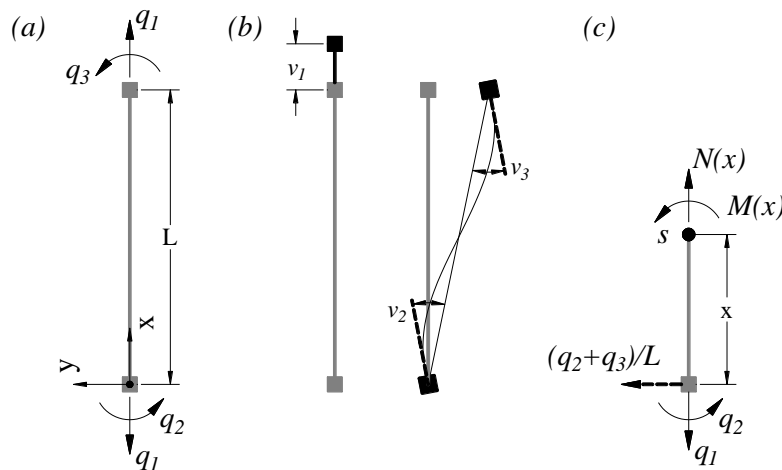


Figure 3.2 - (a) Element basic force system; (b) basic deformation system; (c) forces at the section level

Sectional forces (within the element length) are defined by the end forces and internal applied loads in the form

$$\mathbf{s}(x) = \mathbf{b}(x)\mathbf{q} + \mathbf{s}_p(x) \quad (3.3)$$

where $\mathbf{s}_p(x)$ are the internal element loads which are set to zero for this study, and the sectional forces of interest comprise an axial force and a moment: $\mathbf{s}(x) = [N(x) \quad M(x)]^T$ which can be coupled (e.g., PM interaction) with a fiber section model. The shear force along the element is constant and will not consider inelastic effects for this study.

Interpolation matrix $\mathbf{b}(x)$, relates the end forces to the section forces in a linear manner:

$$\mathbf{b}(x) = \begin{bmatrix} 1 & 0 & 0 \\ 0 & x/L - 1 & x/L \end{bmatrix} \quad (3.4)$$

At the section level the deformation vector, $\mathbf{e}(x) = [\varepsilon_a(x) \quad \kappa(x)]^T$, comprises an axial strain at the centroid of the cross section and its curvature. These two parameters are sufficient to describe the uniaxial strain of any particle in the cross section. **Figure 3.3** shows the parameters that define a fiber section along with a representation of section deformations assuming plane sections remain plane before and after the deformation. Also shown are the parameters defining the geometry of each fiber, its uniaxial strain, and its constitutive material model.

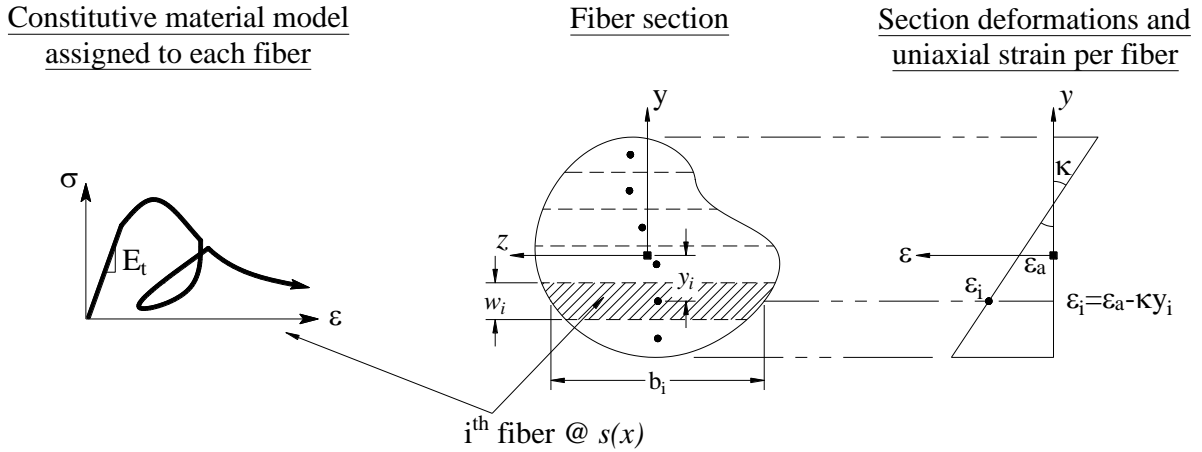


Figure 3.3 - Fiber section geometry, deformations and material constitutive model parameters.

The principle of virtual forces allows formulating compatibility relations between the section deformations, \mathbf{e} , and the element deformation, \mathbf{v} according to

$$\mathbf{v} = \int_0^L \mathbf{b}^T(x) \mathbf{e}(x) dx \quad (3.5)$$

The derivative of **Equation (3.5)** with respect to the basic force system defines the element flexibility matrix, \mathbf{f} :

$$\mathbf{f} = \frac{\partial \mathbf{v}}{\partial \mathbf{q}} = \int_0^L \mathbf{b}^T(x) \mathbf{f}_s(x) \mathbf{b}(x) dx \quad (3.6)$$

where \mathbf{f}_s is the section flexibility matrix estimated as the inverse of the section stiffness matrix, \mathbf{k}_s^{-1} . The section stiffness matrix can be formed by integration as follows

$$\mathbf{k}_s = \frac{\partial \mathbf{s}}{\partial \mathbf{e}} = \begin{bmatrix} \partial N / \partial e_a & \partial N / \partial \kappa \\ \partial M / \partial e_a & \partial M / \partial \kappa \end{bmatrix} = \int E_t \begin{bmatrix} 1 & -y \\ -y & y^2 \end{bmatrix} dA \cong \sum_{i=1}^{nFibers} E_{t,i} \begin{bmatrix} 1 & -y_i \\ -y_i & y_i^2 \end{bmatrix} b_i w_i \quad (3.7)$$

where E_t represents the tangent modulus of the assigned material and y the location of the material points across the section. In the discrete version of this equation, the integral is replaced by a summation over all the fibers of the cross section, with each fiber having area $A_i = b_i w_i$ (**Figure 3.3**).

3.3.2 Force-based and displacement-based beam-column element formulation comparison

Distributed plasticity formulation of beam-column elements offers a flexible platform for modeling structural elements when a critical section location, where inelastic deformations might occur, cannot be predicted prior to the analysis. Three main formulations of distributed plasticity elements are: the force-based, the displacement-based, and the mixed formulation (M. H. Scott & Hamutçuoğlu, 2008). This section focuses on the force-formulation of beam-column elements to model inelastic bar buckling.

The force-based formulation (FBF) of beam column elements (Ciampi & Carlesimo, 1986; Spacone et al., 1996) makes use of the integral form of the compatibility relations between the element end deformations \mathbf{v} , and the section deformation $\boldsymbol{\epsilon}$ within the element (**Equation (3.5)**). This is advantageous because a non-uniform deformation field along the element length can be properly modeled. It is important to note that compatibility in the integral form is only satisfied at the element ends and not at every section. This is a main difference with respect to the displacement-based element formulation (DBF), which is based on standard finite element approach where section deformations are estimated as the derivatives of an imposed displacement field. The FBF also uses the available exact static equilibrium equations between the end nodal forces, \mathbf{q} , and the internal forces, s (**Equation (3.3)**). This results in constant axial force and linear bending moment distribution along the element length. On the other hand, the DBF uses the principle of virtual displacements to formulate “weak” equilibrium between these two sets of forces, resulting in an error where the internal forces at each section are not in equilibrium with the element basic force if fine meshes are not implemented. Due to the enforced displacement field along the element length, the displacement-based element has constant axial deformation and linear curvature distribution. To properly model nonlinear behavior of nonprismatic elements, the displacement based approach requires mesh refinement (i.e., using more elements) to overcome the restrictions in the axial deformation and curvature distribution, while the force-based approach requires the addition of more integration points but still using fewer elements. For a cantilever structural element with transverse lateral loading, the curvature distribution modeled by a single force-based element (FBE) is compared to that of a set of displacement based elements (DBE) in **Figure 3.4**.

3.3.3 Force-based and displacement-based element state determination

In structural analysis problems, a main task is to obtain basic element forces when the model is subjected to nodal displacements. The idea is to estimate the internal resisting forces that are in equilibrium with the applied external forces. For nonlinear models, this is an iterative process, because element stiffness is not constant and is a function of the element deformations (this is explained in detail later). For a displaced structure, element deformations are computed by means of a compatibility matrix relating the global degrees-of-freedom (DOF), \mathbf{u} , and the basic

element deformations, \mathbf{v} . This kinematic relation can account for large displacement with a *corotational* formulation (Filippou & Fenves, 2004).

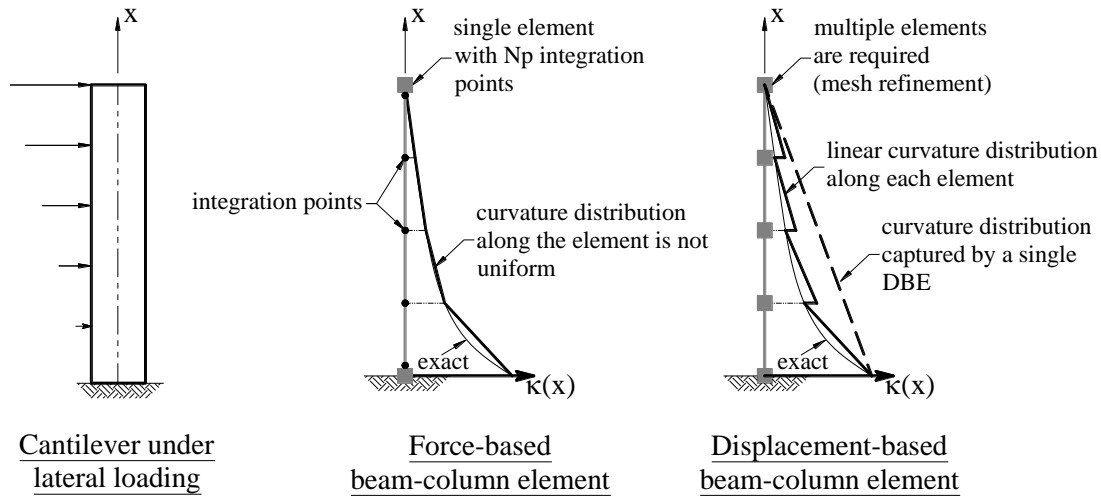


Figure 3.4 - Curvature distribution comparison between a force-based and a displacement-based beam-column element.

Figure 3.5 shows a flow chart where the DBE state determination is depicted. In the DBF, calculation of the basic forces, \mathbf{q} , follows a straight non-iterative path, where, given the element deformations, the section deformations, can be estimated with a function of the form $\mathbf{e}(x) = \mathbf{B}(x)\mathbf{v}$; here $\mathbf{B}(x)$ is an interpolation matrix that relates end flexural deformations (v_2, v_3) with a linear curvature distribution ($\kappa(x)$) and the element axial deformation (v_1) with a constant axial strain at the centroid of the cross section ($\varepsilon_a(x) = \varepsilon_a$). At a section level, this allows calculating a uniaxial strain and stress field ($[\varepsilon(y,x), \sigma(y,x)]$, by means of a material uniaxial constitutive model), which can be integrated to estimate section forces s and finally end basis forces \mathbf{q} .

A complication of the FBF is that there is not a direct relation between the element deformations, \mathbf{v} , and the basic forces, \mathbf{q} , because the compatibility relation between element deformations and section deformations is in integral form (**Equation (3.5)**). Given the element deformations, the resolution of the end basic forces requires nested Newton iterative procedures to find equilibrium between the end deformations and the section deformations. The flow chart on **Figure 3.6** shows some steps of the process for one non-converged iteration at the element level and one converged iteration at the section level.

Even though the FBE formulation is computationally more expensive (due to the required nested iterations at the element level), it is considered more robust because (i) it guarantees exact equilibrium between the end forces of the element and those at the section level, (ii) it allows modeling non-uniform curvature field along the element length, and (iii) its implementation (De Souza, 2000) in OpenSees is simpler since it requires fewer elements to converge to the same solution as the DBE formulation.

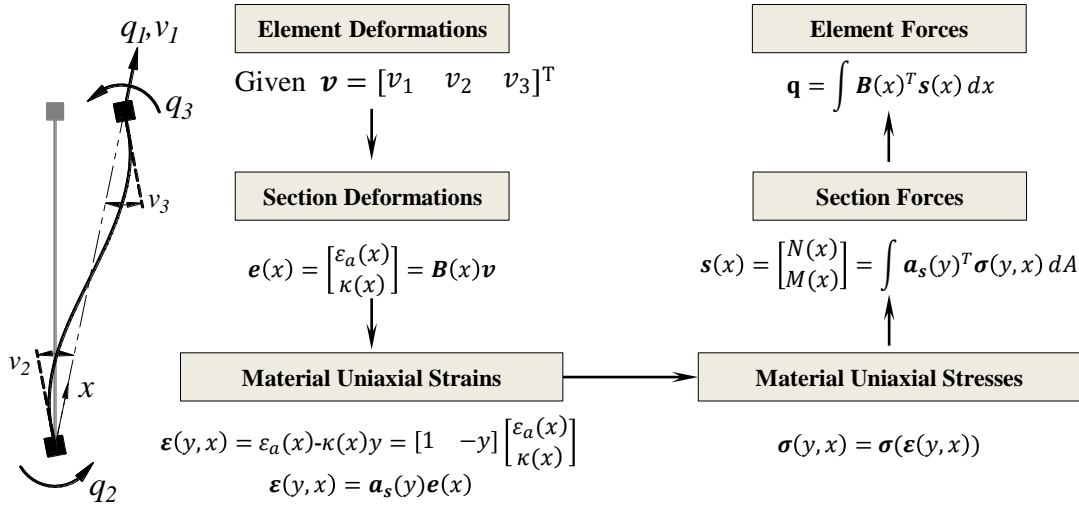


Figure 3.5 - Displacement-based element state determination flow chart.

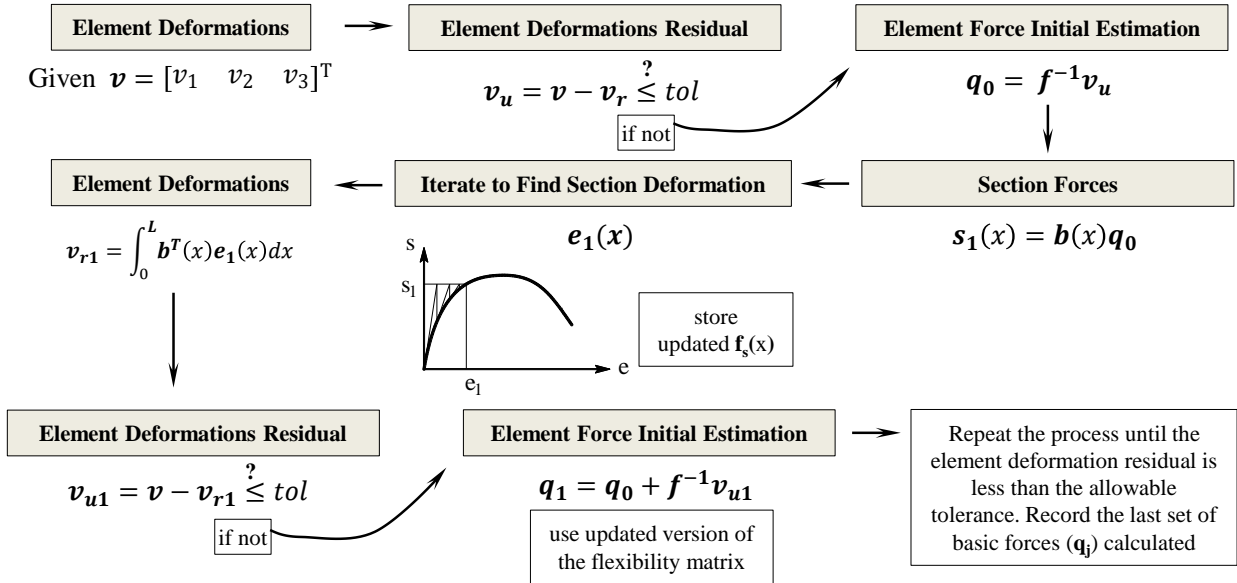


Figure 3.6 - Force-based element state determination flow chart.

3.3.4 Quadrature rule for distributed plasticity beam-column elements

For the computational implementation of the FBE, numerical integration of **Equations (3.5)** and **(3.6)** are required. In a discrete form, these equations are rewritten as

$$\mathbf{v} \cong \sum_{i=1}^{N_p} \mathbf{b}^T(x_i) \mathbf{e}(x_i) w_i \quad (3.8)$$

$$\mathbf{f} \cong \sum_{i=1}^{N_p} \mathbf{b}^T(x_i) \mathbf{f}_s(x_i) \mathbf{b}(x_i) w_i \quad (3.9)$$

where N_p is the number of integration points (IP) along the element length, x_i is the location of each IP within the element length, and w_i is its associated weight.

Gauss-Lobatto quadrature

One integration rule relevant to this study is the *Gauss-Lobatto quadrature*. This rule defines values of x_i and w_i and guarantee certain level of accuracy according to the selected number of IPs. The Gauss-Lobatto integration rule is the default rule in OpenSees and places two integration points at the end of the beam-column element. This is convenient for the analysis of frame elements where maximum bending moment demands are generally expected at the extremes (M.H. Scott, 2011). The order of accuracy is $2N_p-3$. In **Equation (3.9)**, the term $\mathbf{b}^T(x)\mathbf{b}(x)$ contains a second order polynomial; hence, at least 3 IPs ($N_p = 3$) are required to estimate the flexibility matrix adequately, with a linear distribution of $\mathbf{f}_s(x)$. With the same number of IPs, a quadratic distribution of $\mathbf{e}(x)$ can be integrated accurately (**Equation (3.8)**). **Figure 3.7** shows the Gauss-Lobatto integration point locations and weights for 3 and 4 IPs.

<u>Gauss-Lobatto IP Locations and Weights</u>		
N_p	x_i / L	w_i
3	0.000	0.167
	0.500	0.665
	1.000	0.167
N_p	x_i / L	w_i
4	0.000	0.084
	0.277	0.417
	0.723	0.417
	1.000	0.084

Figure 3.7 - Integration points locations and weights for the Gauss-Lobatto quadrature rule.

3.3.5 Nonlinear geometric formulation

Reinforcement buckling modeling requires a formulation that accounts for significant structural geometry changes during the evolution of the phenomenon. The model should be able to account for the change of axial force of the discrete structural component (frame element) due to overturning effects promoted by increasing axial shortening and large lateral displacement. It is also desirable to model nonlinear intra-element geometric effects ($P-\delta$ effect) arising from the eccentricity of the axial force, aligned in the direction of the chord of the deformed element, relative to the deformed shape of the element between the end nodes. For the reason that the observed bar buckling occurs after the reinforcement yields in compression, the formulation of the model should also account for material nonlinearities.

In order to account for nonlinear geometry due to the expected large displacements and rotations, a *corotational* formulation is necessary (Filippou, 2014). This formulation allows writing the equilibrium equations between the basic resisting forces (always aligned with the chord of the deformed element) and the nodal applied forces (in the global coordinate system) in the deformed configuration. **Figure 3.8** shows a frame element in the deformed configuration depicting the basic force and nodal force systems. The nonlinear equilibrium relation between the basic forces \mathbf{q} and the applied end global forces \mathbf{P} is given by

$$P = a_g^T q$$

$$\begin{bmatrix} P_1 \\ P_2 \\ P_3 \\ P_4 \\ P_5 \\ P_6 \end{bmatrix} = \begin{bmatrix} -\frac{\Delta X + \Delta u_x}{L_n} & -\frac{\Delta Y + \Delta u_y}{L_n^2} & -\frac{\Delta Y + \Delta u_y}{L_n^2} \\ \frac{\Delta Y + \Delta u_y}{L_n} & \frac{\Delta X + \Delta u_x}{L_n^2} & \frac{\Delta X + \Delta u_x}{L_n^2} \\ 0 & 1 & 0 \\ \frac{\Delta X + \Delta u_x}{L_n} & \frac{\Delta Y + \Delta u_y}{L_n^2} & \frac{\Delta Y + \Delta u_y}{L_n^2} \\ \frac{\Delta Y + \Delta u_y}{L_n} & -\frac{\Delta X + \Delta u_x}{L_n^2} & -\frac{\Delta X + \Delta u_x}{L_n^2} \\ 0 & 0 & 1 \end{bmatrix} \begin{bmatrix} q_1 \\ q_2 \\ q_3 \end{bmatrix} \quad (3.10)$$

where ΔX and ΔY define the rotation of frame element in the undeformed configuration, with respect to the global reference system; L_n is the deformed element length; Δu_x and Δu_y are the relative horizontal and vertical components of nodal displacement which generate elongation (i.e. without rigid body motion displacements). As it is apparent from the appearance of the displacements Δu_x and Δu_y (which are also involved in the calculation of L_n) in **Equation (3.10)**, the statics of the problem is nonlinear and will require an iterative strategy for its solution because the global stiffness matrix of the system will include these displacements as well.

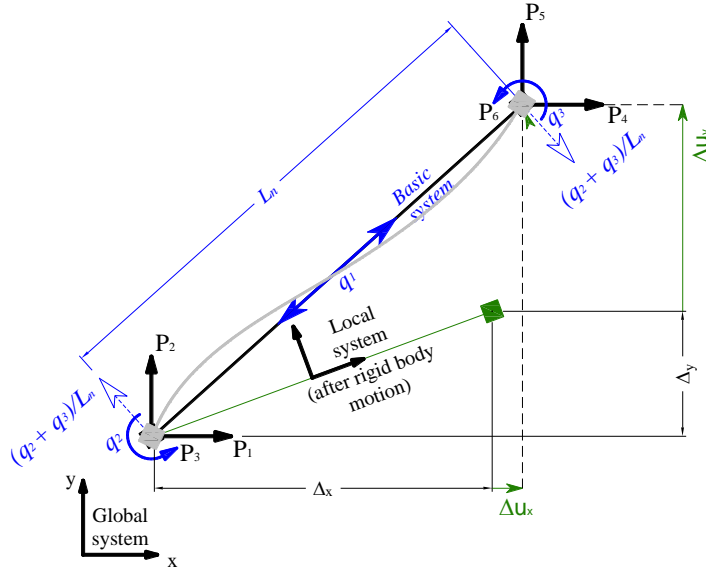


Figure 3.8 - Frame element nonlinear statics under corotational formulation (adapted from (Filippou, 2014)).

As mentioned before, accounting for the influence of the axial force q_1 on the flexural response of the frame element requires the inclusion of the P - δ effect in the formulation of the element stiffness matrix in the basic system. This will create a dependency of the basic end moments q_2 and q_3 on the axial force and, consequently, another nonlinear relation between the basic forces and the end node applied forces will arise. This formulation is computationally expensive, only exact for linear elastic material behavior, and not available in many analysis software packages, including OpenSees.

Considering that the P - δ effect plays an important role when modeling the buckling behavior of a prismatic bar, an alternative procedure, consisting in the subdivision of the member into smaller elements, is required. To show the latter, **Figure 3.9** presents two bars under axial load at the same tip vertical displacement U and lateral displacement w at midspan. It can be assumed that the deformed configuration shown is representative of an axially loaded bar undergoing buckling with fixed boundary conditions. It is apparent that for the model with fewer elements (**Figure 3.9a**) the maximum deviation of the element deformation relative to the chord is larger than that of the more discretized one (i.e., $\delta > \delta'$). Furthermore, it can be observed that this deviation is almost negligible for some elements (for example, element b') and the P - δ effect could be neglected. In summary, the discretization of the axially loaded bar promotes the deformed shape of each element to be close to its unloaded state, hence allowing for the use of element stiffness formulations under linear geometry.

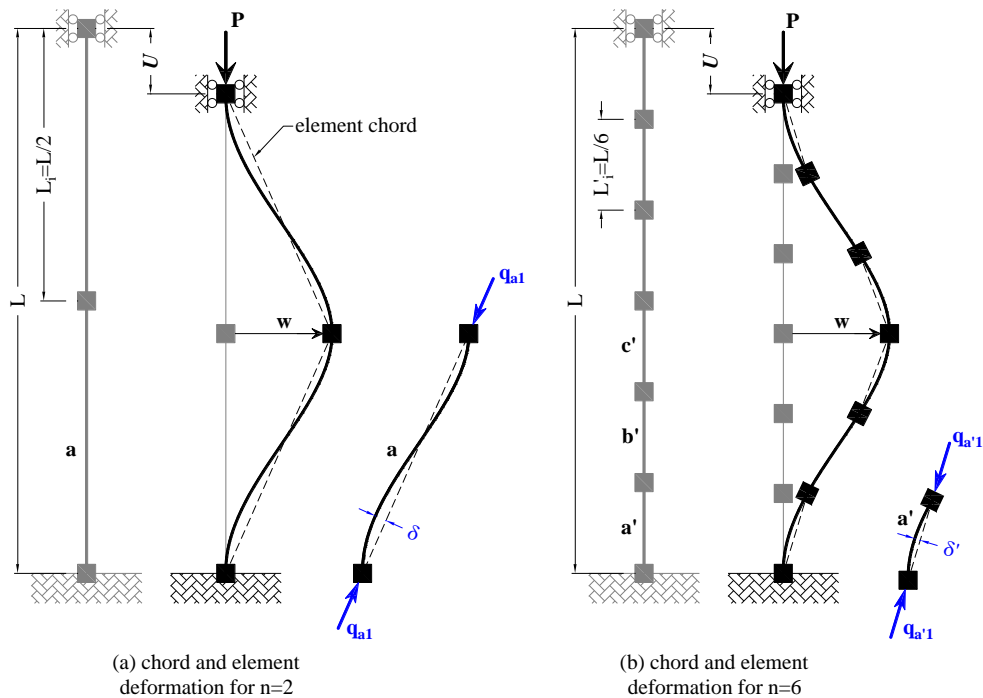


Figure 3.9 - Basic axial force acting on the deformed shaped of the members of a buckled bar: (a) for a two-node discretization; (b) for a six-node discretization.

3.3.6 Nonlinear incremental analysis

The selected finite element model to simulate the inelastic buckling of a longitudinal reinforcement bar under compression is depicted in **Figure 3.10**. The model accounts for the nonlinear geometry considerations described above by proper discretization into smaller elements and by the implementation of a corotational formulation to transform element stiffness and resisting force from the local coordinate system to the global coordinate system. It comprises force-based nonlinear frame elements with distributed plasticity and fiber sections at five integration points (Spacone et al., 1996). The fiber sections can account for cyclic, uniaxial stress-strain relationships of the materials assigned to it. The selected steel stress-strain behavior is assumed to be bilinear with isotropic strain hardening (Filippou et al., 1983) but other material

models were also tested, as described below. This implementation allows approximating the moment-curvature relationships of the elements at different levels of axial force.

Pushover analyses were performed in OpenSees to estimate the response of the prismatic bar under pure compression. To solve for the nonlinear equilibrium equations, a Modified Newton-Raphson algorithm, alternated (when convergence problems were found) with an accelerated Newton algorithm based on Krylov subspaces (M. H. Scott & Fenves, 2010) was utilized. To advance in subsequent states of the response, load factor increments (or decrements) were controlled by specified vertical displacements of the top node of the bar (i.e., displacement control of load factor) or using an Arch-Length algorithm (Crisfield, 1981). The convergence criterion at each iteration is based on work increment.

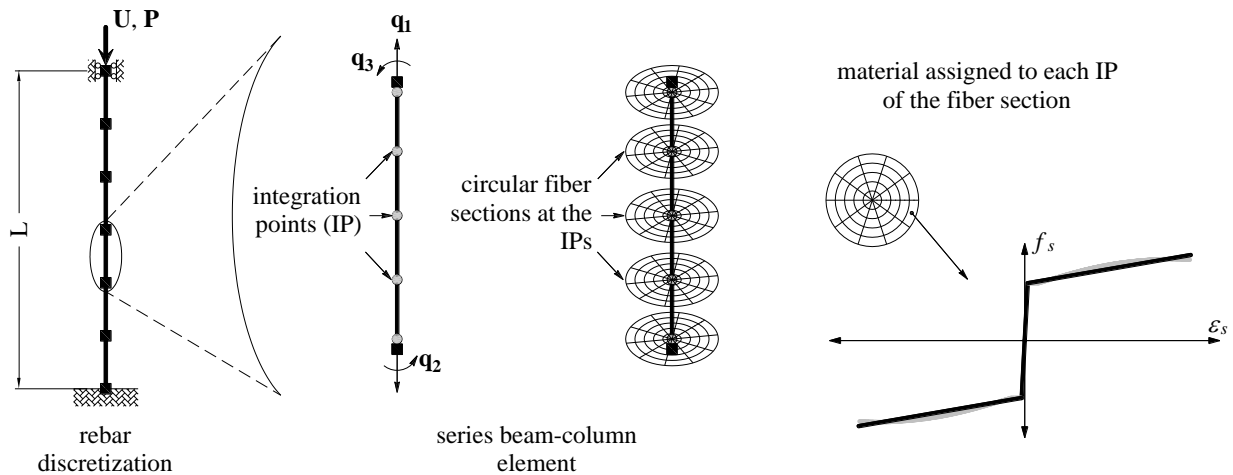


Figure 3.10 - Finite element model to simulate inelastic bar buckling.

Figure 3.11 shows the calibration process to select an appropriate number of fibers and their configuration in the circular section to achieve a stable solution. For this purpose, the bar was modeled with only one element, of length L_o , to inhibit any buckling response and focus on the response given different fiber distributions. The results are contrasted against the stress-strain relationship of the A706 steel model. It is worth noting, that although this very simple case of pure axial demand should give the same results for any fiber configuration because there is no flexure involved, it was found that the circular fiber section coding might not be properly implemented in OpenSees³. Specifically the calculation of the area is not correct as can be seen from the lower axial strength attained by models with a reduced number of sections (e.g., *C4R4*, *C8R8*). For this case a stable solution was found for 120 fibers under a discretization of the cross section comprising 6 radial and 20 circular subdivisions. The later also shows that the error in the code is related to the circular subdivision because section *C20R6* has less than half the number of fibers of section *C16R16* and it did achieve the expected axial capacity. Section *C20R10* was found to be optimal by Berry and Eberhard (2008) under combined axial and flexural response and will be used as the selected discretization scheme to overcome any coding problem in OpenSees.

³ This finding was reported to Frank McKenna, the initial developer of OpenSees, who confirmed the error in the code. It was fixed in version 2.4.3 of OpenSees.

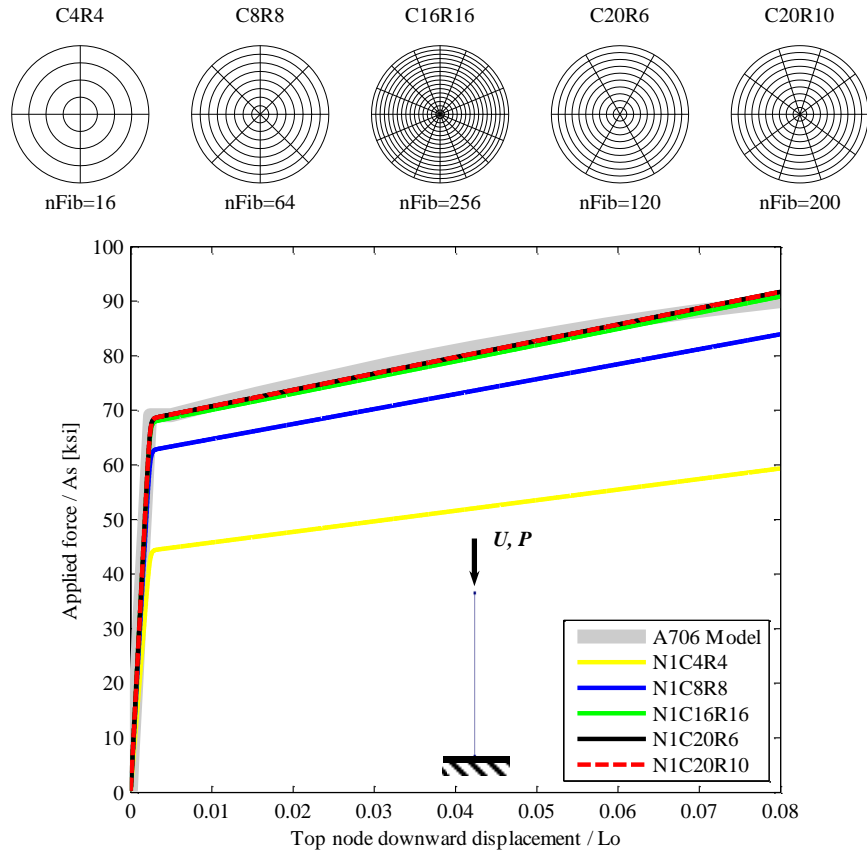


Figure 3.11 - Fiber configuration sensitivity analysis.

Response sensitivity to different element discretization (represented by N = the number of subdivisions), to approximate the intra-element nonlinear geometry, is shown in **Figure 3.12**. The bar shown has both ends restrained against rotation and lateral displacement and depicted is the applied axial load divided by the original area of the bar versus the displacement of top node normalized to the original length of the bar. Slenderness ratio is $L_o/d_b = 11$, where d_b is the diameter of the cross section. Given the large L_o/d_b ratio, inelastic buckling was expected (Monti & Nuti, 1992), therefore, to test the effect of a yield plateau in the material stress-strain relation, the buckling response under two different material models was estimated: (a) model with bilinear steel material (Filippou et al., 1983) and (b) model with a trilinear steel material with yield plateau⁴. To promote buckling of the bar, an initial imperfection, defined as a lateral displacement $w_o = L_o/10,000$ at midspan was introduced.

It is observed that for either material used, the solution converges to a stable response for subdivisions of the bar of at least 6 elements. It is found that these responses are not affected by the presence of a yield plateau and only show minor variations of the softening behavior branch. Though not shown here, this was also confirmed for different number of integration points for each element and different values of the initial lateral imperfection. For $N = 4$ and bilinear steel material, the response of the bar is close to those with larger N ; for the case of trilinear steel material, the onset of buckling occurred at larger strains on the yield plateau. Even though this response is acceptable, the displaced shaped for $N = 4$ shows that the triple curvature

⁴ Implemented by Scott and Filippou. Online <http://opensees.berkeley.edu/wiki/index.php/Hysteretic_Material>.

deformation of the buckling phenomena is hard to model with as few elements. The hardening behavior of the model with $N = 2$ elements and trilinear material suggests that the approximation of the intra-element nonlinear geometry by proper discretization of the bar has an important effect on the response of the bar. Since the behavior for $N = 6$ is close to that of $N = 32$, which is thought of as a subdivision upper bound, the results presented herein will only consider a bilinear steel bar comprising 6 elements, each with 5 integration points with a circular fiber section of 20 circular and 10 radial subdivisions ($N6C20R10$).

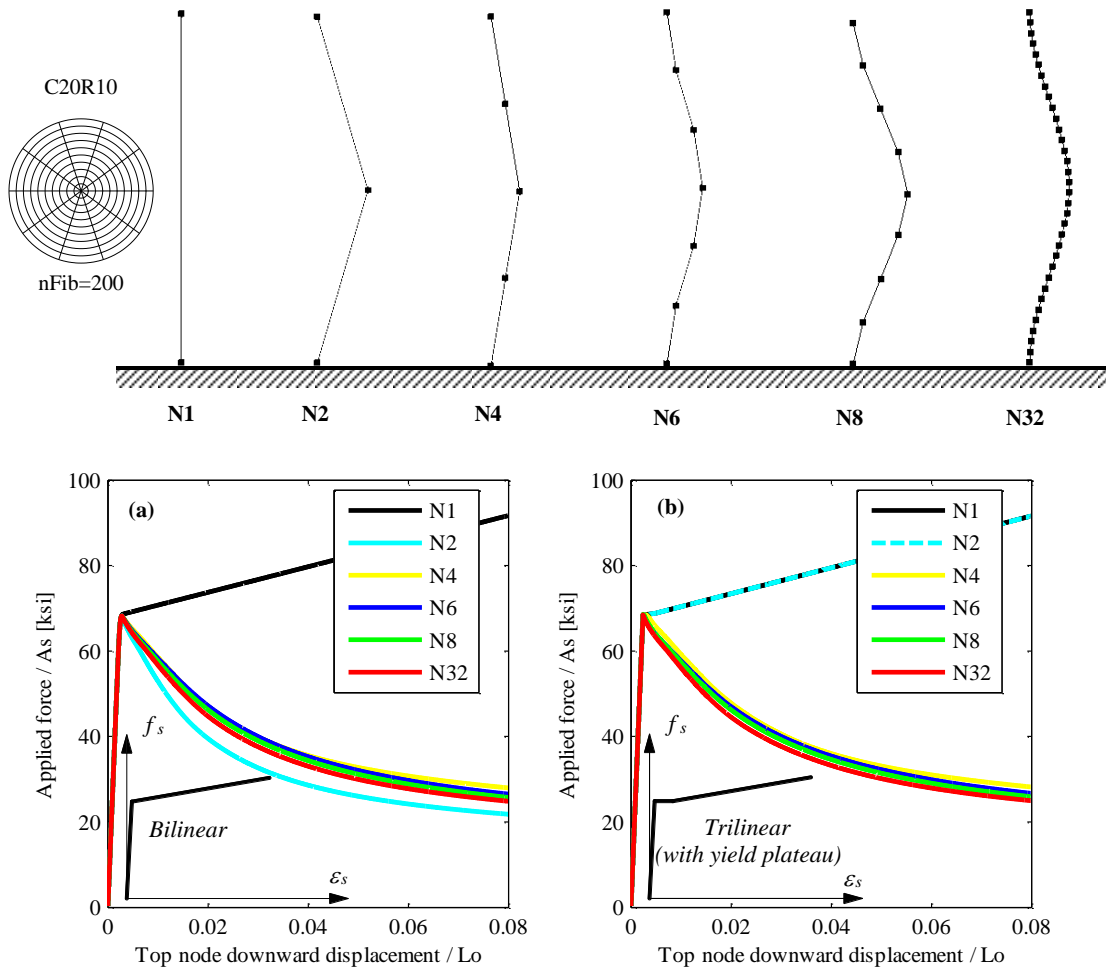


Figure 3.12 - Buckling response comparison for different element discretization and two different steel materials: (a) bilinear steel material; (b) trilinear steel material with yield plateau.

The selected model global response, defined as the applied load normalized by the yield force ($A_s F_y$) versus the average shortening of the bar normalized by the initial length, is shown in **Figure 3.13a**. Onset of buckling occurs once the material reaches its yield strain. Maximum sustained load is equal to the yield force and at large deformations it approaches asymptotically to approximately 35% of that value. Also shown are four different stages of the response: one in the elastic range, another at the onset of buckling, and two more in the plastic range. The displaced shape of the chords of the elements is depicted in **Figure 3.13b** for these stages. The triple curvature of the buckling shape is modeled accurately by the selected discretization.

Distribution of centroidal normal strains (positive in this case for compression) along the height of the bar is shown in **Figure 3.13c**. Strain values for the central and extreme integration points of each element are plotted. The formation of three plastic hinges is apparent. It is interesting to notice that the elements between the plastic hinges (i.e., elements 2 and 5) are almost unstressed and just serve the purpose of transitioning the deformed shaped between the changes in the curvature of the bar. This result is also confirmed by (Dhakar & Maekawa, 2002) with a L_o/d_b ratio of 10 and a greater element discretization (e.g., $N = 12$).

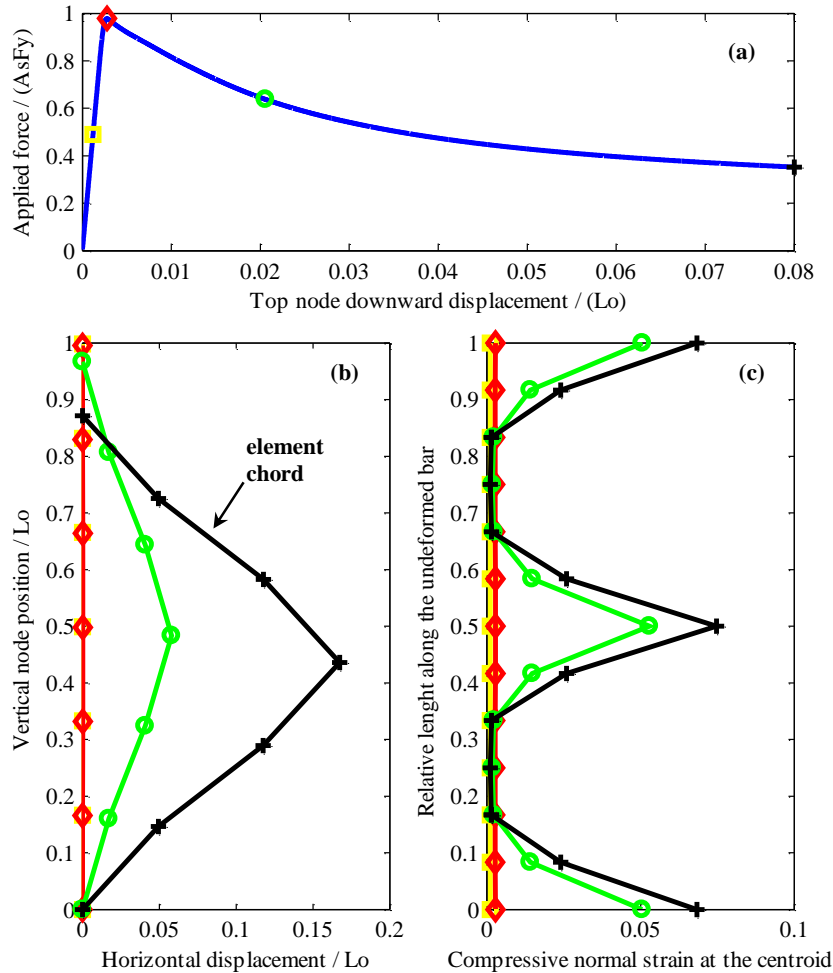


Figure 3.13 - Global and local response of the select model (*N6C20R10*). (a) Normalized applied axial load versus average shortening of the bar; (b) deformed shape; (c) normal strain distribution at the centroid.

Further analysis at a local level, such as the response of individual fibers at an integration point at midspan, is depicted in **Figure 3.14**. **Figure 3.14a** shows the response of a fiber that only sees compressive strains because it is on the concave side of the buckling bar (i.e., to the left of the displaced shape shown in **Figure 3.13b**). **Figure 3.14b** shows the stress-strain response of a centroidal fiber. **Figure 3.14c** shows the response of a fiber that is in compression during the elastic response of the bar and, at the onset of buckling, its strains reverse toward the tensile side due to the overturning moment induced by the buckling phenomena. This result suggests that at a given stage, the model deals with different portions of the section having different moduli which is an expected result as suggested by (Papia & Russo, 1989) and (Pantazopoulou, 1998). **Section**

3.4.1.1 presents a more detailed analysis of the modulus variation across the critical section of a bar undergoing lateral instability.

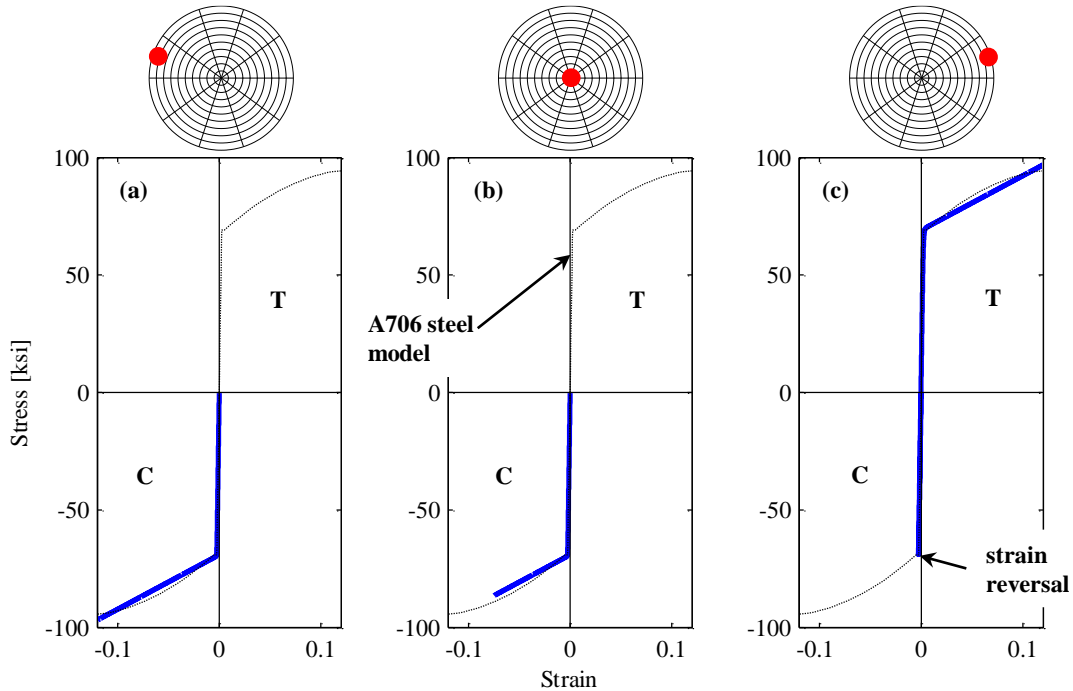


Figure 3.14 - Response at the fiber level at midspan: (a) extreme fiber under compression only; (b) centroidal fiber; (c) extreme fiber under strain reversal after buckling initiates [Note: 1 ksi = 6.9 MPa].

Figure 3.15 presents a comparison of the N6C20R10 model with test results by (Monti & Nuti, 1992). Both cases have comparable geometric characteristics only differing in the material properties (e.g., bilinear model of A706 steel for the analytical curve and FeB44 steel for the experimental data). Also shown is the monotonic A706 steel tensile stress-strain relation. The analytical results obtained are in good agreement with those in the literature and the model is deemed acceptable for use in a larger model with other components of the boundary elements subject of study in this document.

3.4 Modeling Inelastic Buckling of Tied Longitudinal Bars Embedded in Concrete

With the idea of including some of the particularities of the boundary conditions present around a longitudinal bar embedded in concrete, the model presented in **Section 3.3** is extended in this section. For this purpose, transverse truss elements are added to the model to mimic the restraint imposed by a hoop leg or a tie. This restraint assumes perfect contact between the transverse and the longitudinal reinforcement; therefore, tie opening is not accounted for. Additionally, zero-length contact elements are included to mimic the presence of the concrete core, which effectively constrains the lateral instability of the bar to a single direction only. This in turn, prevents higher-mode buckling, which might arise due to the restrictions imposed by the ties along the length of the bar. The model gives insight into the impact of the transverse reinforcement geometric characteristics on the inelastic buckling response of longitudinal bars. Specifically, the relative post yield stiffness (m_h) of the average stress–average strain relation is

studied, along with the plastic strain at the onset of buckling ε_b and the corresponding softening branch slopes.

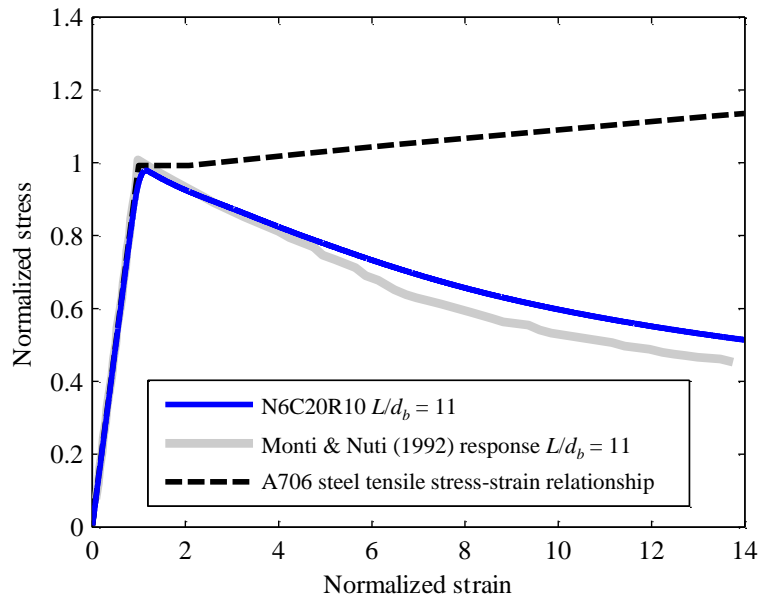


Figure 3.15 - Response comparison with (Monti & Nuti, 1992).

Figure 3.16 presents the general layout of the buckling models used, which have two different configurations of tie layout; in one model (Tie Setup 1), the ties are placed at $s = 8$ in. [203.2 mm] center-to-center and the other (Tie Setup 2) has them placed every 4 in. [101.6 mm] along the length of the longitudinal bar. The longitudinal bars have initial length $L_o = 24$ in. [609.6 mm], corresponding to twice the thickness of the specimens tested in **Chapter 2**. This initial length is longer than the typical buckling length of the bars tested because it is of interest to obtain an average-axial-stress versus average-axial-strain relationship that also includes some elastic portions of the bar. This is to be consistent with the observations reported in **Section 2.6.1** and **Section 2.6.4**, in which the recorded spalling lengths (**Figure 2.11**) contain a smaller portion where bar buckling develops. This will be useful later when the buckling model is used to obtain experimental concrete core stress-strain relationships for different gage lengths. The tie length for the analytical experiment is set to $l_t = 6$ in. [152.4 mm], which corresponds to half the thickness of the specimens. The analytical experiment matrix is developed by varying the longitudinal bar diameter from $d_b = 3/4$ in. [19 mm] to 1 1/4 in. [32 mm], as well as the transverse tie diameter from $d_{bt} = 0$ to 7/8 in. [22 mm].

Table 3.2 contains the experimental variables of interest with some resulting nondimensional quantities such as ratio s/d_b , which represents a relative restrictive tie spacing over which bar buckling is forced into (except for the cases of smaller tie diameters) and ratio $(d_{bt}^2/l_t)/(d_b^2/L_o)$, which represents the relative stiffness of a single transverse tie with respect to the longitudinal bar stiffness. These ratios will be used later as explanatory variables for the model developed in **Section 3.4.2.1**.

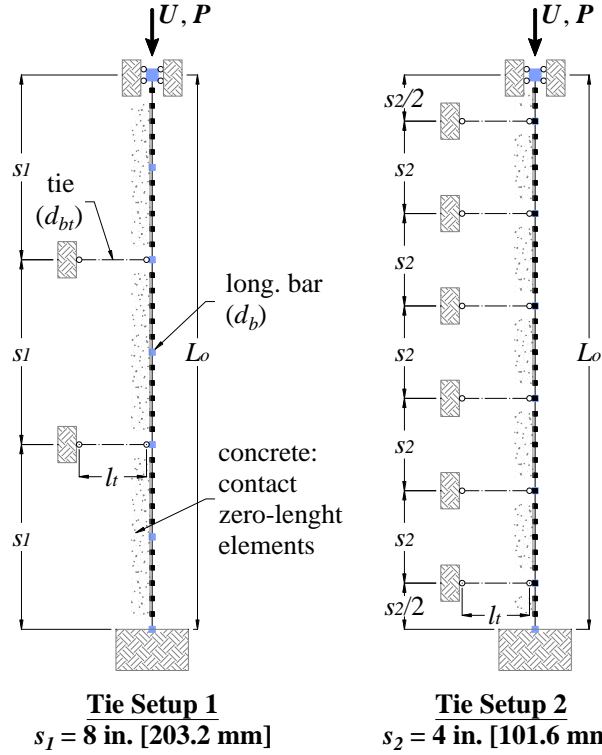


Figure 3.16 – Inelastic buckling models of tied embedded bars.

Table 3.2 – Inelastic buckling analytical experiment matrix [Note: 1 in. = 25.4 mm].

Test ID	s [in.]	d_b [in.]	d_{bt} [in.]	s/d_b	d_{bt}/d_b	$(d_{bt}^2/l_t)/(d_b^2/L_o)$
1	8	3/4	0	10.7	0.0	0.0
2	8	3/4	1/4	10.7	0.3	0.4
3	8	3/4	3/8	10.7	0.5	1.0
4	8	3/4	1/2	10.7	0.7	1.8
5	8	3/4	5/8	10.7	0.8	2.8
6	8	7/8	0	9.1	0.0	0.0
7	8	7/8	1/4	9.1	0.3	0.3
8	8	7/8	3/8	9.1	0.4	0.7
9	8	7/8	1/2	9.1	0.6	1.3
10	8	7/8	5/8	9.1	0.7	2.0
11	8	1	0	8.0	0.0	0.0
12	8	1	1/4	8.0	0.3	0.3
13	8	1	3/8	8.0	0.4	0.6
14	8	1	1/2	8.0	0.5	1.0
15	8	1	5/8	8.0	0.6	1.6
16	8	1 1/4	0	6.4	0.0	0.0
17	8	1 1/4	1/4	6.4	0.2	0.2
18	8	1 1/4	3/8	6.4	0.3	0.4
19	8	1 1/4	1/2	6.4	0.4	0.6
20	8	1 1/4	5/8	6.4	0.5	1.0
21	4	3/4	0	5.3	0.0	0.0
22	4	3/4	1/4	5.3	0.3	0.4
23	4	3/4	3/8	5.3	0.5	1.0
24	4	3/4	1/2	5.3	0.7	1.8
25	4	3/4	5/8	5.3	0.8	2.8
26	4	3/4	3/4	5.3	1.0	4.0
27	4	3/4	7/8	5.3	1.2	5.4
28	4	7/8	0	4.6	0.0	0.0

Test ID	s [in.]	d_b [in.]	d_{bt} [in.]	s/d_b	d_{bt}/d_b	$(d_{bt}^2/l_t)/(d_b^2/L_o)$
29	4	7/8	1/4	4.6	0.3	0.3
30	4	7/8	3/8	4.6	0.4	0.7
31	4	7/8	1/2	4.6	0.6	1.3
32	4	7/8	5/8	4.6	0.7	2.0
33	4	7/8	3/4	4.6	0.9	2.9
34	4	7/8	7/8	4.6	1.0	4.0
35	4	1	0	4.0	0.0	0.0
36	4	1	1/4	4.0	0.3	0.3
37	4	1	3/8	4.0	0.4	0.6
38	4	1	1/2	4.0	0.5	1.0
39	4	1	5/8	4.0	0.6	1.6
40	4	1	3/4	4.0	0.8	2.3
41	4	1	7/8	4.0	0.9	3.1
42	4	1 1/4	0	3.2	0.0	0.0
43	4	1 1/4	1/4	3.2	0.2	0.2
44	4	1 1/4	3/8	3.2	0.3	0.4
45	4	1 1/4	1/2	3.2	0.4	0.6
46	4	1 1/4	5/8	3.2	0.5	1.0
47	4	1 1/4	3/4	3.2	0.6	1.4
48	4	1 1/4	7/8	3.2	0.7	2.0

3.4.1 Typical response

This section presents typical response of a tied bar undergoing inelastic lateral instability. Interaction of the different components during the evolution of Test 29 (**Table 3.2**) is presented in **Figure 3.17**. This test comprises a 7/8 in. [22 mm] longitudinal bar, modeled under Tie Setup 2 ($s = 4$ in. [101.6 mm]), with 1/4 in. [6.4 mm] diameter transverse ties. **Figure 3.17a** presents the relationship between the average-axial-stress, that is, the quotient between applied force, P , and the cross-sectional yield strength, $A_s f_y$, and the average-axial-strain, which is defined as the downward displacement U divided by the initial length L_o . The response shows a linear elastic trend up to yielding, followed by a strain hardening portion with a post yield slope smaller than the monotonic one for tension, and a softening branch that develops after the onset of bar buckling. For the sake of contextualizing all the response presented, four instances highlighted correspond to average-axial-strain (U/L_o) equal to 2, 5, 10 and 30 times the longitudinal bar yield strain. **Figure 3.17b** shows the evolution of the cross-sectional tangent flexural stiffness $E_t I$ normalized by initial stiffness $E_o I$, where E_o corresponds to the initial elastic Young's modulus of the steel and I is the inertia of the longitudinal bar. Extracted from the formulation in **Equation (3.7)**, the cross-sectional tangent flexural stiffness is estimated as

$$\frac{\partial M}{\partial k} = E_t I = \sum_{i=1}^{n^{Fiber}} E_{t,i} y_i^2 A_{fib,i} \quad (3.11)$$

where $A_{fib,i}$ is the area of the i^{th} fiber (see **Section 3.3.1** and **Figure 3.3** for the variables definition).

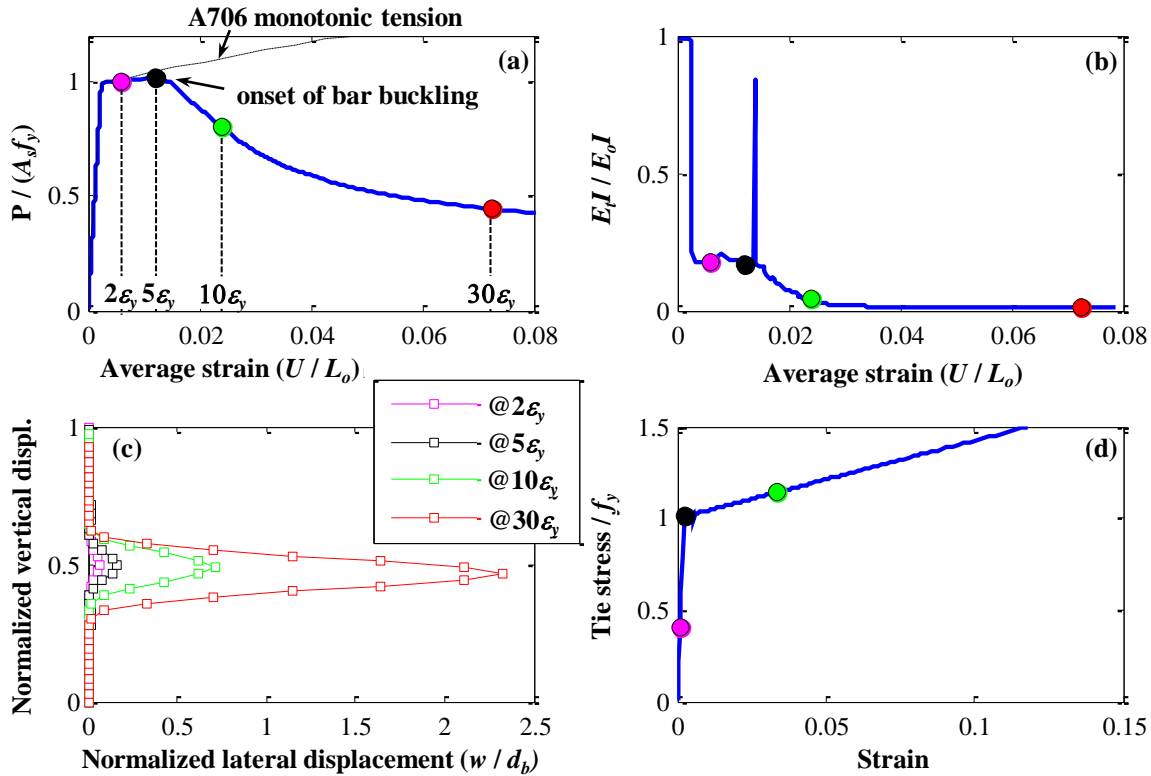


Figure 3.17 - Buckling response of Test 29 ($d_b = 7/8$ in., Tie Setup 2, $d_{br} = 1/4$ in.): (a) average stress versus average axial strain relationship; (b) normalized tangent moduli evolution with average axial strain; (c) deformed shape; (d) stress strain relationship of the tie adjacent to mid height.

It is observed that bar yielding is associated with an approximate 82% reduction in flexural tangent stiffness, and bar buckling further reduces this value to 1% of the initial stiffness (which is the post yield slope of the material model, relative to E_o). **Figure 3.17c** depicts the deformed shaped of the longitudinal bar at the aforementioned levels of average axial strain. The lateral displacement w shown is normalized by bar diameter, d_b . **Figure 3.17d** shows the demand, in terms of the axial stress-strain relationship, of the restraining tie close to mid height. Bar yielding is apparent, and the strain level demand is likely to surpass the rupture strain in this case.

3.4.1.1 *Double modulus analysis*

Before the onset of bar buckling, all sections along the length of the bar are under uniform compressive strain. After inelastic buckling is triggered, lateral displacement of the bar also requires that flexural deformations develop, specifically in sections within the plastic hinges (see **Section 3.3.6**). For portions of the bar near the central plastic hinge, this flexural deformation promotes unloading (toward the tensile side) of those material points in the convex part of the cross section (see **Figure 3.14**). For this reason, the material in some areas of the cross section is in the strain hardening portion of the stress-strain curve, with tangent modulus E_t and others start unloading with the initial modulus E_o . This behavior is described by the *Double Modulus Theory*, first presented by Engesser in 1895 and von Karman in 1908 (Chakrabarty, 2006; Papia et al.,

1988), which is also recognized as the so-called “double modulus approach” (Pantazopoulou, 1998; Papia & Russo, 1989).

To illustrate the fact that different moduli coexist within the critical cross section of a bar undergoing later instability, **Figure 3.18** and **Figure 3.19** show the strain field and tangent modulus distribution of the fibers in the critical section of Test 29. To create the images presented, a linear interpolation process is implemented to fill the gaps between the centroids of the fibers, which are the monitoring points (see top left corner of **Figure 3.19**) where the strains and tangent moduli are estimated. The images are created at the four instances described above (for example, at $U/L_o = 2, 5, 10$ and $30\varepsilon_y$) and at yielding ($U/L_o = 1\varepsilon_y$). **Figure 3.18** shows the evolution of the strain field with average axial strain. It is observed that the strain field evolved from a purely compressive state at yielding ($U/L_o = 1\varepsilon_y$) to a flexural-compression state developing large curvatures at intermediate average axial strain demand (for example, at $U/L_o \geq 10\varepsilon_y$). The onset of bar buckling occurs for average axial strain in excess of $5\varepsilon_y$; at this instant, the cross section is mostly under compressive strains, but it is already showing signs of unloading in the concave part of the bar (right hand side). After bar buckling occurs, the neutral axis migrates toward the centroid of the bar (from right to left) leaving larger portions of the cross section under tensile strains.

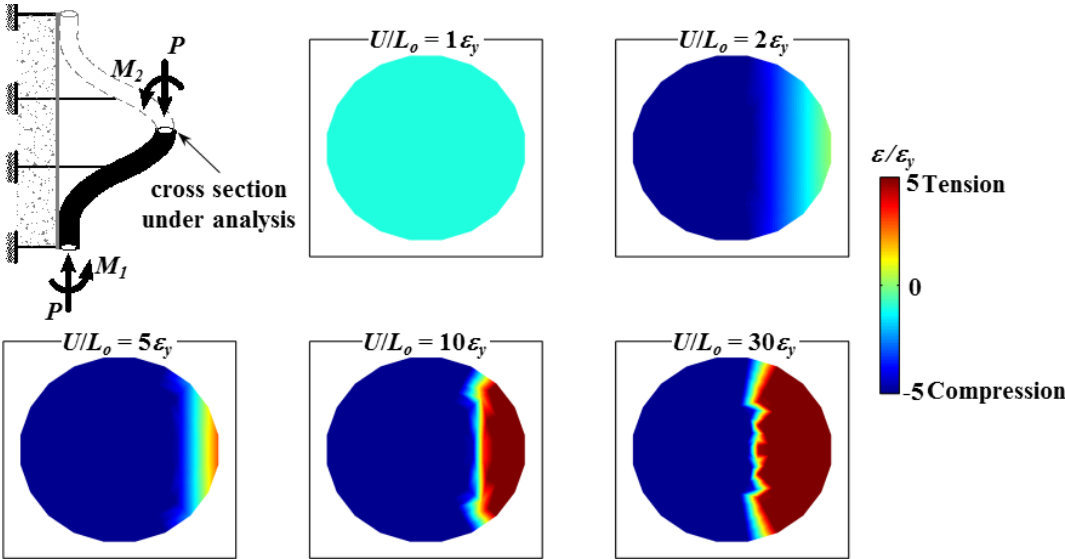


Figure 3.18 - Strains in the midspan cross section at different levels of average axial strain (Test29).

Given the large curvature developed for average axial strain larger than $2\varepsilon_y$, most of the material points of the cross section are in the strain hardening portion of the constitutive stress-strain curve. This is evident in **Figure 3.19**, which presents instantaneous tangent modulus of the material points of the section. This figure also shows the flexural stiffness of the section, as calculated with **Equation (3.11)**, normalized to E_oI . It is observed that even at low levels of plastic axial strain demand only a few material points of the section have tangent modulus equal to the elastic one E_o . This results in a reduced section tangent flexural stiffness equal to 18% of the elastic, for axial strains along the strain hardening portion of the response (at $U/L_o = 2\varepsilon_y$ and $U/L_o = 5\varepsilon_y$). The onset of buckling forces the unloading of additional material points, as the neutral axis moves toward the centroid. At large average axial strain demand, only a narrow band

of a few material points having the modulus E_o is observed. It is worth mentioning that the constitutive material model accounts for early yielding on strain reversal (to approximate the Bauschinger effect), therefore, the tangent modulus can actually have several values other than the strain hardening modulus E_h or the initial modulus E_o . **Figure 3.20** illustrates this idea by showing the history of the stress-strain relationship in the fibers of the section. The fibers that show strain reversal correspond to those close to the concave portion of the bar (to the right of centroid of the cross section). It is apparent that some material points see diverse tangent moduli along the evolution of the test, which reveals the complexity of the problem.

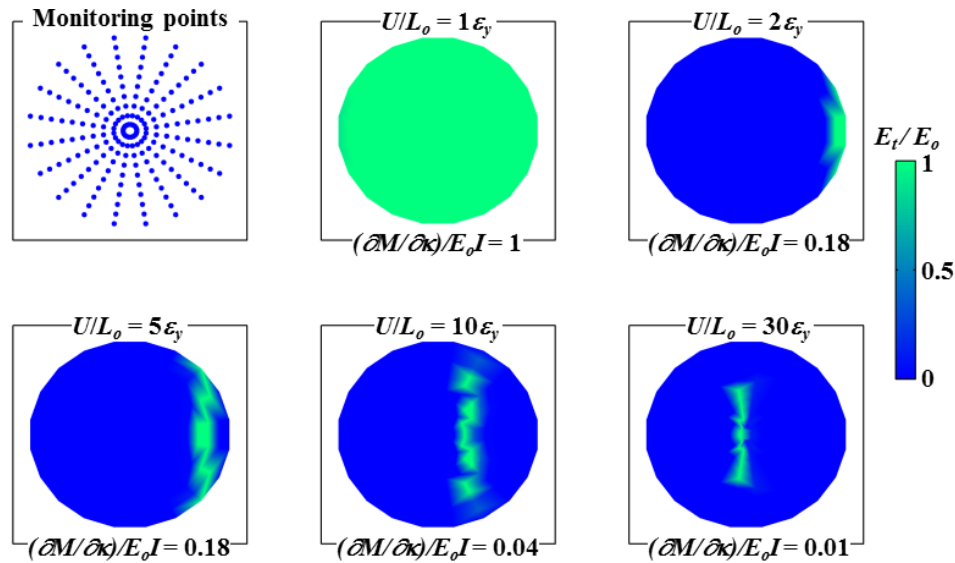


Figure 3.19 - Normalized tangent moduli distribution within the critical cross section at different levels of average axial strain (Test 29)

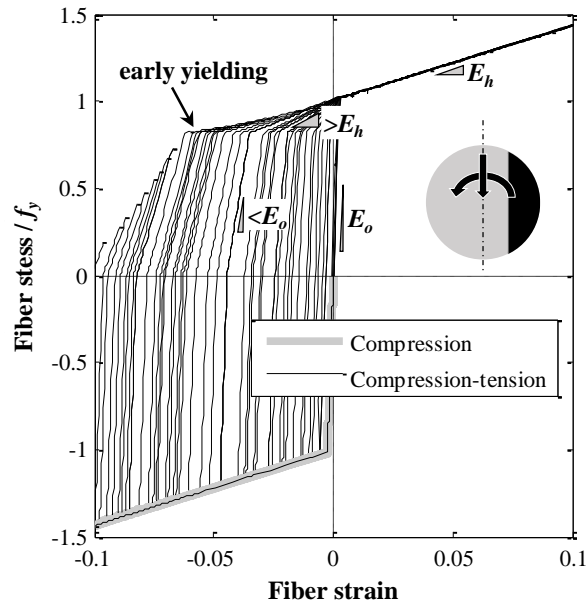


Figure 3.20 – Evolution of the stress-strain relationship of the fibers in the critical section of Test 29.

For the analysis of the response in the vicinity of the onset of bar buckling, Test 28 is studied next. This test is appropriate because the lack of transverse ties promoted bar buckling as the yield strength was reached. The average response of Test 28 is presented on the top left part of **Figure 3.23**. It is characterized by a linear portion followed by a sharp transition to the softening branch for strains larger than ε_y . A rapid loss of strength for small increments of strain after the onset of buckling is observed. Of particular interest is the evolution of the test in the vicinity of the onset of buckling. The complexity of the load deflection path is apparent in **Figure 3.21a**, which presents the average axial stress-strain curve in a region close to buckling initiation. **Figure 3.21b** shows the evolution of section flexural stiffness EI with increasing average strain. The response is linear up to point **i**, where a first deviation from the elastic slope is observed, mainly a product of the lateral imperfection imposed in the unstressed state. The section stiffness is reduced to approximately 65% of the initial stiffness at the strain level of point **j**, and it further reduces until the maximum (yield) strength is reached at point **k**. A small plateau develops up to point **l**, and “snap-back buckling” is properly modeled from this point, thanks to the Arch Length algorithm (Clarke & Hancock, 1990; Crisfield, 1981) employed in the solution strategy of the inelastic mathematical model. Unloading is initiated with a strain reversal up to point **m**. Stiffening of the cross section is apparent from point **k** to point **m**. This occurs because the increased curvature promotes strain reversal in some material points, which unload with tangent modulus E_o from a strain hardening state in compression, where they had tangent modulus $E_h = 0.01E_o$. At point **n** the softening branch is already stabilized. Comparison of points **l** and **n** is interesting because they are under the same average axial strain demand, have approximately equal section flexural stiffness (**Figure 3.21d**) but their load carrying capacity differs by 25%. This difference is because, although the curvature remains essentially constant from point **l** to point **n**, reduction of the centroidal strain, along with migration of the neutral axis toward the center of the section (**Figure 3.21c**), occur. This in turn, creates internal tensile stresses that counteract the compressive stresses that were equilibrating the larger force.

The Euler equation for buckling of slender columns gives the critical stress at buckling according to

$$f_{cr} = \frac{\pi^2 EI}{L^2 A} \quad (3.12)$$

where $L = 0.5L_o = 12$ in. [304.8 mm] for the bar of Test 28, which is under fixed-end; A and I are the area and inertia of the 7/8 in. [22 mm] diameter bar; and E is the modulus of elasticity. By making $E = E_o$, solution of **Equation (3.12)** gives $f_{cr} = 95$ ksi [655 MPa] $> f_y$, therefore inelastic buckling is expected. A main interest is finding the appropriate reduced modulus of elasticity that agrees with the inelastic solution presented in this section. By making $f_{cr} = f_y$, a reduced modulus of elasticity is found to be $E_r = 0.74E_o$, which approximately coincides with reduction in section flexural stiffness reported for point **j** in **Figure 3.21b**, where the first sign of deviation from the linear elastic trend was observed. For point **j** reported $E_I/E_oI = 0.65$. This is not always applicable for the case of tied bars, where reduction of the tangent modulus is also observed without apparent lateral instability.

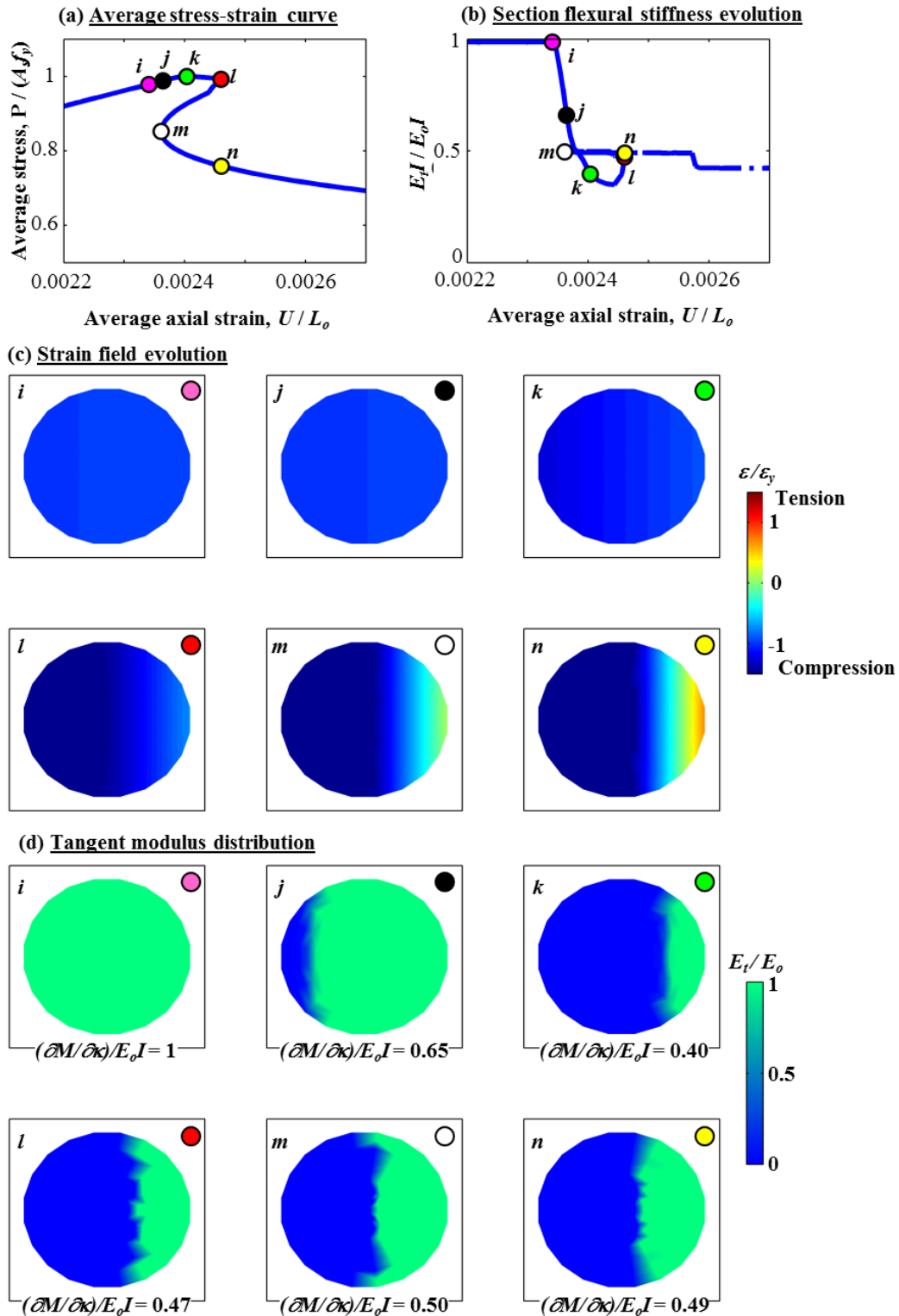


Figure 3.21- Response of Test 28 close to the onset of buckling ($d_b = 7/8$ in. [22 mm], Tie Setup 2, $d_{bt} = 0$): (a) average stress versus average axial strain relationship; (b) normalized section flexural stiffness evolution with average axial strain; (c) strain field evolution of the critical section; (d) tangent modulus distribution.

3.4.1.2 Local versus global average axial strains

Response of the Test 29 bar undergoing inelastic lateral instability is further studied in **Figure 3.22**. The displaced shape of the bar and the axial strain per element are shown in **Figure 3.22a** and **Figure 3.22b**, respectively, for the instance where $U/L_o = 10\varepsilon_y$. The locations where the tie restrains acts along the length of the bar are highlighted with black markers, along with the identification of some elements of interest. For the case shown, the tie diameter is relatively small ($d_{bt} = 1/4$ in. [6.4 mm]), therefore the buckling process provokes their extension. For larger tie diameter, lateral displacement at the location of all ties is restricted to small values and the buckling length is restricted to s . The axial strain field is not uniform, showing strain concentration in locations within the buckling length. **Figure 3.22c** shows axial-strain at the element level versus the average axial strain, U/L_o . Element 18 is part of the central plastic hinge as described in **Section 3.3.6** and develops the largest axial strain demand compared to the adjacent elements. This element develops a maximum axial strain of approximately 9% at an approximate average axial strain of 6%. Elements 17 and 16 develop axial strain at a lower rate, plateauing at approximately 1/4 to 1/3 of the maximum strain developed by Element 18. Relaxation of Element 16 is apparent for average strain larger than 1.5% approximately. In all cases, element strains deviate from the average strain after the yield strain is attained. The results shown in **Figure 3.22c** support the experimental observations presented in **Section 2.6.2** and **Section 2.6.4** (**Figure 2.9** and **Figure 2.13**).

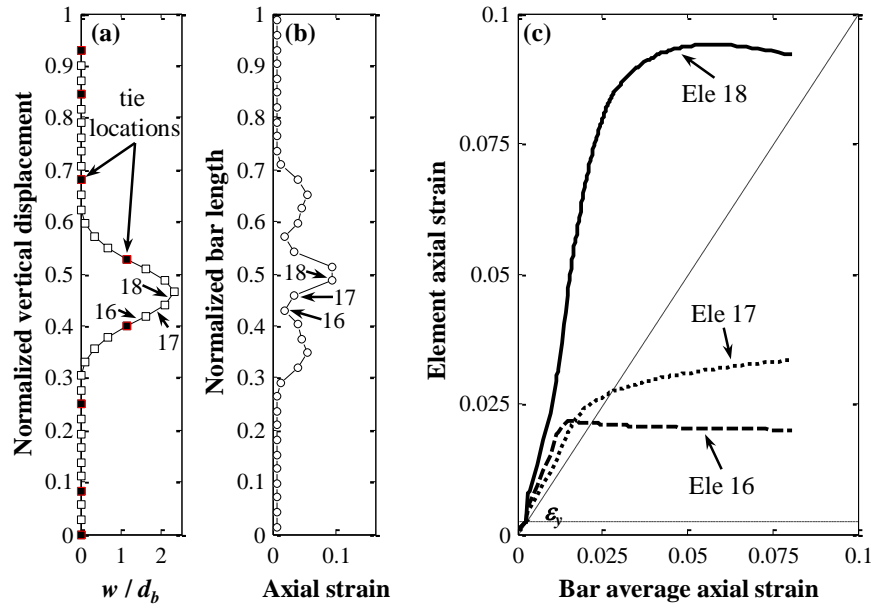


Figure 3.22 – Deformed shape and local strains of Test 29: (a) normalized lateral displacement at $U/L_o = 10\varepsilon_y$; (b) distribution of element axial strains at $U/L_o = 10\varepsilon_y$; (c) element axial strain versus average axial strain relationship for three elements (16, 17 and 18) within the buckling length of the bar.

Appendix B contains plots similar to those in **Figure 3.17** to **Figure 3.22**, describing the series of tests 28 to 34, comprising a 7/8 in. [22 mm] longitudinal bar under Tie Setup 2, at various diameters of cross ties ($0 \leq d_{bt} \leq 7/8$).

3.4.1.3 Effect of crosstie diameter

Crosstie diameter d_{bt} has an impact on the response of the longitudinal bars undergoing lateral instability. Three tests in **Table 3.2** are selected to demonstrate this: Tests 28, 30, and 33. While the bar in Test 28 has no lateral restraint, transverse tie diameter in Tests 30 and 33 are 3/8 in. [10 mm] and 3/4 in. [19 mm], respectively.

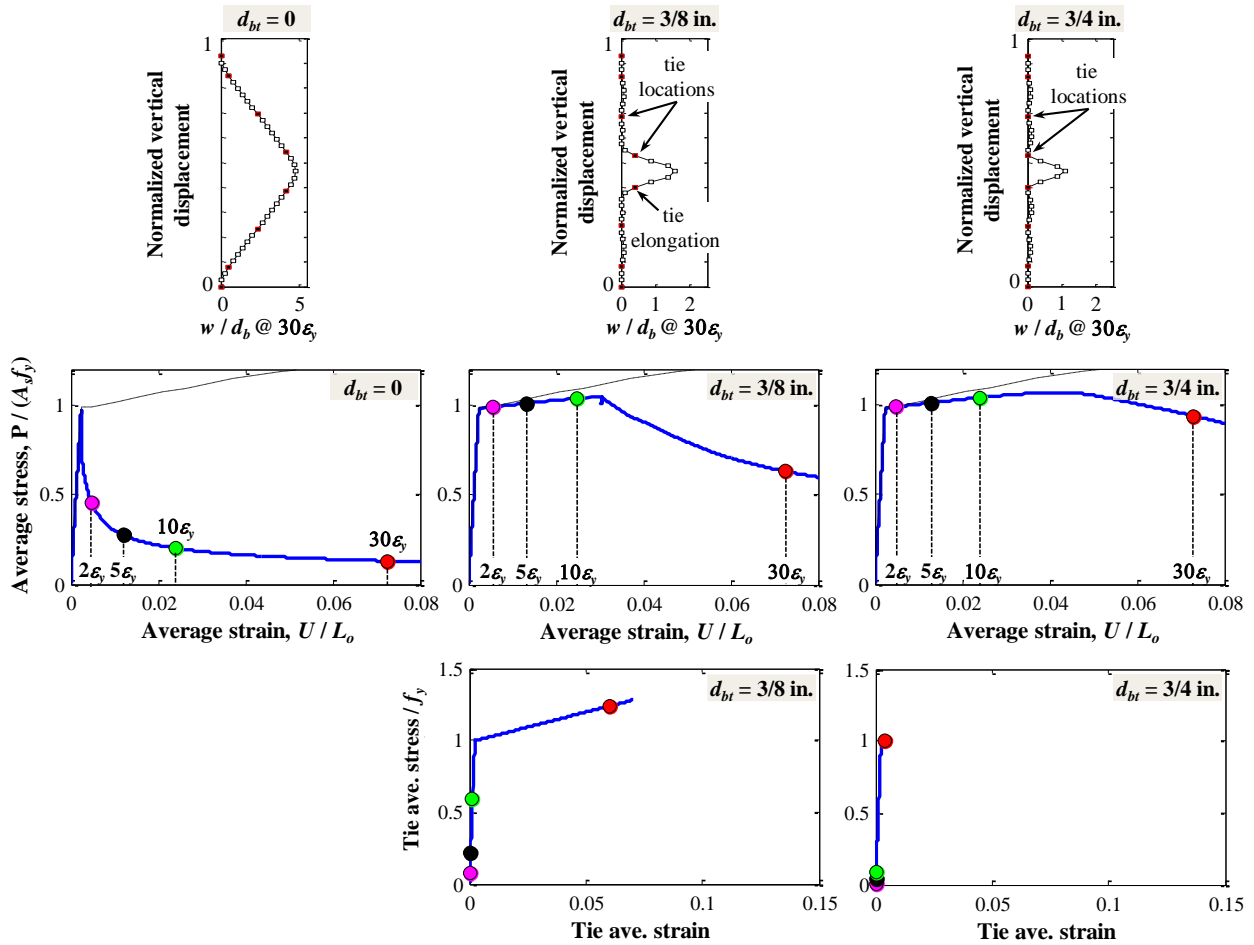


Figure 3.23 – Buckling response variation with transverse tie diameter (from left to right, Test 28, 30 & 33).

The central row in **Figure 3.23** depicts the normalized average stress ($P/A_s f_y$) versus average strain (U/L_o) relationship for the 7/8 in. [22 mm] diameter bars in the tests. Additionally, for the cases with transverse restraint, the bottom row shows the demand on the tie adjacent to mid height (where the maximum lateral displacement occurs), which is presented in terms of its average stress-strain relationship. Four instances highlighted with circular markers correspond to U/L_o equal to 2, 5, 10, and 30 times the longitudinal bar yield strain, as before. It is observed that the bar with no crossties buckles as it reaches its yield strength, with a large loss of load carrying capacity for small increments of strain past yielding. On the other hand, the bars with ties develop a post yield strain hardening branch, as well as a strain softening portion after bar buckling is triggered. While the slope of the strain hardening portion does not seem to be influenced by the tie diameter, its extension, as well as the slope of the softening branch does. Tie yielding is apparent for the smaller tie diameter case, while the tie with the larger diameter remains elastic up to the average axial strain level at which the test was concluded (8%). The top

row in **Figure 3.22** shows that tie elongation defines the buckling length of the specimens because the nodes adjacent to them may or may not displace laterally depending on the stiffness of the restraint. For the cases presented, buckling length was 27.0, 7.6 and 4.6 d_b for $d_{bt} = 0, 3/8\text{in.}$ [10 mm] and $3/4\text{ in.}$ [19 mm], respectively. Tie yielding prevention is a factor to consider when proper lateral restraint of longitudinal bars is required.

3.4.2 Inelastic buckling model of tied bars

The inelastic buckling of tied bars is a complex structural problem, highly nonlinear in geometry and material response, involving intricate load-deflection relationships. Many components are involved in the model, which makes it computationally intensive and prone to convergence problems. Additionally, bifurcation problems and stiffness matrix singularities have to be sorted out to find the proper solution for each variation of the experimental variables. This is a time consuming process requiring careful consideration, one at a time, of the solutions corresponding of each test.

A simple model describing the complete stress-strain curve of the tests in **Table 3.2** is proposed in this section. Given that minimum $d_b = 3/4\text{ in.}$ [19 mm] and $L_o = 24\text{ in.}$ [610 mm], all the experiments resulted in inelastic buckling, which is expected according to **Equation (3.12)**. **Figure 3.24** presents the proposed model of tied longitudinal bars, with a graphical representation of the variables of interest. From the descriptions in the previous section, it is concluded that the response of the bars is characterized by an initial linear elastic portion, up to yielding. Bars not buckling at yielding develop a strain hardening branch with slope $m_h E_o$, up to the buckling strain ε_b . In the proposed model, the strain hardening branch is represented by a straight line and ε_b is defined as the strain at which the maximum load is attained. The post buckling softening branch is described by the relative load carrying capacity at discrete strain increments ε_p past the buckling strain. For example, $f_r(\varepsilon_p)$ indicates the strength capacity with respect to the buckling strength f_b at a strain increment of ε_p past ε_b :

$$f_r(\varepsilon_p) = \frac{f_p(\varepsilon_p)}{f_b} \quad (3.13)$$

where $f_p(\varepsilon_p)$ is the strength at strain $\varepsilon = \varepsilon_b + \varepsilon_p$. Given m_h and ε_b , buckling strength f_b is estimated by

$$f_b = f_y + m_h E_o (\varepsilon_b - \varepsilon_y) \quad (3.14)$$

Variables ε_b , m_h and $f_r(\varepsilon_p)$ are estimated in the following sections from statistical analysis of the models in **Table 3.2**.

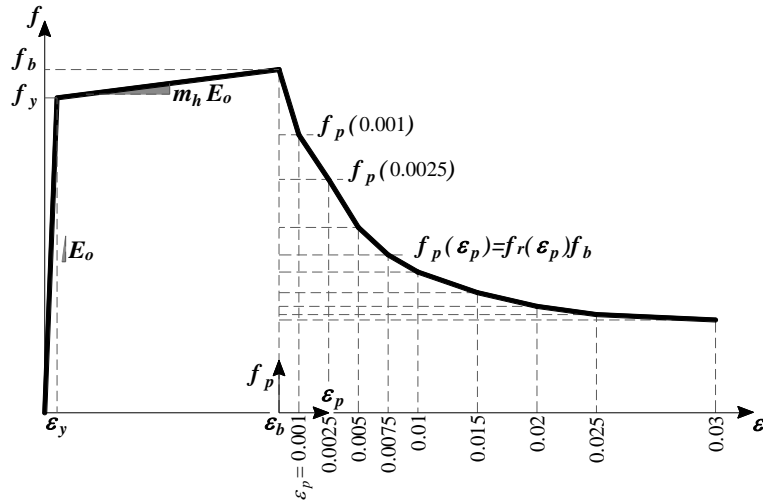


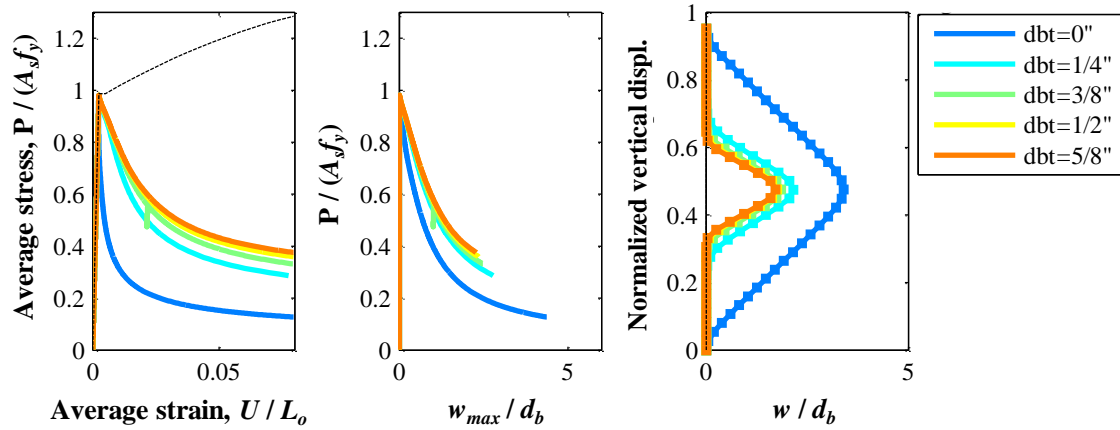
Figure 3.24 – Model describing the average axial stress – strain response of tied bars undergoing inelastic buckling.

3.4.2.1 Average axial stress-strain curves

The average axial stress-strain curves of the buckling tests are the main data source for the purpose of statistical analysis of the variables of interest. An example of these curves is shown in **Figure 3.25** for the experiments with $d_b = 1$ in. [25 mm], under Tie Setup 1 and Tie Setup 2. Also shown are the relationships between the average stress and the mid span displacement (w_{max}). Additionally, the displaced shape at $U/L_o = 20\varepsilon_y$, which might or might not include buckling, depending on the tie diameter and spacing, is presented as well. Similar plots for the tests with other longitudinal bar diameters are presented in **Appendix B**. It was found that for any d_b , Tie Setup 1 did not promote inelastic buckling past the yield strength. This is an expected result explained by the fact that minimum s/d_b was 6.4. The main response variation for this tie setup is observed in the post buckling slope, which becomes stiffer as s/d_b decreases. On the other hand, under Tie Setup 2, the response is highly dependent on s/d_b . Buckling strain ε_b and the post buckling stiffness parameter m_h increase as s/d_b decreases. The average stress versus lateral displacement w_{max} is also highly affected by ratio s/d_b .

Isolation of the post buckling branch of the response is convenient for the development of the simpler buckling model. **Figure 3.26a** and **Figure 3.26b** present plots of f_r versus ε_p for Tie Setup 1 and 2, respectively. Except for the cases where $d_{bt} = 0$, the post buckling response under Tie Setup 2 is noticeable stiffer than the response under Tie Setup 1. Under Tie Setup 2, lines not reaching limit strain $\varepsilon_p = 0.06$ correspond to specimens that buckled at large plastic strains, hence their post buckling strain history ended early because all analyses were finished at $\varepsilon = U/L_o = 0.08$. It is important to clarify that the softening branch slopes observed in **Figure 3.26** are a function of the specimen length L_o . This is due to the relaxation of the elements adjacent to the buckling length, which elongate toward the buckled portion forced by the end axial restrictions. This results in steeper slopes of the softening branches for larger lengths of the elastic portion of the bar (for example, those outside the buckling length). The subject of non-objectivity of the softening response in material constitutive models has been discussed in detail in **Section 1.2** and **Section 2.6.5** of this document. Regularization of the softening portion of the model is left for further research.

(a) Tie Setup 1 – $s/d_b = 8$



(b) Tie Setup 2 – $s/d_b = 4$

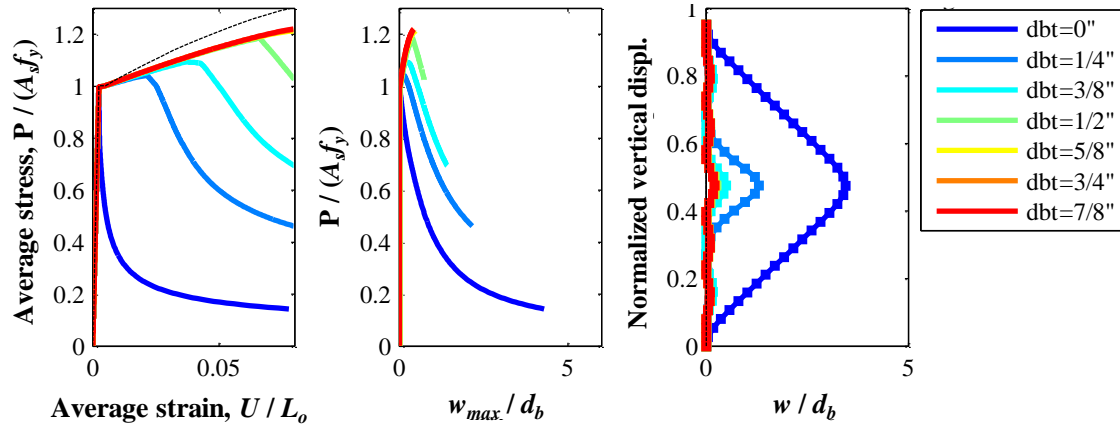


Figure 3.25 - Response of Tests 11 to 15 (Tie Setup 1) and Tests 35 to 41 (Tie Setup 2) ($d_b = 1$ in. [25mm]).

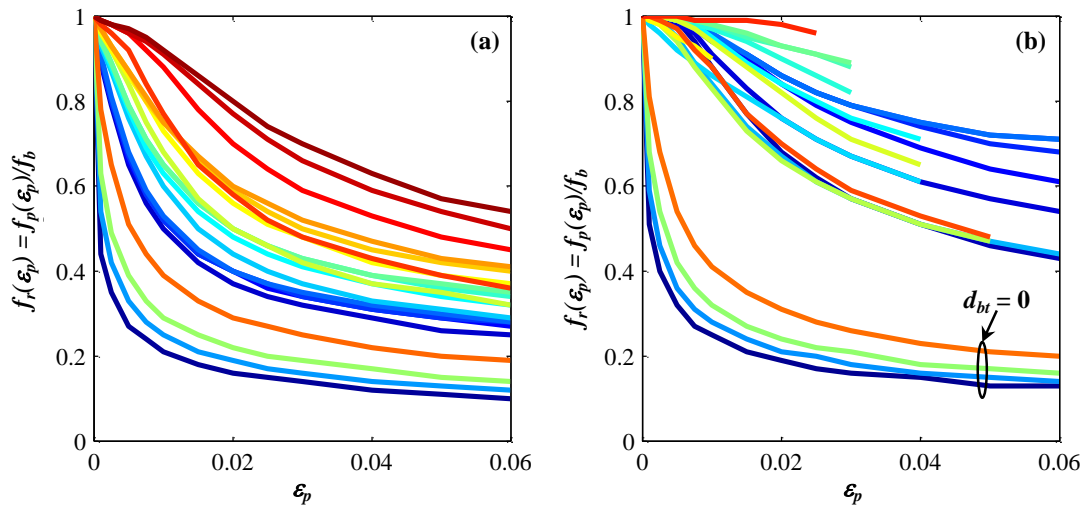


Figure 3.26 – Post buckling response in terms of f_r and ϵ_p for: (a) Tie Setup 1 and (b) Tie Setup 2.

3.4.2.2 Inelastic model variables

Variables ε_b , m_h and $f_r(\varepsilon_p)$ were extracted from the average stress-strain curves described above for the 48 cases in **Table 3.2**. Three-dimensional surfaces were then interpolated from these discrete data points in terms of two explanatory variables: (i) s/d_b , which represents a relative restrictive tie spacing over which bar buckling is forced into (except for the cases of smaller tie diameters) and (ii) $(d_{bt}^2/l_t)/(d_b^2/L_o)$, which represents the relative stiffness of a single transverse tie with respect to the longitudinal bar stiffness. In order to tabulate the variables of interest in term of the explanatory variables, the three-dimensional surfaces were intersected at discrete values of s/d_b , generating marginal relationships between the response variables and $(d_{bt}^2/l_t)/(d_b^2/L_o)$. In this manner, one only has to estimate $(d_{bt}^2/l_t)/(d_b^2/L_o)$ and intersect the proper s/d_b value to obtain ε_b , m_h and $f_r(\varepsilon_p)$.

Figure 3.27 to **Figure 3.29** present the described joint and marginal distributions of s/d_b and $(d_{bt}^2/l_t)/(d_b^2/L_o)$ that explain ε_b , m_h and f_r . This latter is presented at $\varepsilon_p=0.02$ as an example but was estimated at 12 incremental strains in the range $0.001 \leq \varepsilon_p \leq 0.06$ for the sake of providing a good resolution to describe the softening branch of the model. Variables ε_b and m_h increase monotonically with increments of the explanatory variables, resulting in a smooth three-dimensional surface. **Table 3.3** and **Table 3.4** give smoothed-out values of these variable for the range $0 \leq (d_{bt}^2/l_t)/(d_b^2/L_o) \leq 3$ and $s/d_b = 3.5, 4.0, 4.5, 5.0, 5.5$ and 6.5 . Tests with larger values of s/d_b did not show a strain hardening portion, therefore, $\varepsilon_b = \varepsilon_y$ and $m_h = 0$ for $s/d_b \geq 6$. The results suggest that due to flexibility of the restraints (ties), s/d_b has to be as small as 4.5 to effectively prevent buckling up to $U/L_o=0.08$, strain at which the tests were concluded. Nonetheless, if proper tie stiffness is provided, inelastic buckling can be delayed up to $10 \varepsilon_y$ for s/d_b as large as 5.0.

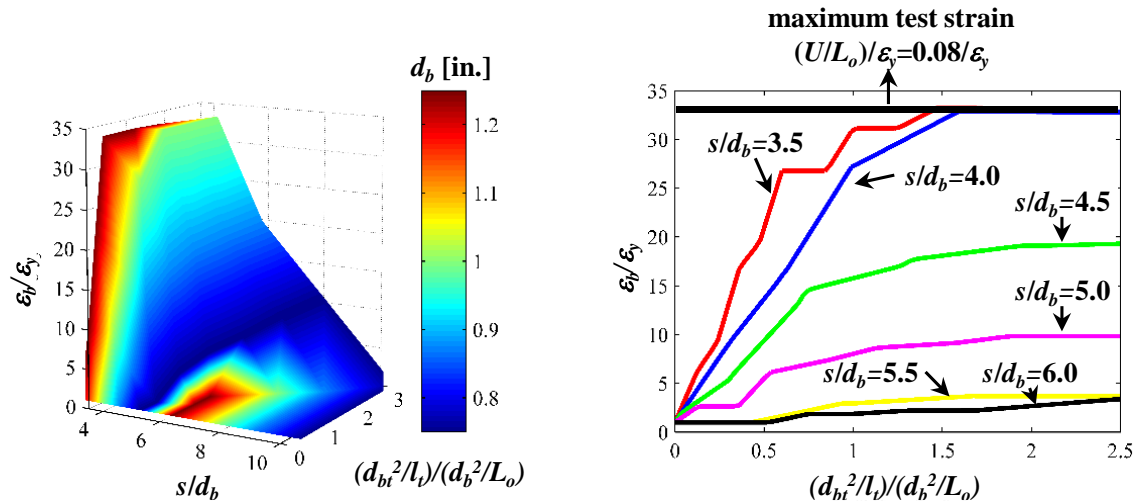


Figure 3.27 – Normalized buckling strain in terms of s/d_b and $(d_{bt}^2/l_t)/(d_b^2/L_o)$. (Note: 1 in. [25mm]).

Portions of the domain of f_r showed to be complex (non-smooth) in the range close to $s/d_b=6.4$ and $(d_{bt}^2/l_t)/(d_b^2/L_o)<1$. This discontinuity is mainly influenced by the response of the 1 1/4 in. [32 mm] diameter bars under Tie Setup 2, which buckled with a stiffer softening slope with respect to the neighboring tests. Since the idea was to estimate f_r using only the two variables discussed, this discontinuity proposed some difficulties for the tabulation of f_r because the resulting post yield slopes lost their shape after the interpolation and intersection process,

showing trends not corresponding to the physical phenomenon (as the ones in **Figure 3.26**). This problem was overcome by fitting rational polynomials to the discrete slope points, and assigning weights to each data point according to their quality (0 for bad quality or 1 for good quality). Resulting smoothed values of f_r as presented in **Table 3.5** to **Table 3.7**.

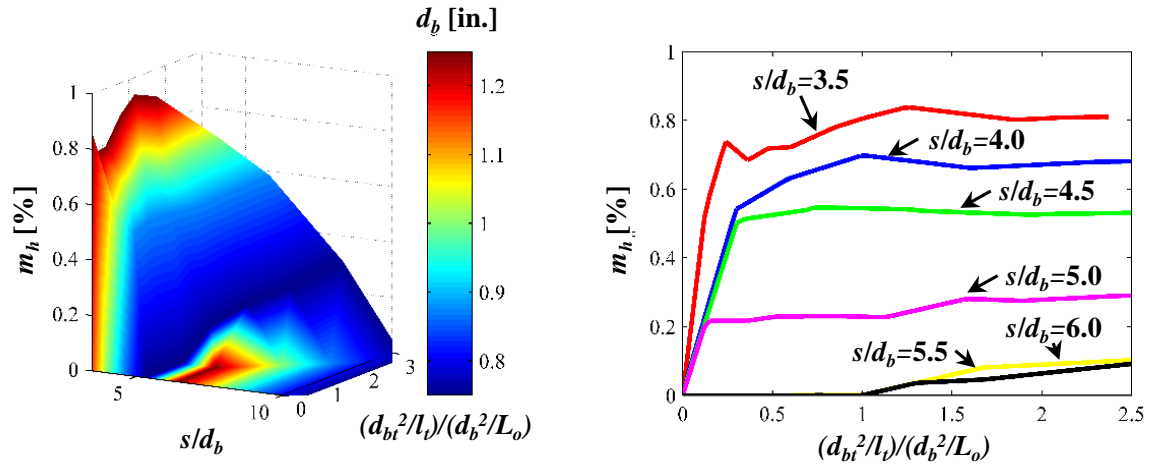


Figure 3.28 - Post yield slope coefficient in terms of s/d_b and $(d_{bt}^2/l_t)/(d_b^2/L_o)$. (Note: 1 in. [25mm]).

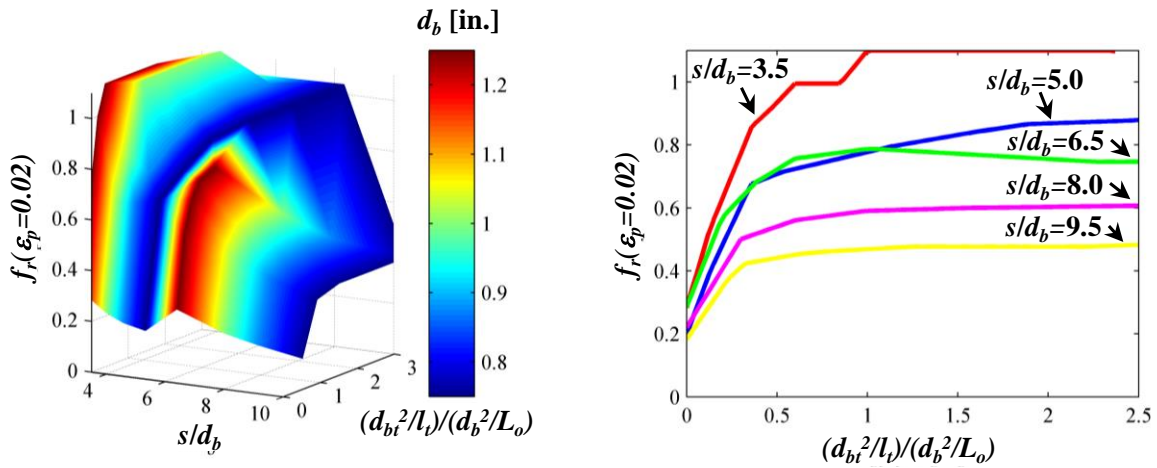


Figure 3.29 - Post buckling relative strength f_r at $\epsilon_p=0.02$ in terms of s/d_b and $(d_{bt}^2/l_t)/(d_b^2/L_o)$. (Note: 1 in. [25mm]).

Table 3.3 - Buckling strain ε_b normalized to yield strain.

$(d_{bt}^2 / l_t) / (d_b^2 / L_o)$	$\varepsilon_b / \varepsilon_y$					
	$s/d_b=3.5$	$s/d_b=4$	$s/d_b=4.5$	$s/d_b=5$	$s/d_b=5.5$	$s/d_b=6$
0.00	1.0	1.0	1.0	1.0	1.0	1.0
0.25	11.8	7.6	5.6	3.4	1.0	1.0
0.50	22.6	14.2	10.2	5.8	1.0	1.0
0.75	28.0	20.8	14.5	7.0	2.1	1.0
1.00	29.9	27.2	15.8	8.1	3.0	1.0
1.25	31.9	29.8	17.2	8.8	3.3	1.0
1.50	33.0	32.4	18.1	9.2	3.7	1.0
1.75	DNB	33.0	18.8	9.6	3.8	1.0
2.00	DNB	DNB	19.2	9.8	3.8	1.0
2.25	DNB	DNB	19.2	9.8	3.8	1.0
2.50	DNB	DNB	19.2	9.8	3.8	1.0
2.75	DNB	DNB	19.2	9.8	3.8	1.0
3.00	DNB	DNB	19.2	9.8	3.8	1.0

DNB= do not buckle in the range $0 \leq U/L_o \leq 0.08$.

Table 3.4 – Post yield slope m_h .

$(d_{bt}^2 / l_t) / (d_b^2 / L_o)$	m_h [%]					
	$s/d_b=3.5$	$s/d_b=4$	$s/d_b=4.5$	$s/d_b=5$	$s/d_b=5.5$	$s/d_b=6$
0.00	0.00	0.00	0.00	0.00	0.00	0.00
0.25	0.74	0.47	0.40	0.22	0.00	0.00
0.50	0.76	0.58	0.52	0.23	0.00	0.00
0.75	0.78	0.63	0.53	0.25	0.00	0.00
1.00	0.80	0.68	0.54	0.26	0.00	0.00
1.25	0.82	0.69	0.54	0.27	0.03	0.00
1.50	0.82	0.69	0.54	0.28	0.06	0.00
1.75	0.82	0.69	0.54	0.29	0.09	0.00
2.00	0.82	0.69	0.54	0.29	0.09	0.00
2.25	0.82	0.69	0.54	0.29	0.09	0.00
2.50	0.82	0.69	0.54	0.29	0.09	0.00
2.75	0.82	0.69	0.54	0.29	0.09	0.00
3.00	0.82	0.69	0.54	0.29	0.09	0.00

Values of 0 mean that no strain hardening portion is developed.

Table 3.5 – Post buckling strength coefficients f_r for $e_p = 0.001, 0.0025, 0.005, 0.0075$.

$f_r(\epsilon_p = 0.001)$						$f_r(\epsilon_p = 0.0025)$					
$\frac{(d_{bt}^2/l_t)}{(d_b^2/L_o)}$	s/d_b					$\frac{(d_{bt}^2/l_t)}{(d_b^2/L_o)}$	s/d_b				
	3.5	5	6.5	8	9.5		3.5	5	6.5	8	9.5
0	0.80	0.71	0.74	0.65	0.52	0	0.60	0.55	0.57	0.48	0.40
0.25	1.00	0.96	0.96	0.93	0.88	0.25	1.00	0.91	0.91	0.85	0.77
0.5	1.00	1.00	0.99	0.97	0.94	0.5	1.00	0.99	0.97	0.92	0.86
0.75	1.00	1.00	0.99	0.97	0.94	0.75	1.00	0.99	0.98	0.92	0.86
1	1.00	1.00	0.99	0.97	0.94	1	1.00	1.00	0.98	0.93	0.86
1.25	1.00	1.00	0.99	0.97	0.94	1.25	1.00	1.00	0.98	0.92	0.86
1.5	1.00	1.00	0.99	0.97	0.94	1.5	1.00	1.00	0.98	0.92	0.86
1.75	1.00	1.00	0.99	0.97	0.94	1.75	1.00	1.00	0.98	0.92	0.86
2	1.00	1.00	0.99	0.97	0.94	2	1.00	1.00	0.98	0.92	0.86
2.25	1.00	1.00	0.99	0.97	0.94	2.25	1.00	1.00	0.98	0.92	0.86
2.5	1.00	1.00	0.99	0.97	0.94	2.5	1.00	1.00	0.98	0.92	0.86
2.75	1.00	1.00	0.99	0.97	0.94	2.75	1.00	1.00	0.98	0.92	0.86
3	1.00	1.00	0.99	0.97	0.94	3	1.00	1.00	0.98	0.92	0.86

$f_r(\epsilon_p = 0.005)$						$f_r(\epsilon_p = 0.0075)$					
$\frac{(d_{bt}^2/l_t)}{(d_b^2/L_o)}$	s/d_b					$\frac{(d_{bt}^2/l_t)}{(d_b^2/L_o)}$	s/d_b				
	3.5	5	6.5	8	9.5		3.5	5	6.5	8	9.5
0	0.50	0.43	0.43	0.38	0.32	0	0.41	0.38	0.37	0.33	0.27
0.25	0.97	0.83	0.84	0.75	0.64	0.25	0.92	0.77	0.78	0.67	0.57
0.5	1.00	0.96	0.93	0.84	0.74	0.5	1.00	0.93	0.90	0.77	0.65
0.75	1.00	0.97	0.95	0.85	0.75	0.75	1.00	0.95	0.91	0.79	0.66
1	1.00	0.98	0.95	0.86	0.75	1	1.00	0.96	0.92	0.80	0.67
1.25	1.00	0.99	0.96	0.86	0.75	1.25	1.00	0.97	0.93	0.80	0.67
1.5	1.00	0.99	0.96	0.86	0.75	1.5	1.00	0.97	0.93	0.80	0.67
1.75	1.00	0.99	0.96	0.86	0.75	1.75	1.00	0.97	0.93	0.80	0.67
2	1.00	0.99	0.96	0.86	0.75	2	1.00	0.98	0.93	0.80	0.67
2.25	1.00	0.99	0.96	0.86	0.75	2.25	1.00	0.98	0.93	0.80	0.67
2.5	1.00	0.99	0.96	0.86	0.75	2.5	1.00	0.98	0.93	0.80	0.67
2.75	1.00	0.99	0.96	0.86	0.75	2.75	1.00	0.98	0.93	0.80	0.67
3	1.00	0.99	0.96	0.86	0.75	3	1.00	0.98	0.93	0.80	0.67

Table 3.6 – Post buckling strength coefficients f_r for $e_p = 0.01, 0.015, 0.02, 0.025$.

$f_r(\varepsilon_p = 0.01)$						$f_r(\varepsilon_p = 0.015)$					
$\frac{(d_{bt}^2 / l_t)}{(d_b^2 / L_o)}$	s/d_b					$\frac{(d_{bt}^2 / l_t)}{(d_b^2 / L_o)}$	s/d_b				
	3.5	5	6.5	8	9.5		3.5	5	6.5	8	9.5
0	0.38	0.34	0.32	0.30	0.24	0	0.32	0.30	0.28	0.26	0.20
0.25	0.87	0.72	0.73	0.61	0.51	0.25	0.79	0.64	0.64	0.52	0.43
0.5	0.99	0.90	0.86	0.71	0.59	0.5	0.96	0.83	0.80	0.62	0.49
0.75	1.00	0.92	0.88	0.74	0.60	0.75	1.00	0.85	0.82	0.65	0.51
1	1.00	0.93	0.90	0.75	0.61	1	1.00	0.87	0.84	0.67	0.52
1.25	1.00	0.95	0.90	0.75	0.61	1.25	1.00	0.89	0.84	0.67	0.52
1.5	1.00	0.95	0.90	0.75	0.61	1.5	1.00	0.90	0.84	0.67	0.52
1.75	1.00	0.95	0.90	0.75	0.61	1.75	1.00	0.91	0.84	0.67	0.52
2	1.00	0.96	0.90	0.75	0.61	2	1.00	0.91	0.84	0.67	0.52
2.25	1.00	0.96	0.90	0.75	0.61	2.25	1.00	0.92	0.84	0.67	0.52
2.5	1.00	0.96	0.90	0.75	0.61	2.5	1.00	0.92	0.84	0.67	0.52
2.75	1.00	0.96	0.90	0.75	0.61	2.75	1.00	0.92	0.84	0.67	0.52
3	1.00	0.96	0.90	0.75	0.61	3	1.00	0.92	0.84	0.67	0.52

$f_r(\varepsilon_p = 0.02)$						$f_r(\varepsilon_p = 0.025)$					
$\frac{(d_{bt}^2 / l_t)}{(d_b^2 / L_o)}$	s/d_b					$\frac{(d_{bt}^2 / l_t)}{(d_b^2 / L_o)}$	s/d_b				
	3.5	5	6.5	8	9.5		3.5	5	6.5	8	9.5
0	0.29	0.27	0.25	0.23	0.18	0	0.27	0.24	0.23	0.21	0.16
0.25	0.71	0.58	0.58	0.47	0.39	0.25	0.66	0.53	0.53	0.42	0.35
0.5	0.93	0.76	0.74	0.56	0.44	0.5	0.90	0.71	0.68	0.50	0.40
0.75	1.00	0.79	0.76	0.59	0.46	0.75	1.00	0.74	0.70	0.54	0.42
1	1.00	0.82	0.78	0.60	0.47	1	1.00	0.76	0.73	0.55	0.43
1.25	1.00	0.84	0.79	0.61	0.47	1.25	1.00	0.79	0.73	0.56	0.43
1.5	1.00	0.85	0.79	0.61	0.47	1.5	1.00	0.80	0.73	0.56	0.43
1.75	1.00	0.86	0.79	0.61	0.47	1.75	1.00	0.82	0.73	0.56	0.43
2	1.00	0.87	0.79	0.61	0.47	2	1.00	0.83	0.73	0.56	0.43
2.25	1.00	0.88	0.79	0.61	0.47	2.25	1.00	0.84	0.73	0.56	0.43
2.5	1.00	0.88	0.79	0.61	0.47	2.5	1.00	0.85	0.73	0.56	0.43
2.75	1.00	0.88	0.79	0.61	0.47	2.75	1.00	0.86	0.73	0.56	0.43
3	1.00	0.88	0.79	0.61	0.47	3	1.00	0.86	0.73	0.56	0.43

Table 3.7 – Post buckling strength coefficients f_r for $e_p = 0.03, 0.04, 0.05, 0.06$.

$f_r(\varepsilon_p = 0.03)$						$f_r(\varepsilon_p = 0.04)$					
$\frac{(d_{bt}^2/l_t)}{(d_b^2/L_o)}$	s/d_b					$\frac{(d_{bt}^2/l_t)}{(d_b^2/L_o)}$	s/d_b				
	3.5	5	6.5	8	9.5		3.5	5	6.5	8	9.5
0	0.25	0.23	0.22	0.19	0.15	0	0.23	0.20	0.20	0.16	0.14
0.25	0.61	0.49	0.49	0.39	0.32	0.25	0.54	0.44	0.44	0.34	0.29
0.5	0.88	0.66	0.63	0.46	0.38	0.5	0.83	0.59	0.56	0.40	0.34
0.75	1.00	0.69	0.66	0.50	0.40	0.75	1.00	0.63	0.59	0.44	0.36
1	1.00	0.72	0.68	0.51	0.41	1	1.00	0.66	0.61	0.46	0.37
1.25	1.00	0.75	0.69	0.52	0.41	1.25	1.00	0.69	0.62	0.46	0.37
1.5	1.00	0.77	0.69	0.52	0.41	1.5	1.00	0.71	0.62	0.46	0.37
1.75	1.00	0.79	0.69	0.52	0.41	1.75	1.00	0.75	0.62	0.46	0.37
2	1.00	0.80	0.69	0.52	0.41	2	1.00	0.78	0.62	0.46	0.37
2.25	1.00	0.82	0.69	0.52	0.41	2.25	1.00	0.79	0.62	0.46	0.37
2.5	1.00	0.83	0.69	0.52	0.41	2.5	1.00	0.81	0.62	0.46	0.37
2.75	1.00	0.83	0.69	0.52	0.41	2.75	1.00	0.82	0.62	0.46	0.37
3	1.00	0.84	0.69	0.52	0.41	3	1.00	0.82	0.62	0.46	0.37

$f_r(\varepsilon_p = 0.05)$						$f_r(\varepsilon_p = 0.06)$					
$\frac{(d_{bt}^2/l_t)}{(d_b^2/L_o)}$	s/d_b					$\frac{(d_{bt}^2/l_t)}{(d_b^2/L_o)}$	s/d_b				
	3.5	5	6.5	8	9.5		3.5	5	6.5	8	9.5
0	0.22	0.18	0.18	0.14	0.13	0	0.21	0.16	0.17	0.13	0.11
0.25	0.49	0.40	0.40	0.31	0.26	0.25	0.46	0.37	0.37	0.28	0.24
0.5	0.79	0.55	0.50	0.37	0.32	0.5	0.76	0.51	0.47	0.35	0.29
0.75	1.00	0.59	0.54	0.40	0.33	0.75	1.00	0.55	0.51	0.37	0.31
1	1.00	0.62	0.56	0.42	0.34	1	1.00	0.59	0.54	0.40	0.32
1.25	1.00	0.66	0.57	0.43	0.34	1.25	1.00	0.63	0.54	0.41	0.32
1.5	1.00	0.70	0.57	0.43	0.34	1.5	1.00	0.67	0.54	0.41	0.32
1.75	1.00	0.74	0.57	0.43	0.34	1.75	1.00	0.71	0.54	0.41	0.32
2	1.00	0.77	0.57	0.43	0.34	2	1.00	0.76	0.54	0.41	0.32
2.25	1.00	0.79	0.57	0.43	0.34	2.25	1.00	0.79	0.54	0.41	0.32
2.5	1.00	0.81	0.57	0.43	0.34	2.5	1.00	0.81	0.54	0.41	0.32
2.75	1.00	0.82	0.57	0.43	0.34	2.75	1.00	0.82	0.54	0.41	0.32
3	1.00	0.82	0.57	0.43	0.34	3	1.00	0.82	0.54	0.41	0.32

Bilinear interpolation may be required to estimate specific values of the variables of interest $r = f(s/d_b, (d_{bt}^2/l_t)/(d_b^2/L_o)) = \varepsilon_b, m_h$ or $f_r(\varepsilon_p)$. Given the pair $[s/d_b, (d_{bt}^2/l_t)/(d_b^2/L_o)]$, the interpolation is done by selecting from the available tables, four values r_{ij} neighboring the one of interest. The variable of interest r is then estimated as

$$r[(s/d_b), (d_{bt}^2/l_t)/(d_b^2/L_o)] \approx b_{11}r_{11} + b_{12}r_{12} + b_{21}r_{21} + b_{22}r_{22} \quad (3.15)$$

and coefficients b_{ij} are estimated according to

$$\begin{bmatrix} b_{11} \\ b_{12} \\ b_{21} \\ b_{22} \end{bmatrix} = \left(\begin{bmatrix} 1 & x_1 & y_1 & x_1 y_1 \\ 1 & x_1 & y_2 & x_1 y_2 \\ 1 & x_2 & y_1 & x_2 y_1 \\ 1 & x_2 & y_2 & x_2 y_2 \end{bmatrix}^{-1} \right)^T \begin{bmatrix} 1 \\ (s/d_b) \\ [(d_{bt}^2/l_t)/(d_b^2/L_o)] \\ (s/d_b)[(d_{bt}^2/l_t)/(d_b^2/L_o)] \end{bmatrix} \quad (3.16)$$

where x_i and y_j represent respectively, which are explanatory variables of r_{ij} (which are actually contained in the tables). **Appendix B** contains a MATLAB[®] algorithm that uses this interpolation process for obtaining ε_b , m_h or $f_r(\varepsilon_p)$ given s/d_b and $(d_{bt}^2/l_t)/(d_b^2/L_o)$.

3.4.2.3 *Inelastic buckling model verification*

Tests contained in **Table 3.8** are used to verify the complete average axial stress-strain curves predicted by the buckling model. The selected tests are of interest because their geometry is close to that of specimens W5 to W12 in **Chapter 2**. It is observed in **Figure 3.30** that the model adequately predicts whether a post yield strain hardening portion develops and its slope. The buckling strain and corresponding stress are also properly estimated. The softening branch of the models seems to be stiffer than the experiments for those cases of inelastic buckling developing in the strain hardening portion. This was an expected result due to the non-smooth nature of $f_r(\varepsilon_p)$ but the observed difference is within tolerable limits.

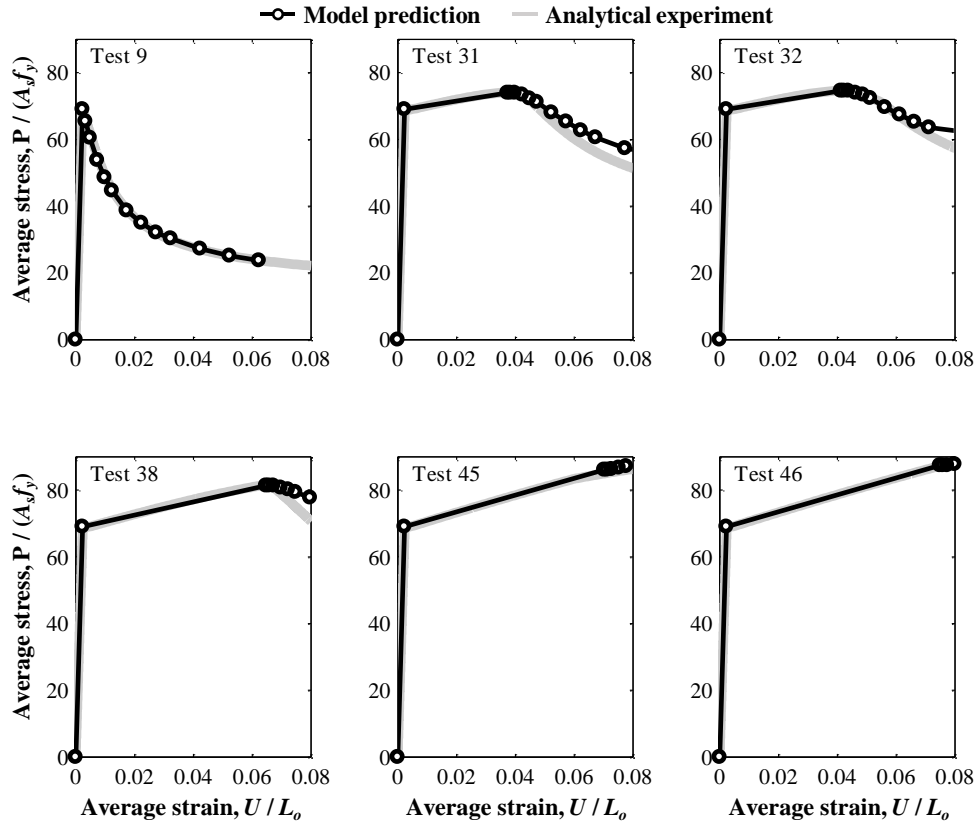


Figure 3.30 - Model prediction versus analytical experiment.

Table 3.8 – Tests selected [Note: 1 in. = 25.4 mm].

Test ID	s [in.]	d_b [in.]	d_{bt} [in.]	s/d_b	$(d_{bt}^2/l_t)/(d_b^2/L_o)$
9	8	7/8	1/2	9.1	1.3
31	4	7/8	1/2	4.6	1.3
32	4	7/8	5/8	4.6	2.0
38	4	1	1/2	4.0	1.0
45	4	1 1/4	1/2	3.2	0.6
46	4	1 1/4	5/8	3.2	1.0

Figure 3.31 presents a comparison of the observed and the estimated values of ε_b and m_h for all the tests. Observations for the small sample presented above are confirmed in this figure. The model estimation is in good agreement with the experimental data observations, except in a few cases. To explain this mismatch, **Figure 3.32** shows residuals of ε_b and m_h (in terms of the relative error) versus s/d_b and $(d_{bt}^2/l_t)/(d_b^2/L_o)$. In general, the residuals behave in an acceptable manner with respect to the explanatory variable but for the data points corresponding to the 3/4 in. [19 mm] diameter longitudinal bar under Tie Setup 2. For these points the model predicts larger buckling strains. The larger error is explained because these data points lay on the sharp transition of the three dimensional surface (**Figure 3.27**) at around $s/d_b = 5.3$; therefore the interpolation process is done between two discrete s/d_b -curves (for example, $s/d_b = 5$ and 5.5) between which ε_b does not vary linearly.

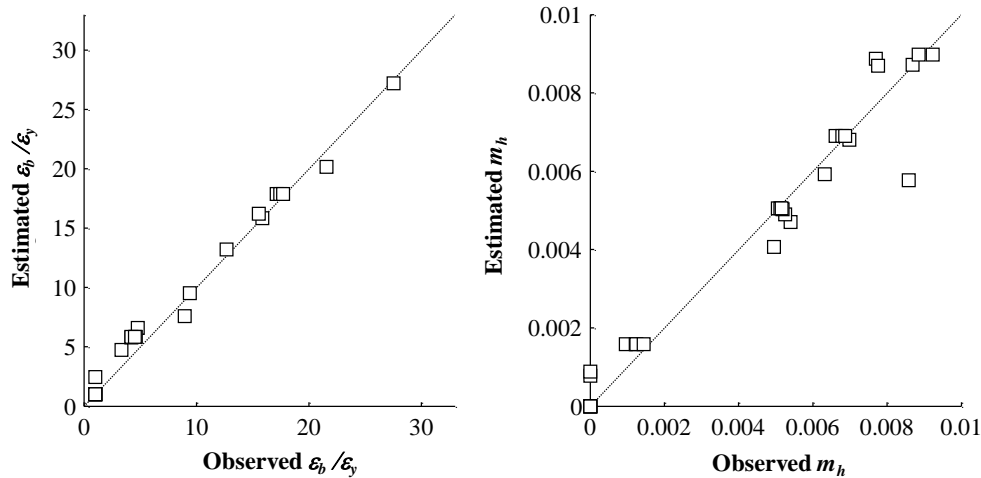


Figure 3.31 - Estimated versus observed values of ε_b and m_h .

3.5 Final Comments

A finite element based model was presented to describe the inelastic buckling process of tied longitudinal bars embedded in concrete, subjected to compressive stresses. The model implements the force-based formulation of beam-column elements with distributed plasticity, adequately replicating laboratory tests of bare bars undergoing inelastic buckling. An extension of the model was proposed to include lateral restraining actions, such as that offered by cross-ties and the concrete core on one side of a longitudinal bar embedded in a reinforced concrete element. The model does not account for: (i) external restrictions such as concrete cover that may impact the onset of the buckling phenomenon depending on its crushing strain; or (ii) tie hook opening which reduces the tie effective stiffness. Regardless, the finite element setup offers a

flexible platform to conduct numerical experimentation of inelastic buckling, offering insight into the interaction of its different components. For example, analysis of the distribution of local versus average axial strains within the buckling length confirmed some of the experimental observations of longitudinal bar buckling presented in **Chapter 2**.

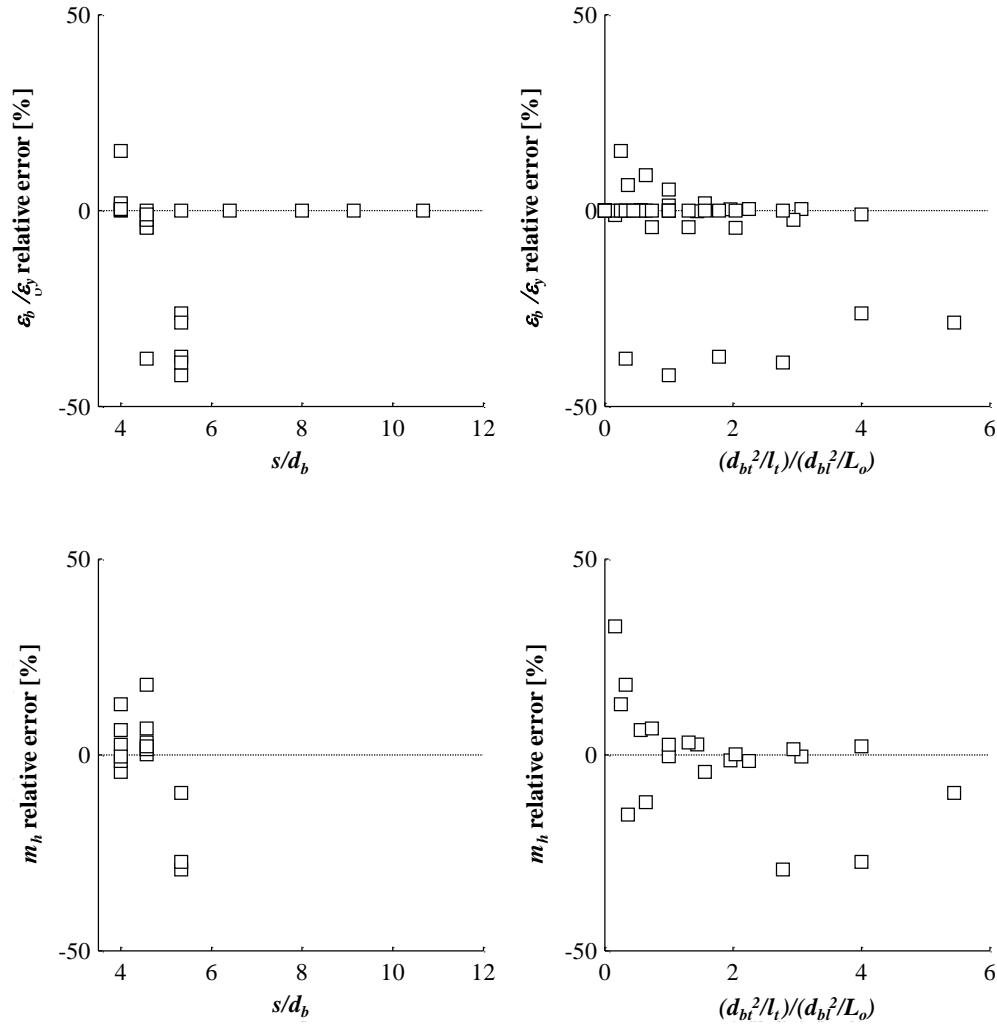


Figure 3.32 - Analysis of residuals for ϵ_b and m_h .

With the proposed platform, forty-eight analytical experiments were carried out to test the impact of tie and longitudinal bar geometry on the inelastic buckling response. As a main result, a simple methodology is presented to estimate the complete average axial stress-strain curve of tied A706 bars in compression. These curves can be included in a more complex model comprising other elements within a reinforced concrete section to obtain average or localized force-shortening relationships. Additionally, the following conclusion can be stated from the analytical results:

- i. Inelastic buckling past the yield strength can be modeled with available nonlinear structural analysis software. The behavior of tied bars undergoing lateral instability in the inelastic range is highly influenced by (i) s/d_b , which represents the relative restrictive tie spacing over which bar buckling is forced into (except for the cases of smaller tie diameters), and

- (ii) $(d_{bt}^2/l_t)/(d_{bt}^2/L_o)$, which represents the relative stiffness of a transverse tie with respect to the longitudinal bar stiffness.
- ii. Study of the evolution of the strain field and distribution of the tangent modulus of the material points within the critical cross section demonstrated the complexity of the inelastic buckling phenomenon. The tangent flexural stiffness EI of the critical cross section (at mid span) is highly unstable when transitioning from the elastic to the strain hardening portion of the average stress-strain curves. Additionally, a stiffening effect is observed at the onset of lateral instability, which might discard attempts to select a specific reduced tangent modulus to plug into the standard Euler buckling formulation for predicting inelastic buckling. Depending on the strain level at which inelastic buckling is triggered, the material of the critical cross section may have several tangent moduli at a specific state of average strain. This is because the strain history of individual fibers differs among the various fibers, in such manner that some material points are in the strain hardening portion of the constitutive material relationship with tangent modulus E_h , while others are unloading with slope E_o or reloading toward the tensile side with an intermediate tangent modulus $E_h \leq E_t \leq E_o$.
 - iii. The numerical experiments showed that due to flexibility of the restrains (ties), s/d_b has to be as small as 4.5 to effectively prevent buckling in the range $U/L_o \leq 0.08$, strain at which the tests were concluded. Nonetheless, if proper tie stiffness is provided, inelastic buckling can be delayed up to $10 \varepsilon_y$ for s/d_b as larger as 5.0. For $s/d_b \leq 6$, the buckling strain estimated with the models did not surpass the yield strain.
 - iv. An average axial stress-strain constitutive relationship for tied A706 bars embedded in concrete, subjected to compressive strains, is proposed. The model comprises a linear portion offering the possibility of linear strain hardening up to the buckling strain, given a proper tie layout is provided. The post buckling branch is described discretely, at twelve strain values past the buckling strain. Model coefficients are tabulated for ease of use at discrete values of s/d_b and $(d_{bt}^2/l_t)/(d_{bt}^2/L_o)$. The simple model results are in good agreement with the analytical experiments by adequately predicting buckling strain ε_b and strength f_b .
 - v. For the cases where buckling occurs in the strain hardening region, the softening portion of the model seems to be stiffer than those of the analytical experiments. This is explained by the none-smooth nature of the surfaces describing the post buckling loss of strength in term of s/d_b and $(d_{bt}^2/l_t)/(d_{bt}^2/L_o)$. This mismatch could be overcome if a more complex model with additional descriptive variables is used, but that would defeat the simplicity purpose. Additionally, the softening branches of the model proposed are particular to the initial length used, and may need to be regularized for other lengths.
 - vi. Restriction of tie stiffness to force inelastic bar buckling over one tie spacing is an interesting subject that requires further research, specifically for the cases of small s/d_b ratios. Results presented here showed that, assuming that hook opening is not likely, tie diameters required to fully restrain buckling within one hoop spacing might be larger than those used in practice.

Chapter 4 - Analytical Investigation Part II: R/C Sections

Two models of the expected and the observed response of the reinforced concrete prisms tests described in **Chapter 2** are presented herein. The first one is an analytical “blind” prediction model corresponding based on the assumption that plasticity spreads along the entire height of the elements. Its results are contrasted with the empirical force-average strain curves obtained in the laboratory. The second model comprises a hybrid formulation, that uses the empirical force-shortening relationships at the global and the local level of deformation, along with the rebar buckling model in **Chapter 3**, to estimate semi-empirical core concrete stress-strain relationships. Summary statistics of the confined concrete strain limits are proposed at different levels of post peak strength based on different gage lengths. Three average monotonic stress-strain curves proposed are representative of the confined core concrete material of the specimens tested. These constitutive models are described for different gage lengths over which strains are measured.

4.1 Confined Concrete Models in the Literature

Concrete confinement is a subjected that has been extensively studied for more than one hundred years. According to Richart et al. (1929), an early report on the effects of steel confinement in the axial load capacity of reinforced concrete prisms was presented by Considère (1903). Considère stated “*certain principles regarding the effect of lateral restraint in raising the ultimate strength of concrete...One of these is that the strength of hooped concrete may be considered as being the sum of two essentially unlike quantities: a resistance proportional to the strength of the concrete itself, and an added strength which is a function of the lateral restraint applied by the hooping*” (Richart et al., 1929). At the present day, the same principle is still valid.

As described in **Chapter 1**, more recent studies of reinforced concrete prisms in compression have focused on testing confinement effectiveness of various layouts of longitudinal and transverse reinforcement (Mander et al., 1988a; Moehle & Cavanagh, 1985; B. D. Scott et al., 1982; Sheikh & Uzumeri, 1980; Vallenias et al., 1977). Some of these tests resulted in well-known analytical models to predict the stress-strain response of confined concrete (Mander et al., 1988b; Sheikh & Uzumeri, 1982). These enlarged the already ample library of confinement models described in (Sheikh, 1982), of which, the Kent and Park (1971) and the Roy and Sozen (1965) models are two of the most reknown ones. Other popular models among the engineering community comprise the Saatcioglu and Razvi (1992) model, as well as the Paultre and Legeron (2008) model. More recently Moehle (2014) proposed a hybrid approach that accounts for the formulations in (Mander et al., 1988b; Paultre & Legeron, 2008; Razvi & Saatcioglu, 1999; Sheikh & Uzumeri, 1982) and is simpler to implement.

The Mander et al. (1988b) and the Saatcioglu and Razvi (1992) models are of interest because have been specifically validated with rectangular cross sections. The Mander et al. (1988b) analytical model is supported by the experimental work on thirty-one reinforced concrete columns, of circular, square and recangular cross section contained in (Mander et al.,

1988a; B. D. Scott et al., 1982). The test description of the rectangular walls is presented with some detail in **Section 1.2** of this document. The analytical model by Saatcioglu and Razvi (1992) is based on the data collected in the experimental work of several researchers (Mander et al., 1988a; Razvi & Saatcioglu, 1989; B. D. Scott et al., 1982; Sheikh & Uzumeri, 1980), including eighty-five prismatic specimens of rectangular, circular, and square cross sections. The models propose expressions for the increase of the confined concrete strength f'_{cc} as a function of the confining pressure provided by the transverse reinforcement. Estimation of the confining pressure accounts for differences in geometry and confinement characteristics in the two orthogonal directions of rectangular sections. The expression proposed in (Saatcioglu & Razvi, 1992) is simple and has the form

$$f'_{cc} = f'_c + 6.7 f_{le}^{0.83} \quad (4.1)$$

where f'_c is the unconfined concrete strength and f_{le} [MPa] is the equivalent uniform pressure, which is a function of the transverse reinforcement ratio and the confinement steel strength. The analogous expression for f'_{cc} in (Mander et al., 1988b) also involves f'_c and a form of f_{le} . Both models account for arching action and confinement effectiveness by treating the confining pressure as a three dimensional entity, highly effective near the ties or hoop legs and reduced away from them in the horizontal (along distance h'_x between ties or hoop legs), as well as in the vertical direction (along distance s ; see **Figure 2.3**). The strain ε_{cc0} at peak strength of the confined concrete is estimated the same way in both models, and is known to have a good correlation with experimental results (Moehle, 2014):

$$\varepsilon_{cc0} = \varepsilon_{c0} \left(1 + 5 \left(\frac{f'_{cc}}{f'_{c0}} - 1 \right) \right) \quad (4.2)$$

where ε_{c0} is the strain corresponding to peak strength of unconfined concrete.

Both models propose algebraic expressions to describe the stress-strain curve of the confined concrete. In (Saatcioglu & Razvi, 1992) a parabolic ascending branch is defined up to ε_{cc0} with a linear descending branch that flattens at $0.2f'_{cc}$ residual strength. The following expression defines the stress-strain relation of the initial parabola.

$$f_{cc}(\varepsilon_{cc}) = f'_{cc} \left[2 \left(\frac{\varepsilon_{cc}}{\varepsilon_{cc0}} \right) - \left(\frac{\varepsilon_{cc}}{\varepsilon_{cc0}} \right)^2 \right]^{1/\left(2\frac{f'_{cc}}{f'_c}-1\right)} \quad 0 \leq \varepsilon_{cc} \leq \varepsilon_{cc0} \quad (4.3)$$

The slope of the descending branch is controlled by parameter ε_{cc85} , which is the strain corresponding to a 15% drop in the confined concrete strength. For example, the descending branch starts at point $(\varepsilon_{cc}, f'_{cc})$, passes through $(\varepsilon_{cc85}, 0.85f'_{cc})$ until it reaches $0.2f'_{cc}$. Parameter ε_{cc85} is estimated as

$$\varepsilon_{cc85} = 260 \frac{\sum A_{st}}{s(b_{cx} + b_{cy})} \varepsilon_{c0} + \varepsilon_{c085} \quad (4.4)$$

where $\sum A_{st}$ is the total area of transverse reinforcement provided in both direction within distance s ; b_{cx} and b_{cy} are the length and width of the core; and ε_{c085} is the strain corresponding to $0.85f'_c$ in the empirical unconfined concrete stress-strain curve. The stress-strain curve proposed in (Mander et al., 1988b) is continuous for the entire range of the confined concrete strains:

$$f_{cc}(\varepsilon_{cc}) = \frac{f'_{cc} \left(\frac{\varepsilon_{cc}}{\varepsilon_{cc0}} \right)^r}{r - 1 + \left(\frac{\varepsilon_{cc}}{\varepsilon_{cc0}} \right)^r} \quad (4.5)$$

where parameter r controls the pre- and post-peak slopes of the curve

$$r = \frac{E_c}{E_c - \frac{f'_{cc}}{\varepsilon_{cc0}}} \quad (4.6)$$

The modulus of elasticity of the concrete can be estimated as $E_c = 57,000\sqrt{f'_c}$ [psi], following ACI-318 recommendations. **Equations (4.5) to (4.6)** can be appropriately modified to describe the behavior of the unconfined concrete using the equivalences in **Table 4.1**.

Table 4.1 - Parameter substitution for modeling unconfined concrete.

Confined concrete parameters		Unconfined concrete parameters
f_{cc}		f_c
ε_{cc}	→	ε_c
f'_{cc}		f'_c
ε_{cc0}		ε_{c0}

A main difference in the models in discussion is the definition of the ultimate compressive strain ε_{ccu} of the confined concrete. While (Saatcioglu & Razvi, 1992) limit their recommendation to the projection of the post peak branch down to $0.2f'_{cc}$, the confined concrete ultimate strain in (Mander et al., 1988b) is defined as that where the first fracture of transverse reinforcement is expected. The formulation presented in the latter is based on an energy-balance model requiring cumbersome numerical integration for the estimation of ε_{ccu} . As described in **Section 1.2**, limiting compressive strains reported for prismatic reinforced concrete elements in compression expand over a large range. The scatter is believed to be mainly due to differences in the confinement reinforcement layouts under study, but the softening nature of the post peak response also plays an important part in dispersing the data. Bias introduced by different gage lengths over which strains are estimated is hard to quantify; in addition to this, exact definition of the portion where damage localizes is not always feasible before the tests are concluded. Recording of undisturbed measurements of displacement in the most damage zone also offers additional difficulties, especially after the peak load is attained because concrete cover spalls off an interact with the instruments, or because inclined failure planes, not covered by the instrumentation, may form.

The latter discussion calls for the use of a simple expression for the estimation of ε_{ccu} . The one adopted here is developed by Moehle (2014) by fitting the lower bound of the strain limits reported in (Mander et al., 1988b; Moehle & Cavanagh, 1985; B. D. Scott et al., 1982) (see **Figure 1.5** in **Section 1.2**) to a straight line that is a function of the minimum confining stress:

$$\varepsilon_{ccu} = 0.004 + 0.25 \frac{f_{le,min}}{f'_c} \quad (4.7)$$

where $f_{le,min}$ is the minimum effective confining stress (pressure) of the two orthogonal directions in a rectangular section. For the case of interest here, $f_{le,min}$ is the confining stress in the through-thickness direction of the boundary element specimens described in **Chapter 2**. As tested values of $f_{le,min}$ are contained in **Table 4.3**.

Specimen W7 is selected to compare the confined concrete models described above using the in-situ material characteristics (see **Table 2.1**). The effective confining stress calculations needed for the models are not presented here for the sake of brevity, but the reader is referred to the sources cited above. **Figure 4.1** presents the confined concrete stress-strain curves for Specimen W7. Expected limiting strain at first fracture of transverse reinforcement is $\epsilon_{ccu} = 0.019$, although it is worth mentioning that tie or hoop fracture was not observed in the experiments described in **Chapter 2**. For comparison, strength at ϵ_{cc85} is also shown for the (Saatcioglu & Razvi, 1992) model. Both models predict virtually the same confined concrete strength of around $1.45f_c$ but the (Saatcioglu & Razvi, 1992) model is evidently softer over most of the range of strains shown. It is important to recognize that none of the models is based on experiments comprising sections with bars solely restrained by the flexural stiffness of hoops, as are almost half the longitudinal bars in Specimen W7.

Given the similarities in the constitutive stress-strain relations provided, in the remainder of the chapter the Mander et al. (1988b) model will be the preferred one, along with the simpler ultimate strain estimation proposed in (Moehle, 2014).

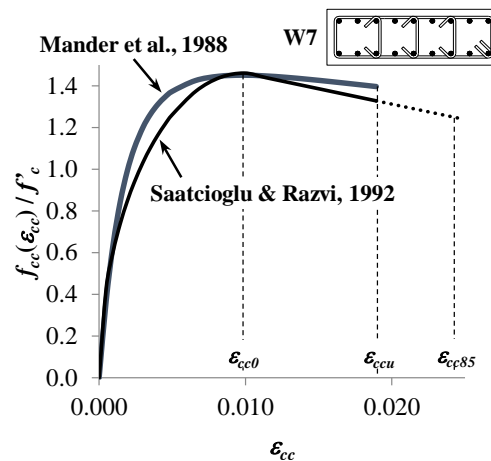


Figure 4.1 – Comparison of the (Mander et al., 1988b) and (Saatcioglu & Razvi, 1992) confined concrete models for the geometry of specimen W7.

4.2 Equilibrium Requirements for Ductile Behavior in Compression

One of the requisites for a reinforced concrete element in pure compression to behave in a ductile manner is that, after spalling, the confined core axial strength is larger than that of the unconfined gross cross section. Strain-hardening of the core after initial spalling produces a spread of plasticity in which undamaged sections lose their cover progressively avoiding the concentration of deformation in a single location. **Figure 4.2** helps present this idea with two different equilibrium situations just before and after the concrete cover has spalled off the critical section:

(i) **Figure 4.2a** and **Equations (4.8)** and **(4.9)** present stresses and forces acting on the unconfined gross cross section (at the onset of spalling) and the confined core (after spalling) without anticipating longitudinal reinforcement buckling:

$$P_0 = f'_c(A_g - A_s) + A_s f_y \quad (4.8)$$

$$P_{00} = f'_{cc}(A_{ch} - A_s) + A_s f_y \quad (4.9)$$

where P_0 is the axial strength of the column at the onset of spalling; P_{00} is the post-spalling strength for strain just beyond the spalling strain.

(ii) **Figure 4.2b** and **Equations (4.8)** and **(4.10)** present stresses and forces acting on the unconfined gross cross section and the confined core (after spalling) accounting for some loss of capacity in part of the longitudinal steel due to buckling:

$$P_{b00} = f'_{cc}(A_{ch} - A_s) + A_{sr} f_y + A_{sb}(\alpha f_y) \quad (4.10)$$

where P_{b00} is the post-spalling strength accounting for partial reinforcement buckling for strain just beyond the spalling strain; A_{sr} and A_{sb} are the areas of restrained (by a tie or hoop leg) and buckled longitudinal bars in the critical section, respectively; α is a factor between zero and one to account for smaller stress capacity in the buckled portion of the reinforcement (see **Equation (2.5)** in **Section 2.6.4**).

Equation (4.11) presents the condition for ductile behavior for both situations:

$$P_{00} > P_0 \quad (4.11a)$$

$$P_{b00} > P_0 \quad (4.11b)$$

Manipulation of **Equations (4.8)**, **(4.9)** and **(4.11a)** results in the following requirement to achieve a ductile behavior for the case of non-buckled reinforcement after spalling takes place:

$$f'_{cc} > \frac{(A_g - A_s)}{(A_{ch} - A_s)} f'_c \approx \frac{A_g}{A_{ch}} f'_c \quad (4.12)$$

Similarly, for the case presented in **Figure 4.2b**, manipulation of **Equations (4.8)**, **(4.10)** and **(4.11a)**, and assuming $A_{sr} = A_{sb} = 1/2 A_s$, leads to the following expression to ensure a ductile behavior:

$$f'_{cc} > \frac{A_g}{A_{ch}} \left(f'_c + \rho f_y \left(\frac{1 - \alpha}{2} \right) \right) \quad (4.13)$$

where ρ is the ratio of area of steel to gross area of concrete cross section.

According to this formulation, compliance with **Equation (2.2)** (ACI318-11-Eq.21-4) will lead to satisfaction of **Equation (4.12)** to achieve a ductile behavior under the assumption that no bar will buckle after spalling takes place, while compliance with **Equation (2.3)** will only do so if the gross area to core area ratio (A_g/A_{ch}) is smaller than 1.3 (which is harder to accomplish by smaller sections and typical reinforcement cover). For this to happen, given the geometries of the specimens studied, the in-situ confined concrete strength must reach 1.9 times the unconfined concrete strength. These properties of the confined concrete are achievable with the addition of transverse reinforcement in sufficient quantities, as demonstrated by (Mander et al., 1988a) where values of f'_{cc}/f'_c in the range of 1.35 to 2.15 are reported.

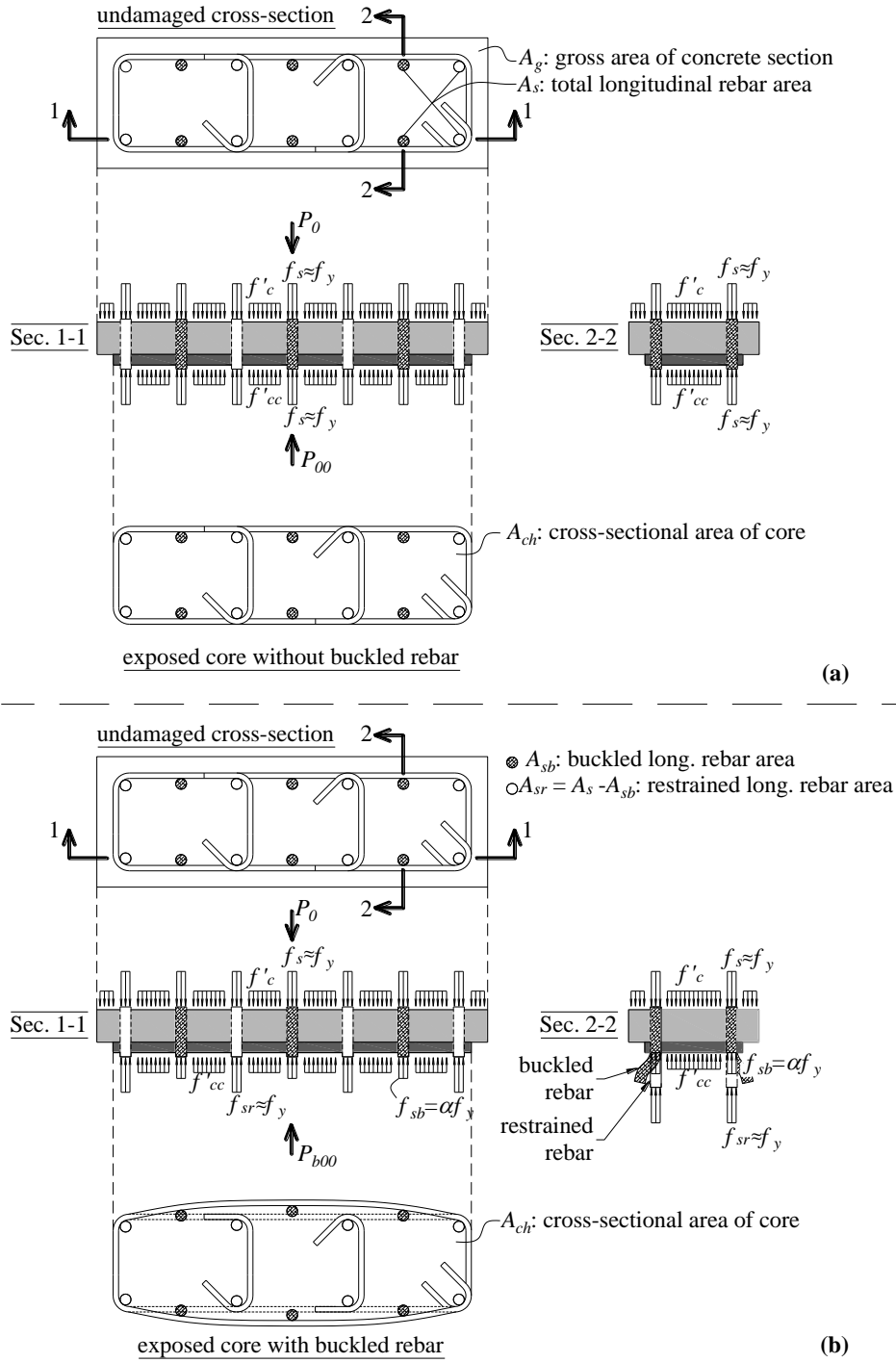


Figure 4.2 Stresses and forces acting on the critical cross section: (a) non-buckling rebar case; (b) case of partial buckling in rebar of the confined core.

Fulfilling **Equation (4.13)** is more challenging because the confined concrete would need to achieve even higher strengths to compensate for bar buckling strength loss. As an example, for the geometries of the specimens **W3** to **W7**, in a hypothetical case where the stress capacity of the buckled rebar is 40% of the non-buckled one ($\alpha=0.40$), which is a lower bound for non-restrained bars under pure compression (Monti & Nuti, 1992) and consistent with **Equation (2.5)**

in **Section 2.6.4** for the buckling lengths observed in **Chapter 2**, satisfying **Equation (4.13)** would have required the confined concrete strength to achieve values in the range of 1.7 to 2.0 times that of the unconfined concrete. Even obtaining these confined concrete strengths may be insufficient for ductile behavior because buckling of the longitudinal bars typically results in loss of additional concrete from the core, thereby further reducing the effective core area. The inability for sustaining load with increasing deformation is due in part to initiation of buckling of the non-tied longitudinal bars which is also associated with the onset of concrete cover separation from the core. This behavior introduces a weakening mechanism on the exposed core section, forcing all the deformation into a small region, resulting in low overall displacement capacity.

4.3 Parallel Model for Prediction of Responses

A simple procedure to estimate the inelastic response of reinforced concrete members in compression is presented by (Moehle, 2014). An extension of this model was developed prior to the laboratory test program, with the idea of providing blind predictions of the prism tests. The model corresponds to a simple system that treats all the materials providing axial strength in the boundary element as springs in parallel. The following assumptions apply: (i) there is no localization of damage; (ii) the longitudinal steel remains straight and does not buckle; (iii) there is no interaction of the materials in the transverse direction (i.e. the expected expansion of the core does not promote cover spalling nor buckling of the reinforcement). **Figure 4.3** depicts the geometry of the parallel model with a representation of the uniaxial materials assigned to each one of the three springs used.

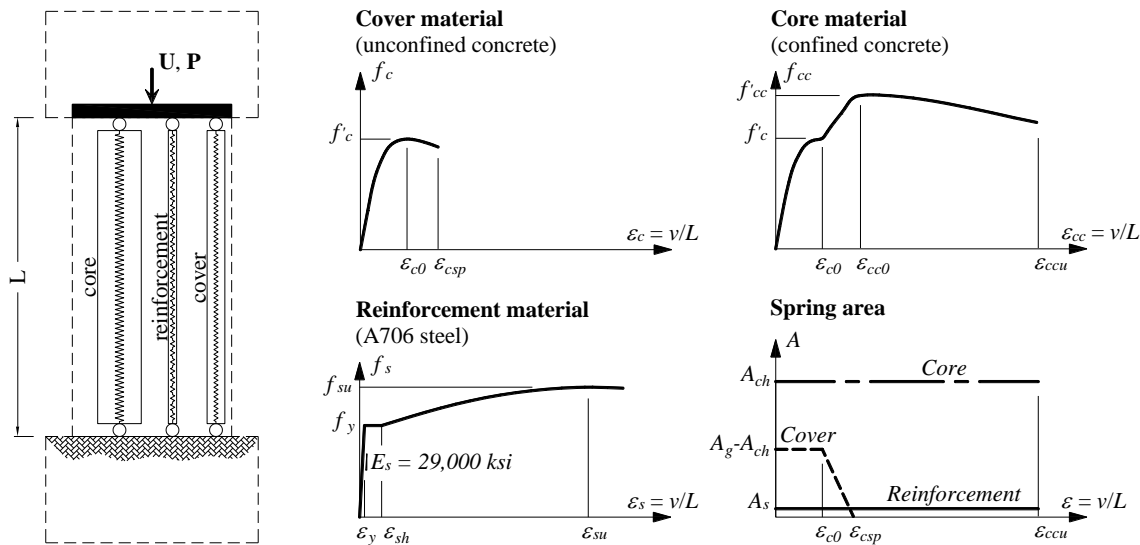


Figure 4.3 Parallel model geometry and materials definition.

4.3.1 Geometry and materials constitutive description

All elements have the same initial length L . The materials constitutive description is solely based on monotonic compressive loading without strain reversals. The core spring has area A_{ch} while the cover spring area is $(A_g - A_{ch})$. Their material uniaxial stress-strain relationship follows the (Mander et al., 1988b) formulae for monotonic compressive loading describe in **Equations (4.5)**

and (4.6). To account for a gradual effective confinement achievement, the confined concrete uniaxial model is slightly modified and three portions are defined: (i) from zero strain up to ε_{c0} , the material behaves as unconfined concrete; (ii) from ε_{cc0} to ε_{ccu} , the material follows the relationships in **Equations (4.5) and (4.6)**; (iii) from ε_{c0} to ε_{cc0} , the concrete stress follows a linear path from f'_c to f'_{cc} .

The longitudinal reinforcement steel has area A_s and its material stress-strain relationship represents engineering properties of ASTM 706 Grade 60 steel⁵. For this material, the elastic stress is proportional to the strains according to $f_s(\varepsilon_s) = E_s \varepsilon_s$ for $|\varepsilon_s| \leq \varepsilon_y$, where $E_s = 29,000 \text{ ksi}$ is the Young's modulus of the material and ε_y the yield strain. The strain hardening portion under monotonic loading can be described algebraically by (Mander, 1984)

$$f_s(\varepsilon_s) = f_{su} + (f_y - f_{su}) \left(\frac{\varepsilon_{su} - \varepsilon_s}{\varepsilon_{su} - \varepsilon_{sh}} \right)^q \quad \text{for } |\varepsilon_s| > \varepsilon_{sh} \quad (4.14)$$

where f_y is the yield stress, f_{su} is the tensile strength, ε_{su} is the corresponding strain, ε_{sh} is the strain at the onset of strain hardening and

$$q = E_{sh} \left(\frac{\varepsilon_{su} - \varepsilon_s}{f_{su} - f_y} \right) \quad (4.15)$$

where E_{sh} is the strain hardening tangential modulus. The yield plateau is assumed to have stress equal to yield stress and is defined in the range $\varepsilon_y < |\varepsilon_s| \leq \varepsilon_{sh}$.

4.3.2 Parallel spring model description and state determination

The response of a system of springs in parallel is governed by the kinematic relation between the individual element deformation v_i and the global system deformation U according to

$$U = v_i = v \quad (4.16)$$

where U can be thought of as the shortening of the boundary element under pure compression. At the element level, the deformations in each spring can be transformed to strains by dividing by length L . In this manner, the relation between global shortening of the system and average strains in the material of each spring is

$$\varepsilon = \varepsilon_c = \varepsilon_{cc} = \varepsilon_s = v/L = U/L \quad (4.17)$$

where subscript c , cc and s correspond to the cover concrete, the core concrete and the steel spring, respectively.

The static equilibrium relation of the system states that the total resisting force P of the system is equal to the sum of the resisting forces of its components

$$P = q_c + q_{cc} + q_s = \sum_{i=1}^3 f_i A_i \quad (4.18)$$

⁵ Even though the reinforcing steel material is subjected to compression, an engineering stress-strain relation definition based on tensile tests will be used because of the availability of experimental parameters. This assumption will not have a major repercussion in the results because the expected compressive strains on the reinforcement are rather low.

where f_i and A_i are the stress and area of the spring at a given level of deformation and the corresponding element resisting forces for the cover, core and steel springs are q_c , q_{cc} , and q_s , respectively. To determine the resisting force of the system at each given value of strain (ϵ), the constitutive model of each material provides the corresponding stress ($f_i(\epsilon)$) and the total resisting force can be calculated with **Equation (4.18)**. It is worth mentioning that for the purpose of modeling the elements of this document, the cover area is assumed to spall-off progressively (see **Figure 4.3**) in a linear manner according to

$$\begin{aligned}
 A_c(\epsilon) &= A_g - A_{ch} && \text{if } |\epsilon| \leq \epsilon_{c0} \\
 &= \frac{(A_g - A_{ch})}{(\epsilon_{sp} - \epsilon_{c0})} (\epsilon_{sp} - \epsilon) && \text{if } \epsilon_{c0} < |\epsilon| \leq \epsilon_{sp} \\
 &= 0 && \text{if } |\epsilon| > \epsilon_{sp}
 \end{aligned} \tag{4.19}$$

The stiffness of the system is given by the sum of the individual element stiffness

$$K = k_c + k_{cc} + k_s = \sum_{i=1}^3 \frac{E_i A_i}{L} \tag{4.20}$$

where E_i is the tangent modulus of the spring at a given level of deformation.

4.3.3 Force-shortening response prediction

As an example, **Figure 4.4** depicts the global force-shortening response of specimen W7 calculated with the procedure described above. **Table 4.2** contains the geometric and material parameters for each spring. In this example, the state determination of the system is a simple process in which monotonic increasing average strains ($\epsilon = U/L$) are given. The corresponding material strains are associated uniquely to stresses by means of the uniaxial constitutive models and areas per strain value are also calculated. Finally, resisting forces at the element and at the global level are calculated according to **Equation (4.18)**.

Table 4.2 - Spring parameter for modeling of specimen W7.

Cover		Core		Reinforcement	
A_g	432 in ²	A_{ch}	297 in ²	A_s	10.8 in ²
ϵ_{c0}	0.003*	$f_{te,min}$	0.26 ksi	f_y	69.6 ksi*
f'_c	4.35 ksi*	ϵ_{cc0}	0.01	ϵ_{sh}	0.005*
ϵ_{sp}	0.005	f'_{cc}	6.31 ksi	ϵ_{su}	0.14*
		ϵ_{ccu}	0.019	f_{su}	95.0 ksi*

*correspond to measured values.

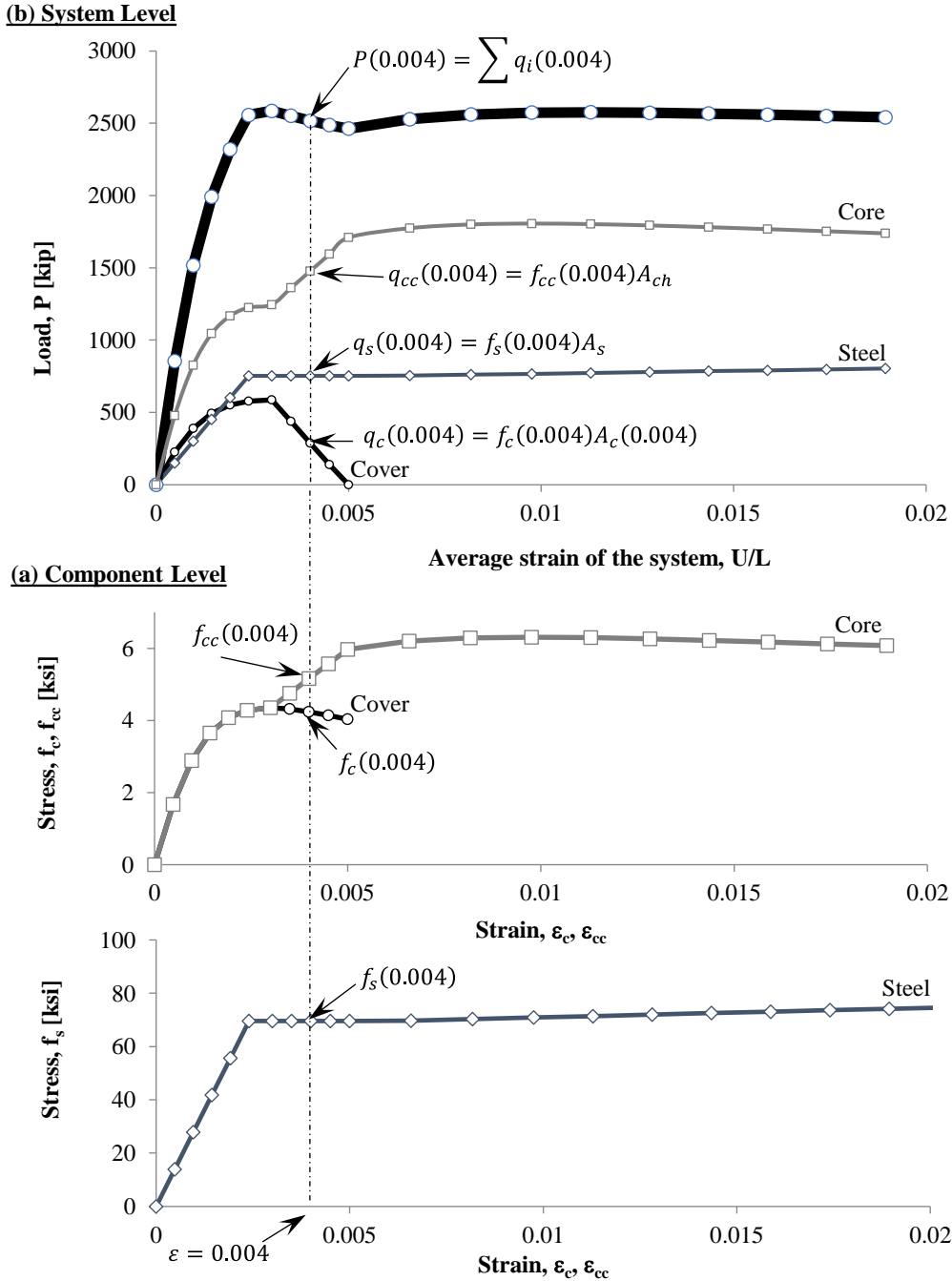


Figure 4.4 Example of the state determination of the springs-in-parallel model. (a) given strains and corresponding stresses of each spring; (b) resisting force-average strain relation of each spring and the system.

Comparison of the predictive models and actual response is presented in **Figure 4.5** for specimens W3 to W12. The average strain of the experimental curves is estimated from the shortening of the portions between the loading heads, using a gage length equal to the specimen height $h_w = 72$ in. [1828 mm]. The models were developed using actual material properties of the unconfined concrete and reinforcing steel. The maximum reported strains are based on estimations using the actual confining stress $f_{le,min}$ (in the through-thickness direction of the prims, see **Table 4.3**) and **Equation (4.7)**. The models estimate reasonably well the maximum

load attained by the specimens. The difference in the ascending branch of the curves, being softer for the test curves, is explained by the fact that the shortening of the wall was measured at the edge of the top and bottom heads and not in the main body of the specimens. Although not shown here, average strains measured from strain gages on the longitudinal reinforcement give a closer matching for the ascending branch of the curves.

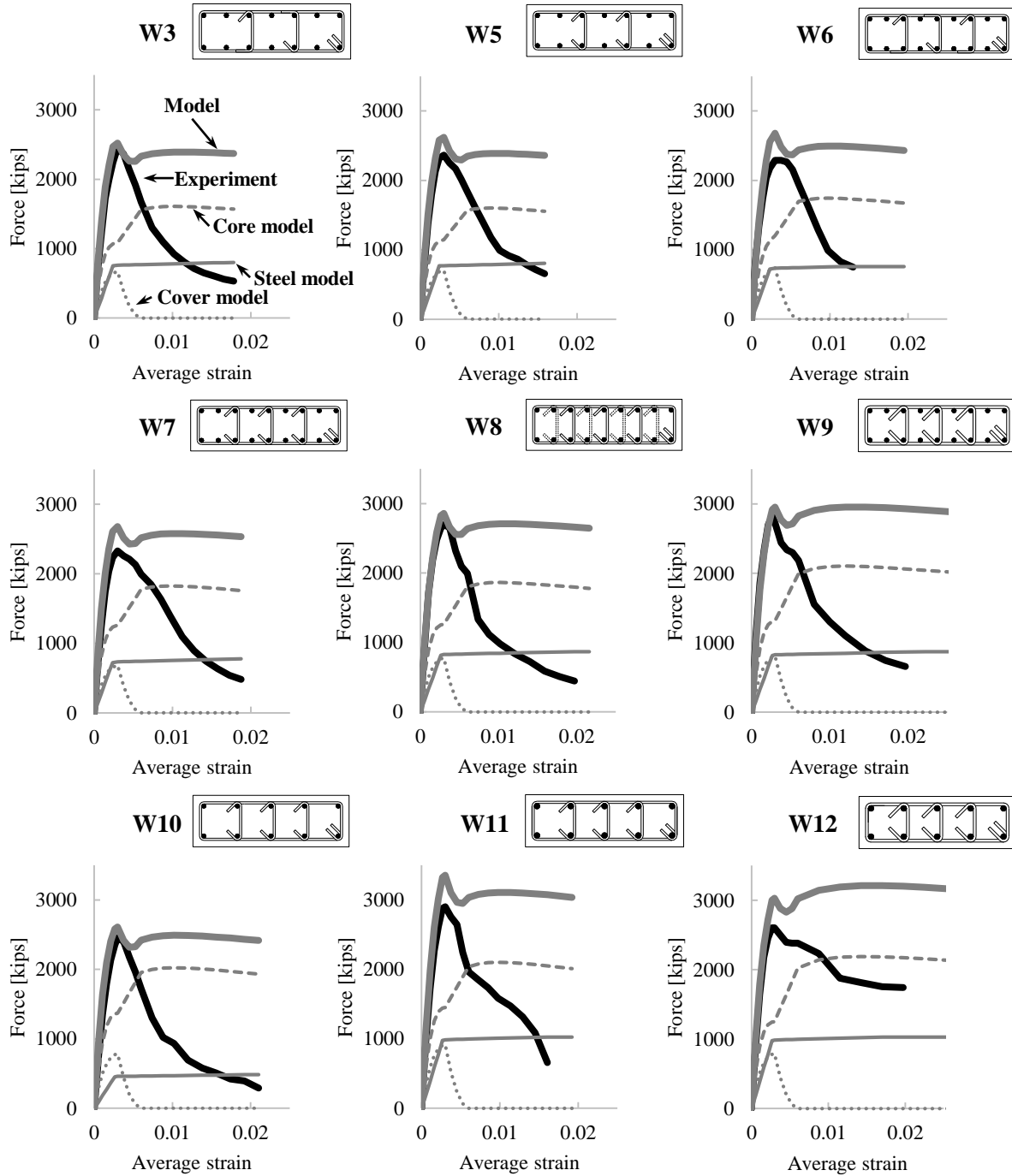


Figure 4.5 Experimental and “blind” prediction of axial load versus average strain relations. (Note: gage length for the experimental curves is 72 in. [1828 mm]).

Table 4.3 – Confined concrete model parameters.

ID	L_{DZ}/t_w	$f_{le,min}/f'_c$ (model)	f'_{cc}/f'_c (model)	ϵ_{cc0} (model)	ϵ_{ccu} (model)
W3	1.81	0.076	1.48	0.010	0.023
W5	2.29	0.048	1.40	0.009	0.016
W6	2.08	0.062	1.45	0.010	0.019
W7	2.75	0.059	1.45	0.010	0.019
W8	2.50	0.070	1.48	0.010	0.022
W9	3.06	0.093	1.60	0.012	0.027
W10	2.71	0.068	1.48	0.010	0.021
W11	2.83	0.061	1.45	0.010	0.019
W12	2.71	0.107	1.75	0.014	0.031

After cover spalling, the longitudinal reinforcement model carries approximately one-third of the total load, while the core carries the rest. As described in **Chapter 2**, due to the localization of damage, bar buckling and the out-of-plane displacement observed in the tests, the post-peak behavior of the model misses completely the actual behavior of the boundary elements. This is recognized in **Section 4.4**, where an attempt to recover the force-shortening relationship of the most damaged zone is presented. This will be consistent with the experimental procedures that form the basis for the empirical confined concrete models proposed.

4.4 Local Force-Shortening Relationship Estimation

4.4.1 Force-shortening relationship within the damage zone

An approximation of the force-shortening relationship of the damaged zone (DZ) of specimens W3 to W12 is presented here. The DZ is the portion of the specimen where cover spalling was observed, which includes the smaller length where bar buckling developed. The force-shortening relationship of the DZ is recovered using a hybrid model which assumes that the specimens behave as a system of two springs in series. One spring represents the DZ, while the other represents the undamaged zone (UDZ) where no cover spalling was observed (**Figure 4.6a**). Supported by the response described in **Section 2.6.5** and **Figure 2.14**, it is also assumed that the UDZ spring unloads after the maximum load is attained, with initial stiffness equal to

$$K_{DZO} = 1/(h_w - L_{DZ})[E_c(A_g - A_s) + E_s A_s] \quad (4.21)$$

where L_{DZ} is the average length of the damaged zone (see **Table 4.3**).

To recover the force-shortening relationship of the DZ, the deformation (shortening displacement) in the springs is estimated as follows, using the empirical global force-shortening relationships: (i) up to the peak load, the deformation in each spring is distributed proportionally to its initial stiffness; (ii) for deformations larger than that corresponding to the peak load, the displacements in the DZ spring are estimated by subtracting the displacements of the UDZ spring (which is in a unloading state) from the empirical displacements (**Figure 4.6b**). An example of the resulting force-average strain relationship of the damaged zone, the un-damaged zone and the whole specimen is presented in **Figure 4.6c**. The average strains of the DZ spring are estimated using gage length L_{DZ} , which corresponds to the average spalling length in **Figure 2.11** and are summarized in **Table 4.3**.

Given tie spacing s , longitudinal bar diameter d_b , and transverse tie diameter d_{bt} , it is a straight-forward process to include the inelastic buckling model of **Chapter 3**, to modify the predictive model presented in **Section 4.3.3**. **Figure 4.7** shows a comparison of the semi-empirical force-average strain relationships of the DZ with such modified model. It is worth mentioning that the inelastic buckling model was conceived for a gage length of $2t_w$, which approximately coincides with the values of L_{DZ} used to recover the average-strains in the DZ. This is of relevance because the softening nature of the postbuckling slopes of the steel is dependent on the modeling gage length. The buckling model is slightly modified to delay buckling of the rebar after spalling is initiated (for example at average strains larger than 0.003). While this effectively varies the $\varepsilon_b/\varepsilon_y$ ratio, the post buckling response is kept unmodified.

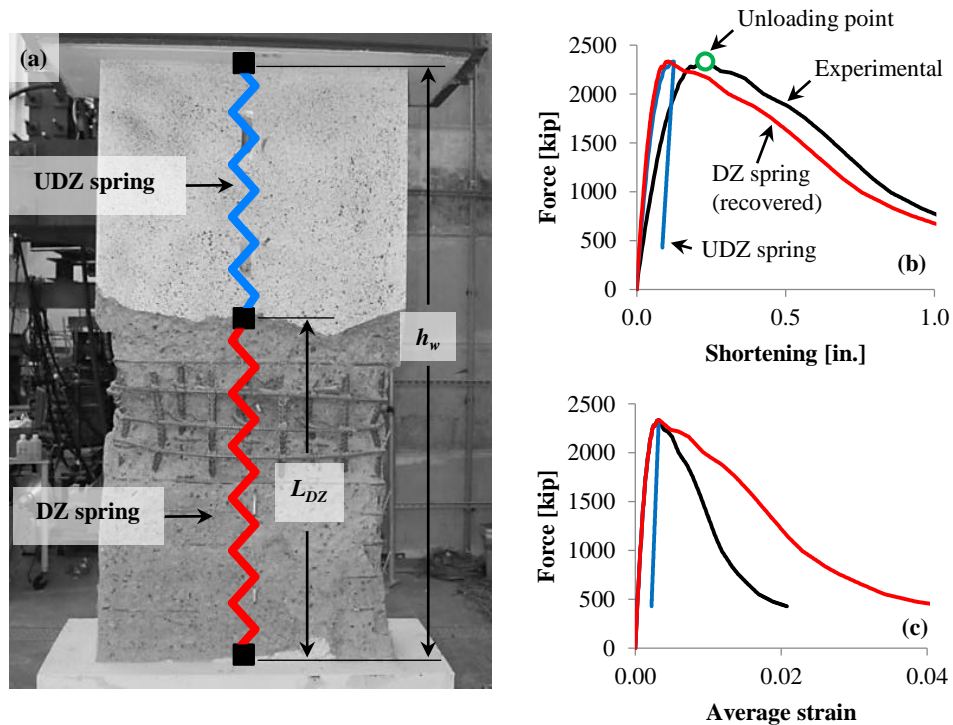


Figure 4.6 - Model to estimate the force-shortening response of the most damage zone:(a) spring in series representation of the specimen; (b) force-shortening relationship of the different portions of the wall; (b) force-average strain relationships (Note: average strains of the DZ spring are estimated using gage length L_{DZ} equal to the average spalling lengths in **Figure 2.11**).

Given the relatively small s/d_b ratio of the tied longitudinal bars, the inelastic bar buckling model implemented predicts that buckling strains are larger than the range of strains of interest in **Figure 4.7** for the DZ curves. On the other hand, for the non-tied bars, and for those of specimen W8 (which has double the spacing of the ties), the buckling strain is equal to that of the onset of cover spalling. For the sections with non-tied bars (W3 to W9), the steel contribution to the DZ model shows a gentle softening slope after the onset of buckling. This is explained by the fact that the force carried by the steel has two contributions with different responses: (i) one that buckles at the onset of cover spalling (for example, the non-tied bars), and (ii) other that strain hardens past the strains shown (for example, the tied bars). Although the DZ semi-empirical curves presented in **Figure 4.7** show a shallower post peak response as compared to

the global average strain curves presented in **Figure 4.5**, the post peak load carrying capacity is still over predicted.

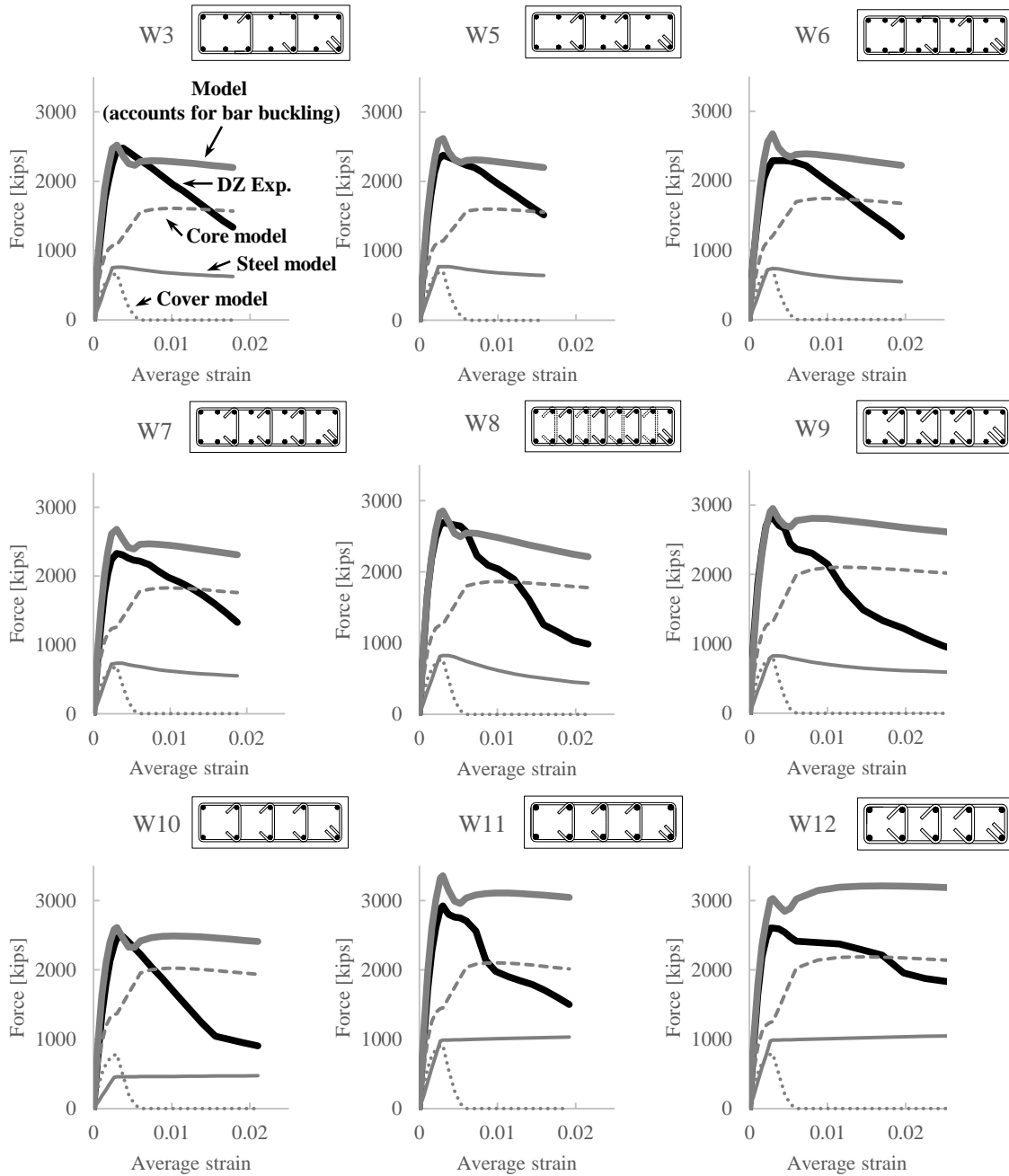


Figure 4.7 Semi-empirical and prediction of axial load versus average strain relations for the damage zone (DZ). (Note: average strains of the DZ curves are estimated using gage length L_{DZ} equal to the average spalling lengths in **Table 4.3**).

4.4.2 Point wise force-average shortening relationship

The force versus core strain relationships presented in **Figure 2.14** are used as a third source of empirical response in this section. For this purpose, the most demanded core strain gages (CO_{SG}) are selected to compare their response with the force-average strain relationship at the global

level (over the entire height h_w), as well as at the DZ level (**Figure 4.8**). The core strain gages selected are CO_{SG3}, CO_{SG3}, CO_{SG4}, and CO_{SG3} for specimens W8, W9, W11, and W12, respectively. It worth recalling that those specimens had embedded core strain gages, and did not suffer from sudden loss of load carrying capacity. **Figure 4.8** also presents the model for the DZ. The average strains are estimated over gage lengths equal to 2.4 in. [60 mm] and 72 in. [1828 mm], for the core strain and the global levels of deformation, respectively. Gage lengths for the DZ are 30.0, 36.8, 34, and 32.5 in. [762, 933, 864, 826 mm], for specimens W8, W9, W11 and W12, respectively.

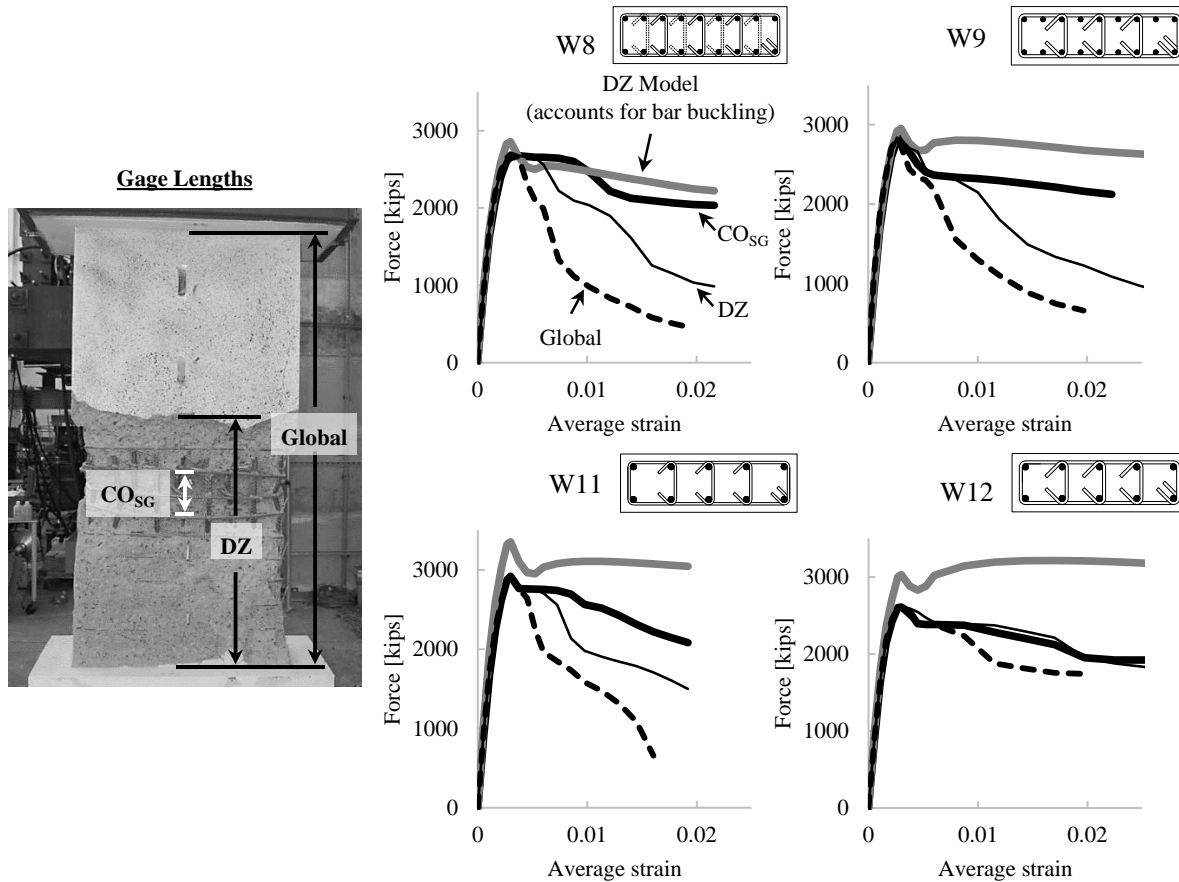


Figure 4.8 Experimental and predictive model of axial load versus average strain relations for different gage lengths. (Note: average strains gage lengths are: 72 in. [1828 mm] for the Global curves; L_{DZ} equal to the average spalling lengths in **Table 4.3** for the DZ curves; and 2.2 in. [60mm] for the core strain gages CO_{SG} curves).

It is observed that the core strains curves are closer to the models, as compared to the global and the DZ curves. This is expected because the point wise core strains are measured at locations close to the most damage region (for example within the buckling length of the longitudinal bars), while the other two gage lengths include portions of the specimen that relax (expand) over this zone of excessive deformation, therefore, resulting in steeper post peak responses. Specimens W8, W9 and W11 exhibit a point wise response closer to the prediction models, with respect to their global and DZ levels of response. The post peak strength of the latter two are not as close to the predictive model. Specimen W12 exhibits the most ductile response among all specimens, showing the smallest variation in response from the global to the point wise level of strain demand. This means that a large portion of the specimen was strained

uniformly. As described in **Chapter 2**, bar buckling was inhibited for this specimen, and global buckling was the failure mechanism. The fact that the maximum predicted load was not reached by this specimen, leads to the hypothesis that some out-of-plane displacement may have affected its response, perhaps also impacting its ductility capacity due to flexural action.

4.5 Empirical Core Stress-strain Curves

4.5.1 Confined concrete response in the damage zone

Assuming the damaged zone (DZ) spring is an inelastic system composed of three springs in parallel, analogous to the description in **Figure 4.3**, the recovery of the empirical stresses in the confined core can be achieved by subtraction of the force carried by the longitudinal steel and the cover from the total recorded force. The stresses are derived through the following process for each strain data point: (i) at each strain increment, the forces in the cover concrete and the longitudinal reinforcement are estimated using analytical models for the stress-strain relations (including buckling) and known areas for the cover and reinforcement (see **Figure 4.3**); (ii) forces in the cover concrete and longitudinal reinforcement are subtracted from the total force to obtain the core concrete force; and (iii) the core concrete force is divided by the core area taken to the outside of the hoop. **Figure 4.9** summarizes this process for the estimation of the core stress in the DZ of specimen W7.

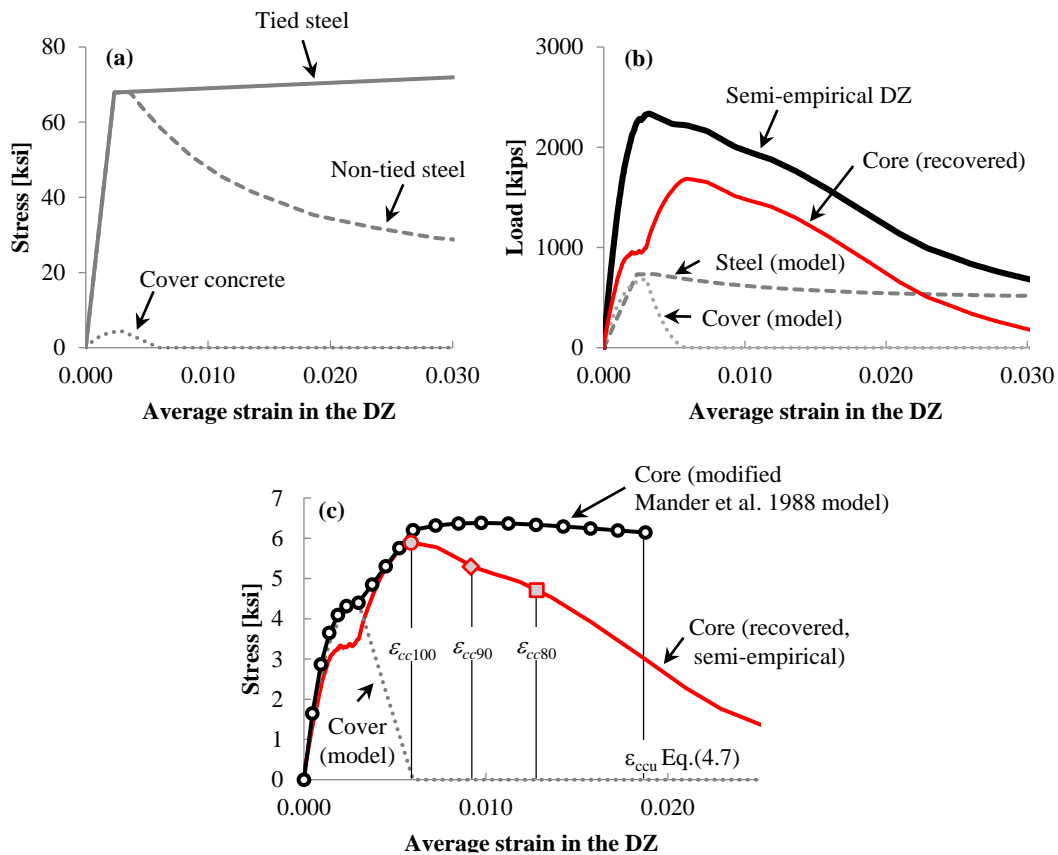


Figure 4.9 - Core empirical stress-strain relationship estimation for the DZ: (a) constitutive model for the steel and cover (unconfined) concrete; (b) recovered force-average shortening relation for the confined core; (c) recovered confined core stress-average strain relationship for the DZ. (Note: average strains gage length is equal to L_{DZ} in **Table 4.3** for specimen W7).

Figure 4.9a presents the constitutive relationships used to model the materials representing the unconfined concrete, the tied longitudinal reinforcement, as well as the non-tied bars, which are allowed to buckle. **Figure 4.9b** shows the recovered force of the confined core. The forces in the core, along with those carried by the steel and the cover models, add up to the force of the DZ at each strain level. **Figure 4.9c** shows the recovered (experimental) confined core stress versus average strain relationship in comparison with the model by (Mander et al., 1988b), as modified by (Moehle, 2014). Also shown are three levels of strain denoted ε_{cc100} (circular markers), ε_{cc90} (diamond markers) and ε_{cc80} (squared markers). These define, respectively, the confined core strain at which the maximum confined core strength f'_{cc} is attained, and the strain at which the core strength drops to 90% and 80% of the maximum.

Figure 4.10 shows results of confined core concrete stress versus average strain derived for the damaged zones of specimens W3 to W12. Derived stress-strain relations are compared with the theoretical models by (Mander et al., 1988b), with a variation to represent gradual confinement achievement of the confined concrete, and to include limiting strain ε_{ccu} from **Equation (4.7)**. The empirical curves are normalized by ratio P_{max}/P_0 , to reduce the PM-interaction effects on the maximum strength. Consistent with the results presented in **Section 4.4.1**, it is observed that albeit reaching in most cases at least 90% of the strength predicted by the model, the deformation ductility capacity prediction is not comparable to the experimental data. It is hypothesized that buckling of non-restrained rebar prevented the confined core section from achieving effective confinement through large strains.

Specimens W9 and W12 show an apparent discrepancy in strength with the models. These two specimens are compliant with ACI 318-14 and have the largest effective confining strength f_{le} (see **Table 4.3**), which greatly impacts the analytical confined core strength f'_{cc} estimation. Effective confining strength is a function of the volume of transverse steel provided, relative to the volume of the confined core within spacing s ; it is also proportional to the expected stress demand f_s in the transverse reinforcement. In estimating f_{le} , it was assumed f_s was equal to the yield strength f_{yt} , which might not be accurate according to the experimental tie strain demand recorded at different levels along the specimen height. The empirical data showed that tie strains were approximately half the yield strain when the peak load was attained; hence, it is believed that such large confining stresses were not as effective to increase the core capacity in such a large manner. **Figure 4.11** presents this information for three stages of the response of specimens W9 and W12.

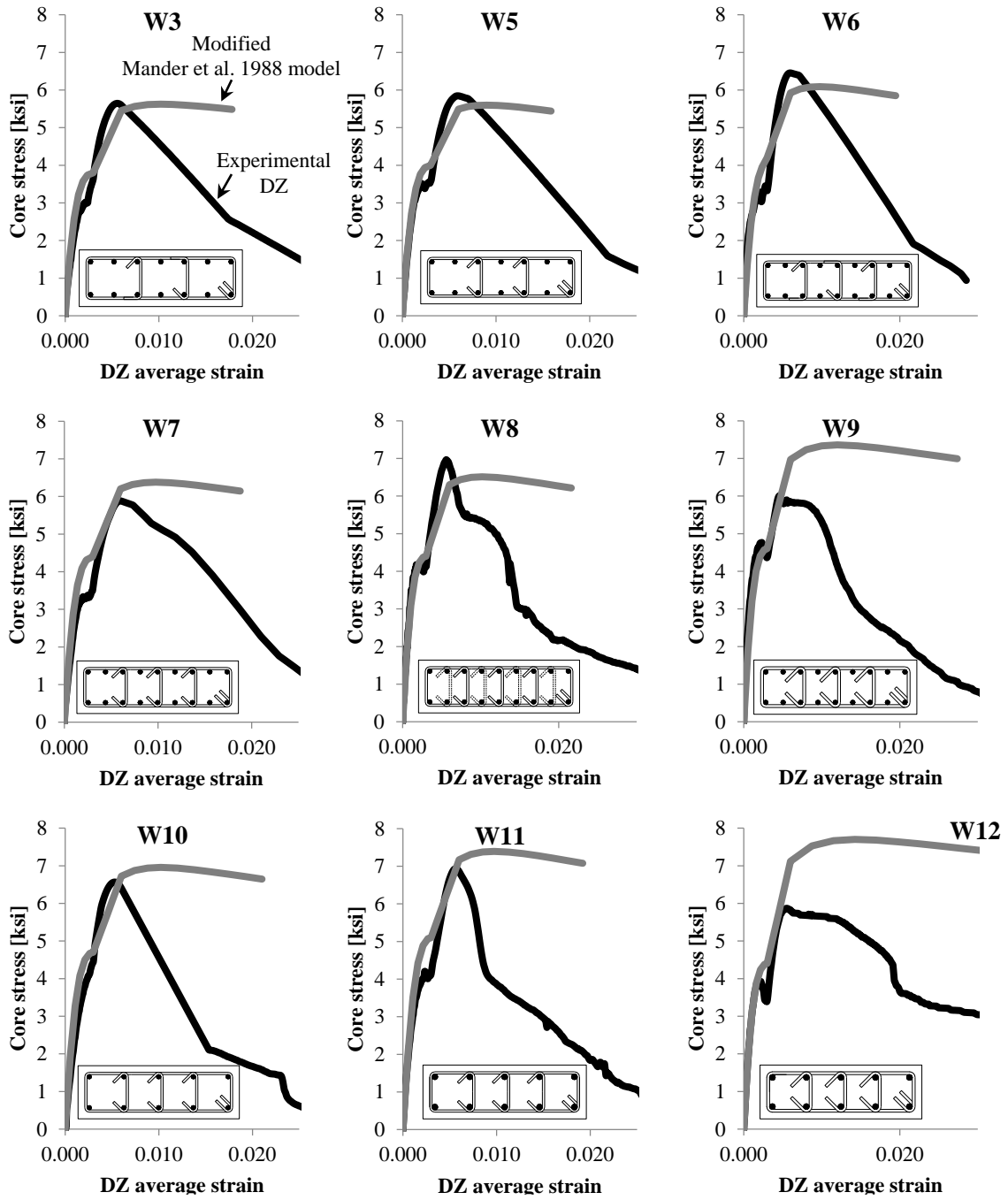


Figure 4.10 Empirical stress-strain relations of the confined core from the damaged zone of specimens W3 and W12.

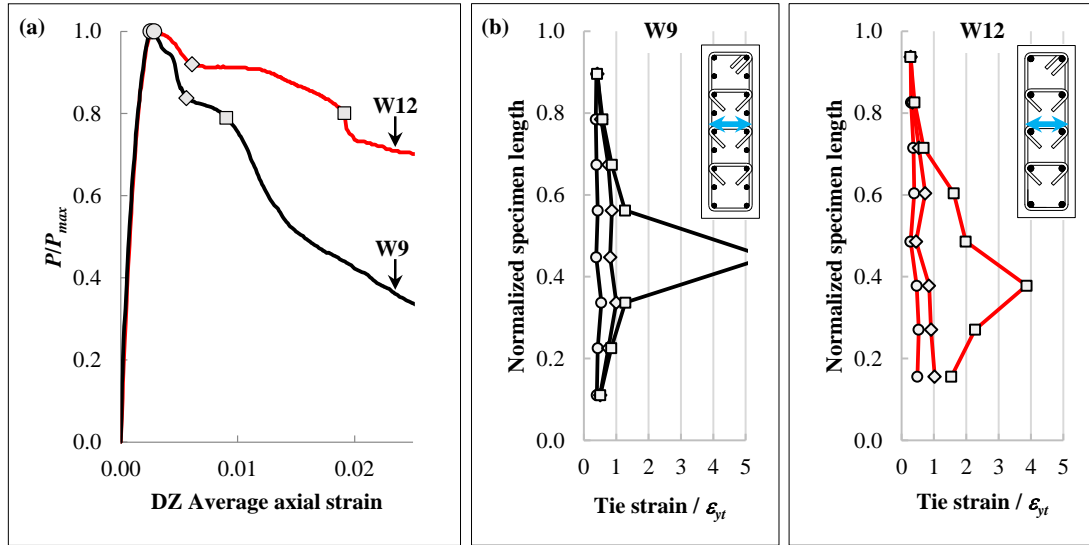


Figure 4.11 Strain demand distribution in ties of specimens W9 and W12: (a) normalized force versus average axial strain in the DZ; (b) transverse strain demand on the central tie of specimen W9 and W12 at three stages of the force-shortening relationship.

4.5.2 Statistics of the empirical confined core stress-strain relationship in the damage zone (DZ)

Recovered confined-to-unconfined-strength ratio are in the range $1.31 \leq f'_{cc}/f'_c \leq 1.58$ (**Figure 4.12**). Mean f'_{cc}/f'_c is 1.42 with COV=7%. Experimental values of ϵ_{cc100} , ϵ_{cc90} and ϵ_{cc80} are plotted against the corresponding damage zone length in **Figure 4.13a**. Empirical values of ϵ_{cc80} are considered as ultimate limiting strain of stable core behavior. Mean values for the instants of interest are $\widehat{\epsilon_{cc100}} = 0.56\%$, $\widehat{\epsilon_{cc90}} = 0.89\%$ and $\widehat{\epsilon_{cc80}} = 1.10\%$. It is observed that the dispersion increases as the strength loss, at which the strains are recorded, increases. This is due to the highly variable post peak response observed in the confined concrete empirical stress-strain relationships.

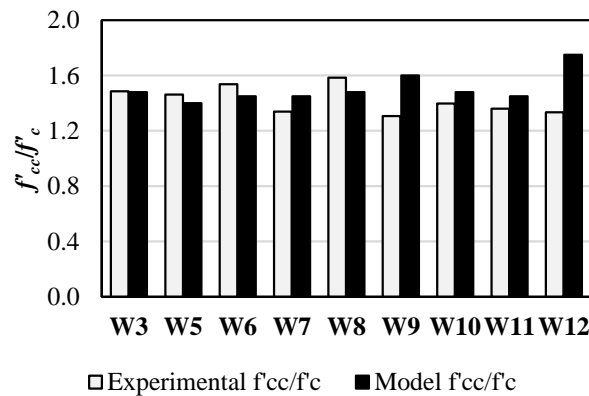


Figure 4.12 Model and empirical core strength comparison.

Figure 4.13b summarizes the statistics corresponding to the median, 1st and 3rd quartiles, and maximum and minimum values of the laboratory data. These are compared with the statistics of the analytical estimates of ϵ_{cc0} and ϵ_{ccu} , obtained using Equation (4.2) and (4.7), respectively,

calculated using as-tested material properties. While the ratio between the average analytical strain at peak strength ε_{cc0} , and the average strain at peak strength of the unconfined concrete ε_{c0} , (see **Figure 2.2**) is 3.5, the ratio $\varepsilon_{cc100}/\varepsilon_{c0}$ is 1.9, showing a smaller migration of the empirical confined strain at peak. The scatter of ε_{cc100} is also much smaller supporting the observation that the specimens were not able to recover the load carrying capacity past the onset of concrete cover spalling. Although it is recognized that the definition of ε_{ccu} differs from that of ε_{cc80} , at the mean level, analytical ultimate strains approximately double those of the experiments. The minimum and maximum experimental strains in stable response are $\varepsilon_{cc80,min} = 0.008$ and $\varepsilon_{cc80,max} = 0.018$.

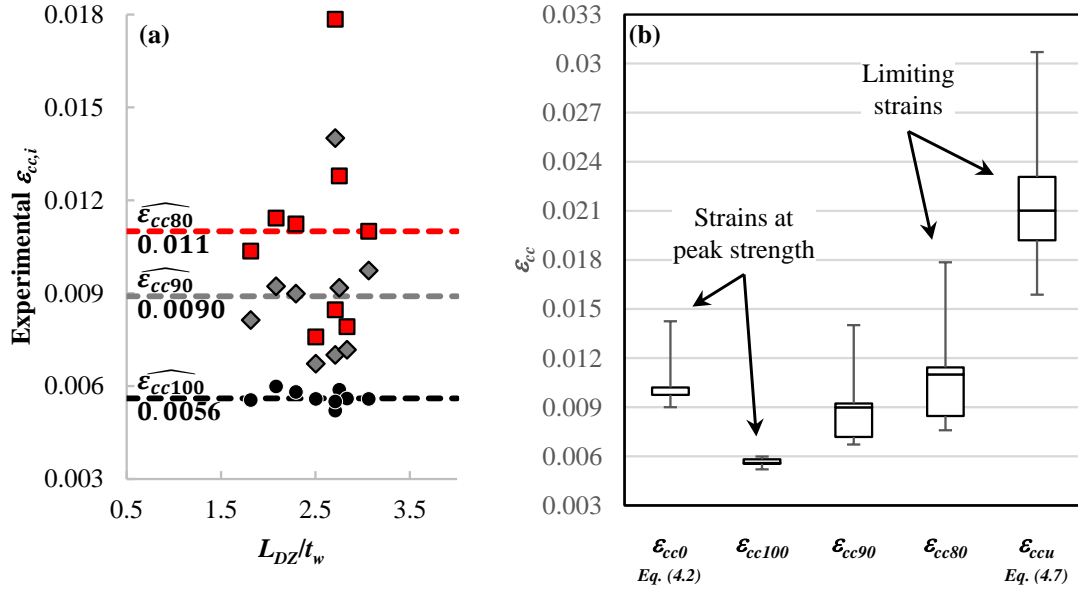


Figure 4.13 Confined core strains at different levels of strength loss. (a) scatter of recorded values of strain and corresponding damage zone length for specimens W3 to W12; (b) box plots comparing the dispersion of the empirical data and models for different confinement strain measures.

4.5.3 Statistics of pointwise empirical confined core stress strain relationships

A similar approach to that exposed in **Section 4.5.1** was followed to estimate empirical confined concrete stress-strain relationships using the pointwise force-strain curves presented in **Section 4.4.2**. With this motivation, the most demanded core strain gage of specimens W8, W9, W11 and W12 were selected: CO_{SG3}, CO_{SG3}, CO_{SG4}, and CO_{SG3}, respectively. In addition to this, the same procedure was followed using the two adjacent most demanded strain gages. For this purpose, the following core strain gages were averaged with the latter set: CO_{SG4}, CO_{SG4}, CO_{SG5}, and CO_{SG2}, for specimens W8, W9, W11, and W12, respectively. Gage length for the single gage set, denoted 1CO_{SG}, is $0.2t_w = 2.4$ in. [60 mm], and it is assumed to be $1.2 t_w = 14.4$ in. [366 mm] for the 2CO_{SG} set, since that is the length that two adjacent core strain gages bridge. **Figure 4.14** presents comparison of the core strength estimation from the 1CO_{SG} and 2CO_{SG} sets. As expected, the core concrete strength measurement is almost invariant to the gage length over which it is measured, because of the non-decreasing nature of the force-average strain curves up to peak load. Both sets produce similar results with mean f'_{cc}/f'_c equal to 1.42 and 1.40, respectively. Mean value for the DZ set of the corresponding specimens and that of the predictive model are 1.40 and 1.57, respectively.

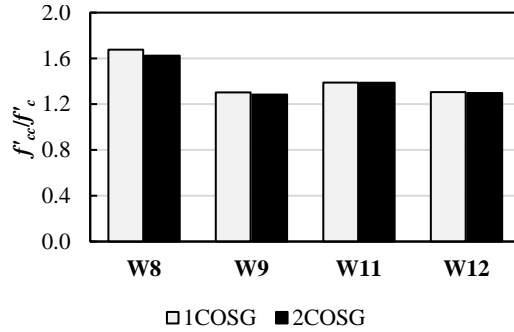


Figure 4.14 Confined core strength for two strain gage lengths.

Mean values of strain at different strength levels are presented in **Figure 4.15** for the 1CO_{SG} and 2CO_{SG} datasets. Data for the DZ of the same four specimens (W8, W9, W11 and W12) is shown as well, along with mean analytical values of ϵ_{cc0} and ϵ_{ccu} . Although not shown here, the DZ semi-empirical curves agree with the empirical curves corresponding to the average of the three adjacent core strains gages with the largest strain demand; these have gage lengths that approximate those of the DZs. It is observed that the smaller the gage length, the larger the strain measured at any given strength level. This confirms the conclusion that plasticity does not spread over a large portion of the specimens. Although pointwise empirical values are closer to the analytical estimates, the model still over predicts the strain a peak strength by 69% for the smallest gage length data set. While maximum stable mean core strain is $\epsilon_{cc80} = 0.02$ for gage length of $0.2t_w$, this number reduces 65% for length comparable to the specimen width (for example, $1.2t_w$).

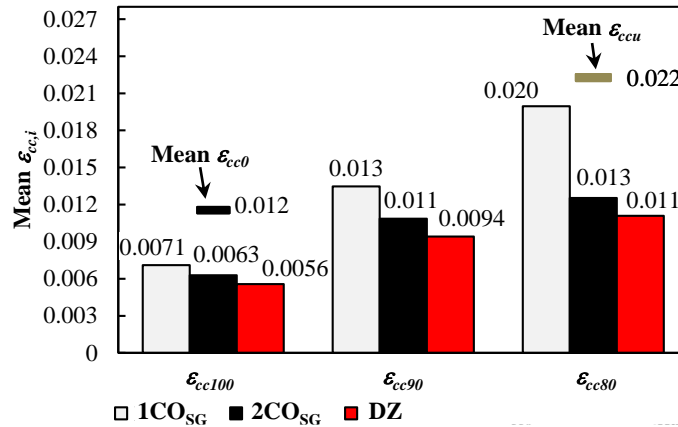


Figure 4.15 Mean confined core strains at different levels of strength loss for specimens W8, W9, W11 and W12 (Note: gage length for the 1CO_{SG} and 2CO_{SG} are $0.2t_w = 2.4$ in. [60 mm] and $1.2 t_w = 14.4$ in. [366 mm], respectively; mean gage length for the DZ series is $2.5t_w = 30$ in. [762 mm]).

4.5.4 Confined concrete stress strain relationships for modeling

Modeling the response of the rectangular prisms tested, as part of a shear wall prototype under seismic action, requires the definition of material models that represent their observed behavior. For this purpose, confined concrete stress-strain curves are constructed in **Figure 4.16** using mean values of the empirical confined concrete strength $\widehat{f'_{cce}}$, and strains $\widehat{\epsilon_{cc100}}$, $\widehat{\epsilon_{cc90}}$, and $\widehat{\epsilon_{cc80}}$, for the three gage lengths: $0.2t_w = 2.4$ in. [60 mm], $1.2 t_w = 14.4$ in. [366 mm], and $2.5t_w =$

30 in. [762 mm]. The data used for the two smaller gage lengths comprises that of specimens W8, W9, W11, and W12, while the data for the largest gage length is more robust, summarizing the response of all specimens.

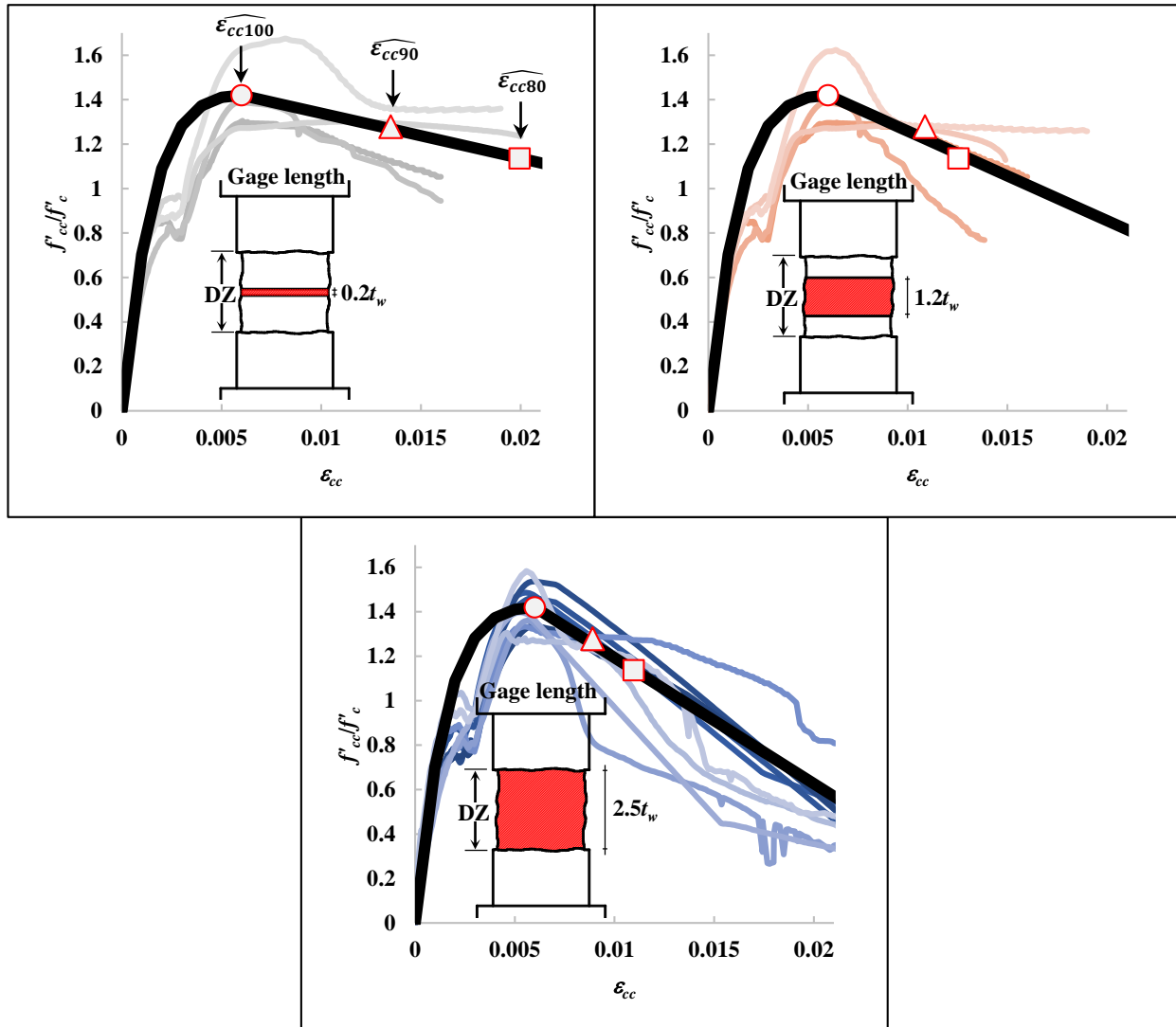


Figure 4.16 - Proposed confined concrete stress-strain relationships for different gage lengths. (Note: gage length for the 1CO_{SG} and 2CO_{SG} are $0.2t_w = 2.4$ in. [60 mm] and $1.2 t_w = 14.4$ in. [366 mm], respectively; mean gage length for the DZ series is $2.5t_w = 30$ in. [762 mm]).

The model describes the relationship between the normalized confined concrete stress f'_{cc}/f'_c , and the confined concrete strain ϵ_{cc} . It is a hybrid function comprising an ascending branch that follows the mathematical expression of (Mander et al., 1988b) up to peak strength, and a linear portion to model the post peak behavior. The post peak branch passes through points $(\widehat{\epsilon}_{cc100}, \widehat{f'_{cce}}/f'_c)$ and its slope m_{cc} is estimated from a linear fit of the data points $(\widehat{\epsilon}_{cc100}, \widehat{f'_{cce}}/f'_c)$, $(\widehat{\epsilon}_{cc90}, 0.9\widehat{f'_{cce}}/f'_c)$, and $(\widehat{\epsilon}_{cc80}, 0.8\widehat{f'_{cce}}/f'_c)$. **Equation (4.22)** defines the model and **Table 4.4** contains its parameters. The shape of the ascending branch for the three gage lengths is set to be unique, and is controlled by parameter $r_e = 1.38$, which is estimated using the mean

value of E_c from the empirical data. This works well for unconfined compressive strengths in the range of those of the tests, that is $3.8\text{ksi}[26\text{MPa}] \leq f'_c \leq 5.1\text{ksi}[35\text{MPa}]$.

$$\frac{f_{cc}(\varepsilon_{cc})}{f'_c} = \frac{\widehat{f'_{cce}}/f'_c \left(\frac{\varepsilon_{cc}}{\varepsilon_{cc100}} \right)^{r_e}}{r_e - 1 + \left(\frac{\varepsilon_{cc}}{\varepsilon_{cc100}} \right)^{r_e}} \quad 0 \leq \varepsilon_{cc} \leq \widehat{\varepsilon_{cc100}} \quad (4.22)$$

$$\frac{f_{cc}(\varepsilon_{cc})}{f'_c} = \widehat{f'_{cce}}/f'_c - m_{cc}(\varepsilon_{cc} - \widehat{\varepsilon_{cc100}}) \quad \widehat{\varepsilon_{cc100}} < \varepsilon_{cc} \leq \widehat{\varepsilon_{cc80}}$$

Table 4.4 – Confined concrete stress-strain model parameters.

Gage Length	$\widehat{f'_{cce}}/f'_c$	Strain at peak $\widehat{\varepsilon_{cc100}}$	Parameter r_e	Post peak slope m_{cc}	Ultimate strain $\widehat{\varepsilon_{cc90}}$	Ultimate strain $\widehat{\varepsilon_{cc80}}$
0.2 t_w				20.3	0.013	0.020
1.2 t_w	1.42	0.006	1.38	40.3	0.011	0.013
2.5 t_w				56.7	0.009	0.011

The approximate curves proposed are not an average model of the empirical confined concrete stress-strain curves, mainly because of the dispersion of ε_{cc90} and ε_{cc80} , but constitute a simple approximation that allows the definition of backbone constitutive models for analysis purposes. The initial stiffness and the strain at peak of the models, represent well the empirical data for any gage length. The increase in the post peak slope, and the reduction in the ultimate strain capacity $\widehat{\varepsilon_{cc80}}$ are apparent for increasing gage lengths.

4.6 Final Comments

Experimental and predictive models of the confined concrete response showed a discrepancy, mainly after the peak strength was attained. Stability of the steel cage surrounding the concrete was not guaranteed because of two main factors: (i) the low stiffness of the long leg of the perimeter hoops did not provide effective restraint to the non-tied bars; and (ii) the 90- and 135-degree tie hooks opened due to the pressure exerted by the longitudinal bars undergoing lateral instability. Therefore, at small strain increments past the peak load, the confined concrete core lost its restraining mechanism, facilitating rapid loss of load carrying area. Additionally, out-of-plane instability of the specimens after the onset of cover concrete crushing played an important role in their response by preventing a uniform compressive strain demand through the thickness of the specimens.

Three confined concrete stress-strain relationships are proposed. These are constitutive models which are a function of the gage length over which their strains are measured. The estimation of the curves utilized cover concrete and steel models that represented the as-tested properties of the materials. Additionally, bar buckling effects were accounted for the estimation of the confined core strengths. The simple models are close to those in the literature, only if empirical point wise strain measurements are utilized. The peak confined concrete strength proposed is 1.42 times the unconfined concrete strength. The strain at peak strength is set to 0.6%, and the ultimate strains for stable core responses are 0.20, 0.013 and 0.011 for gage lengths equal to $0.2t_w = 2.4$ in. [60 mm], $1.2t_w = 14.4$ in. [366 mm], and $2.5t_w = 30$ in. [762 mm], respectively.

Chapter 5 - Implications of Results

This chapter presents a methodology to evaluate the implications of the results described in **Chapter 2** through **Chapter 4** with a hazard consistent basis. The methodology is based on the Conditional Scenario Spectra (CSS) to estimate the risk of structural response quantities. The CSS are a set of realistic earthquake spectra with assigned rates of occurrence that reproduce the hazard at a site over 10^{-2} to 10^{-5} annual exceedance for periods of 0.1 to 4 seconds. A numerical example of a prototype code-compliant special structural wall under seismic shaking is presented to show an implementation of the hazard-consistent response assessment methodology. The impact of the reinforced concrete material behavior described throughout this document is discussed in terms of its risk. The example is utilized to describe the implication of the strain limits proposed in previous chapters in a hazard-consistent manner.

5.1 Engineering Demand Parameter (EDP) Risk

The PEER methodology for performance based earthquake engineering (PBEE) offers a robust framework to assess the expected performance of civil structures subjected to seismic hazard (Moehle & Deierlein, 2004). It decomposes the development of PBEE into separate tasks such as:

- *Seismic hazard analysis* to determine $\lambda_{IM}(im)$, which is the mean annual rate of exceedance of certain ground motion intensity (or intensity measure, IM). Typically, selected IM include spectral accelerations $S_a(T_i)$ at several periods, and their rate (hazard) is estimated by means of a *Probabilistic Seismic Hazard Analysis* (PSHA).
- *Structural demand analysis* to determine $G_{EDP}(edp | im)$, which is the probability of exceeding certain structural response given different levels of IM . The structural demand responses of interest are also called engineering demand parameters (EDP), and typically include drift ratios and accelerations because these can be related to damage measures of structural and non-structural components. This task is generally done by means of computer models simulating structural responses under several different ground motions of increasing intensity.
- *Damage modeling* to determine $G_{DM}(dm | edp)$, which is the probability of exceeding certain damage state (or damage measures, DM), given different levels of EDP. For structural components, this may include levels of cracking, fracture, and buckling, among others. This task is typically done in the laboratory, where a robust EDP, that is, one that can be modeled accurately in the structural demand analysis phase, is selected to be correlated to different DM s. In this manner, for example, a column element can be tested under increasing cyclic lateral displacement, which represents the drift EDP, and different damage states (for example, crack width, cover spalling, bar fracture, and collapse) are recorded during the evolution of that EDP.
- *Loss analysis* to determine $G_{DV}(dv | dm)$, which is the probability of exceeding certain decision variable (DV) limit, given different damage states. The decision variable may include economic losses, down time for repairs, and life loss, among others. This task

requires information relating the aforementioned DVs to the DMs. For example, how much money costs and how long it takes to repair certain reinforced concrete beam with a specific level of cracks width.

With these definitions, the PEER PBEE framework defines the mean annual rate with which the decision variable is exceeded as

$$\lambda(dv) = \iiint G_{DV}\langle dv|dm\rangle|dG_{DM}\langle dm|edp\rangle||dG_{EDP}\langle edp|im\rangle||d\lambda(im)| \quad (5.1)$$

where im (or IM), edp (or EDP), dm (or DM) and dv (or DV) are the intensity measure, engineering demand parameter, damage measure and decision variable, respectively. The conditional complementary cumulative density functions $G_X\langle x|y\rangle$ are of the following form: $Pr(x < X|Y = y) = 1 - Pr(X \leq x|Y = y)$. For example, if one selects the roof drift ratio (RDR) of a cantilever wall as the EDP of interest, and the spectral acceleration at the fundamental period of the wall $S_a(T_1)$, as the intensity measure, $G_{EDP}(edp|im)$ has the form $Pr(edp \leq RDR|S_a(T_1) = im)$. Specifically one could be interested in the probability that the roof drift ratio is equal to or larger than 2% given $S_a(T_1) = 0.5g$, thus $G_{EDP}(edp|im) \equiv Pr(RDR \geq 2\%|S_a(T_1) = 0.5g)$.

5.1.1 Seismic hazard estimation

The seismic hazard at a site, influenced by k sources (e.g. faults), can be estimated by the integral in **Equation (5.2)**.

$$\lambda(im) \equiv \nu(S_a(T) > z) = \sum_{k=1}^{\#Faults} N_k(M_{min}) \iint f_{M,k}(m) f_{R|M,k}(r|m) P(S_a(T) > z|M, R) dr dm \quad (5.2)$$

where $\nu(S_a > z)$ is the annual frequency with which spectral acceleration (at a given period) z is exceeded; M is the earthquake magnitude, and R is the distance from the source to the site; $N(M_{min})$ is the annual rate of earthquakes with magnitude greater than or equal to M_{min} ; $f(m)$ and $f(r|m)$ are probability density functions expressing the relative change of occurrence of different earthquake scenarios; $P(S_a(T) > z|M, R)$ is the conditional probability of observing a ground motion parameter, such as spectral acceleration (S_a) (at a given period) greater than z , for a given earthquake magnitude and distance. Typically this conditional probability is estimated using available empirical Ground Motion Prediction Equations (GMPEs) (Abrahamson et al., 2014; Boore et al., 2014; Campbell & Bozorgnia, 2014; Chiou & Youngs, 2014; Idriss, 2014), but could also be estimated by scenario-based simulations of seismic wave propagation.

As an example, Yerba Buena Island in California, United States is selected as a site of interest for the purpose of estimating the seismic hazard and code-based seismic demand for the design of a reinforced concrete structure. The site is located in the San Francisco Bay Area with coordinates (37.810491°N, 122.368317°W). This area is known to be an active crustal region of high seismicity; specifically, the San Andreas and Hayward faults flank the selected site and are the two main sources of seismic hazard. Hazard curves from a PSHA for the site are depicted in

Figure 5.1a for different periods. The hazard deaggregation gives the fractional contribution of different scenario pairs (e.g. earthquake magnitude and distance) to the total hazard. For the Yerba Buena Island site, contribution to a selected hazard level of 4×10^{-4} , corresponding to a return period of $TR = 2,500$ years is dictated by earthquake scenarios with distance to seismic source $R = 5$ to 30 km, and Moment Magnitude $M_w = 6.0$ to 8.5 . The selected NEHRP soil class is C with V_{s30} in the range 360 to 760 m/s. **Figure 5.2** describes the contribution of the (M,R) pairs to the seismic hazard at two different spectral periods.

Following conventional practice using ASCE 7 (2010), Maximum Considered Earthquake (MCE) seismic demand parameters are obtained at the short period, and at the one-second period. These are adjusted for site effects, and then further adjusted to the design level by factor $2/3$. The resulting design spectral acceleration parameters are $SDS = 1.00$ and $SDI = 0.52$. Assuming the structure of interest is Risk Category I, and has $(0.50 \leq SDS)$ and $(0.20 \leq SDI)$, it is assigned to Seismic Design Category D. For design, the elastic design response spectrum will be reduced by response modification factor R to account for the expected inelastic behavior. **Figure 5.1b** shows the MCE and design (DBE) level code-based response spectra, along with an estimated Uniform Hazard Spectrum (UHS) for a return period of 2,500 years. The UHS is a spectrum constructed by selecting a hazard level (return period), and intersecting the hazard curves of different periods to select corresponding S_a values. These (T, S_a) pairs conform the UHS, which spectral coordinates have the same rate of exceedance, and do not correspond to the response spectrum of any particular ground motion, as it is the envelope of all possible ground motions that went into the calculation of the hazard at a given period.

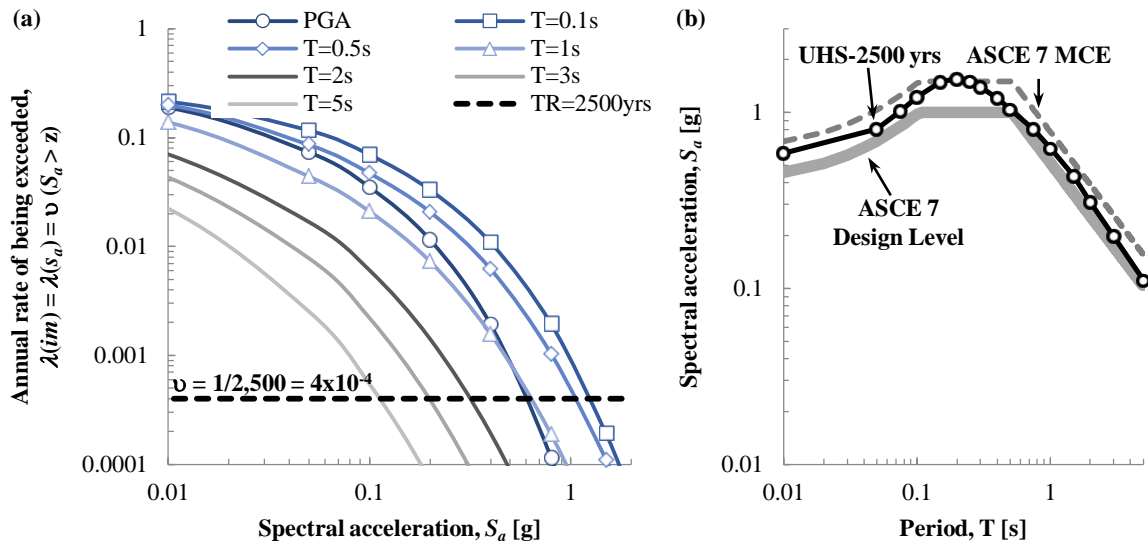


Figure 5.1 – Seismic hazard: (a) hazard curves for several structural periods for the Yerba Buena Island site; (b) uniform hazard spectrum for 2,500 years return period and code-based response spectra (5% damped).

Y.B. Deagg. TR 2,500 yrs - T=0.5 s

Y.B. Deagg. TR 2,500 yrs - T=2 s

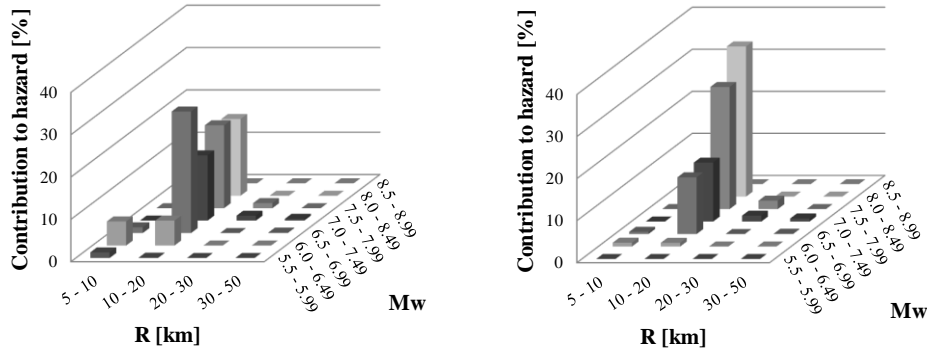


Figure 5.2 - Deaggregation of the seismic hazard for PE 2 % / 50yrs.

5.1.2 EDP risk per PEER PBEE framework

The remainder of this chapter will focus on the *EDP - IM* relationship, specifically on the EDP risk, which is a function of IM. The term “risk” will be used for the rate of exceedance of a consequence. For example, the annual rate of exceedance of an EDP is the inverse of the return period of a given structural response. This information is useful to evaluate structural behavior with a hazard-consistent basis.

According to the PEER PBEE framework, the EDP risk is defined as

$$\lambda(edp) \equiv \lambda(EDP > edp) = \int G_{EDP}(edp|im)|d\lambda(im)| \quad (5.3)$$

where $\lambda(EDP > edp)$ is a non-increasing function defined as the annual rate with which *EDP* level *edp* is exceeded; $d\lambda(im)$ is the rate of occurrence of the IM, which is the slope of the hazard curve. Fragility curves are plots of $G_{EDP}(edp|im)$ versus *im*. They describe the probability of a consequence as a function of the ground motion intensity level. Typically, the consequence is stated in a discrete manner; for example, three different fragility curves for the roof drift ratio have to be estimated if the chance of exceeding RDR equal to 0.5%, 2%, and 6%, given IM, needs to be evaluated. Their construction requires relating increasing values of IM with the EDP. Since G_{EDP} is a strictly increasing function, it is required that structural responses increase with increasing values of IM. This is not always the case, since IM are usually elastic response spectrum values that might not necessarily correlate positively with inelastic structural responses. In other words, the IM is a variable describing a single characteristic of the ground motion (for example, the elastic spectral shape) and the EDP of interest may also depend on other descriptive variables such as duration, or inelastic response spectrum shape, among others.

One way of avoiding the lack of correlation between EDP and IM, is by performing Incremental Dynamic Analysis (IDA) (Vamvatsikos & Cornell, 2002). This analysis methodology uses a set of seed ground motions which are scaled progressively to perform response history analyses of the structural model in consideration. Per scaling factor, each ground motion has an associated *im* value, and a corresponding peak structural response of interest (*edp* value). The ground motions scaling factor are incremented until a response threshold is surpassed for each ground motion. At the end of the analysis process, each EDP level of interest is associated to a distribution of IM values. **Figure 5.3** shows an example of the

IDA results, along with the estimation of two points of the corresponding fragility curve of certain EDP level. The process consists of counting the proportion of IM realizations of ground motion that result in the EDP level under consideration. A lognormal distribution is usually fitted to the empirical probability function estimated (Baker, 2015). A main disadvantage of the IDA methodology is that the structural responses will vary, depending on the seed ground motions used. Also, the scaling factors used to increase the intensity of each ground motion may produce unrealistic spectral shapes, because the shapes are constant, but they should depend on the hazard level (e.g., spectra are more peaked at the low probability levels). This may produce unlikely structural responses, that are not necessarily consistent with the estimated hazard. Additionally, assigning rates of occurrence to the scaled ground motions is difficult.

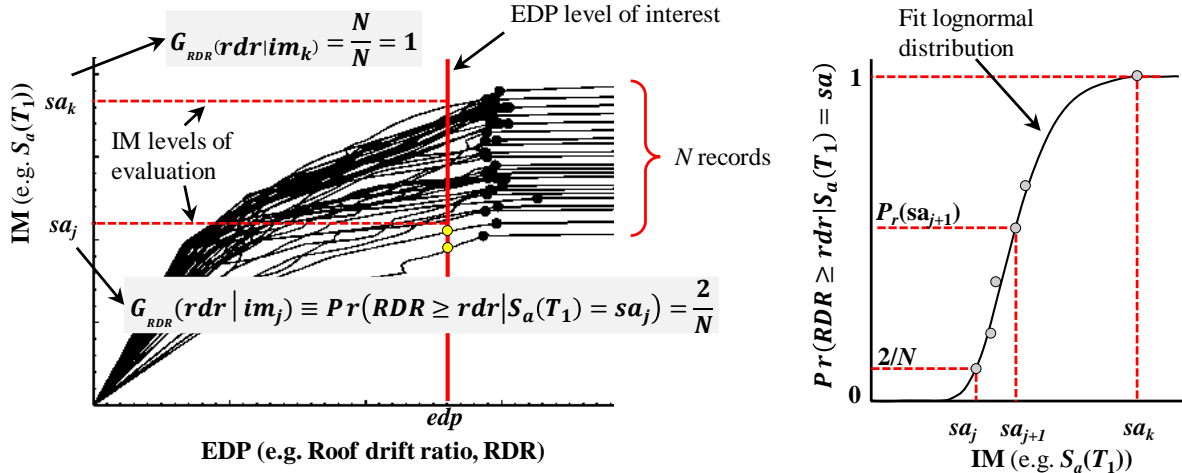


Figure 5.3 - IDA results and corresponding fragility curve estimation (adapted from (Haindl et al., 2015))

With the fragility curve in terms of the spectral acceleration, and the slopes of the hazard available (dv/dz), rate $\lambda(EDP > edp)$ can be estimated as

$$\lambda(EDP \geq edp) = \int \frac{-dv(S_a(T) > z)}{dz} Pr(EDP \geq edp | S_a(T) = z) dz \quad (5.4)$$

where a minus sign is included to correct for the negative slope of the hazard curve. The negative sign arises because the hazard is a complementary cumulative distribution where rate of exceedance are used.

5.1.3 Conditional scenario spectra (CSS) for EDP risk estimation

As an alternative to the procedure shown in Section 5.1.2, this section presents a methodology that allows estimating the resulting risk of engineering demand parameters (EDP). As mentioned before, these may comprise structural responses at the global level such as maximum story drift, base shear force, and partial or total collapse. In this study, another EDP of interest at the local structural level of response, is the uniaxial strain demand at the critical section of structural walls. The EDP risk is estimated by means of nonlinear dynamic analyses under a large suite of ground motions selected and scaled based on the so-called Conditional Spectra (CS) (Lin, Harmsen, et al., 2013; Lin, Haselton, et al., 2013). The Conditional Spectra Scenario (CSS) are a set of realistic earthquake spectra with assigned rates of occurrence based on their spectral shape

and intensity. To ensure that each spectrum has the correct shape, the CSS ground motion selection procedure makes use of estimated Conditional Mean Spectra (CMS) (Baker, 2011), anchored at a conditioning period, at different hazard levels. Given the occurrence of the spectral acceleration of a UHS at a conditioning period, the CMS provides the geometric mean response spectrum at all periods of interest. Ground motion time series are selected based on the hazard deaggregation at the site, and are scaled to account for the peak and trough variability around a CMS at various hazard levels. The initial assigned rate of occurrence for each time series is based on the hazard level of the Uniform Hazard Spectrum (UHS) at the conditioning period of the aforementioned CMS. The assigned rates to each time series are then numerically optimized such that their calculated hazard matches the target hazard curves for a range of hazard levels and frequencies of interest. The hazard estimated with the CSS is given by

$$\lambda(im) \equiv \nu(S_a(T) > z) = \sum_{i=1}^{\#recordings} Rate_{CS,i} H(S_{a,i}(T) - z) \quad (5.5)$$

where $S_{a,i}(T)$ is the spectral acceleration of the i^{th} recording, z is a test level, and H is the Heavyside function (for example, $H(x) = 1$ for $x > 0$ and $H(x) = 0$ for $x \leq 0$). For a given period, only the recordings with spectral acceleration larger than test level z (for example, larger than certain value of S_a) will contribute to the hazard.

The step by step procedure to estimate the CSS set is as follows:

1. Select candidate spectra (recordings) from hazard deaggregation based on (M,R) and spectral shape at conditioning period T_o , for a specific hazard level (for example, 10^{-4}). For a careful ground motion selection, the CSS is not too sensitive to the conditioning period, because the distribution of response spectra (of the selected recordings) are consistent with the ground motion hazard curves of the site at all relevant periods (Lin, Haselton, et al., 2013). **Figure 5.4** shows 118 unique sets of 2-horizontal-component records from scenarios that are consistent with the hazard at the Yerba Buena site. This set was originally selected by Professor Norm Abrahamson, from the University of California, Berkeley, for the analyses presented in **Appendix C**.

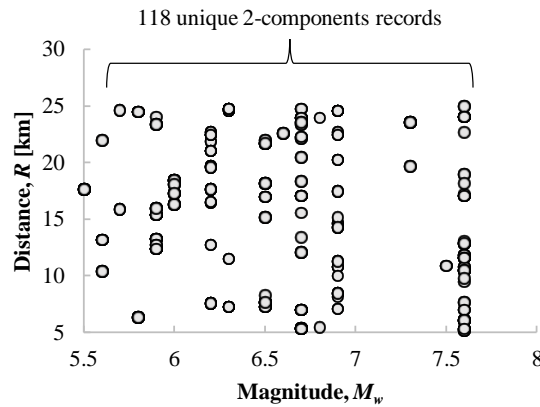


Figure 5.4 - Magnitude-distance pairs for selected seed ground motions (unique scenario spectra).

2. Estimate target UHS with several rates of exceedance, representative of the hazard levels of interest (for example, from 10^{-2} to 10^{-5}). This step is effectively discretising the hazard

for a proper recording selection at various levels (**Figure 5.5**). For the selected set, the hazard discretization comprises 9 levels.

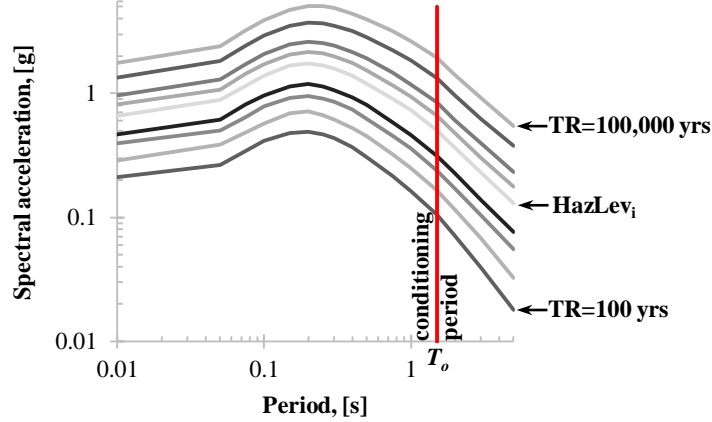


Figure 5.5 – Target UHS spectra for different hazard levels.

3. Estimate target CMS's with spectral coordinates that matches the midpoint between two consecutive UHS's at the anchoring period T_o . Account for the peak-to-trough variability by estimating spectra with a range of ± 2.5 standard deviations around the CMS. The procedure to estimate the CMS and variability around it, is described in detailed by Baker (2011). **Figure 5.6** summarizes this process, which requires the estimation of (a) the mean spectrum $\widetilde{S}_a(T_i|M, R)$ and corresponding standard deviation $\sigma(T_i) = \sigma(T_i|M, R)$ (in log units) at all periods, for the commanding scenario (M, R), from the GMPEs employed in the hazard estimation. (b) Parameter *epsilon* at the conditioning period $\varepsilon(T_o)$ is the “spectral distance” in terms of the number of standard deviations separating the UHS (at the hazard level of interest) and the mean spectrum $\widetilde{S}_a(T_o)$

$$\varepsilon(T_o) = \frac{\ln S_{a,UHS}(T_o) - \ln \widetilde{S}_a(T_o|M, R)}{\sigma(T_o)} \quad (5.6)$$

- (c) Estimate correlation coefficient $\rho(T_i|T_o)$ (Baker & Jayaram, 2008) that relates *epsilon* at T_o and *epsilon*s at different periods (T_i). Estimate the CMS for each hazard level as

$$CMS_{T_o}(T_i) = \widetilde{S}_a(T_i) \exp(\rho(T_i|T_o) \varepsilon(T_o) \sigma(T_i)) \quad (5.7)$$

- (d) Compute the standard deviation $\sigma_{CMS,T_o}(T_i)$ for the CMS as

$$\sigma_{CMS,T_o}(T_i) = \sigma(T_i) \sqrt{1 - \rho^2(T_i|T_o)} \quad (5.8)$$

- (e) Finally, estimate the spectra that expands the variability around the CMS by a selected number of *epsilon*s ε_{CMS,T_o}

$$CMS_{T_o}(T_i) \exp(\pm \varepsilon_{CMS,T_o} \sigma_{CMS,T_o}(T_i)) \quad (5.9)$$

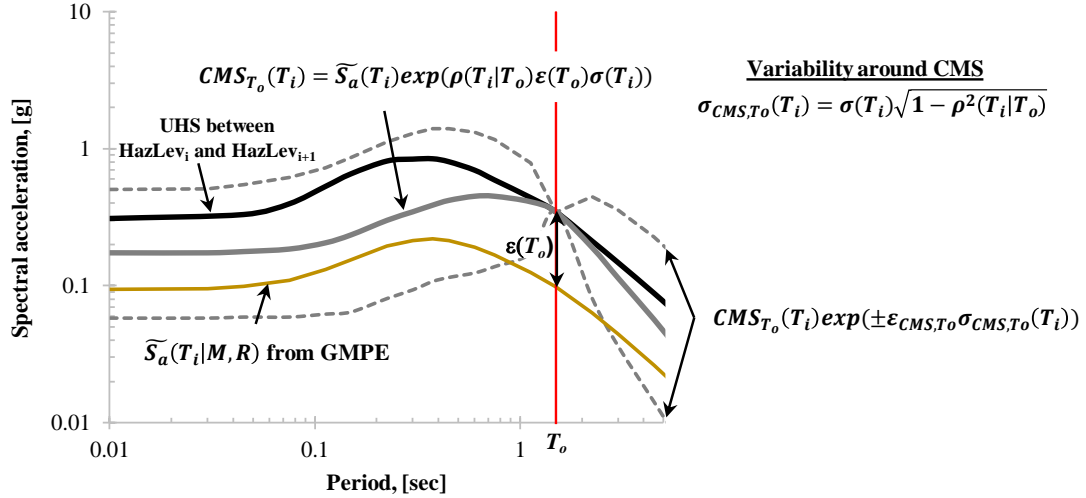


Figure 5.6 – CMS construction.

4. Select a subset of N recording pairs per hazard level. Estimate their geometric mean spectra and scale them to match the midpoint between UHS at Hazard Level (i) and UHS at Hazard Level ($i+1$) at T_o . Keep those ground motions that fall within the ± 2.5 *epsilon* range around the CMS. These are the conditional scenario spectra per hazard level. They have the correct spectral shape accounting for the peak-to-trough variability of the ground motions.

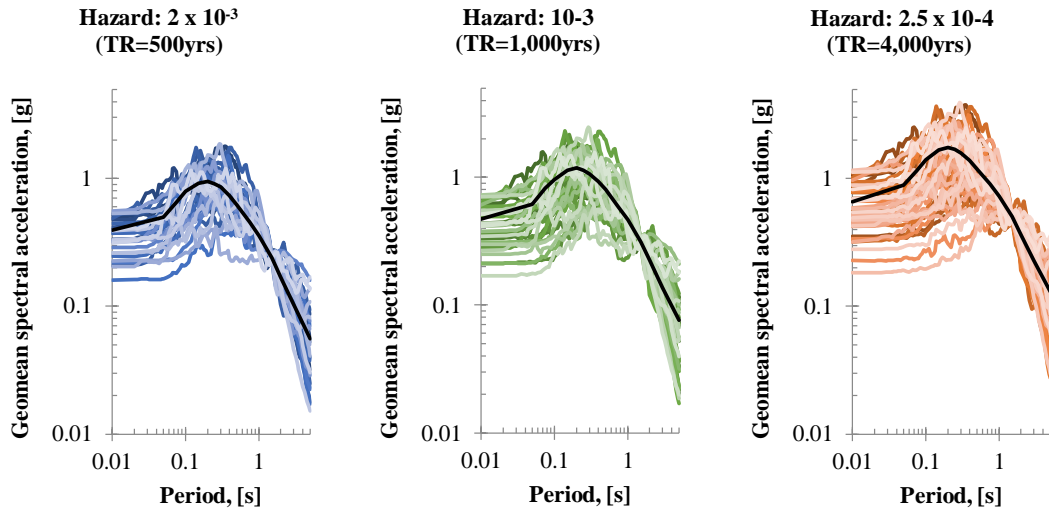


Figure 5.7 – Scenario spectra for hazard levels 2×10^{-3} , 1×10^{-3} and 2.5×10^{-4} .

5. Assign initial rate of occurrence to the selected subset per hazard level

$$Rate_{CS,i} = \frac{HazLev_i - HazLev_{i+1}}{N} \quad (5.10)$$

6. Numerically optimized the rates until the estimated hazard (using **Equation (5.6)**) matches the target hazard for a range of frequencies and hazard levels of interest.

Figure 5.8a presents the set of 402 ground motion spectra used for this study along with their final assigned rates of occurrence (**Figure 5.8b**). As mentioned before, the main feature of the CSS is that the suite of records used, and their assigned rates, allow recovering the hazard at a site over a range of periods. The hazard recovered from the CSS is estimated by means of **Equation (5.5)**, and is contrasted with the target hazard curves of Yerba Buena Island (estimated in a PSHA, see **Figure 5.1a**) in **Figure 5.9**. The target and recovered hazard curves are shown for hazard levels from 10^{-2} to 10^{-5} at three different periods. Recovered hazard curves are in good agreement with the target seismic hazard curves for the Yerba Buena Island site, being closer for periods adjacent to the conditioning period $T_o = 1.5s$.

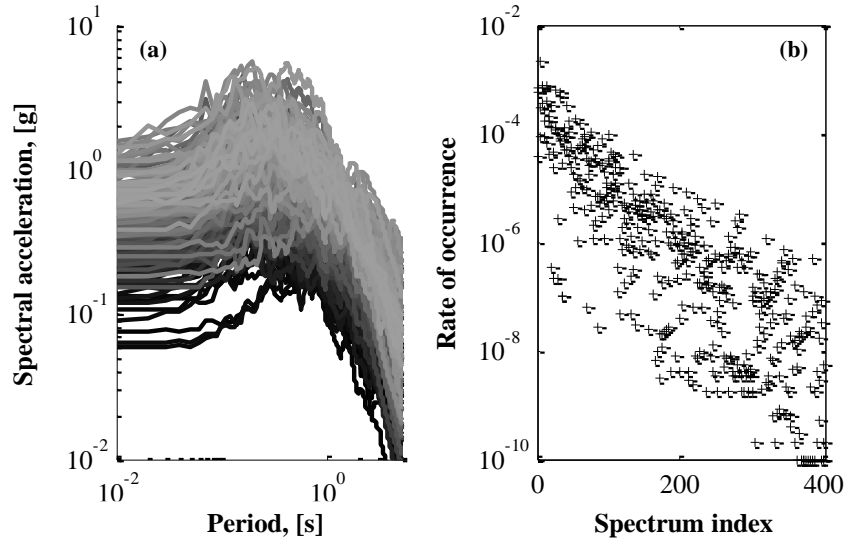


Figure 5.8 - Scenario spectra: (a) 402 scenario spectra (5% damped); (b) assigned rate of occurrence for each spectrum of the CSS

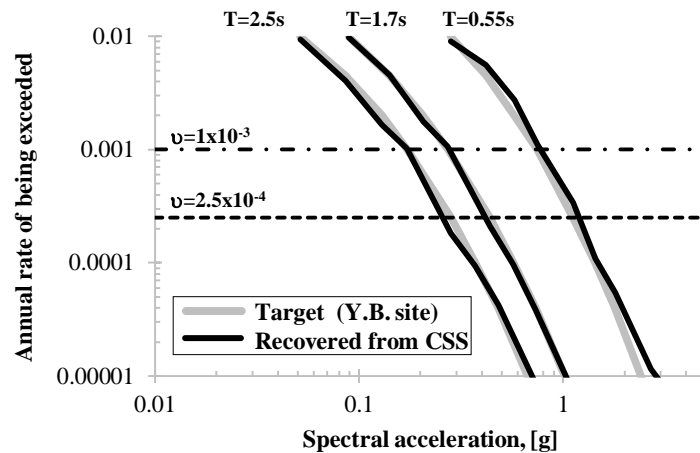


Figure 5.9 - Hazard curves at different periods recovered from the conditional scenario spectra.

5.1.3.1 EDP risk curves from CSS

An example of the dataset obtained by means of structural demand analyses, using the CSS set described above, is presented in **Figure 5.10**. The EDPs shown correspond to the maximum roof drift ratio (RDR) and maximum base shear normalized by seismic weight ($V_{b,max}/W$) of an

inelastic reinforced concrete frame model described in **Appendix C**. The CSS set covers a wide range of ground motion intensities which allows assessing the response of the structure in the elastic range, and well within the inelastic range of response, up to collapse. Once the responses from the CSS runs are gathered, proper statistical treatment of the data allows estimating EDP fragility curves with ease, which can be plugged-in **Equation (5.4)** to estimate EDP rates of exceedance. More importantly, the structural responses from the CSS, along with the assigned rates of each time series, allow direct estimation of the EDP risk using **Equation (5.11)**.

$$\lambda(edp) \equiv v(EDP > d) = \sum_{i=1}^{\#recordings} Rate_{CS,i} H(EDP - d) \quad (5.11)$$

where $v_{EDP}(EDP > d)$ is the annual frequency with which demand level d is exceeded; and as before, $H(EDP - d)$ is either 1 or 0, per the Heaviside function H , depending on whether or not the EDP from time series i exceeds level d .

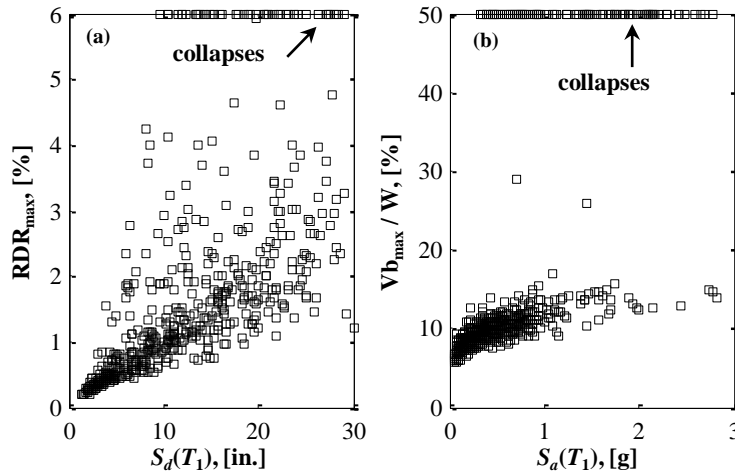


Figure 5.10 – Global EDPs from CSS runs of models in **Appendix C**: (a) maximum roof drift ratio (RDR) versus spectral displacement S_d ; (b) maximum base shear versus spectral acceleration S_a .

Figure 5.11 shows risk curves examples estimated with **Equation (5.11)**, for the maximum RDR and the normalized maximum base shear of the structure described in **Appendix C**. Useful information readily available from these curves is the return period of certain EDP level. This, for example, may help evaluate if the code-based design philosophy is met or simply, if the risk associate to demand level d is acceptable or not.

The following section will present other uses of the EDP risk-estimation methodology presented above. Another interesting application is presented in **Appendix C**, in which the risk that is achieved by two ground motion modification procedures is compared with that from the CSS. This allows grading the simplified method for ground motion selection.

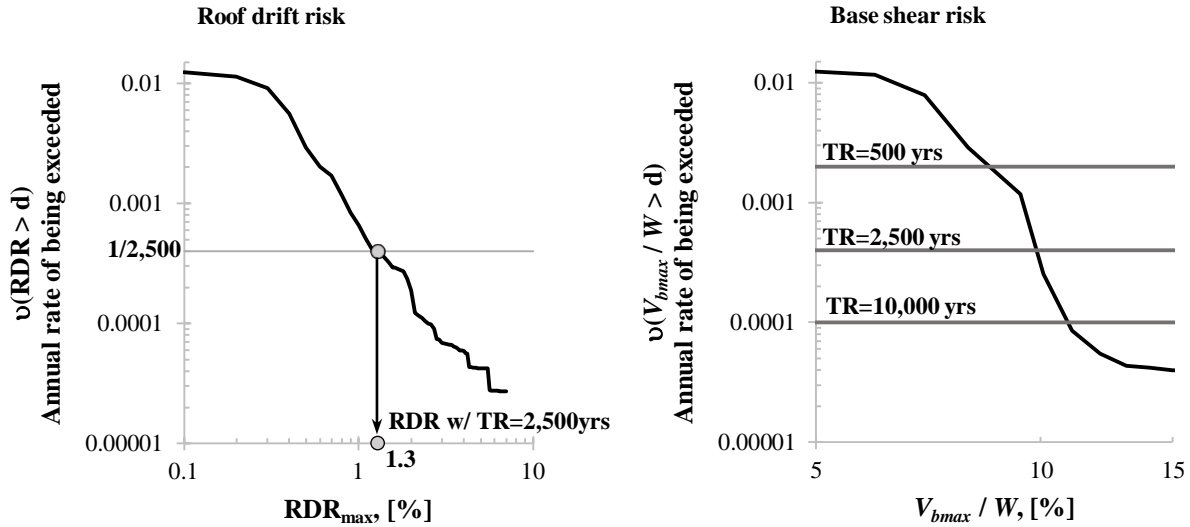


Figure 5.11 – Structural responses (EDP) risk curves example.

5.2 Risk-based Implications of Limited Strain Capacity in Boundary Elements

A distributed plasticity force-based finite element model of a shear wall is constructed to test the implications of the strain limits proposed in **Sections 4.5.4** with a hazard-consistent basis. The results presented serve also as an application example to the methodology developed in the previous section. A 7-story cantilever T-wall prototype is designed such that its critical section comprises a special boundary element (SBE) consistent with those tested in **Chapter 2**. The prototype was defined from a one-half scale section designed by a team of researchers led by Doctor John Wallace at the University of California, Los Angeles, who is one of the principal investigator of the prism tests in **Chapter 2**. **Figure 5.12** presents the geometry of the wall in elevation, the details of the cross section reinforcement, as well as some modeling details.

5.2.1 Prototype analysis and design

The prototype wall is 7.5 ft [2.30 m] long, with web and flange thickness of 12 in. [305 mm]. The 84 ft [25.5 m] bearing wall is the lateral load resisting system of 2100 ft² [190 m²] of surrounding floor area. The special reinforced concrete shear wall was analysed for combined gravity and lateral seismic loads following ASCE-7. The expected axial load on the wall is $0.10A_g f'_c$, this was kept invariant for elastic and inelastic analyses purposes. For drift calculations, the effective inertia was set to 35% of the gross inertia. A response modification factor $R = 5$, and a deflection amplification factor $C_d = 5$, were selected. The concrete was assumed normal weight ($\gamma_c = 150 \text{ lb/ft}^3$ [24 kN/m³]) with nominal strength $f'_c = 4.5 \text{ ksi}$, which is close to the average strength of the tests (**Table 2.1**). The elastic modulus of the reinforced concrete structural elements was computed as $57000\sqrt{f'_c}$ [psi]. Reinforcing steel was assumed ASTM A706 with nominal yielding strength of $f_y = 60 \text{ ksi}$ [420 MPa]. Seismic load effects on the structural members were calculated by means of the Equivalent Lateral Force Analysis described in ASCE 7. The seismic forces are defined based on the design spectrum depicted in **Figure 5.1** after reducing it by R . The approximate period used for this purpose was estimated as $C_u T_a = 0.78\text{s}$. Design base shear including response modification factor R was $V = 315 \text{ kip}$ [1390

kN] which is 13% of the seismic weight. Design maximum roof drift ratio was 0.98%. The maximum story drift ratio was kept below the 2% code limit. The design was performed in accordance with provisions for special structural walls in ACI-318 (2011). The SBE on the stem has longitudinal steel ratio $\rho_{SBE} = 2.9\%$, and transverse reinforcement ratio $A_{st}/(sb_c)$ equal to 1.1% in the through-thickness direction of the wall. The flange side of the wall is reinforced as a SBE as well, with longitudinal steel ratio of 3.5%, which includes a protected area within the web. The longitudinal and transverse steel ratio of the web is $\rho_l = \rho_t = 0.0046$, providing protection against shear failure in case the flexural capacity of the wall is reached.

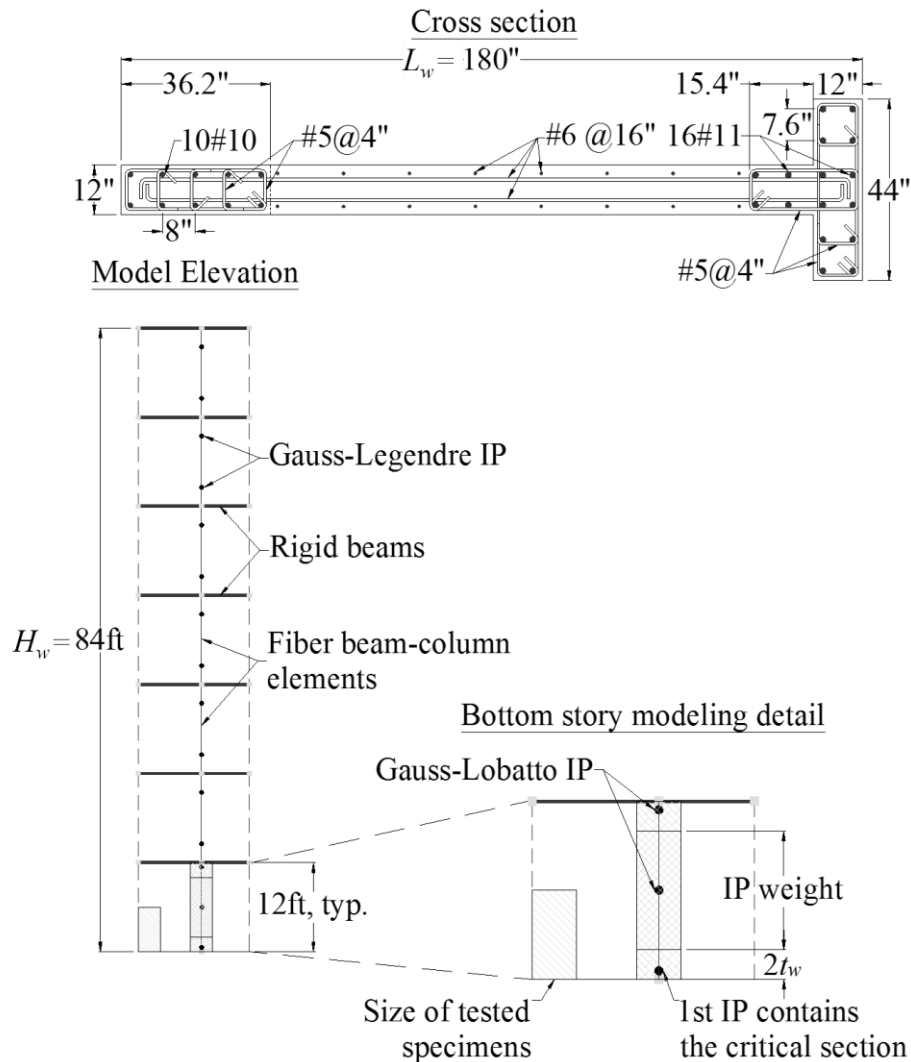


Figure 5.12 – Geometry, reinforcement and model of the T-wall studied.

5.2.2 Inelastic modeling

Two models of the wall are constructed to show the effects of the softening response of the confined concrete in the boundary element region, on the global displacement capacity. The one model that accounts for softening response of the SBE, as the one observed in the tests, is denoted SoM (soft-model). The other model does not degrade with large compressive strains and is denoted DuM (ductile-model). The cantilever wall geometry, material characteristics and

reinforcement were programmed in OpenSees. The centerline of the elements representing the wall coincides with the centroid of the cross section and does not migrate with the neutral axis location. This means that rotations at the base pivot around a non-zero elongation point (the centroid), which might not be accurate, but is not considered a fundamental flaw. The structural elements were modeled to include axial and flexural deformations only. Shear deformations and nonlinear shear responses were not modeled. The force-based formulation described in **Section 3.3.1** through **Section 3.3.6** was employed for the construction of the model. Two quadrature schemes were used in this case: (i) Gauss-Lobatto with three integration points (IP) for the first story element, and (ii) Gauss-Legendre with 2IP for the rest (**Figure 5.12**). A physical interpretation often given to the weights of the quadrature rules used in the formulation of distributed plasticity elements is related to the spread of plasticity within the element. For softening behavior, it is expected that the inelastic demand over the element concentrates on a single integration point. In flexure, this result in high curvature demand at the section level, which in turns reduces the total deformation capacity of the system.

For the reasons exposed across this document, it is always desirable to have integration point weights representative of the expected size over which plasticity concentrates, and that are consistent with the gage lengths used to define the constitutive material models. Given the geometric constraints imposed by the first story height of typical walls, and the fact that cross section geometries may have wide range of dimensions, these two requirements are difficult to conciliate with a single strategy. This is so, because plastic hinge region extension is usually defined in terms of the wall length. To produce objective displacement results, that is, a response not dependent on the number of integration points, material regularization (Coleman & Spacone, 2001; M. H. Scott & Fenves, 2006) is typically required to accommodate the available integration point weight at the critical section (which is associated to the number of IP and quadrature rule selected). This procedure effectively modifies the softening slopes of the material constitutive model to produce global displacement responses that are independent from the integration scheme, at the expense of producing unrealistic deformations at the section level (for example, curvature or uniaxial strains). Here, the integration scheme selected for the wall results in a first IP weight which has an associated length equivalent to $2t_w$. This corresponds to a lower bound of the mean damage zone length reported in **Chapter 2**, and is considered appropriate for the sake of the analysis presented without requiring material regularization. This will ensure that the global displacements and the local strain measurements are consistent.

5.2.2.1 *Materials*

The confined concrete constitutive model implemented for the SoM corresponds to that of the damage zone (DZ) in **Section 4.5.4** (see **Figure 4.16**). Gage length for this model is approximately equal to the integration point length at the critical section. This ensures that the local uniaxial strains obtained from the analysis adequately represent the physical phenomenon. The model implemented for the DuM has the same ascending branch as that of the SoM but the post peak response holds the strength in a ductile manner up to ultimate strain $\varepsilon_{cu} = 2.2\%$, which is the mean ultimate strain estimate for specimen W3 to W12 from **Section 4.3.3**. Concrete was modeled as confined or unconfined, depending on the location within the cross section, using the stress-strain relationship proposed in (Kent & Park, 1971), as modified by B. D. Scott et al. (1982) to include the tensile behavior of concrete. For the SoM model, the OpenSees material model Concrete02 was calibrated to mimic the stress strain curve of the DZ with the parameters

contained in **Table 4.4**. On the other hand, for the DuM model, the strength degradation at ϵ_{cu} was set to 5% of the peak, which matches well the stress-strain curve estimation using the Mander et al. (1988b) model for the geometry, materials and reinforcement layout of the stem SBE in the wall. Due to the material model capabilities in OpenSees, it is not expected that the DuM model reproduces the actual behavior at the section level for large compressive strains because it does not degrade in strength. The hysteretic behavior of the concrete under stress reversal is modeled according to Mohd Yassin (1994), including gradual degradation of stiffness under unloading and reloading in compression (Spacone et al., 1996). **Figure 5.13** depicts the compression region of the constitutive model backbones for the SoM and DuM models. The longitudinal reinforcing steel stress-strain behavior was assumed to be bilinear with isotropic strain hardening (Filippou et al., 1983). It was modeled with material model Steel02 in OpenSees, except for the stem of the SoM model. There, a hysteretic material, as implemented by M.H. Scott and Filippou in OpenSees, was used to approximate the rebar buckling phenomena under compressive strains larger than a threshold value consistent with the observations in **Chapter 3**. It does not account for buckling under tensile strains due to previous large tensile excursions.

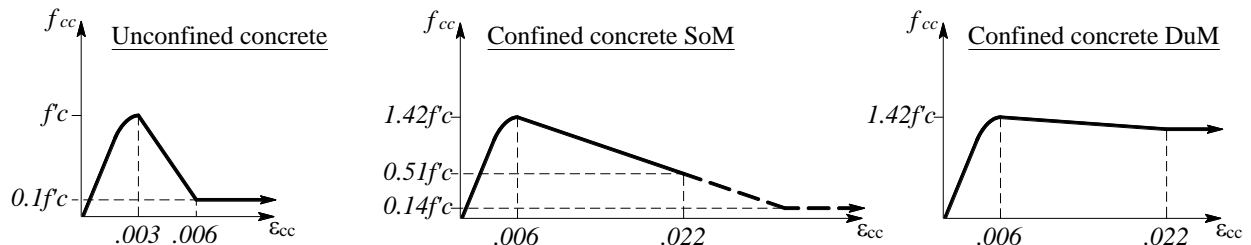


Figure 5.13 – Compression quadrant of the concrete models for nonlinear analysis.

5.2.2.2 *Cyclic pushovers: static response*

Cyclic pushover analyses were conducted over the aforementioned models using an inverted triangular load pattern with horizontal forces proportional to the height of each floor. The models account for P-Delta effect, which effectively reduces the tangent stiffness of the system by accounting for the action of the axial loading on the laterally deformed shape of the model. **Figure 5.14** and **Figure 5.15** show a summary of the SoM and DuM models response. Plot (a) shows the normalized base shear versus roof drift ratio (RDR) relationship, along with the code base shear demand. Up to 2.7% RDR, minimum over strength factor is 1.1 for the direction compressing the flange, and approximately 2.0 for the direction compressing the narrow stem. The minimum over strength factor for the DuM model is expected to grow if larger RDR values are used, but the softening behavior of the SoM model response commanded the limit present. It is worth noting that the proposed code-based over strength factor for special shear walls is $\Omega = 2.5$, per ASCE 7. As expected, the static response of both models differ for the direction compressing the narrow stem because the confined concrete model on the SoM model is allowed to soften. For the SoM model, the RDR at the onset of load carrying capacity loss is approximately 1.7%.

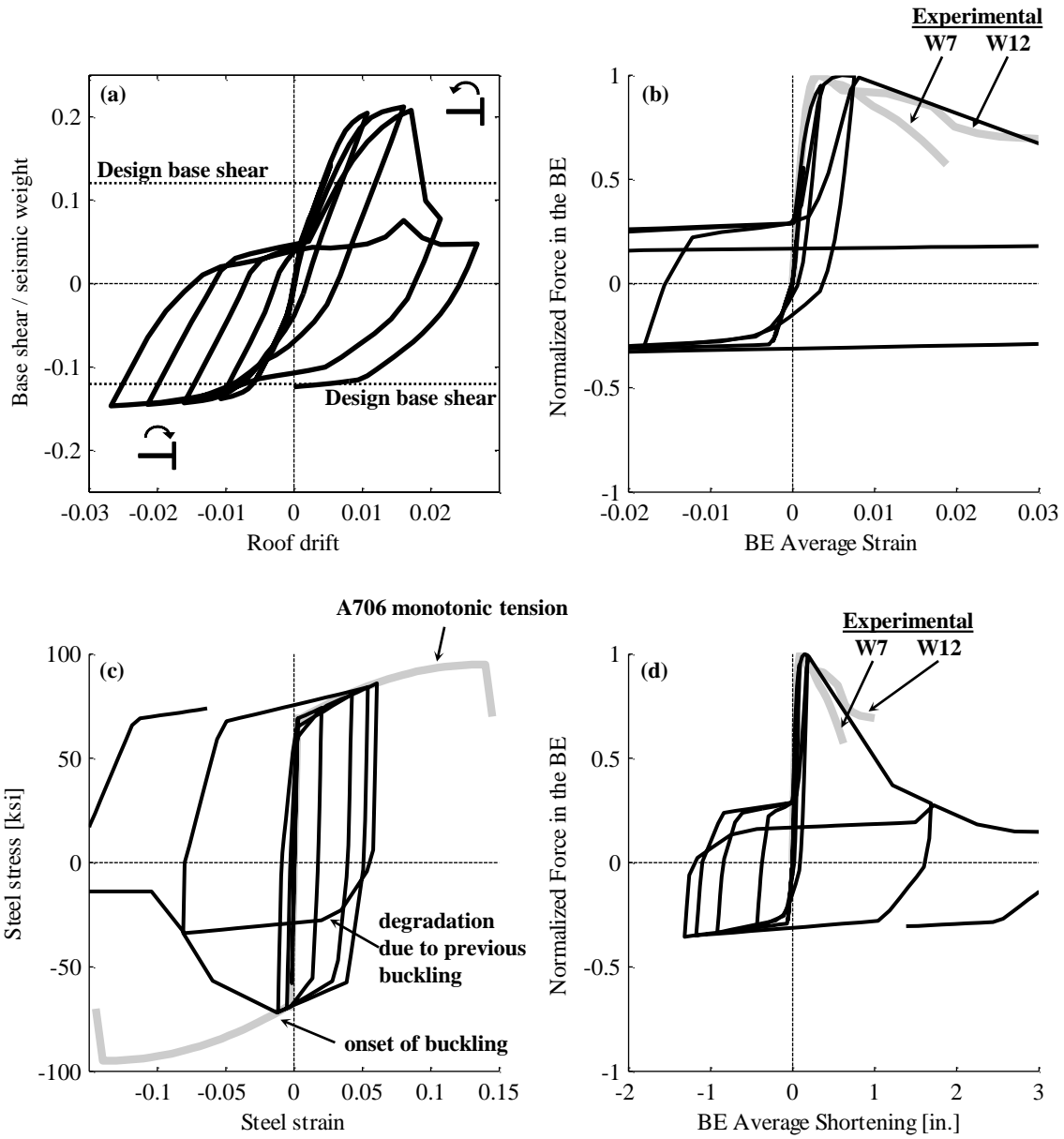


Figure 5.14 – Cyclic “pushover” analysis results for the SoM model: (a) base shear versus roof drift; (b) force versus average strain in the stem boundary element; (c) cyclic response of the steel model; (d) force versus average shortening in the stem boundary element.

The average force in the boundary at each step of analysis is estimated by the summation of the product of the area of each fiber and the corresponding instantaneous stress from the assigned constitutive model. This force is normalized by the maximum load, and is plotted against the average strain and average shortening of the boundary element in box (b) and (c), respectively. The average shortening is estimated as the average strain times the plastic hinge length (associated to the first IP weight). Experimental data gathered from the DZ of specimens W7 and W12 is also presented. The DuM model shows a ductile behavior with no strength loss in either direction. On the other hand, given the selected plastic hinge length, combined with the

fact that the material model was estimated using a similar gage length, the SoM response at the section level shows a softening behavior that approximates well the experimental data. The steel model response is shown in plot (d) of the aforementioned figures. Steel buckling is simulated for the SoM model, which softens at certain levels of compressive strain, and degrades the strength capacity for further cycles. This behavior is just an approximation of the actual expected buckling response in which tensile excursions of the reinforcing steel highly influence the onset of bar buckling (Gomes & Appleton, 1997; Monti & Nuti, 1992; Rodriguez et al., 1999), but it is considered adequate to study the response of the boundary element in the stem the wall.

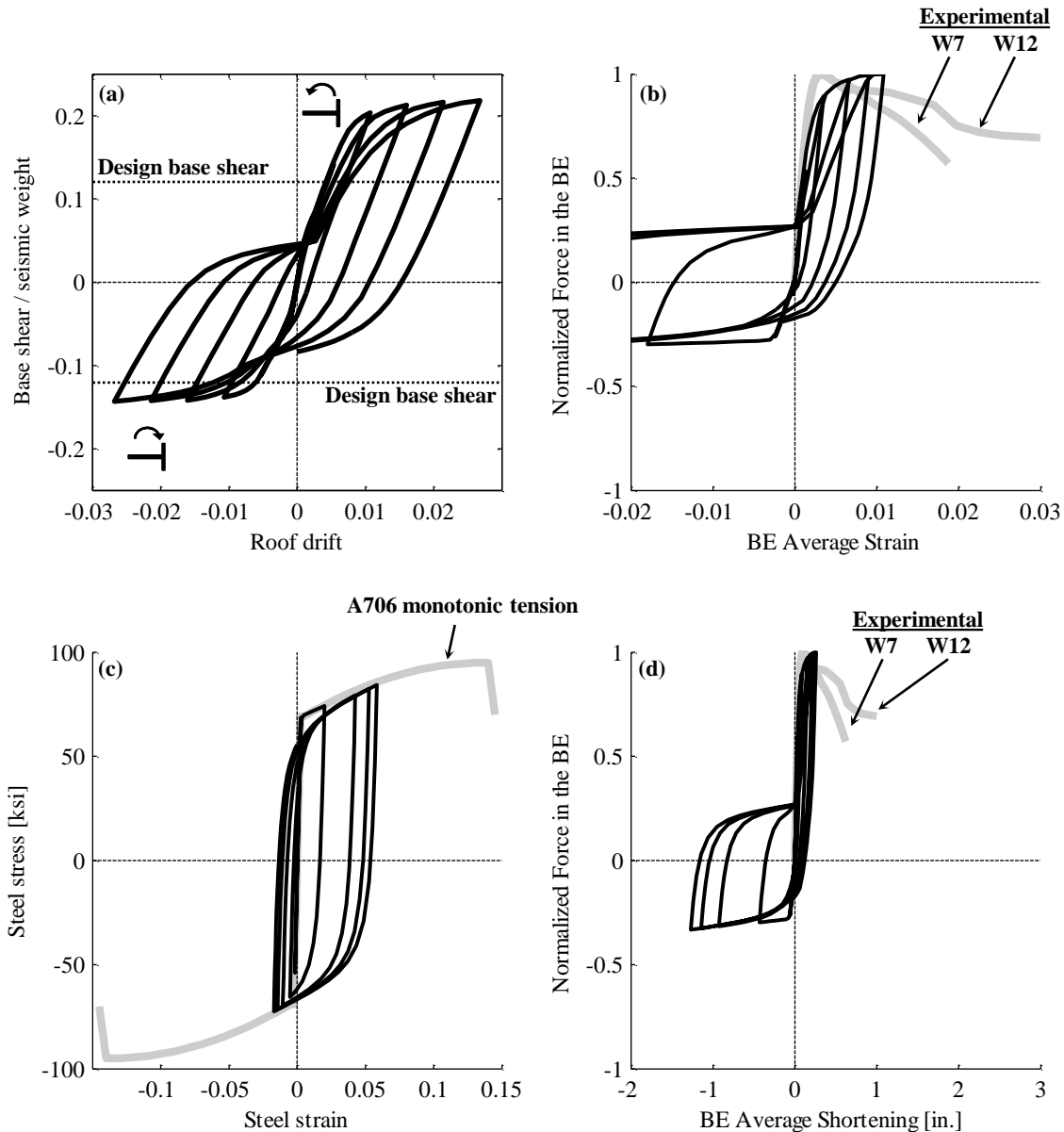


Figure 5.15 – Cyclic “pushover” analysis results for the DuM model: (a) base shear versus roof drift; (b) force versus average strain in the stem boundary element; (c) cyclic response of the steel model; (d) force versus average shortening in the stem boundary element.

The cyclic moment-curvature relations at the integration point locations of the first story element are presented in **Figure 5.16**. Two main conclusions can be stated from these responses up to RDR = 2.7%: (i) at the critical section level, the curvature ductility demand of the non-ductile model (SoM) grows rapidly after the onset of load carrying capacity, reaching demands that are approximately three times larger than those in the DuM; and (ii) while for both models the plastic demand spreads between the first and second IP for the direction that compresses the flange, it concentrates in the first integration point for the SoM model when the stem is compressed.

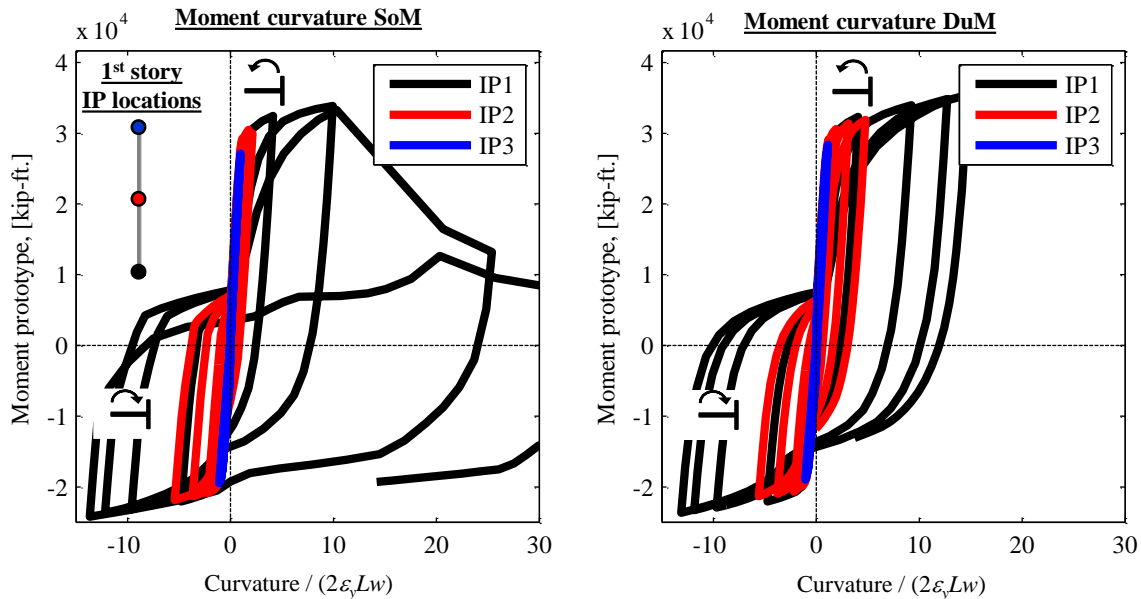


Figure 5.16 – Cyclic moment-curvature relationships at the integration point locations of the first story element.

It is concluded that the response at the section and at the global level, under static inverted triangular loading, is similar for both models in the direction compressing the flange, but it is evidently different when the SBE on the narrow stem is compressed. While flexural compression of the flange offers a large area where the concrete stresses remain low, flexural compression of the stem requires large compressive strain demands to develop stresses that equilibrate the large tensile forces on the opposite side. This results in early exhaustion of concrete strength capacity of the material model implemented for the SoM model. The remaining sections of this chapter use nonlinear dynamic analysis to obtain a broader understanding of the impact of the material characteristics on the response of the wall.

5.2.2.3 Response history analysis (RHA): dynamic behavior

Dynamic nonlinear analyses were performed on the models to compare their response under increasing intensity of seismic shaking. This section contains some typical responses to contextualize the discussion in **Section 5.2.3** regarding the hazard-consistent response evaluation using the CSS set. The global and local response history of the SoM and DuM models are compared under three different accelerograms, selected from the CSS set at different hazard levels. For nonlinear dynamic analyses, mass and stiffness-proportional Rayleigh damping was used to simulate the energy dissipation characteristics of the building that is not accounted for by

the nonlinear behavior of the structural elements. The Rayleigh damping coefficients were established to achieve a damping ratio of $\zeta = 2.5\%$ at periods corresponding to the first and third translational vibration modes of the linear model. Calculated periods for the nonlinear models were obtained after applying the vertical load, therefore some initial service level cracking is accounted for. The first and second periods of the nonlinear model are: $T_{1NL} = 1.08\text{s}$ and $T_{2NL} = 0.17\text{s}$, which are larger than the approximate elastic period $CuTa = 0.78\text{s}$, used to estimate the code-based forces. The selected accelerograms with their corresponding elastic response spectrum, 5% damped, are present in **Figure 5.17**. Also shown are the conditioning period T_0 of the CSS set, and T_{1NL} and T_{2NL} . It is worth commenting that the pulse-type accelerograms selected from the HazLev6 and HazLev8 bin are consistent with the expected demand at the Yerba Buena Island site.

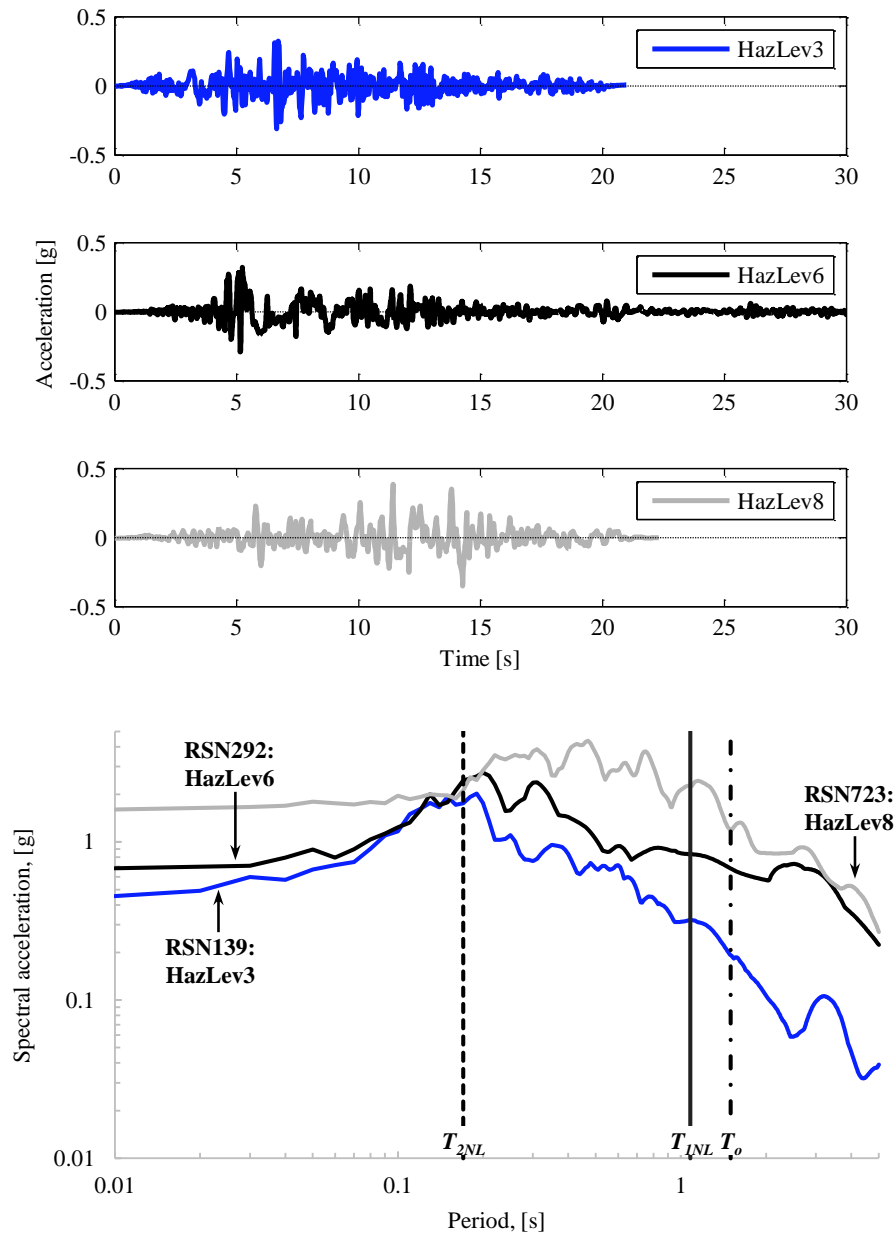


Figure 5.17 – Seismic demand corresponding to three different hazard level, for nonlinear dynamic analyses purpose (Note: the spectra are constructed for a 5% damping ratio).

The spectral acceleration of the selected motions increase with hazard level for the conditioning period, as it does for the fundamental period of the inelastic model. The same trend is expected for values of degraded structural periods. Four EDPs are selected to depict the difference in response between the SoM and DuM models: (i) roof drift ratio (RDR) (**Figure 5.18**); (ii) base shear normalized by seismic weight (V_b/W) (**Figure 5.19**); (iii) uniaxial strain demand in the centroid of the flange of the wall (**Figure 5.20**); and (iv) uniaxial strain demand in the centroid of the stem SBE (**Figure 5.21**). Before the apparent instability, the displacement response of both models is identical, matching the peaks and trough of the wave form. While the DuM model response is stable at all levels of demand, only showing a minor permanent drift in the free vibration portion of the run under the HazLev8 ground motion, that of the SoM model exhibits permanent drifts for the two ground motion with the largest intensity. It is observed that both models vibrated with an approximate period of $1.5T_{INL}$ under the lower intensity ground motion. This number migrates to approximately $2T_{INL}$ for the larger demand under pulse-type seismic shaking. Due to confined concrete crushing and bar buckling, the permanent displacements in the SoM model occurs for the direction compressing the wall stem. The base shear demand is similar in both models, showing slightly larger values for the non-degrading model (DuM) after concrete crushing in the SoM model is observed. The higher mode effects push the resultant of inertial forces downward, generating larger base shear demand than the capacity exhibited in the pushover analyses under inverted triangular load pattern. The flange strain response is relatively stable for both model, and shows a low flexural compressive demand for all ground motion intensities. This is consistent with the expected lower compressive stress that is required to equilibrate the forces in the section when the stem boundary element is stretched. On the other hand, the stem SBE strain history of the SoM model shows an apparent instability for the two ground motions with larger intensity. This occurs for compressive strain values in excess of 0.6%, which is the strain at the onset of the post peak descending branch in the confined concrete (**Figure 5.13**). **Figure 5.22** shows a detailed version of the compression strain history at the centroid of the SBE in the stem of the wall for the HazLev6 and HazLev8 ground motions. The EDPs response of the DuM model are stable for the intensity levels shown, exhibiting only minor residual deformations for HazLev8. Although this is considered an unrealistic behavior promoted by the non-degrading nature of its constitutive material models, it serves as a basis for comparison with the non-ductile model.

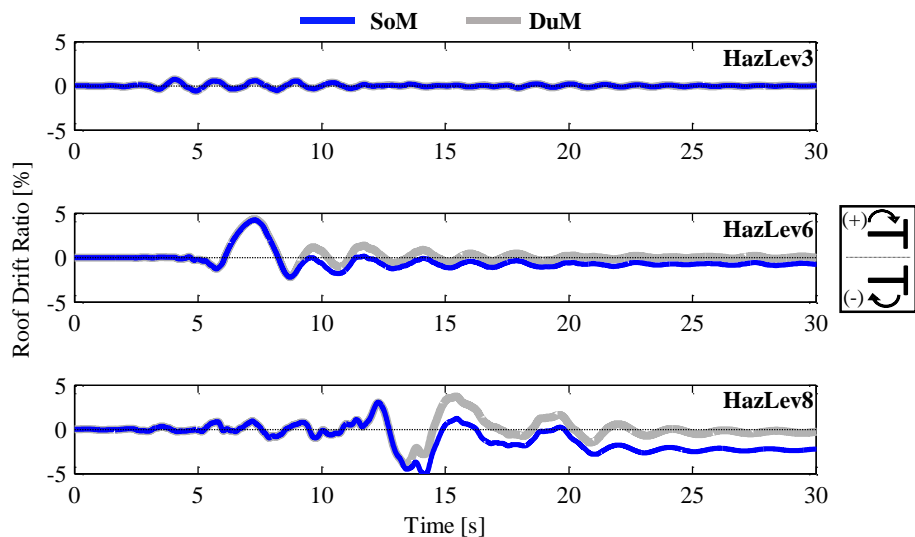


Figure 5.18 – Roof drift ratio response comparison.

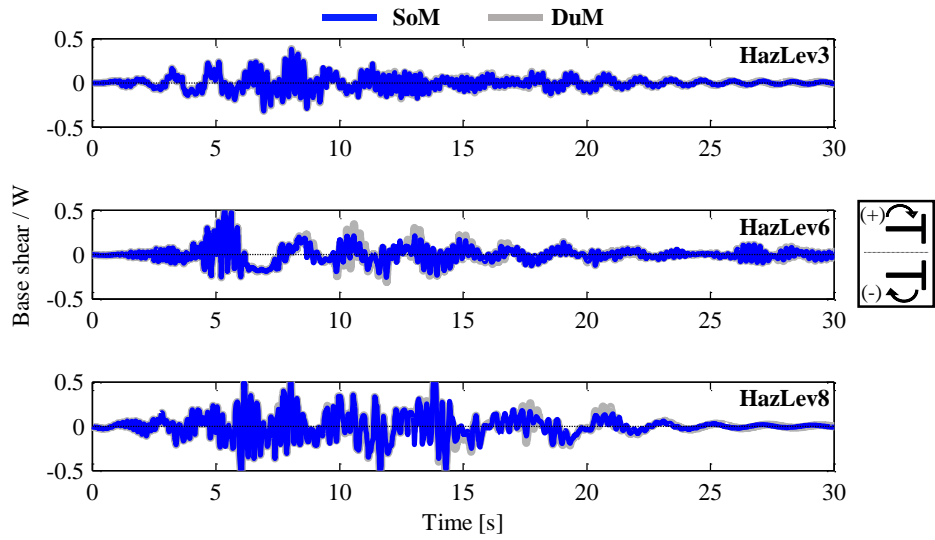


Figure 5.19 – Base shear response comparison.

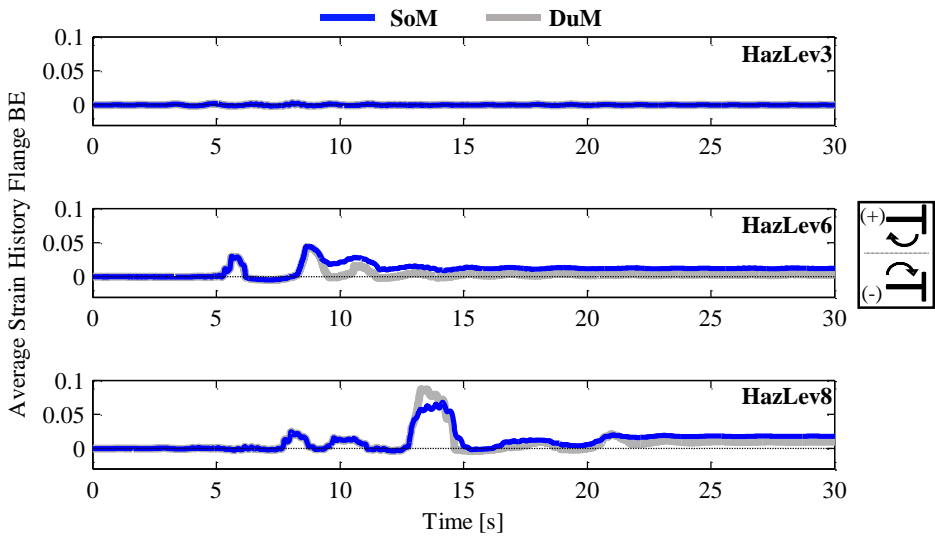


Figure 5.20 – Strain response history in the centroid of the flange.

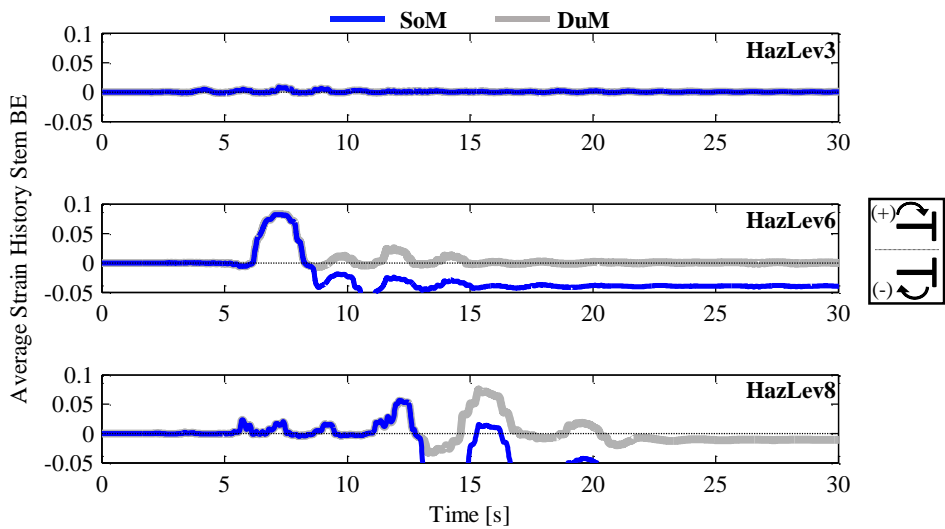


Figure 5.21 – Strain response history in the centroid of the SBE of the stem.

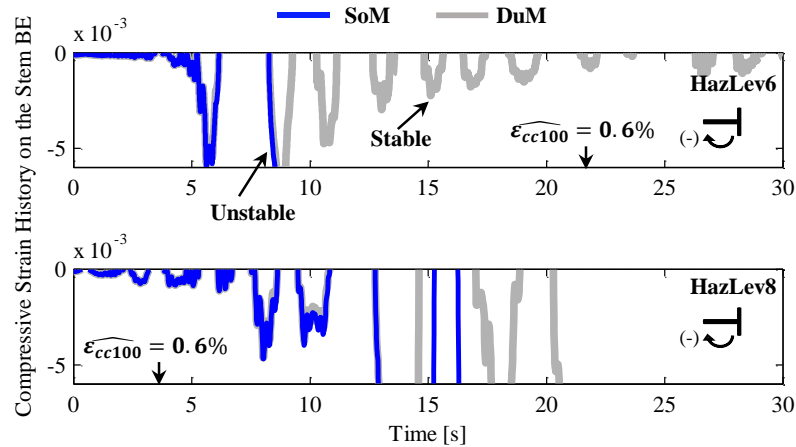


Figure 5.22 – Compressive strain response history in the centroid of the SBE of the stem.

5.2.3 Hazard-consistent structural response assessment with the CSS methodology

This section presents results of the structural response (or EDP) assessment of the SoM model by means of the Conditional Scenario Spectra (CSS) methodology presented in **Section 5.1.3**. Response of the SoM model is of interest because its plastic region geometry is calibrated to represent the average response of the specimens tested; specifically, for the case where flexural compression softening is expected. Additionally, its material model has been defined in such a manner that the gage length over which the strains are estimated, coincides with the size of the integration point containing the critical section. This methodology eliminates the need for material regularization, while maintaining global displacement and section level deformations within reasonable limits, representative of the expected behavior. Although only a single case prototype structure is studied by means of numerical analysis, the findings will serve two main purposes: (i) to give an insight into the implication of the compression strain limits proposed in previous chapters, and (ii) to present a complete example of EDP risk estimation by mean of the CSS methodology. **Appendix C** contains a second example in which the CSS is used for the hazard-consistent evaluation of two ground motion modification procedures.

5.2.3.1 *CSS ground motion set description*

Construction of the CSS required matching the geometrical mean spectrum of two horizontal ground motion record components to CMS's with the same spectral coordinate as nine UHS's with increasing return period. For the analyses presented in this section, the two components of the aforementioned *geommean* spectra are utilized. This effectively maintains the component-to-component variability of the ground motion, providing a total of 804 accelerograms to perform inelastic RHAs. To avoid double-counting the rate of occurrence, each component is assigned one-half the rate of the corresponding spectrum in the CSS. This does not affect the hazard recovery estimation, as is evidenced in **Figure 5.9**, which was constructed with the 804 aforementioned spectra. Furthermore, it does have the benefit of preventing the pinching at the conditioning period, which also helps reducing the result dependence on its selection. **Figure 5.23** shows examples of the individual component spectra at various hazard levels (from a TR =100 to 100,000 years), along with the corresponding variability of the set, which shows an apparent reduction close to the condition period $T_0 = 1.5s$.

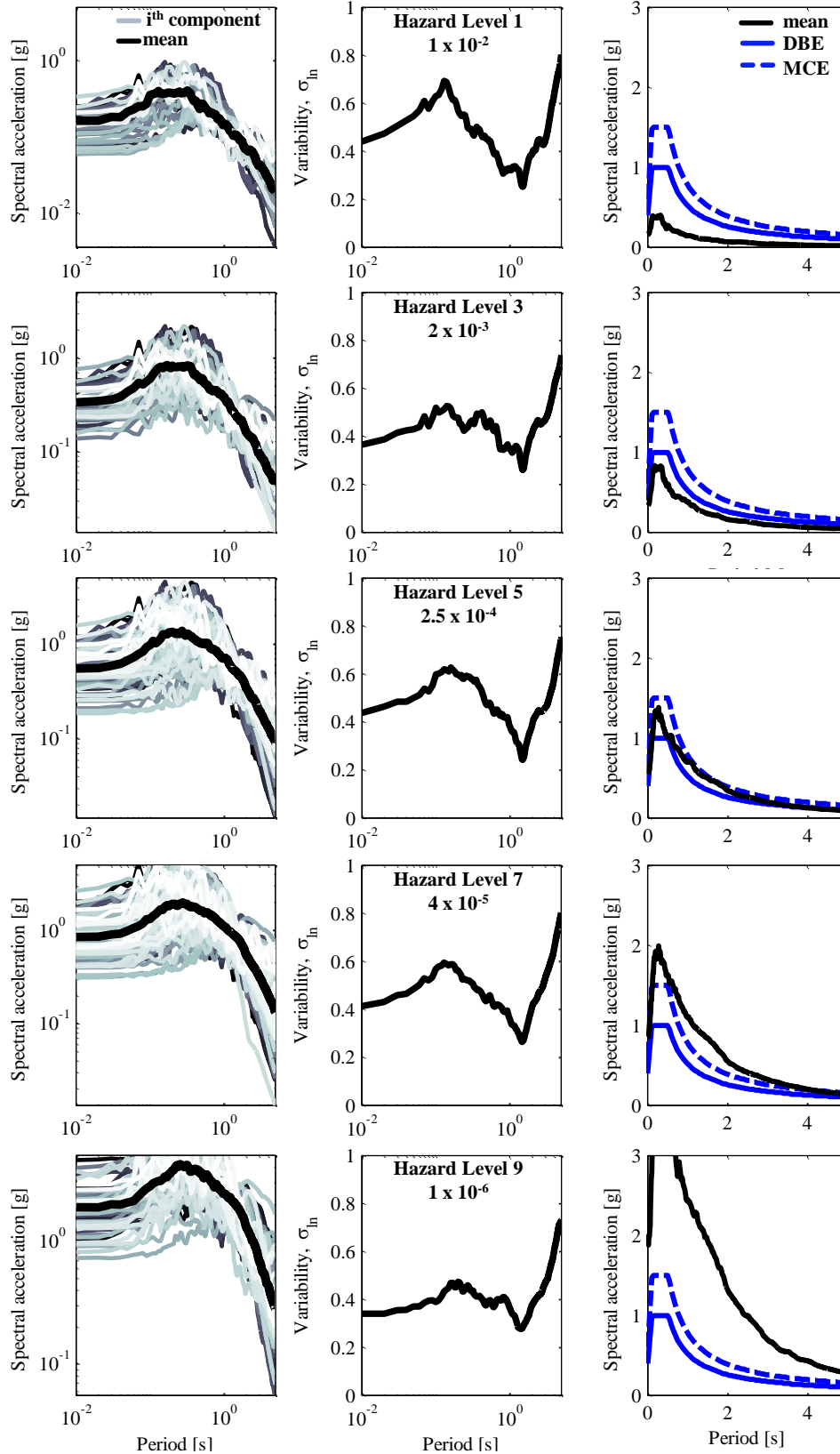


Figure 5.23 – Individual record spectra, variability and comparison with code-based response spectra.

Also shown in **Figure 5.23** are the mean of each set per hazard level is compared with the code-based spectra at the MCE and DBE hazard levels for the Yerba Buena site. Mean spectral coordinates are larger than the MCE spectrum for Hazard Levels 7 through 9. **Table D.1.1** in **Appendix D** contains the metadata to the selected set of 402 ground motions.

5.2.3.2 SoM model EDP analysis

Response history analysis (RHA) of the SoM and the DuM models were performed with the 804 ground motion set. This section focuses on the results of the SoM model because are of most interest, given the softening nature of its response. The DuM model responses are used for comparison later in **Section 5.2.3.3**. **Figure 5.24** presents maximum roof drift ratio (RDR_{max}) versus spectral acceleration relationships. The spectral acceleration $S_a(T_1)$ is estimated at the fundamental period of the nonlinear model. **Figure 5.24a** depicts a scattergram of the data, showing increasing dispersion with increments of $S_a(T_1)$ and/or RDR_{max} . This indicates that elastic spectral acceleration might not be the best predictor for the response in mention. Nevertheless, the empirical data are binned by $S_a(T_1)$ level and lognormal fragility functions are estimated in **Figure 5.24b** using the methodology in (Baker, 2015). The fragility functions are cumulative distribution functions defined by two parameter: the mean (μ_{Sa}) and the standard deviation of the natural logarithm of the intensity measure ($\sigma_{ln,Sa}$). Three curves shown are for $RDR_{max} > 0.5\%$, 2.0% and 4.0% . For $RDR_{max} > 4\%$, the available empirical data are more scattered which impacts the slope of the fragility curve. This slope is a function of the variance estimator of the lognormal fit. According to the data in the fragilities, given that the spectral acceleration corresponding to the design value ($S_a = 0.68$ g) occurs at the Yerba Buena site, there is a 100%, 30% and 5% probability that the maximum roof drift ratio exceeds 0.5%, 2% and 4%, respectively. Per code definition, this acceleration value has a return period close to 475 years.

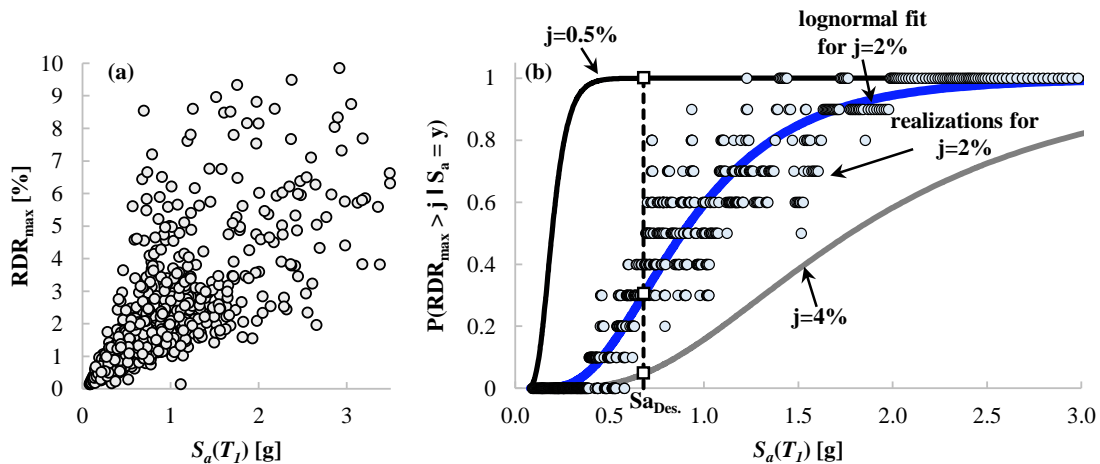


Figure 5.24 – Roof drift ratio versus spectral acceleration relationships: (a) scattergram of RDR_{max} and $S_a(T_1)$; (b) fragility curves for different levels of RDR_{max} .

Scatter plots relating the logarithm of the RDR_{max} , the maximum compressive strain $\epsilon_{c,max}$, and maximum tensile strain $\epsilon_{t,max}$ in the centroid of the SBE at the edge of the stem, are constructed in **Figure 5.25**. Colors in the markers are used to differentiate the hazard level bin of the corresponding accelerograms. Only responses from Hazard Levels 1 through 6 are shown because they demand the structural system, and its constitutive materials to the usable limits.

Dotted lines mark the tensile yield strain of the steel in the model, and the strain at maximum strength of the confined concrete. Plot (a) shows a tri-linear trend between $\epsilon_{t,max}$ and RDR_{max} . The changes in slope of the hypothetical lines are demarked by the yielding strain limit of the steel, and by RDR_{max} close to 1%. **Figure 5.25b** shows the $\epsilon_{c,max}$ versus RDR_{max} relationship, where the 1% RDR_{max} limit seems to intersect the strain $\epsilon_{c,max} = 0.006$, defining the limits of stable behavior of the confined core of the SBE. Larger values of $\epsilon_{c,max}$ are in the downward slope off the confined concrete stress-strain relationship; therefore, an unstable behavior of the member is evidenced by the gap of the vertical-axis data-points. **Figure 5.25c** shows the $\epsilon_{t,max}$ versus $\epsilon_{c,max}$ relationship, where a linear trend (shown with dashed lines) with slopes between 2 and 3⁶, in the log-log space, seem to fit the data well up to the compressive strain limit of 0.006. In **Figure 5.25a**, a slope of 3/2 is reasonable to approximate $\epsilon_{t,max}$ from RDR_{max} for the whole range shown, accepting some over prediction for tensile strains below yielding. For the compressive strain, the data are heteroscedastic, that is, variability of $\epsilon_{c,max}$ depends on the predictive parameter.

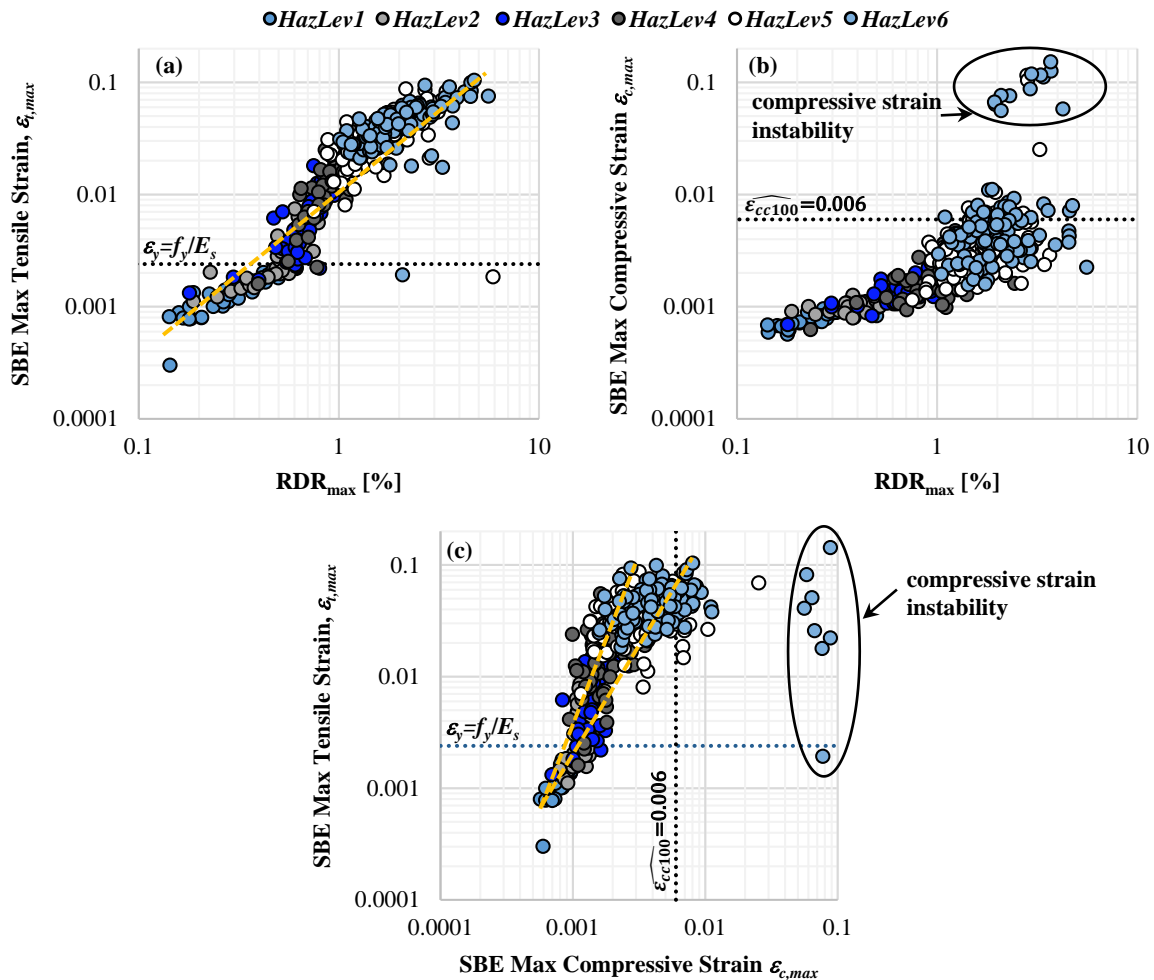


Figure 5.25 – Relationships of roof drift ratio, tensile and compressive strains in the centroid of the SBE at the edge of the stem: (a) scattergram of maximum tensile strains $\epsilon_{t,max}$ and RDR_{max} ; (b) scattergram of maximum compressive strains $\epsilon_{c,max}$ and RDR_{max} ; (c) $\epsilon_{t,max}$ versus $\epsilon_{c,max}$ relationship.

⁶ In the log-log space, slope = $\ln(y_2/y_1)/\ln(x_2/x_1)$.

An alternative evaluation of the $\varepsilon_{c,max}$ - RDR_{max} relationship is presented in **Figure 5.26**. Fragility functions, based on a cumulative lognormal distribution, estimate the probability of exceeding certain compressive strain levels given RDR_{max} are estimated for $\varepsilon_{c,max} = 0.003$ and 0.006. These strain limits correspond to the strain at the onset of cover spalling and the strain at peak strength of the confined concrete model. The lognormal fit approximates moderately well the empirical data, showing some misfit for the lower portion of the curves. The median RDR_{max} likely to produce cover crushing is 1.15%, and that to compress the SBE beyond its stable capacity is 1.78%. This value is consistent with the roof drift ratio at which the wall prototype loses its lateral load carrying capacity, according to the inelastic static analysis described in **Section 5.2.2.2**.

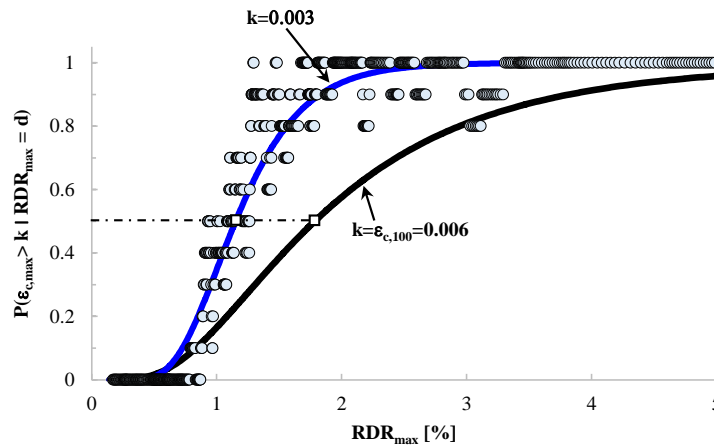


Figure 5.26 – Lognormal fragility curves of $\varepsilon_{c,max}$ in terms of RDR_{max} .

5.2.3.3 *EDP risk comparison*

The structural response assessments presented above are conditioned to certain ground motion intensities for which rates of occurrence are not always available if, for example, alternative analysis methodologies such as IDA are used to evaluate the EDPs at increasing levels of seismic shaking. This section presents an innovative approach to study structural responses from a hazard-consistent point of view. The assessment is based on the methodology described in **Section 5.1.3** for EDP risk estimation by means of the Conditional Scenario Spectra (CSS). The methodology offers a robust alternative to evaluate structural response by answering questions such as, “when does certain EDP level observed matter” or “what is the return period of a certain structural response value”. The results of this section use the same 804 data-points per EDP as the analyses in the previous section, to evaluate the behavior of the SoM and DuM models. To offer the alternative point of view, the same rate of occurrence is assigned to the EDP and the ground motion generating it (see **Figure 5.8**). This allows estimating the annual frequency with which demand level d is exceeded $\nu_{EDP}(EDP > d)$ using **Equation (5.11)**. The return period of the EDP is the inverse of ν_{EDP} .

Figure 5.27 shows scatter plots relating three EDPs of interest with the corresponding rate of occurrence of the *geomean* spectra, which is effectively twice the final rate assigned to each EDP data point. The RDR_{max} rate cloud is continuous, showing a small number of outliers. A main assumption underlying the risk estimation methodology is that rates of occurrence are related to the spectral shape, and that ground motions with larger rate of occurrence produce smaller EDP values. This idea is supported by the fact that frequent ground motions are

associated with lower intensity values. **Figure 5.27a** shows an example where a large rate is detected at a large RDR_{max} value. This will produce “jumps” in the corresponding risk curve, depending on the discretization level of the hazard. Again, this is another sign that elastic spectral accelerations might not be the best predictor of inelastic structural responses. A vector of parameters may be a better approach that would lead to smoother scaling with the ground motion levels. For example, a vector containing the spectral acceleration at different structural periods, and the duration of the ground motion, may improve the correlation between the predictors and the structural responses (Raghunandan & Liel, 2013). A discontinuity in the $\epsilon_{c,max}$ cloud is apparent (**Figure 5.27b**) for strain values in excess of that at which the peak strength in the SBE is attained. This affects the EDP risk curve by flattening it, making the risk invariant to increasing levels of strain demand beyond the instability point. Analogous data are presented in **Appendix D** for the non-degrading model (DuM).

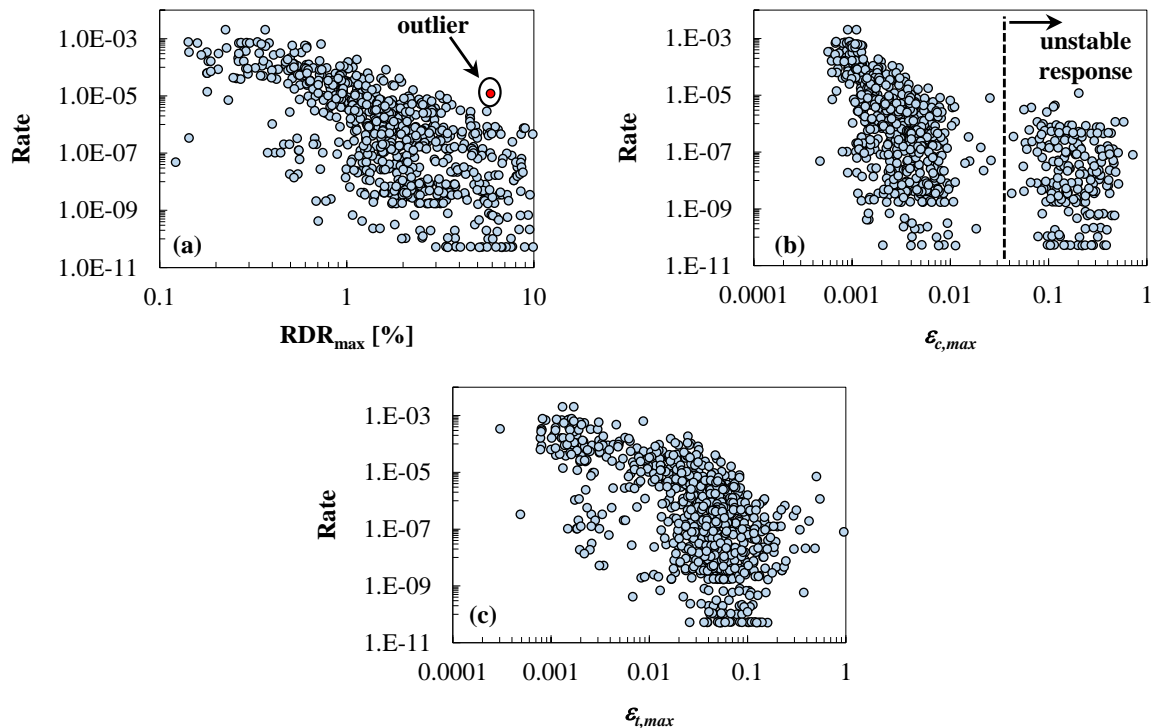


Figure 5.27 – Rate versus EDP level: (a) rates of occurrence for maximum roof drift ratio; (b) rates of occurrence for maximum compressive strain in the stem SBE; (c) rates of occurrence for maximum tensile strain in the stem SBE.

The data reported in **Figure 5.27** and **Figure D.1.1** are used to estimate risk curves of the corresponding EDPs for the SoM and DuM models. It is worth recalling that the response of the DuM model is unrealistically ductile in the direction compressing the SBE in the stem, because of the non-degrading nature of its material models. Nevertheless, its responses are useful as an upper bound of proper behavior to contrast the result of the more realistic SoM model. The EDP risk of both models are presented in **Figure 5.28** through **Figure 5.30**. **Figure 5.28** shows that the risk of the maximum tensile strain $\epsilon_{t,max}$, in the boundary element of the stem edge, is virtually identical for both models at all levels of demand. This result is consistent with the inelastic static results, because compression of the flange results in ductile response. As an application example, the total strain amplitude ϵ_a is defined as the average of the maximum

tensile and maximum compressive strain in a bar. Brown and Kunnath (2004) propose an expression for ε_a in terms of the number of half-cycles N_f , to attain low-cycle fatigue rupture. For a #9 bar, this expression is expressed as: $\varepsilon_a = 0.07(2N_f)^{-0.31}$. Amplitude ε_a reduces for larger diameter bars such as those in the SBE in the stem of the prototype wall (for example, #10 bars). Assuming that the maximum tensile-to-maximum compressive strain relationship in the SBE is $\varepsilon_{t,max} = e^2 \varepsilon_{c,max}$ (see **Figure 5.25** and corresponding discussion) one can estimate the risk of low-cycle fatigue fracture from the $\varepsilon_{t,max}$ risk curve by making $\varepsilon_a = (\varepsilon_{t,max} + \varepsilon_{c,max})/2 = \varepsilon_{t,max}(1 + 1/e^2)/2$. Bounding the number of half cycles between 1 and 10, the maximum tensile strain the SBE may attain to avoid bar fracture is 0.1 and 0.05, respectively. The risk associated with the larger number of cycles is found by intersecting the SoM curve from below. The associated return period is approximately 13,500 years, therefore, bar rupture is not likely. The risk corresponding to $N_f = 1$ is very small, outside the chart presented. It is also observed that the risk of exceeding the yield strain is below the design return period, as it is expected for tension-controlled reinforced concrete sections.

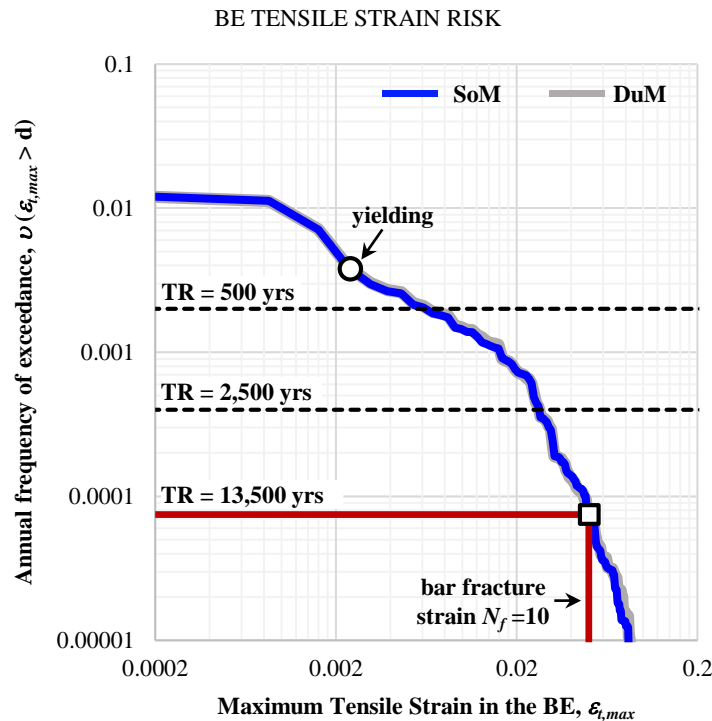


Figure 5.28 –Maximum SBE tensile strain risk for the SoM and DuM models.

The risk of maximum compressive strain $\varepsilon_{c,max}$ at the centroid of the SBE is shown in **Figure 5.29**. In this case, the SoM and DuM risk differ for strains larger than 0.003, which is associated with the onset of unconfined concrete crushing. Load redistribution due to loss of capacity of the cover generates additional stress demand in the adjacent material, consequently exacerbating the compressive strain demand on the confined concrete model. The ductile nature of the concrete model of the DuM model can take this additional demand without much loss of load carrying capacity, while the confined concrete model of the SoM may be pushed into the descending post peak slope. Two of the usable limits proposed for the confined concrete

recovered from the damaged zone (for example, for gage length $2.5t_w$ in **Table 4.4**) are: $\widehat{\varepsilon}_{cc100} = 0.006$ and $\widehat{\varepsilon}_{cc80} = 0.011$. These strain values intersect the SoM risk curve at TR = 19,400 and 36,800 years, respectively. In general, strain values in excess of 0.003 have a low associated risk, therefore, it is concluded that unstable flexural-compression behavior of the boundary element is not likely.

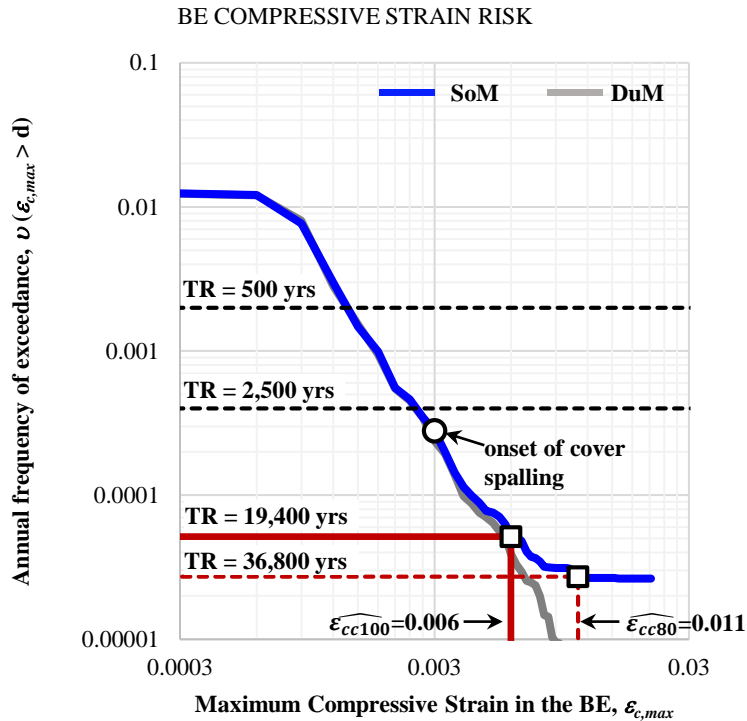


Figure 5.29 – Maximum SBE compressive strain risk for the SoM and DuM models.

Risk curves for the maximum roof drift ratio are presented in **Figure 5.30**. The return period for the design roof drift (approximately 1%) is 1,100 years, which contrasts the 475 years return period accounted for by the code. This is explained by the fact that the elastic forces used for the estimation of the design drift were consistent with a lower structural period, as compared to the nonlinear model. At the same hazard level as that of the design, the nonlinear model was affected by lower spectral acceleration demand. Although both models differ in their constitutive relation of the confined concrete, and the steel in compression, the RDR_{max} risk curves only start to diverge at risk levels as low as 3×10^{-3} (TR = 3,500 years approximately). This risk level is consistent with that of the onset of cover crushing, and the same reason exposed above apply for the differences in displacement demand. The roof drift ratio at the MCE level of demand (for example, 2500 year) is below that producing cover spalling, therefore small damage in the system may be expected at that hazard level.

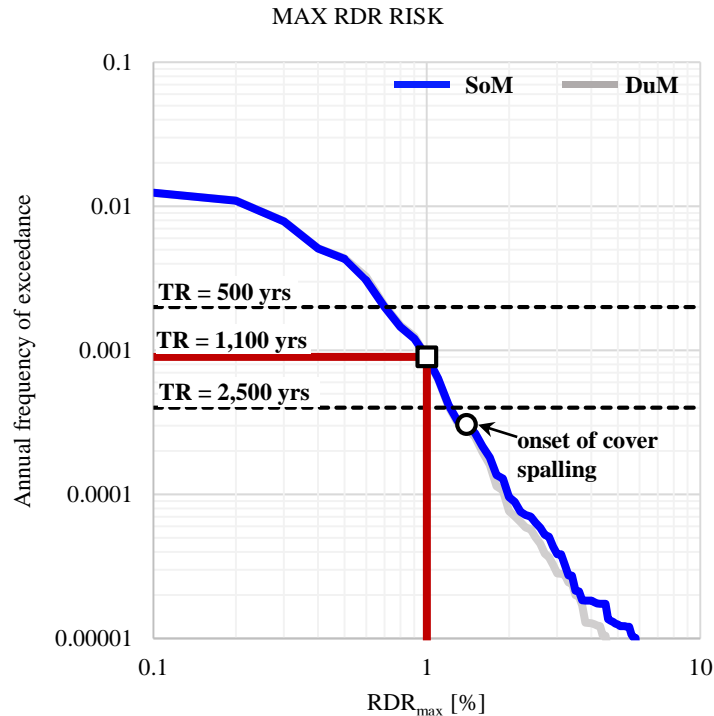


Figure 5.30 – Maximum roof drift ratio risk for the SoM and DuM models.

5.3 Final Comments

This closure chapter was conceived to give a real application significance to the results obtained in the laboratory. A methodology to estimate the risk of several structural responses was presented. The methodology is based on the Conditional Scenario Spectra (CSS), which is a set of realistic earthquake spectra with assigned rates of occurrence that reproduce the hazard at a site. A procedure to estimate the CSS set is presented, which involves the selection of a large set of ground motions with spectral shape consistent with the hazard at a site. A numerical example of a code-compliant special structural wall is used to show the implementation of a hazard-consistent response assessment methodology. The example is utilized to describe the implication of the strain limits proposed in previous chapters. For this purpose, programming of the model involved careful selection of the quadrature scheme to fulfill two main requirements: (i) the number of integration points was sufficient to ensure an adequate level of accuracy for the numerical integration at the element level; and (ii) the integration point weight of the element at the critical section was representative of the extension of the damage observed in the field and in the laboratory. Additionally, to ensure consistency between the global displacements and the deformations at the section level, the constitutive relations of the material models were measured over gage length that approximates well the aforementioned plastic hinge extension. Although a single numerical case is studied, the findings gave an insight into the implication of the compression strain limits proposed with a hazard-consistent basis. For the model studied, the poor ductility capacity of the confined concrete material, which represents the laboratory observations, is only likely to negatively impact the behavior of the system at risk levels beyond the code-based expectations. This conclusion is applicable to the case study presented. It may not apply in other building designs.

Chapter 6 – Summary and Conclusion

Field observations during the 2010 Maule Earthquake in Chile concluded that a large number of multistory shear wall buildings suffered from damage at the extreme portion of their walls, near their base. The crushed boundaries presented buckled rebar, with damage localized over a small height, and with apparent failure of their unconfined core. All these suggested the occurrence of a relatively brittle failure that was thought to be, at least in part, due to the poor detailing of the extreme portions of the wall. A study founded in laboratory tests and numerical analysis was undertaken to answer the question of whether thin walls with improved boundary element detailing would behave in a ductile manner. Ten full-scale reinforced concrete boundary element specimens were tested in the laboratory under pure compression. The chapters in this dissertation revolve around this experimental program.

In **Chapter 1** field observations of damaged walls after the Chile (2010) and New Zealand (2011) earthquakes were introduced as the main motivation to undertake this investigation. A simple plastic hinge model describing the compatibility relations of a cantilever multistory shear wall allowed relating global drift capacity with strains at the critical section. This permitted concluding that some cross section geometries, in association with intermediate axial load demand, may result in excessive strain demand in the flexural compression zone of walls. A literature review of well-known compression tests of reinforced concrete prisms described the difficulties in measuring objective values of strain capacity when softening behavior controls the response of structural elements. The reported limiting strain values at first rupture of transverse reinforcement are in the range 1.7 to 7.3%, with mean value of 4.1%, and coefficient of variation of 38%. The dispersion is mainly due to differences in transverse reinforcement layouts, but also strongly affected by the measuring technique. It is concluded that reported strain capacities are inconsistent among researchers, because of the different gage length used to measure the shortening of a damage zone that softens under moderate compressive strains, and because the differences in the procedures utilized for this purpose. A literature review of the response of three sets of tests on thin walls was also presented. The tests were performed on specimens having a wide range of longitudinal and transverse reinforcement detailing, and axial load varying from 3% to 35% of $A_g f'_c$. One set of experiments mimicked the walls damaged in the Chile (2010) earthquake. Another set comprised non-symmetric specimens with a ductile column on one edge, and a poorly detailed boundary element on the other; this was done to force the damage into the non-ductile edge to study its compressive strain capacity. The third set of experiments was representative of modern construction in the Western United States. It was concluded that average damage extension was approximately two-and-a-half times the wall thickness (t_w) for the asymmetric set with poor detailing at one edge, and for those mimicking the Chilean practice. Reported drift capacity was in the range 0.7 to 2.0%, and was highly impacted by the axial load. For thin wall specimens under comparable axial load and moment gradient, the addition of crossties along the web length and at the boundary elements at the edges, only offered a slight ductility capacity improvement with respect to specimens with poor detailing at the edges. It was concluded that the small thickness of the specimens was the most important variable commanding their response. The specimens with poor detailing reached their flexural drift capacity (0.4 to 1.05%) with ultimate compressive strain in the extreme fiber in the range 0.66 to 0.84%. A specimen with detailing of modern seismic walls in the United

States, with no splices at the base, showed limited drift capacity as low as 0.9%, promoted by crushing of the boundary region. It is important to recall that the drift ratio definition was not consistent among the tests summarized, nor was the pattern of the applied seismic load, which results in different gradients of moment demand along the tested specimens. This is likely to add bias to the results reported. Lastly, a discussion of the impact in the compression capacity of rectangular prisms with ordinary (OBE) and special (SBE) detailing, subjected to prior monotonic and cyclic tensile excursions, was presented. The results of these tests led to the conclusion that specimens that meet the minimum requirement for OBE and SBE per ACI-318-14, do not necessarily achieve expected deformation capacities in compression.

Chapter 2 presented the results of laboratory experiments involving ten reinforced concrete rectangular prisms, representative of special boundary elements of relatively thin, multistory reinforced concrete shear walls. Results from the tests suggest that ductile behavior of thin boundary elements of special structural walls under pure compression is not achievable by only complying with ACI 318 detailing provisions. The global force shortening behavior of the specimens was controlled by a thin core whose integrity can be compromised due to cover spalling, rebar buckling, and out-of-plane instability. Enhanced detailing (increasing the volumetric ratio of confinement reinforcement and decreasing its horizontal spacing) improved behavior but did not produce ductile response. Buckling of the longitudinal reinforcement both (a) reduced post-spalling axial capacity of the longitudinal bars and (b) reduced post-spalling axial capacity of the confined core. These two effects led to post-spalling strength that was substantially less than the spalling load, such that plasticity did not spread along the test specimen height. For a reinforced concrete shear wall, the repercussions of the flexural-compression zone not achieving a desired ductility level are associated with localization of damage, which may lead to local instability of the edges, and lower overall displacement capacity. This could also exacerbate the demand on other structural elements with possible negative repercussions. Detailed conclusions of the experiments were presented at the end of the chapter, some of which are restated here:

- i. Cover spalling was observed over average length comprising between 2 to 3 times the specimen thickness.
- ii. Buckling of the longitudinal reinforcement was observed at low levels of local plastic axial strain, between 0.9 and 1.5%.
- iii. Recorded buckling length for tied bars extended between 4.5 and 9.5 longitudinal bar diameters ($4.5 \leq d_b \leq 9.5$), and included, in most cases, the opening of the 90- and/or 135-degree hooks of the restraining tie. For non-tied bars, that is, those only restrained by the long leg of the perimeter hoop, buckling length extended between 14 and $18d_b$.
- iv. Usable strain limits were proposed to be a function of the gage lengths over which they are applicable. The dependence of the strain limits on gage length was introduced because of the softening nature of the response observed. For example, the deformation limiting the stable behavior of the specimens were set at strains values past that at peak strength, and lay on a softening branch (with negative slope) of the force-strain curves. For gage length equal to 2.5 times the wall thickness, the usable strain capacities range from 0.68 to 1.25% at strength level for which the load carrying capacity has dropped 20% after the maximum load is attained.

Bar buckling reduced the load carrying capacity of the reinforced concrete prisms because of the strength loss suffered by the longitudinal reinforcement, and also because it

prevented the effective confinement of the concrete core. **Chapter 3** presented a finite element-based model to describe the inelastic buckling process of tied longitudinal bars embedded in concrete, subjected to compressive stresses. A numerical experiment comprising 48 analytical specimens allowed studying the relationship between (a) tie spacing and stiffness and (b) the diameter and length of the longitudinal bars. The behavior of tied bars undergoing lateral instability in the inelastic range is highly influenced by (i) s/d_b , which represents the relative tie spacing over which bar buckling is forced, and (ii) $(d_{bt}^2/l_t)/(d_b^2/L_o)$, which represents the relative stiffness of a transverse tie with respect to the longitudinal bar stiffness. The numerical experiments showed that, due to flexibility of the restraints (ties), s/d_b has to be as small as 4.5 to effectively prevent buckling in the axial strain range of interest (for example, smaller than 8%). For large enough tie stiffness, inelastic buckling can be delayed up to $10\varepsilon_y$ for s/d_b as large as 5. For $s/d_b \geq 6$, the buckling strain estimated with the models did not surpass the yield strain. An average axial stress-strain constitutive relationship for tied A706 bars embedded in concrete, subjected to compressive strains, was proposed in terms of s/d_b and $(d_{bt}^2/l_t)/(d_b^2/L_o)$. The simple model results are in good agreement with the analytical experiments by adequately predicting buckling strain ε_b and the softening slopes after the onset of the lateral instability.

Chapter 4 combined the empirical data from the previous two chapters to recover the stress-strain curves of the confined core concrete. Blind predictions of the test (conducted prior to testing) were introduced early in the chapter, and were compared with the force-average strain response of the tested elements. This comparison showed poor correlation for strains larger than that at peak load, due to damage concentration over a small height of the specimens. Several confined concrete stress-strain relationships were estimated based on different gage lengths: 0.2, 1.2, and 2.5 times the wall thickness (approximately). For example, an average relationship for the most damage zone was estimated from the global force-average strain curves by means of a simple model of spring in series, which assumes that the plastic shortening is concentrated in the damaged region, while the rest relaxes. Others were estimated using the strains recorded by means of core strain gages embedded in the center of the cross section at different locations along the height of the specimens. To estimate the stress in the core, a model was used in which the force carried by the steel, including bar buckling, and the force carried by the cover, are subtracted from the total force. The resulting force is divided by the core area to obtain the confined concrete stresses. Average confined concrete stress-strain curves representative of the specimens tested were proposed for the three gage lengths mentioned. The peak confined concrete strength proposed was 1.42 times the unconfined concrete strength. The strain at peak strength was set to 0.6% and the ultimate strains for stable core responses were 0.20, 0.013, and 0.011 for gage lengths equal to $0.2t_w$, $1.2t_w$, and $2.5t_w$, respectively.

In **Chapter 5**, the implications of the results were evaluated in terms of the risk of several structural responses as impacted by the limited strain capacity observed in the prism tests. A numerical example of a reinforced concrete wall in cantilever, implanted in a high seismicity zone, was programmed in OpenSees for this purpose. The plastic hinge length of the model is consistent with the expected spread of plasticity at the bottom of the wall. Furthermore, the constitutive model representative of the confined concrete was estimated over a gage length which approximates well that of the plastic hinge. Using this approach, the global displacement and the strains at the critical section are consistent, without requiring material regularization. For the evaluation of the structural responses, the Conditional Scenario Spectra (CSS) methodology for the estimation of Engineering Demand Parameter (EDP) risk was introduced. The CSS is a

set of realistic earthquake spectra with assigned rates of occurrence that reproduce the hazard at a site. An example is presented for the construction of the CSS set at the site of the wall. The resulting 804 ground motions were used to perform inelastic dynamic analyses of the structural model. The rate of occurrence of the ground motions were assigned to the EDPs of interest to estimate their risk. An EDP of interest was the maximum compressive strain in the centroid of the boundary element of the wall. A case study of a single numerical model of a building showed that the limited strain capacity of these elements is only likely to negatively impact the behavior of the system at risk levels beyond the code-based expectations of good behavior. A broader set of building studies is required to more fully understand how risk is affected by the limited strain capacity of thin reinforced concrete boundary elements. The presented methodology is well suited to this type of study.

References

- Abrahamson, N. A., Silva, W. J., & Kamai, R. (2014). Summary of the ASK14 Ground Motion Relation for Active Crustal Regions. *Earthquake Spectra*, 30(3), 1025-1055.
- Acevedo, C., Creagh, A., Moehle, J. P., Hassan, W., & Tanyeri, A. C. (2010). Seismic Vulnerability of Non-special Boundary Element of Shear Wall under Axial Force Reversals. Retrieved from <https://nees.org/education/for-students/reu-program/reu-archive>.
- ACI-Committee-318. (2008). Building Code Requirements for Structural Concrete and Commentary (ACI 318-08). Farmington Hills, MI: American Concrete Institute.
- ACI-Committee-318. (2011). Building Code Requirements for Structural Concrete and Commentary (ACI 318-11). Farmington Hills, MI: American Concrete Institute.
- ACI-Committee-318. (2014). Building Code Requirements for Structural Concrete and Commentary (ACI 318-14). Farmington Hills, MI: American Concrete Institute.
- Alarcon, C., Hube, M. A., & de la Llera, J. C. (2014). Effect of axial loads in the seismic behavior of reinforced concrete walls with unconfined wall boundaries. *Engineering Structures*, 73, 13-23.
- ASCE. (2010). Minimum Design Loads for Buildings and Other Structures (ASCE/SEI 7-10) (pp. 650). Reston, VA: American Society of Civil Engineering/ Structural Engineering Institute.
- ASTM-A706/A706M-9b. (2009). Standard Specification for Low-Alloy Steel Deformed and Plain Bars for Concrete Reinforcement (pp. 6). West Conshohocken, PA: ASTM International.
- ASTM-C39/C39M-12a. (2012). Standard Test Method for Compressive Strength of Cylindrical Concrete Specimens (pp. 7). West Conshohocken, PA: ASTM International.
- Bae, S., Miseses, A. M., & Bayrak, O. (2005). Inelastic buckling of reinforcing bars. *Journal of Structural Engineering*, 131(2), 314-321.
- Baker, J. W. (2011). Conditional Mean Spectrum: Tool for Ground-Motion Selection. *Journal of Structural Engineering*, 137(3), 322-331.
- Baker, J. W. (2015). Efficient Analytical Fragility Function Fitting Using Dynamic Structural Analysis. *Earthquake Spectra*, 31(1), 579-599.
- Baker, J. W., & Cornell, C. A. (2006). Spectral shape, epsilon and record selection. *Earthquake Engineering & Structural Dynamics*, 35(9), 1077-1095.
- Baker, J. W., & Jayaram, N. (2008). Correlation of spectral acceleration values from NGA ground motion models. *Earthquake Spectra*, 24(1), 299-317.
- Bayrak, O., & Sheikh, S. A. (2001). Plastic hinge analysis. *Journal of Structural Engineering*, 127(9), 1092-1100.
- Bazant, Z. P. (1989). Identification of Strain-Softening Constitutive Relation from Uniaxial Tests by Series Coupling Model for Localization. *Cement and Concrete Research*, 19(6), 973-977.
- Berry, M., & Eberhard, M. (2008). *Performance Modeling Strategies for Modern Reinforced Concrete Bridge Columns* (PEER 2007/07). Retrieved from

- Boore, D. M., Stewart, J. P., Seyhan, E., & Atkinson, G. M. (2014). NGA-West2 Equations for Predicting PGA, PGV, and 5% Damped PSA for Shallow Crustal Earthquakes. *Earthquake Spectra*, 30(3), 1057-1085.
- Bresler, B., & Gilbert, P. H. (1961). Tie Requirements for Reinforced Concrete Columns. *ACI Journal Proceedings*, 58(11), 555-570.
- Brown, J., & Kunnath, S. K. (2004). Low-Cycle Fatigue Failure of Reinforcing Steel Bars. *ACI Materials Journal*, 101(6), 457-466.
- Campbell, K. W., & Bozorgnia, Y. (2014). NGA-West2 Ground Motion Model for the Average Horizontal Components of PGA, PGV, and 5% Damped Linear Acceleration Response Spectra. *Earthquake Spectra*, 30(3), 1087-1115.
- Chai, Y. H., & Elayer, D. T. (1999). Lateral stability of reinforced concrete columns under axial reversed cyclic tension and compression. *ACI Structural Journal*, 96(5), 780-789.
- Chakrabarty, J. (2006). *Theory of plasticity* (3rd ed.). Amsterdam: Elsevier Butterworth-Heinemann.
- Chiou, B. S. J., & Youngs, R. R. (2014). Update of the Chiou and Youngs NGA Model for the Average Horizontal Component of Peak Ground Motion and Response Spectra. *Earthquake Spectra*, 30(3), 1117-1153.
- Chu, T. C., Ranson, W. F., Sutton, M. A., & Peters, W. H. (1985). Applications of Digital-Image-Correlation Techniques to Experimental Mechanics. *Experimental mechanics*, 25(3), 232-244.
- Ciampi, V., & Carlesimo, L. (1986). *A nonlinear beam element for seismic analysis of structures*. Paper presented at the 8th European Conference on Earthquake Engineering, Lisbon.
- Clarke, M. J., & Hancock, G. J. (1990). A Study of Incremental Iterative Strategies for Nonlinear Analyses. *International Journal for Numerical Methods in Engineering*, 29(7), 1365-1391.
- Coleman, J., & Spacone, E. (2001). Localization issues in force-based frame elements. *Journal of Structural Engineering*, 127(11), 1257-1265.
- Considère, A. (1903). *Résistance à la compression du béton armé et du béton fretté*: Publications du journal le Genie civil.
- Correlated Solutions, I. (2009). Vic-2D. Columbia, South Carolina.
- Creagh, A., Acevedo, C., Moehle, J. P., Hassan, W., & Tanyeri, A. C. (2010). Seismic Performance of Concrete Special Boundary Element. Retrieved from <https://nees.org/education/for-students/reu-program/reu-archive>.
- Crisfield, M. A. (1981). A Fast Incremental-Iterative Solution Procedure That Handles Snap-Through. *Computers & Structures*, 13(1-3), 55-62.
- CSI. (2011). ETABS Nonlinear. Extended ThreeDimensional Analysis of Building Systems (Version 9.7.4). Berkeley, CA: Computers and Structures Inc.
- De Souza, R. M. (2000). *Force-based Finite Element for Large Displacement Inelastic Analysis of Frames*. (Ph.D.), University of California, Berkeley.
- Dhakal, R., & Maekawa, K. (2002). Modeling for Postyield Buckling of Reinforcement. *Journal of Structural Engineering*, 128(9), 1139-1147.
- Filippou, F. C. (2014). *Nonlinear Structural Analysis*: University of California, Berkeley.
- Filippou, F. C., & Fenves, G. L. (2004). Methods of analysis for earthquake-resistant design. In Y. Bozorgnia & V. V. & Bertero (Eds.), *Earthquake engineering - from engineering seismology to performance-based engineering*. Boca Raton, FL: CRC Press.

- Filippou, F. C., Popov, E. P., & Bertero, V. V. (1983). *Effects of bond deterioration on hysteretic behavior of reinforced concrete joints* (Report UCB/EERC-83/19). Retrieved from Berkeley:
- Gomes, A., & Appleton, J. (1997). Nonlinear cyclic stress-strain relationship of reinforcing bars including buckling. *Engineering Structures*, 19(10), 822-826.
- Haindl, M., Hube, M., & Arteta, C. A. (2015). *Seismic Performance Assessment of a Reinforced Concrete Shear Wall House*. Paper presented at the VII Congreso Nacional de Ingenieria Sismica, Bogota.
- Hancock, J., Bommer, J. J., & Stafford, P. J. (2008). Numbers of scaled and matched accelerograms required for inelastic dynamic analyses. *Earthquake Engineering & Structural Dynamics*, 37(14), 1585-1607.
- Huang, Y. N., Whittaker, A. S., Luco, N., & Hamburger, R. O. (2011). Scaling Earthquake Ground Motions for Performance-Based Assessment of Buildings. *Journal of Structural Engineering*, 137(3), 311-321.
- Hube, M. A., Marihuén, A., de la Llera, J. C., & Stojadinovic, B. (2014). Seismic behavior of slender reinforced concrete walls. *Engineering Structures*, 80, 377-388.
- Idriss, I. M. (2014). An NGA-West2 Empirical Model for Estimating the Horizontal Spectral Values Generated by Shallow Crustal Earthquakes. *Earthquake Spectra*, 30(3), 1155-1177.
- Jayaram, N., Lin, T., & Baker, J. W. (2011). A Computationally Efficient Ground-Motion Selection Algorithm for Matching a Target Response Spectrum Mean and Variance. *Earthquake Spectra*, 27(3), 797-815.
- Kent, D. C., & Park, R. (1971). Flexural Members with Confined Concrete. *Journal of the Structural Division*, 97(7), 1969-1990.
- Kunnath, S. K., Heo, Y., & Mohle, J. F. (2009). Nonlinear Uniaxial Material Model for Reinforcing Steel Bars. *Journal of Structural Engineering*, 135(4), 335-343.
- Lin, T., Harmsen, S. C., Baker, J. W., & Luco, N. (2013). Conditional Spectrum Computation Incorporating Multiple Causal Earthquakes and Ground-Motion Prediction Models. *Bulletin of the Seismological Society of America*, 103(2a), 1103-1116.
- Lin, T., Haselton, C. B., & Baker, J. W. (2013). Conditional spectrum-based ground motion selection. Part I: Hazard consistency for risk-based assessments. *Earthquake Engineering & Structural Dynamics*, 42(12), 1847-1865.
- Lowes, L. N., Lehman, D. E., Birely, A. C., Kuchma, D. A., Marley, K. P., & Hart, C. R. (2012). Earthquake response of slender planar concrete walls with modern detailing. *Engineering Structures*, 43, 31-47.
- Mander, J. B. (1984). *Seismic Design of Bridge Piers*. (Ph.D.), University of Canterbury, New Zealand. (Research Report No. 84-02)
- Mander, J. B., Priestley, M. J. N., & Park, R. (1988a). Observed Stress-Strain Behavior of Confined Concrete. *Journal of Structural Engineering*, 114(8), 1827-1849.
- Mander, J. B., Priestley, M. J. N., & Park, R. (1988b). Theoretical Stress-Strain Model for Confined Concrete. *Journal of Structural Engineering*, 114(8), 1804-1826.
- Markeset, G., & Hillerborg, A. (1995). Softening of Concrete in Compression - Localization and Size Effects. *Cement and Concrete Research*, 25(4), 702-708.
- Mau, S. T., & Elmabsout, M. (1989). Inelastic Buckling of Reinforcing Bars. *Journal of Engineering Mechanics-Asce*, 115(1), 1-17.

- Mazzoni, S., Hachem, M., & Sinclair, M. (2012). *An Improved Approach for Ground Motion Suite Selection and Modification for Use in Response History Analysis*. Paper presented at the 15th World Conference on Earthquake Engineering, Lisbon.
- McKenna, F., Fenves, G. L., Scott, M. H., & Jeremic, B. (2000). Open system for earthquake engineering simulation (OpenSees) (Version 2.4.3.). Berkeley, CA: Pacific Earthquake Engineering Research Center, University of California.
- Moehle, J. P. (1992). Displacement-Based Design of RC Structures Subjected to Earthquakes. *Earthquake Spectra*, 8(3), 403-428.
- Moehle, J. P. (2014). *Seismic design of Reinforced Concrete Buildings*. New York, NY: McGraw-Hill Professional.
- Moehle, J. P., & Cavanagh, T. (1985). Confinement Effectiveness of Crossties in RC. *Journal of Structural Engineering*, 111(10), 2105-2120.
- Moehle, J. P., & Deierlein, G. G. (2004). *A framework methodology for performance-based earthquake engineering*. Paper presented at the 13th World Conference on Earthquake Engineering, Vancouver.
- Moehle, J. P., Ghodsi, T., Hooper, J. D., Fields, D. C., & Gedhada, R. (2011). *Seismic design of cast-in-place concrete special structural walls and coupling beams: A guide for practicing engineers (IST GCR 11-917-11REV-1)*. Gaithersburg, MD.
- Mohd Yassin, M. H. (1994). *Nonlinear analysis of prestressed concrete structures under monotonic and cyclic loads*. Retrieved from
- Monti, G., & Nuti, C. (1992). Nonlinear Cyclic Behavior of Reinforcing Bars Including Buckling. *Journal of Structural Engineering*, 118(12), 3268-3284.
- Pan, B., Qian, K. M., Xie, H. M., & Asundi, A. (2009). Two-dimensional digital image correlation for in-plane displacement and strain measurement: a review. *Measurement Science & Technology*, 20(6), 1-17.
- Pantazopoulou, S. J. (1998). Detailing for reinforcement stability in RC members. *Journal of Structural Engineering*, 124(6), 623-632.
- Papia, M., & Russo, G. (1989). Compressive Concrete Strain at Buckling of Longitudinal Reinforcement. *Journal of Structural Engineering*, 115(2), 382-397.
- Papia, M., Russo, G., & Zingone, G. (1988). Instability of Longitudinal Bars in Rc Columns. *Journal of Structural Engineering*, 114(2), 445-461.
- Paultre, P., & Legeron, F. (2008). Confinement reinforcement design for reinforced concrete columns. *Journal of Structural Engineering*, 134(5), 738-749.
- Priestley, M. J. N., Calvi, G. M., & Kowalsky, M. J. (2007). *Displacement Based Seismic Design of Structures*. Pavia: IUSS Press.
- Priestley, M. J. N., & Park, R. (1987). Strength and Ductility of Concrete Bridge Columns under Seismic Loading. *ACI Structural Journal*, 84(1), 61-76.
- Raghunandan, M., & Liel, A. B. (2013). Effect of ground motion duration on earthquake-induced structural collapse. *Structural Safety*, 41, 119-133.
- Razvi, S. R., & Saatcioglu, M. (1989). Confinement of Reinforced Concrete Columns With Welded Wire Fabric. *ACI Structural Journal*, 86(S60), 615-623.
- Razvi, S. R., & Saatcioglu, M. (1999). Confinement model for high-strength concrete. *Journal of Structural Engineering*, 125(3), 281-289.
- Richart, F. E., Brandtzaeg, A., & Brown, R. L. (1929). *Failure of plain and spirally reinforced concrete in compression*. Retrieved from Urbana, IL:

- Rodriguez, M. E., Botero, J. C., & Villa, J. (1999). Cyclic stress-strain behavior of reinforcing steel including effect of buckling. *Journal of Structural Engineering*, 125(6), 605-612.
- Roy, H. E. H., & Sozen, M. A. (1965). Ductility of Concrete *Flexural Mechanics of Reinforced Concrete* (Vol. SP-12, pp. 213-224). Detroit: American Concrete Institute/ American Society of Civil Engineers.
- Saatcioglu, M., & Razvi, S. R. (1992). Strength and Ductility of Confined Concrete. *Journal of Structural Engineering*, 118(6), 1590-1607.
- Scott, B. D., Park, R., & Priestley, M. J. N. (1982). Stress-Strain Behavior of Concrete Confined by Overlapping Hoops at Low and High Strain Rates. *ACI Journal Proceedings*, 79(1), 13-27.
- Scott, M. H. (2011). Numerical integration options for the force-based beam-column element in OpenSees.
- Scott, M. H., & Fenves, G. L. (2006). Plastic hinge integration methods for force-based beam-column elements. *Journal of Structural Engineering*, 132(2), 244-252.
- Scott, M. H., & Fenves, G. L. (2010). Krylov Subspace Accelerated Newton Algorithm: Application to Dynamic Progressive Collapse Simulation of Frames. *Journal of Structural Engineering*, 136(5), 473-480.
- Scott, M. H., & Hamutçuoğlu, O. M. (2008). Numerically consistent regularization of force-based frame elements. *International Journal for Numerical Methods in Engineering*, 76(10), 1612-1631.
- Shah, S. P., & Sankar, R. (1987). Internal Cracking and Strain-Softening Response of Concrete under Uniaxial Compression. *ACI Materials Journal*, 84(3), 200-212.
- Sheikh, S. A. (1982). A Comparative Study of Confinement Models. *ACI Journal Proceedings*, 79(4).
- Sheikh, S. A., & Uzumeri, S. M. (1980). Strength and Ductility of Tied Concrete Columns. *Journal of the Structural Division-Asce*, 106(5), 1079-1102.
- Sheikh, S. A., & Uzumeri, S. M. (1982). Analytical Model for Concrete Confinement in Tied Columns. *Journal of the Structural Division-Asce*, 108(12), 2703-2722.
- Spacone, E., Filippou, F. C., & Taucer, F. F. (1996). Fibre Beam-Column Model for Non-Linear Analysis of R/C Frame: Part I. Formulation. *Earthquake Engineering and Structural Dynamics*, 25, 711-725.
- Sritharan, S., Beyer, K., Henry, R. S., Chai, Y. H., Kowalsky, M., & Bull, D. (2014). Understanding Poor Seismic Performance of Concrete Walls and Design Implications. *Earthquake Spectra*, 30(1), 307-334.
- Sutton, M. A., Orteu, J. J., & Schreier, H. W. (2009). *Image Correlation for Shape, Motion and Deformation Measurements: Basic Concepts, Theory and Applications*. New York, NY: Springer.
- Takahashi, S., Yoshida, K., Ichinose, T., Sanada, Y., Matsumoto, K., Fukuyama, H., & Suwada, H. (2013). Flexural Drift Capacity of Reinforced Concrete Wall with Limited Confinement. *ACI Structural Journal*, 110(1), 95-104.
- Vallenas, J. M., Bertero, V. V., & Popov, E. P. (1977). *Concrete confined by rectangular hoops and subjected to axial loads* (Report UCB/EERC-77/13). Retrieved from <http://nisee.berkeley.edu/elibrary/>
- Vamvatsikos, D., & Cornell, C. A. (2002). Incremental dynamic analysis. *Earthquake Engineering & Structural Dynamics*, 31(3), 491-514.

- Wallace, J. W., Massone, L. M., Bonelli, P., Dragovich, J., Lagos, R., Luders, C., & Moehle, J. P. (2012). Damage and Implications for Seismic Design of RC Structural Wall Buildings. *Earthquake Spectra*, 28(S1), S281-S299.
- Wallace, J. W., & Orakcal, K. (2002). ACI 318-99 provisions for seismic design of structural walls. *ACI Structural Journal*, 99(4), 499-508.
- Watson-Lamprey, J., & Abrahamson, N. A. (2006). Selection of ground motion time series and limits on scaling. *Soil Dynamics and Earthquake Engineering*, 26(5), 477-482.
- Welt, T., Massone, L., LaFave, J., D., L., McCabe, S., & Polanco, P. (2016). Confinement Behavior of Rectangular Reinforced Concrete Prisms Simulating Wall Boundary Elements. *Journal of Structural Engineering*.

Appendix A - Digital Image Correlation

The use of Digital Image Correlation (DIC) techniques in the field of structural testing is becoming popular among researchers. The main advantage of the technique is that it allows calculating complete surface displacement and strain fields of structural specimens under complex loading. These deformation fields might sometimes be difficult to infer from sensors positioned at discrete locations. For example, it would be cumbersome to reconstruct complete strain fields of a plate with a defect, under pure axial loading, from a discrete set of strains measurements recorded by means of adhered strain gauges. The fact that no sensors need to be attached to the specimen under testing is very convenient because avoids congestions and the possibility of instrument damage (or misreading) due to large deformations. One of the disadvantages of the DIC technique is that it might require complex camera setups with proper lightning conditions. These concepts are foreign to most structural engineering researchers and will require some trial-and-error for proper setup. Also, when the subject of testing deforms or moves out of a fixed plane (e.g. toward or away from a camera), an even more complex setup, with more than one camera, might be required to compensate for spurious displacement measurements due to apparent change in size of the object of interest. Real time estimations of strains and displacements using DIC are still under development because the algorithms used are based on iterative procedures that require some time to finish each calculation.

In this project, three different estimations of strains fields of a prismatic reinforced concrete structural element under pure compression are presented and compared to assess the accuracy of the DIC technique. Errors in strains field measurements from DIC are estimated and an attempt to correct them is described. Results showed that compressive strains measurements from DIC are in average approximately 150 to 200 $\mu\epsilon$ larger than those calculated with strains gages or inferred from localized displacement measurements.

A.1 Brief Summary of DIC Basic Principles

The DIC technique is performed using high resolution digital images taken during the loading evolution of a test specimen. For the pictures to be useful in a computer-aided deformation identification process, a random speckle pattern with high contrast (e.g. black speckles over white paint) has to be applied to the specimen. Evolution of this pattern, picture after picture, allows estimating displacements and strains on the specimen surface (**Figure A.1.1**) by means of a computer algorithm

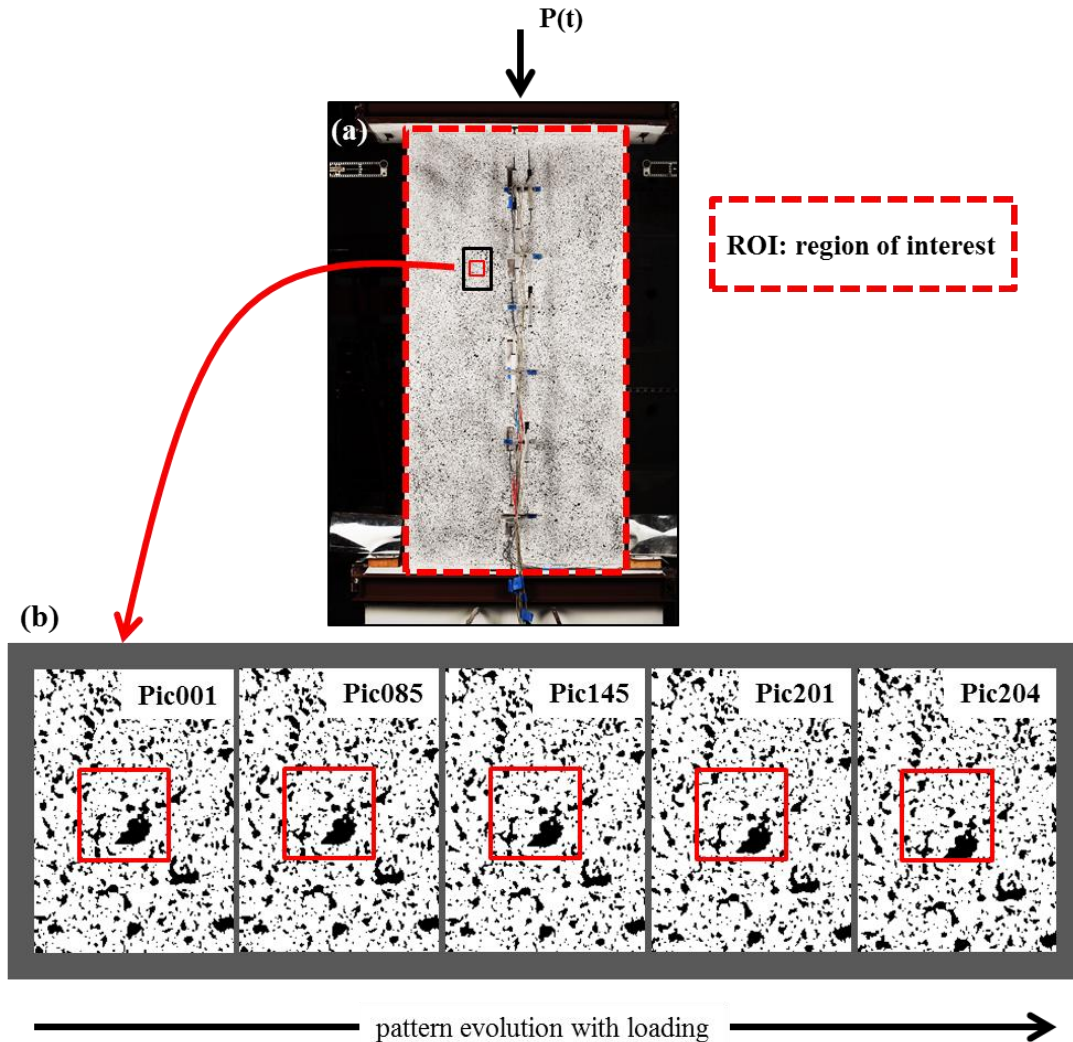


Figure A.1.1 - Evolution of a speckle pattern with loading: (a) prismatic specimen under pure compression prior to loading; (b) evolution of a speckle pattern with increasing compressive loading.

A.2 Displacement Field Estimation

In two-dimensional DIC, two consecutive images, called the “reference” and the “deformed” image are analyzed following these 7 steps to calculate a displacement field:

1. Capture gray scale, high resolution, properly focused, digital images of the specimen at two distinct instants for which deformations have occurred.
2. Divide a previously selected region of interest (ROI), like the portion with speckles on Figure 1a, into subsets of typically squared shape (could be any shape with a center point). These subsets can overlap to enhance resolution of results (at the expense of noise).
3. With an algorithm, measure and store discrete gray levels per pixel of each subset. This will assign a value from 0 to 255 to each pixel and the subset will be uniquely identified (**Figure A.2.1**).

- Fit a continuous gray-value surface (e.g. a polynomial fit) through the discrete values obtained in 3. This will allow achieving sub-pixel accuracy for displacement calculations (**Figure A.2.1**).

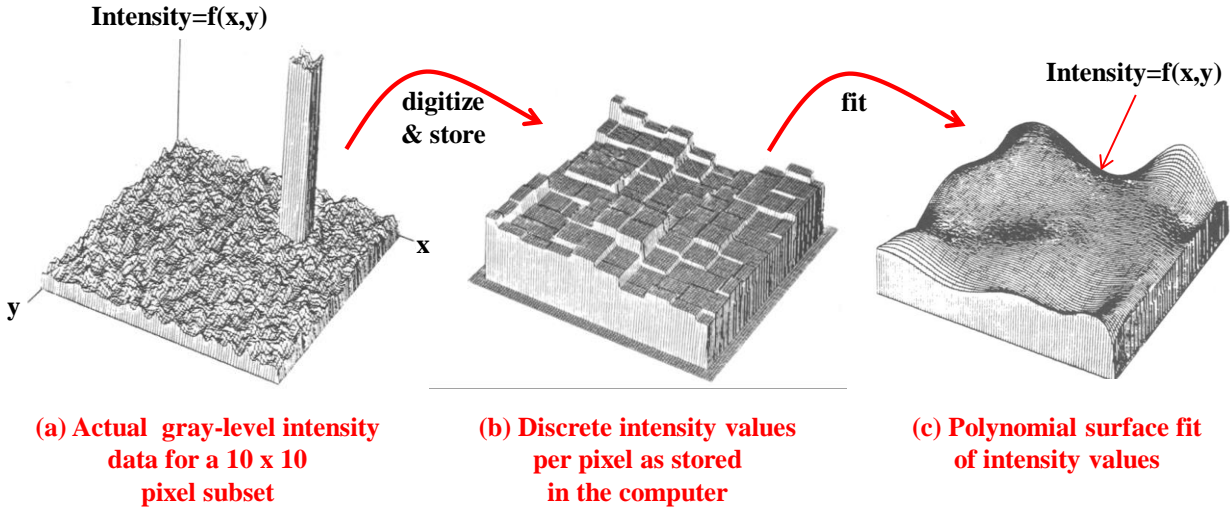


Figure A.2.1 - Subset gray-level intensities, discretization and polynomial fit (adapted from (Chu et al., 1985)).

- Track the points of each subset from the reference to the deformed image. To do so, the procedure described by Chu et al. (1985) could be followed. It is summarized here for the sake of clarity:

As shown in **Figure A.2.2**, consider the subset of interest centered at P in the reference image. In the deformed image, the subset center moves to P^* and the subset also deforms (translates, rotates, deforms in shear and in the two normal directions). The gray-level intensity values at P and P^* can be written as:

$$f(P) = f(x, y) \quad (\text{A.1})$$

$$f^*(P^*) = f^*[x + u(P), y + v(P)] \quad (\text{A.2})$$

Since the position of all points of the subset are of interest, for a point Q located in the reference image at $(x + dx, y + dy)$, the intensities at Q and Q^* can be written as:

$$f(Q) = f(x + dx, y + dy) \quad (\text{A.3})$$

$$f^*(Q^*) = f^*[x + u(Q) + dx, y + v(Q) + dy] \quad (\text{A.4})$$

where u and v are displacements in the x and y direction respectively. Now, assuming the intensity pattern deforms but does not change its local value (i.e. $f(Q) = f^*(Q^*)$):

$$f(P) = f[x + u(P), y + v(P)] \quad (\text{A.5})$$

$$f(Q) = f[x + u(Q) + dx, y + v(Q) + dy] \quad (\text{A.6})$$

Figure A.2.2 shows a subset centered at P before the deformation and centered a P* after it. Assuming the subset is sufficiently small and that straight lights remain straight after the deformation, the position of Q* can be described as:

$$\begin{aligned}
 Q^*(x^{**}, y^{**}) &= (x^* + dx^*, y^* + dy^*) = [x + u(P) + dx^*, y + v(P) + dy^*] \\
 &= [x + u(P) + \frac{\partial u}{\partial x} dx + \frac{\partial u}{\partial y} dy + dx, y + v(P) + \frac{\partial v}{\partial x} dx + \frac{\partial v}{\partial y} dy + dy] \quad (A.7)
 \end{aligned}$$

With **Equations (A.7)** and **(A.6)**, the intensity at Q* can be written as:

$$\begin{aligned}
 f^*[Q^*] &= \left[x + u(P) + \frac{\partial u}{\partial x}(P)dx + \frac{\partial u}{\partial y}(P)dy + dx, y + v(P) + \frac{\partial v}{\partial x}(P) + \frac{\partial v}{\partial y}(P)dy + dy \right] \quad (A.8)
 \end{aligned}$$

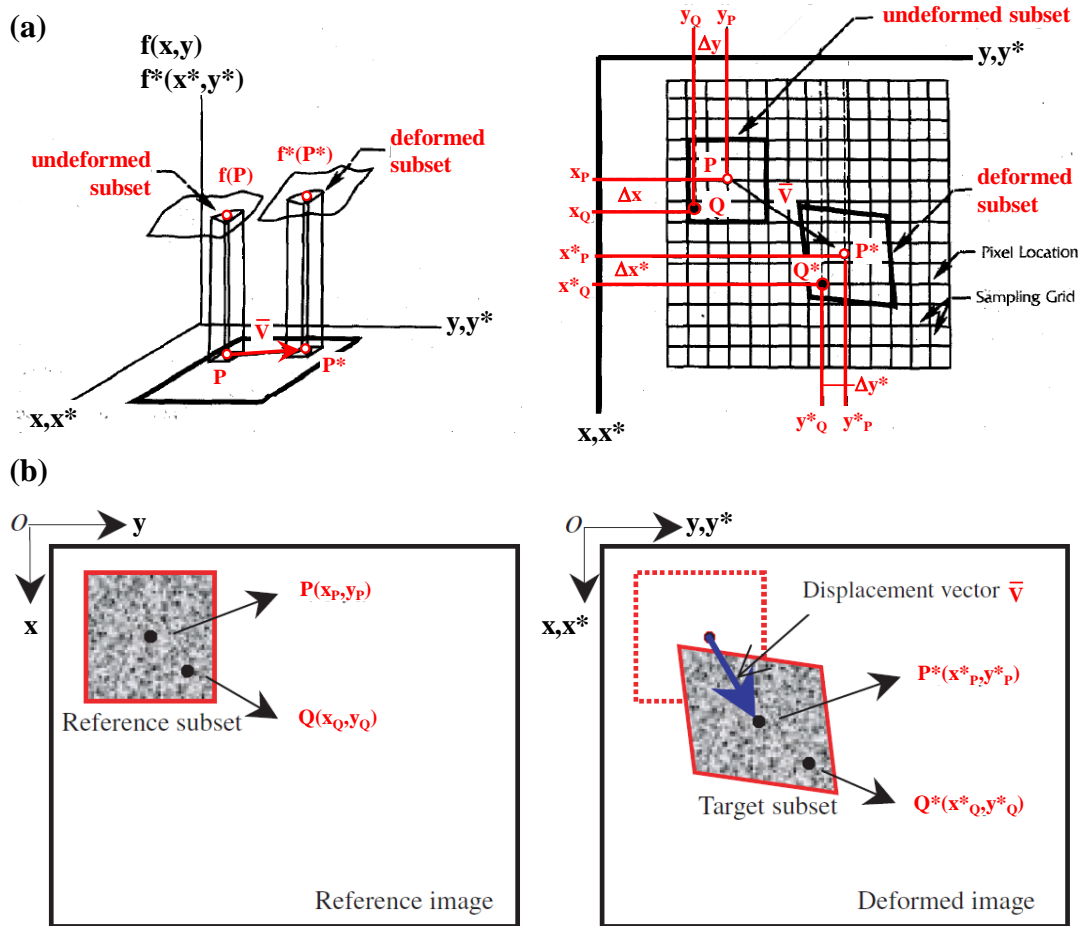


Figure A.2.2 - Reference subset before and after deformation ((a) adapted from Chu et al. (1985); (b) adapted from Pan et al. (2009)).

- Knowing the six variables of interest (SVI) $[u(P), v(P), \frac{\partial u}{\partial x}(P), \frac{\partial u}{\partial y}(P), \frac{\partial v}{\partial x}(P), \frac{\partial v}{\partial y}(P)]$ allows computing estimates of the position P* and all points Q*. The latter is the key for estimation of displacements by mean of DIC. The location estimation of P* and Q* is

done through an iterative process in which the SVI are estimated progressively. Different sets of the SIV are compared by using a cross-correlation coefficient, C (**Equation (A.9)**). The set of the SVI that maximize C, contains the local deformation values for a subset.

$$C\left(u, v, \frac{\partial u}{\partial x}, \frac{\partial u}{\partial y}, \frac{\partial v}{\partial x}, \frac{\partial v}{\partial y}\right) = \frac{\int_{\Delta M^*} f(x, y) f^*(x + \xi, y + \eta) dA}{\sqrt{\int_{\Delta M} [f(x, y)]^2 dA \int_{\Delta M^*} [f^*(x + \xi, y + \eta)]^2 dA}} \quad (\text{A.9})$$

where ΔM = subset in undeformed image, ΔM^* = subset in deformed image, $\xi = u + \frac{\partial u}{\partial x} \Delta x + \frac{\partial u}{\partial y} \Delta y$ and $\eta = v + \frac{\partial v}{\partial x} \Delta x + \frac{\partial v}{\partial y} \Delta y$.

7. Selected another subset and repeat the whole process again until the whole ROI is assessed.

A.3 Strain Field Estimation and Maximum Error

Research work related to the accurate estimation of strain measurements is scarce, arguably because it is thought that strains are readily available once the displacement field is estimated with the procedure described above ((Pan et al., 2009)). A full-field strain distribution can be obtained by means of numerical differentiation of the displacement estimations but this operation could lead to amplification of the noise contained in the displacement field (also explained by the noisy nature of the differentiation process). A procedure where the displacement field is smoothed prior to differentiation may be needed.

The latter can be justified with a simple example by defining strain as $\varepsilon = (\delta_{i+1} - \delta_i) / \Delta x$, where $(\delta_{i+1} - \delta_i)$ is the difference in the displacement (in pixels) between two adjacent subsets (i and i+1) and Δx is the distance between these two adjacent subsets (in pixels). For the purpose of error calculation, Δx is a constant without uncertainty, hence the error in strain can be as high as $\text{Error}(\varepsilon) = [\text{Error}(\delta_{i+1}) + \text{Error}(\delta_i)] / \Delta x$ where $\text{Error}(\delta)$ is the absolute value of the estimated error in displacements. For $\delta_{i+1} = \delta_i = \pm 0.02$ pixels and $\Delta x = 30$ pixels, $\text{Error}(\varepsilon) = [0.02 + 0.02] / 30 = 1333 \mu\varepsilon$. An error of this magnitude is around 45% of the maximum expected strain to be measured on the structural specimen of this appendix.

A.4 Instrumentation and Data Set Description

Available data sets for the test of specimen W7 (**Chapter 2**) are analyzed to attempt correcting problems in strain field calculations. **Figure A.4.1** shows instrumentation and test setup from the experiment. Applied load was measured by a built-in pressure capsule on top of a loading yoke. Average shortening of the specimen was measured by the relative displacement of the bottom and top head using potentiometric displacement transducers (PDT) in the North and South sides of the wall. In order to measure localized deformations, PDTs were mounted between threaded rods embedded in the test specimen and extending perpendicular to the East and West faces of the specimens, enabling measurement of relative displacements of different portions along the test specimen height. String potentiometric displacement transducers

(“wirepots”) were mounted on a distant reference wall in order to measure out-of-plane displacement at each load increment. Strains on the concrete surface on the West face were measured at five different locations along the height with concrete strain gauges (SGC). Digital images of the specimen were taken during the evolution of the test using a high resolution camera located. The camera faced the West surface of the specimen which had a random speckle pattern as shown in **Figure A.1.1**.

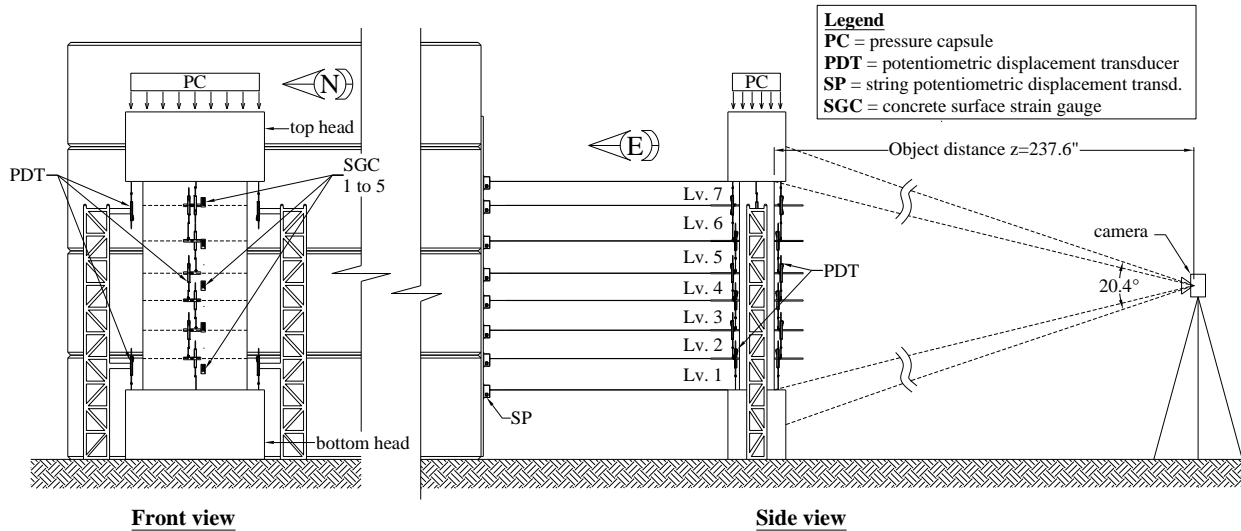


Figure A.4.1 - Instrumentation setup for DIC.

Figure A.4.2 shows states of increasing loading in pure compression for the prismatic element. Displacement and strain fields were estimated over 204 images using the commercial computer program Vic-2D (Correlated Solutions, 2009) which applies a form of the procedure described in Appendix Section A.2. Image 1 was taken at the state of zero loading while Image 204 was taken just after the peak load was attained which also corresponds to the first observation of concrete cover crushing (see top of **Figure A.4.2**). The images are synchronized with the rest of the measurements from the instruments described above to ensure accuracy of the comparisons as the test evolved.

For the purpose of this project, DIC strain fields will be compared with two reference measurements of strains that are believed to represent a more accurate state of strains on the specimen:

- **SGC-strains:** strain fields extrapolated from five concrete strain gages adhered discretely along the surface of the specimen (**Figure A.4.3**).
- **PDT-strains:** average strains extrapolated from localized displacements measured at seven different levels along the height of the specimen (**Figure A.4.3**). The strains calculated from PDTs on the first and seventh level (see **Figure A.4.1** for a reference) will be disregarded because they are biased high due to improper interaction with the boundaries.

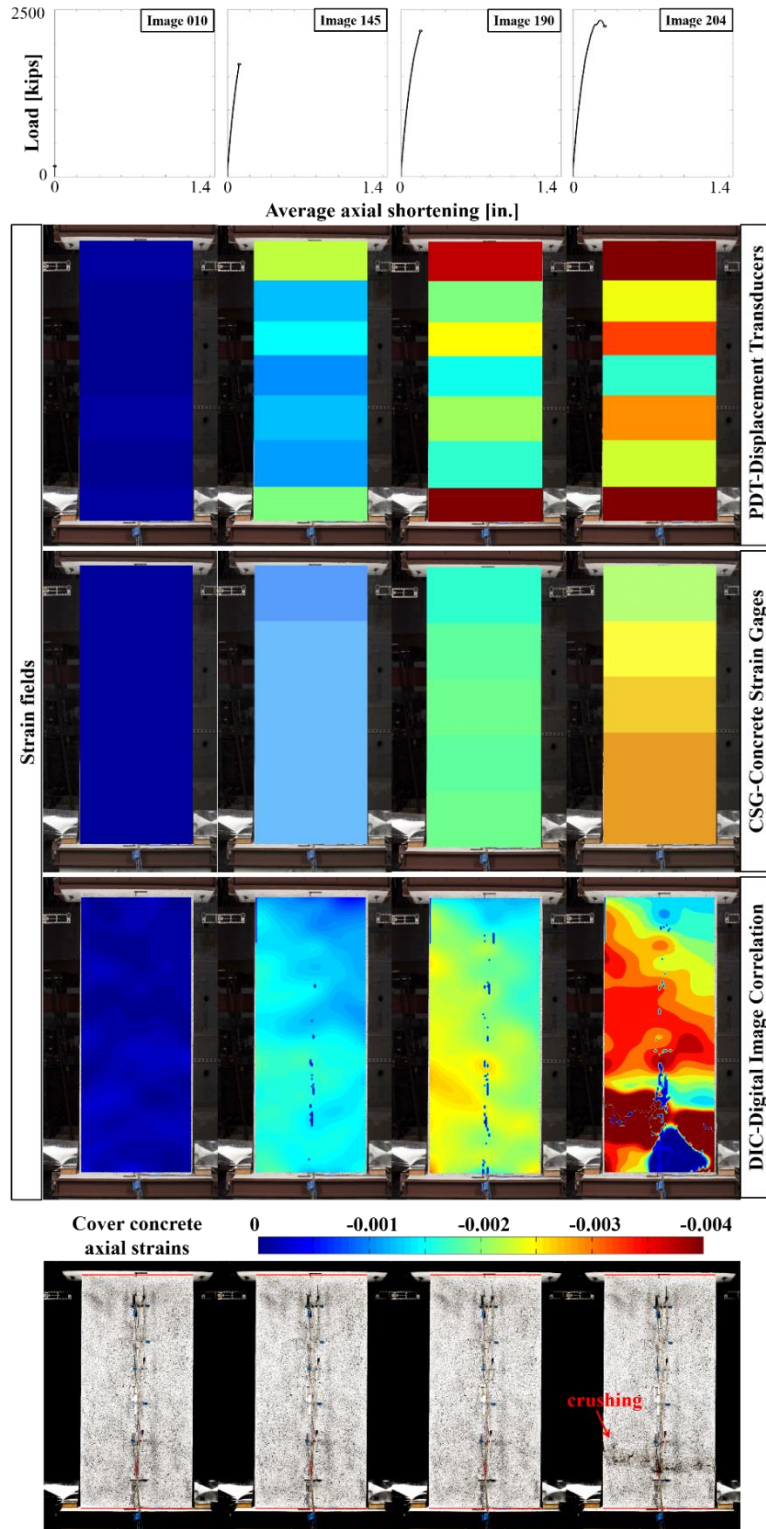


Figure A.4.2 - Test evolution and comparison of axial strains (ϵ_{yy}) from displacement transducers, concrete strain gages and DIC.

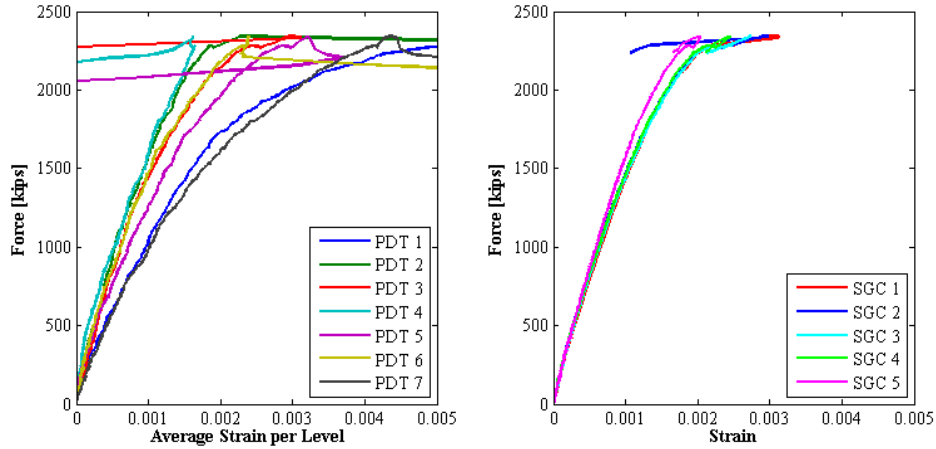


Figure A.4.3 - Load-strain relations for the PDT-strain data set (left) and the SGC-strain data set (right) (in this figures, positive strains are compression).

A.5 DIC-strains and Out-of-plane Correction

From **Figure A.4.2** it is apparent that DIC axial strains (ϵ_{yy}) are smaller than those from SGC-strains and PDT-strains. This strain error will be estimated and an attempt for its correction will be presented in the following sections of this document. Only strains in the axial direction will be analyzed because the reference discrete strains are measured in the vertical direction. It is believed that the source of error is, in part, due to out-of-plane displacement of the tested specimens which creates a false reduction of strains. The rest of the error will be analyzed using standard statistical practices.

Figure A.5.1a depicts out-of-plane displacements of the structural specimen for different loading values. Negative displacements (Δz) are in the direction away from the camera (to the East). Prior to analyzing the error between DIC strains and SGC-strains and/or PDT-strains, a correction for the DIC set will be introduced according to **Equation (A.10)** (Sutton et al., 2009):

$$\begin{aligned} \epsilon_{yyDIC,1} &= \epsilon_{yyDIC,0} + \Delta\epsilon_{yy} \\ \Delta\epsilon_{yy} &= \frac{\partial v}{\partial y} \approx - \left[\frac{\Delta z}{z} \right] \end{aligned} \quad (\text{A.10})$$

where $\epsilon_{yyDIC,1}$ are the strains corrected for out-of-plane displacement and $\epsilon_{yyDIC,0}$ are the original strains obtained from Vic-2D; z is the location of the face of the specimen with respect to the camera lens and Δz is the out-of-plane displacement of the specimen. Movements away from the camera are negative because, optically, these artificially shorten the specimen, generating spurious compressive normal strains ϵ_{yy} . The negative sign in the expression is meant for correcting the error.

The correction of **Equation (A.10)**, depicted in **Figure A.5.1b**, is applied to the DIC strain field at discrete levels (151 total) of the ROI because the field is stored in matrix format analogous to the geometry of the surface (i.e. the strain value stored at 1,1 correspond to the top left portion of the specimen). For the discrete DIC strains at each level, the correction is constant because the out-of-plane displacement is only measured along the axis of the specimen; therefore, extrapolations to the sides are equal to the recorded displacement. **Figure A.5.2** presents the DIC-strain field before and after the correction due to out-of-plane displacements.

Though it is observed that the correction is only apparent at advanced stages of loading (e.g. Image No>190), the corrected DIC-strain set will be the one used in further calculations. Analyzing the strain field of an image at the verge of crushing, such as Image 203, one can observe that maximum average out-of-plane corrections are in the order of $430 \mu\epsilon$ (see **Figure A.5.1b**). This corresponds to approximately 13% of the median strain level of that picture. For early pictures, such as Image 010, the correction is negligible.

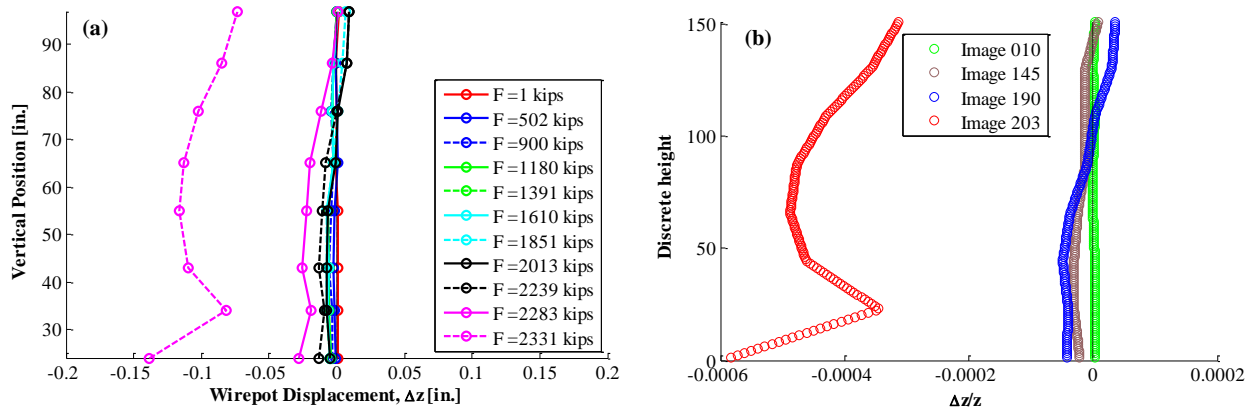


Figure A.5.1 – Out-of-plane evolution of specimen W7. (a) out-of-plane displacement at different loading values; (b) strain correction due to out-of-plane displacement.

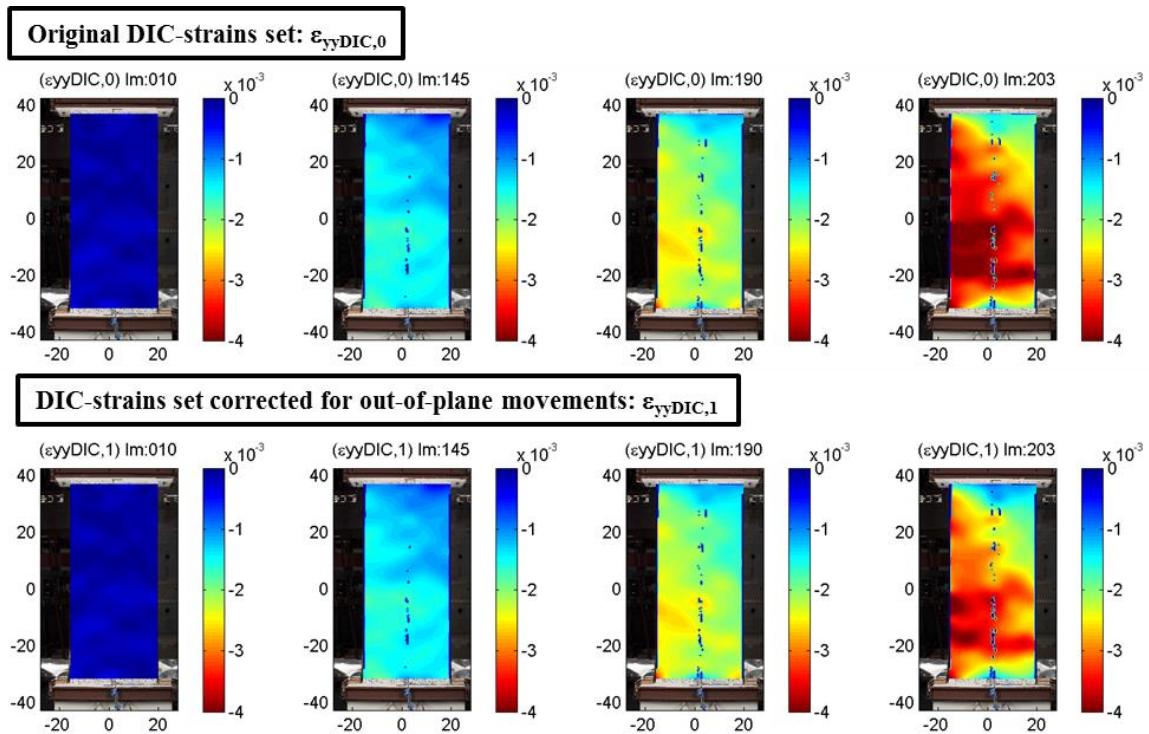


Figure A.5.2 - Comparison of DIC-strains before and after out-of-plane corrections.

A.6 DIC-strains Error Estimation

Errors in strain measurements are calculated for the two pairs of data sets of interest following **Equations (A.11)** and **(A.12)**:

$$\delta_{CSG} = \varepsilon_{yyDIC,1} - \varepsilon_{yyCSG} \quad (\text{A.11})$$

$$\delta_{PDT} = \varepsilon_{yyDIC,1} - \varepsilon_{yyPDT} \quad (\text{A.12})$$

where ε_{yyCSG} are the CSG-strains and ε_{yyPDT} are the PDT-strains; δ_{CSG} and δ_{PDT} are the errors from comparing the DIC-strains with CSG-strains and PDT-strains respectively.

Strain field error estimations are presented in **Figure A.6.1** for the two data sets. For low to moderate levels of loading (e.g. $010 < \text{Image No.} < 190$), the strain errors are constrained in the range $\pm 500 \mu\varepsilon$. These values are considered high given that the maximum expected strain before crushing is around $-3000 \mu\varepsilon$ (average value obtained from uniaxial stress-strain tests on concrete cylinders).

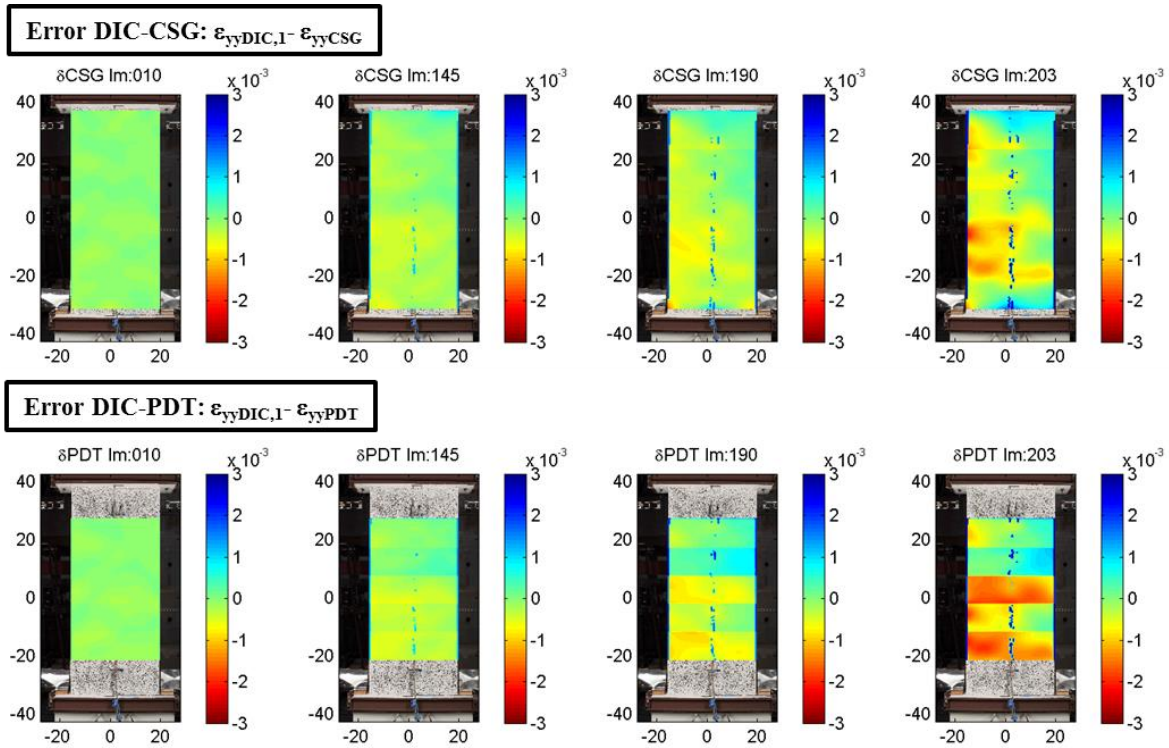
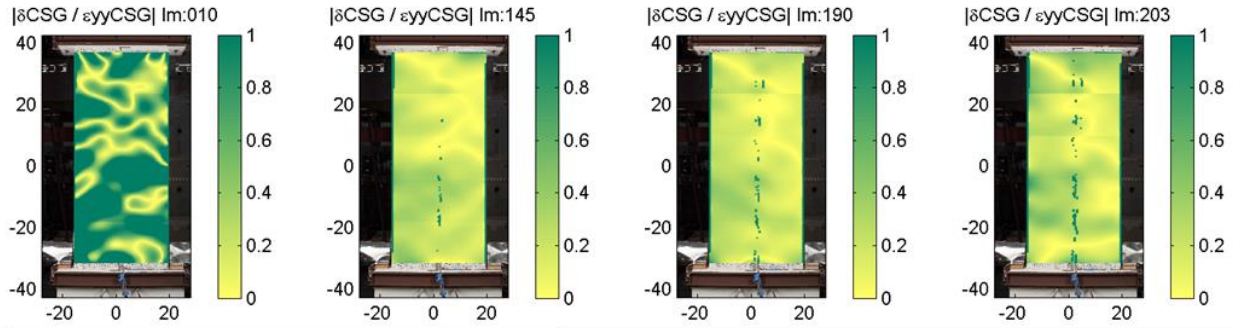


Figure A.6.1 - DIC error estimation.

Figure A.6.2 presents absolute values of relative errors defined as $\delta rel_i = |(\varepsilon_{yyDIC,1} - \varepsilon_{yyi}) / \varepsilon_{yyi}|$, where the subscript i relates to CSG-strains or PDT-strains measurements. **Figure A.6.3**, depicts median level of relative errors as they evolve with the average shortening of the specimen. This median value is a statistic representing all strain values stored per image without regard of their spatial position. Median relative errors are as high as 150% at early loading states and as low as 16%.

Rel. Error DIC-CSG: $|(\epsilon_{yyDIC,1} - \epsilon_{yyCSG}) / \epsilon_{yyCSG}|$



Rel. Error DIC-PDT: $|(\epsilon_{yyDIC,1} - \epsilon_{yyPDT}) / \epsilon_{yyPDT}|$

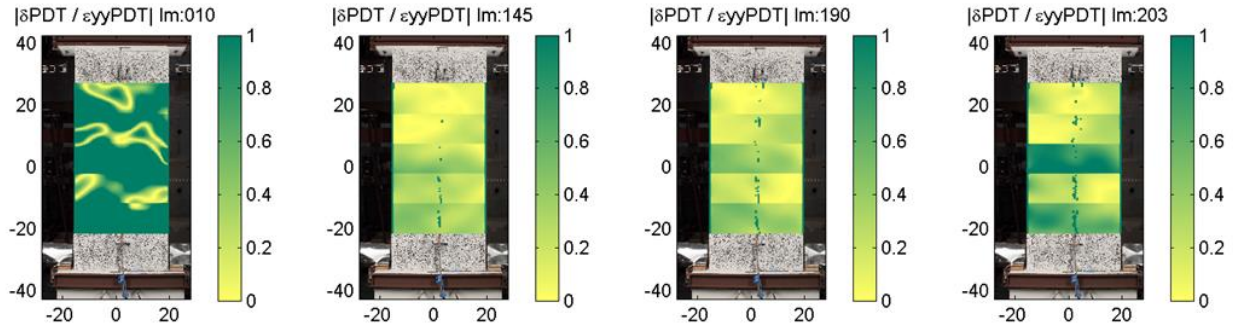


Figure A.6.2 - DIC relative error estimation.

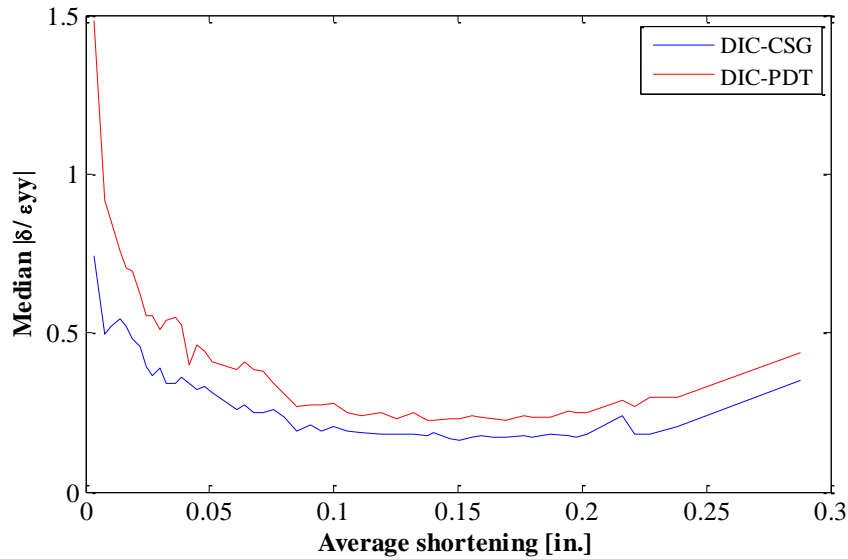


Figure A.6.3 - Median relative error evolution with average shortening of the specimen.

A.7 An Attempt to Correct for DIC-errors

The purpose of the following calculations is to find a single correction number for all strains values of all images. It is recognized that this proposal will not solve the discrepancy in space and in time between measured (CSG and PDT) and estimated strains (DIC) but given the complexity of the problem it is a good starting point for future research work related to the

sources of error in DIC strain estimation. **Figure A.7.1** shows the histograms and the empirical cumulative distribution functions (ECDF) of all the strain errors (per image and in time) estimated using **Equations (A.11)** and **(A.12)**. Their median value is used as the best estimate of error correction. For the case of DIC-strains versus CSG-strains, adding $169 \mu\epsilon$ to the DIC estimates (after correcting for out-of-plane displacement) would be the simplest correction. Adding $179 \mu\epsilon$, would be the correction for comparing DIC-strains versus PDT-strains.

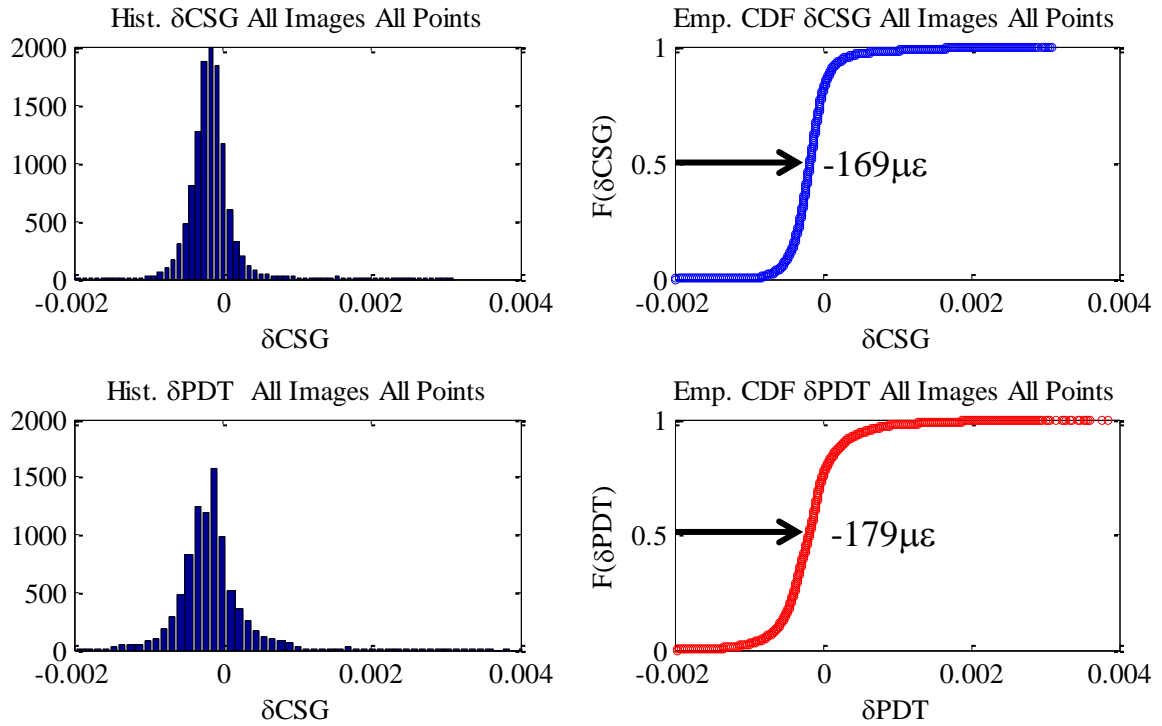


Figure A.7.1 - Strain errors correction estimates.

Figure A.7.2 compares CSG-strain fields with DIC-strain fields after out-of-plane and median error correction. Though DIC corrected strains do not match exactly those from the CSG, the improvement in the strain field is apparent. **Figure A.7.3** depicts the overall reduction in error by showing lower values of median relative errors at intermediate levels of deformation.

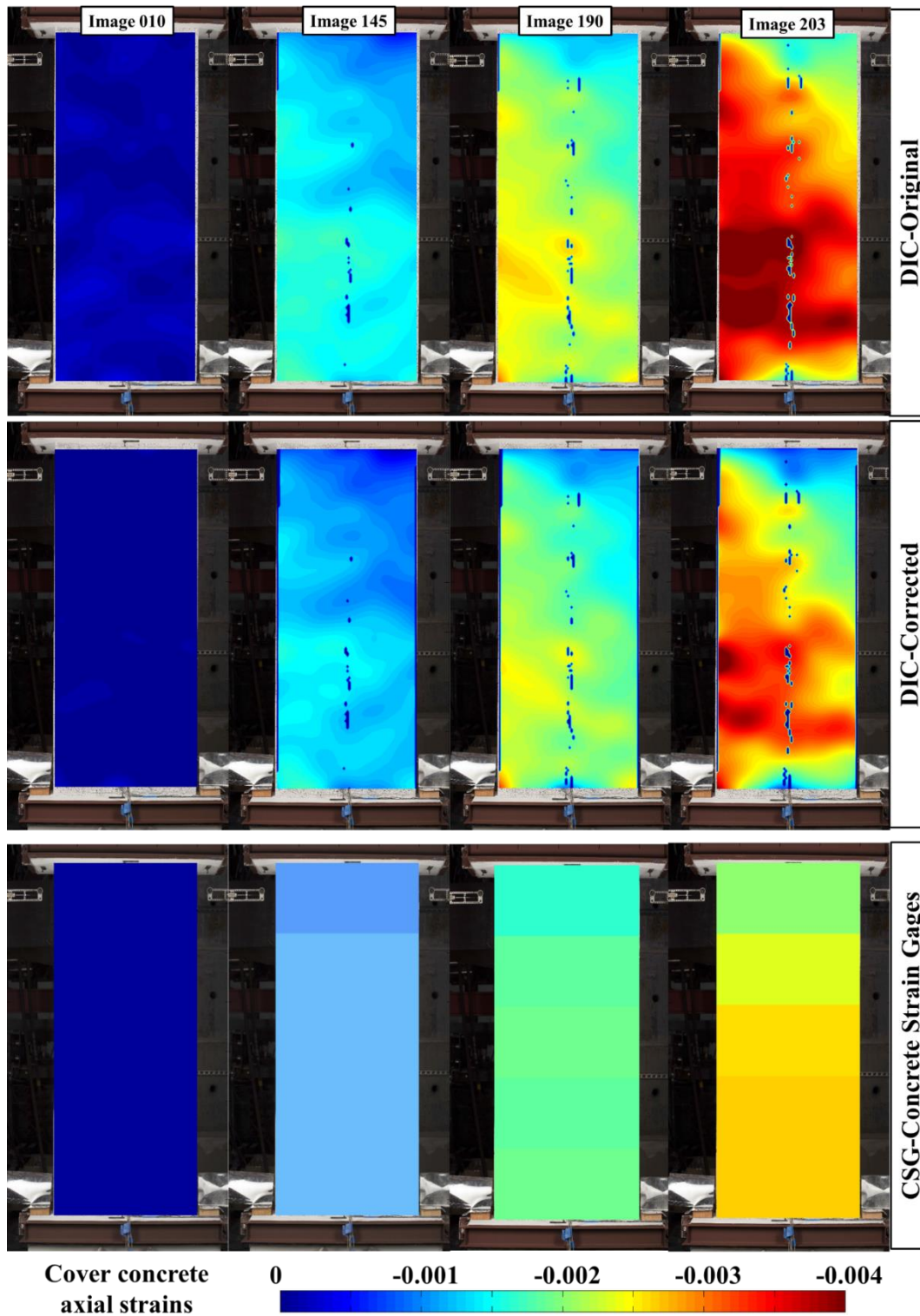


Figure A.7.2 - Comparison of original DIC-strain, corrected DIC-strains and CSG-strains..

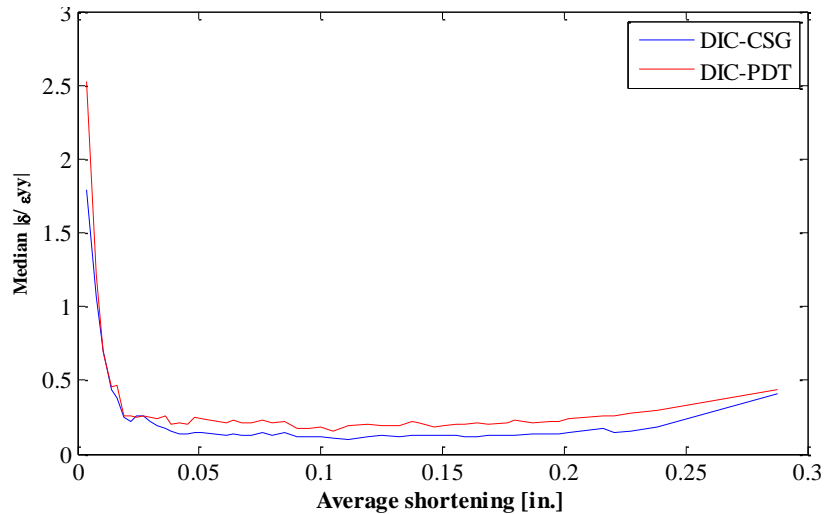


Figure A.7.3 - Median relative error evolution (after correction) with average shortening of the specimen.

A.8 Conclusions

Appendix A presented a case study of error estimation of the digital image correlation (DIC) technique used for structural testing of large specimens. Simple error assessment procedures indicate that median relative error between strain measurements recorded from standard instrumentation, such as concrete strain gages and displacement transducer, and those estimated via DIC can be as high as 150% and as low as 16% for low and intermediate levels of deformation respectively. A simple error correction procedure was presented showing low performance due to the complexity of error distribution in space. After the correction was applied to the DIC-strains set, relative errors at very low levels of deformation grew by 66% but at intermediate levels median relative errors were as low as 12%. More research is required in this area since it is believed that sharpness of the lenses and quality of the recording sensor might have an impact in the results obtained.

A.9 Acknowledgments

I wish to thank Dr. Clement Barthes at the PEER Earthquake Simulation Laboratory, for his support and guidance in developing this appendix. Support by the intern student Jorge Archbold in preparing some of the data set is much appreciated.

Appendix B - Inelastic bar buckling

This Appendix contains figures further describing the series of Tests summarized in **Table 3.2**. Specifically, a complete graphical description of Tests 28 to 34 is presented with the idea of understanding how different components of the model respond during the test evolution and with variation of the variables of interest. The tests comprise a 7/8 in. [22 mm] longitudinal bar under Tie Setup 2 (**Figure 3.16**), and various diameters of cross ties ($0 \leq d_{bt} \leq 7/8$).

Section B.1 presents the relationship between the bar average-axial-stress and the average-axial-strain, along with the evolution of the critical section (at mid span) tangent flexural stiffness $E_t I$ normalized by initial stiffness $E_o I$. The deformed shaped of the longitudinal bar at different levels of average axial strain ($U/L_o = 2, 5, 10$ and $30\varepsilon_y$) is shown as well. The lateral displacement w shown is normalized by bar diameter, d_b . The demand of the restraining tie close to mid height is shown in terms of its average axial stress-strain relationship. The bottom part of the figures of this section show distribution of response quantities along the length of the bar at $U/L_o = 30\varepsilon_y$. At this point all the cases present are at a buckled state. The response quantities shown include the lateral displacement with location of the restraining ties, axial local stress distribution, moment distribution long the length of the bar and local axial strain. **Section B.2** presents the evolution of the strain field of cross section at mid span of the longitudinal bars. The information is presented at the instants where $U/L_o = 1, 2, 5, 10$ and $30\varepsilon_y$. Also shown is the tangent modulus distribution, along with the normalized section tangent flexural stiffness $E_t I/E_o I$ at the aforementioned levels of average axial strain. Finally, **Section B.3** shows the history of the stress-strain relationship in the fibers of the critical section. The fibers that show strain reversal correspond to those close to the concave portion of the bar (to the right of the centroid of the cross section). The average axial stress-strain curves of the buckling tests, along with the average stress versus displacement w_{max} at midspan are presented in **Section B.4**. These set of figures constitute the main data source of the statistical analysis of the variables of interest, presented in **Section 3.4**.

B.1 Average Response, Tangent Modulus Evolution, Displaced Shape, Tie Demand and Axial Strain Distribution.

dbt 0''

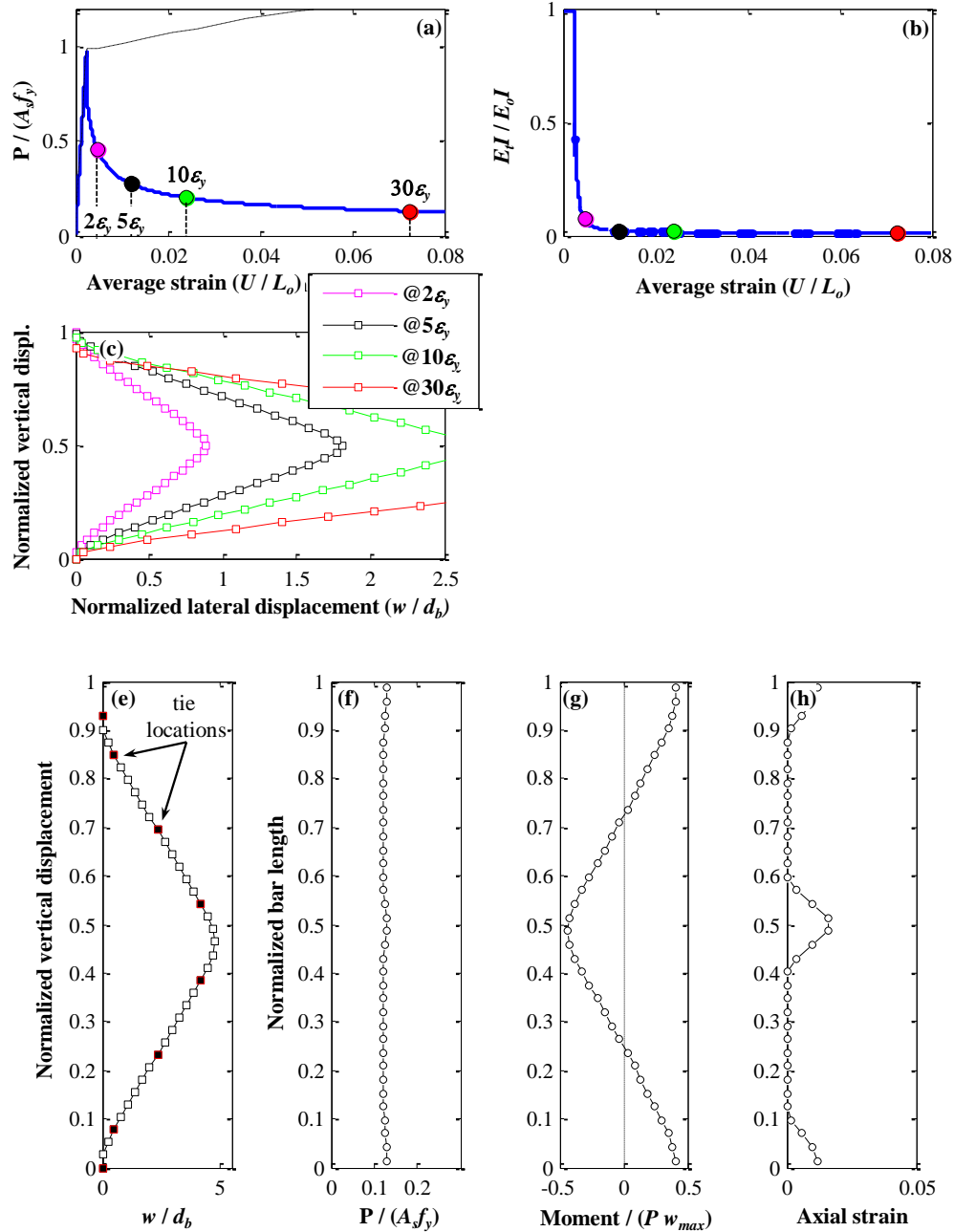


Figure B.1.1 – Test 28: (a) average response; (b) section stiffness evolution; (c) displaced shape. Distribution at $U/L_o = 30\epsilon_y$ of: (e) lateral displacement; (f) axial stress; (g) moment; and (h) axial strain.

dbt 1/4"

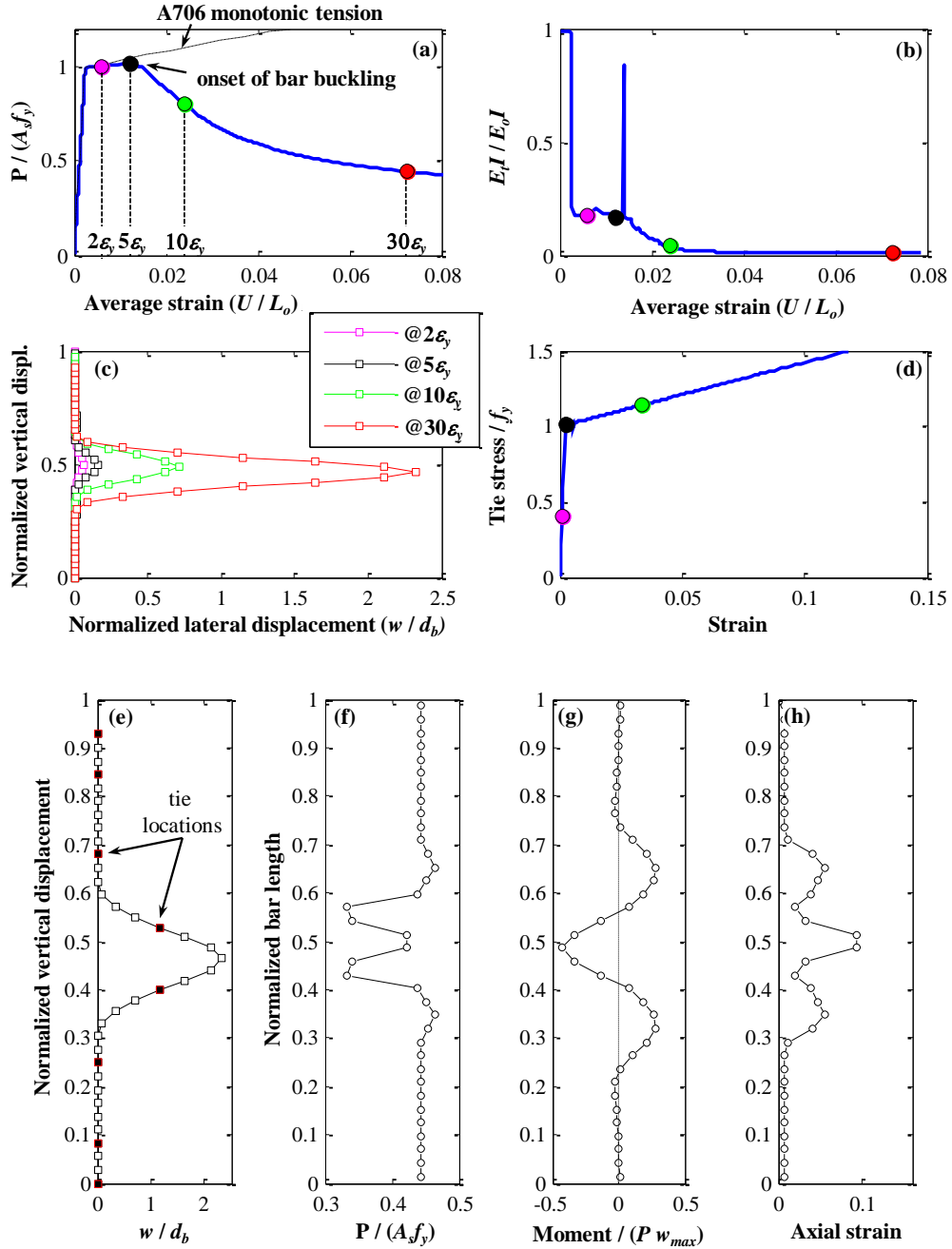


Figure B.1.2 – Test 30: (a) average response; (b) section stiffness evolution; (c) displaced shape; (d) tie response close to mid span. Distribution at $U/L_o = 30\epsilon_y$ of: (e) lateral displacement; (f) axial stress; (g) moment; and (h) axial strain.

dbt 3/8"

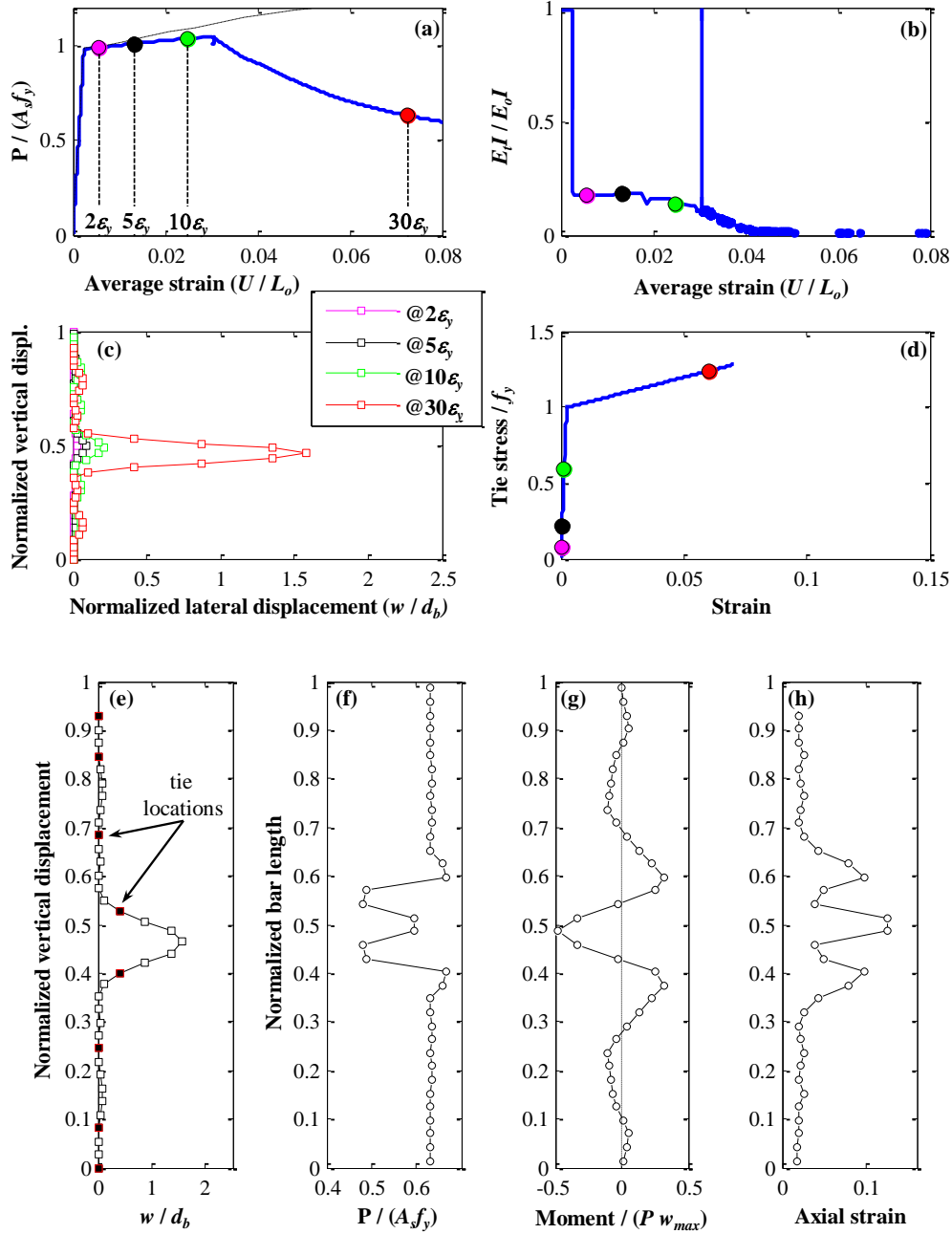


Figure B.1.3 – Test 31: (a) average response; (b) section stiffness evolution; (c) displaced shape; (d) tie response close to mid span. Distribution at $U/L_o = 30\varepsilon_y$ of: (e) lateral displacement; (f) axial stress; (g) moment; and (h) axial strain.

dbt 1/2"

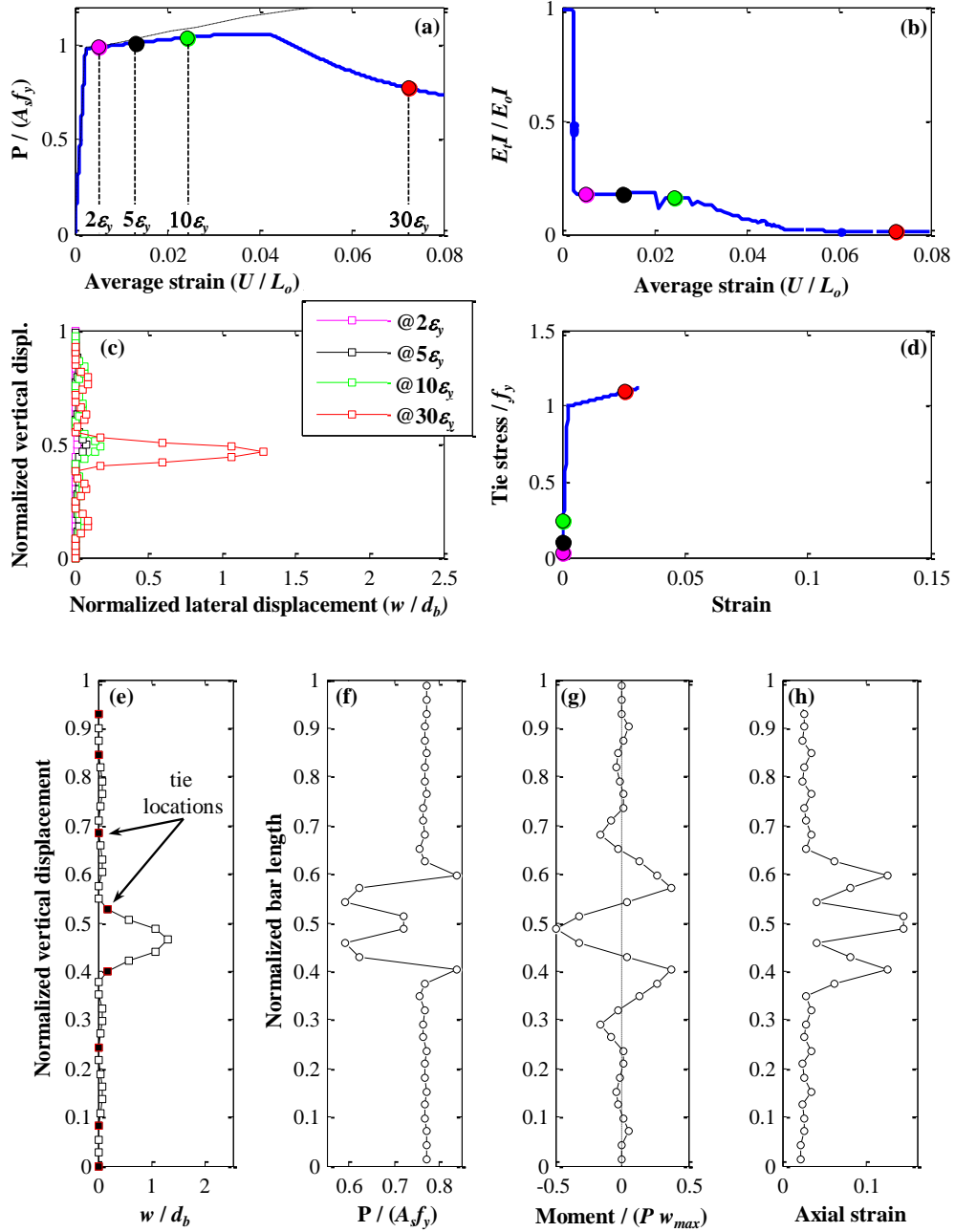


Figure B.1.4 – Test 32: (a) average response; (b) section stiffness evolution; (c) displaced shape; (d) tie response close to mid span. Distribution at $U/L_o = 30\varepsilon_y$ of: (e) lateral displacement; (f) axial stress; (g) moment; and (h) axial strain.

dbt 5/8"

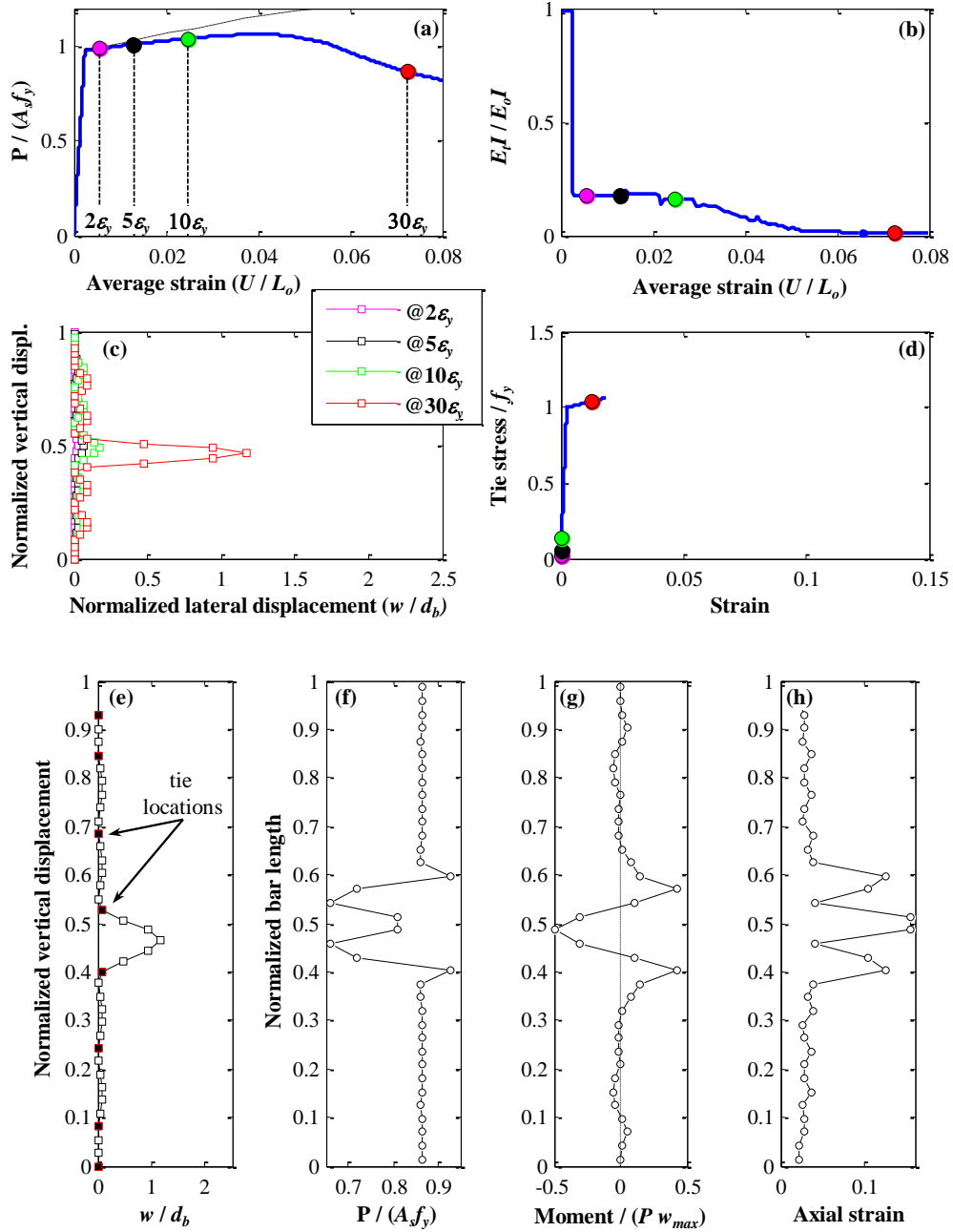


Figure B.1.5 – Test 33: (a) average response; (b) section stiffness evolution; (c) displaced shape; (d) tie response close to mid span. Distribution at $U/L_o = 30\epsilon_y$ of: (e) lateral displacement; (f) axial stress; (g) moment; and (h) axial strain.

dbt 3/4"

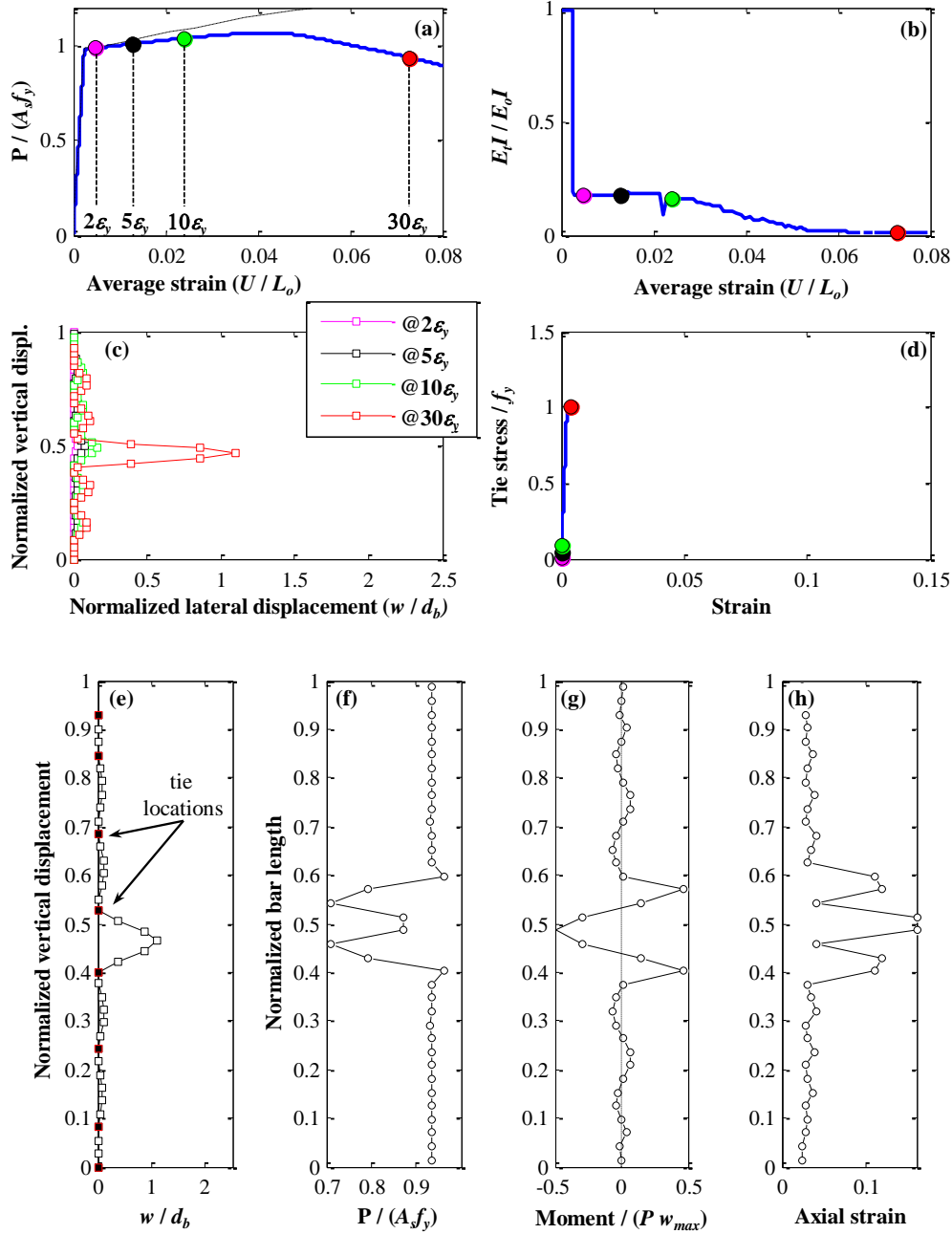


Figure B.1.6 – Test 34: (a) average response; (b) section stiffness evolution; (c) displaced shape; (d) tie response close to mid span. Distribution at $U/L_o = 30\epsilon_y$ of: (e) lateral displacement; (f) axial stress; (g) moment; and (h) axial strain.

dbt 7/8"

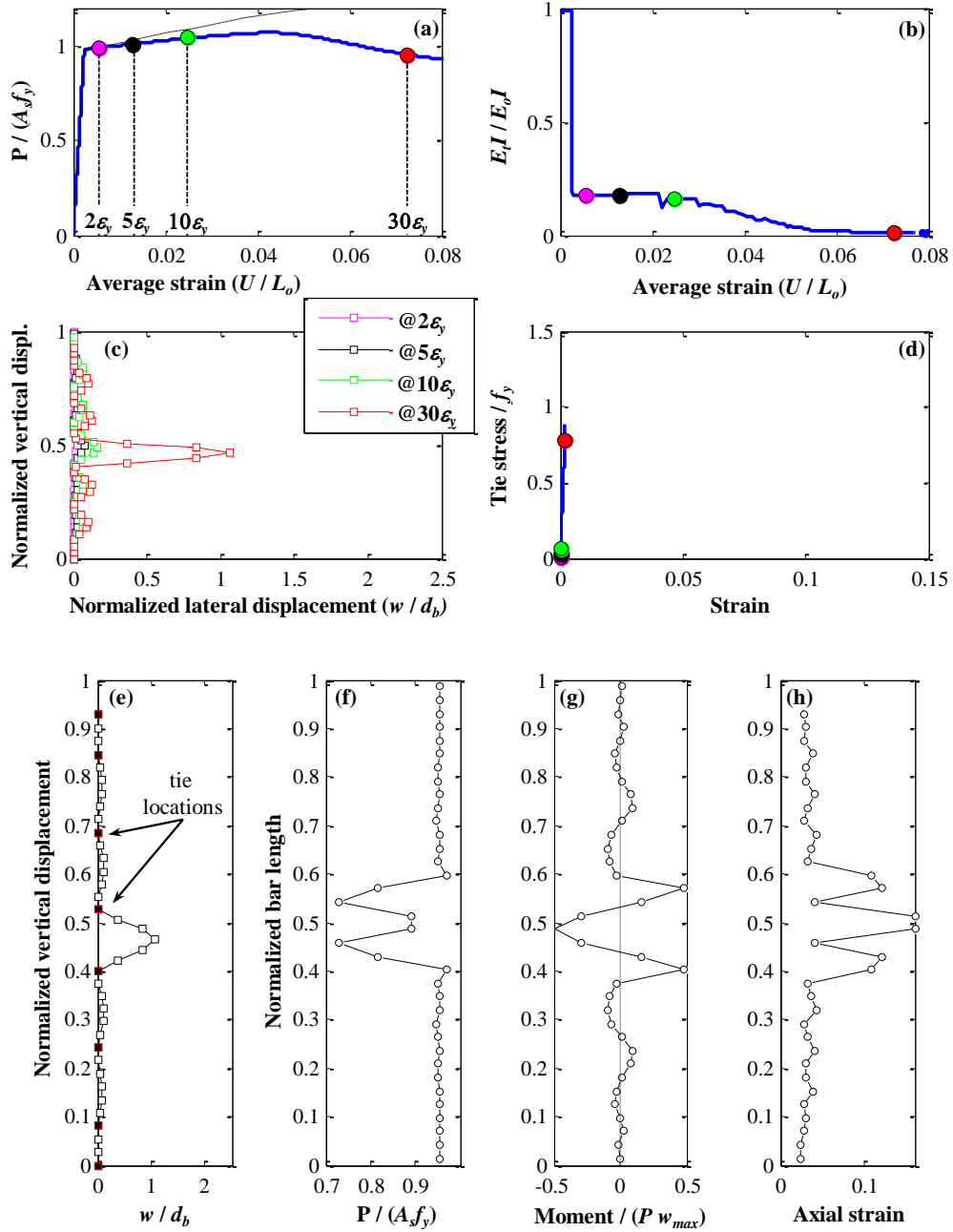


Figure B.1.7 – Test 35: (a) average response; (b) section stiffness evolution; (c) displaced shape; (d) tie response close to mid span. Distribution at $U/L_o = 30\epsilon_y$ of: (e) lateral displacement; (f) axial stress; (g) moment; and (h) axial strain.

B.2 Strain Field Evolution and Tangent Modulus Distribution

dbt 0''

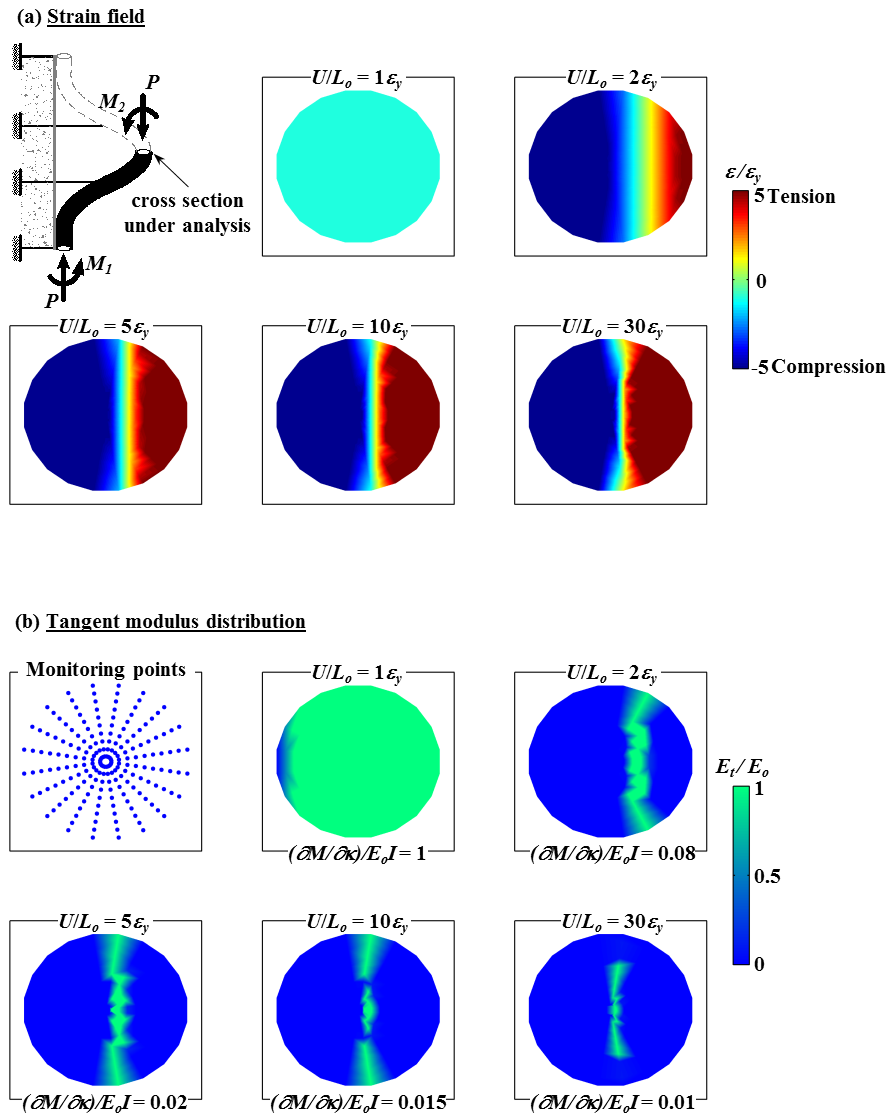


Figure B.2.1 – Test 28: (a) strain field evolution; (b) tangent modulus distribution evolution.

dbt 1/4"

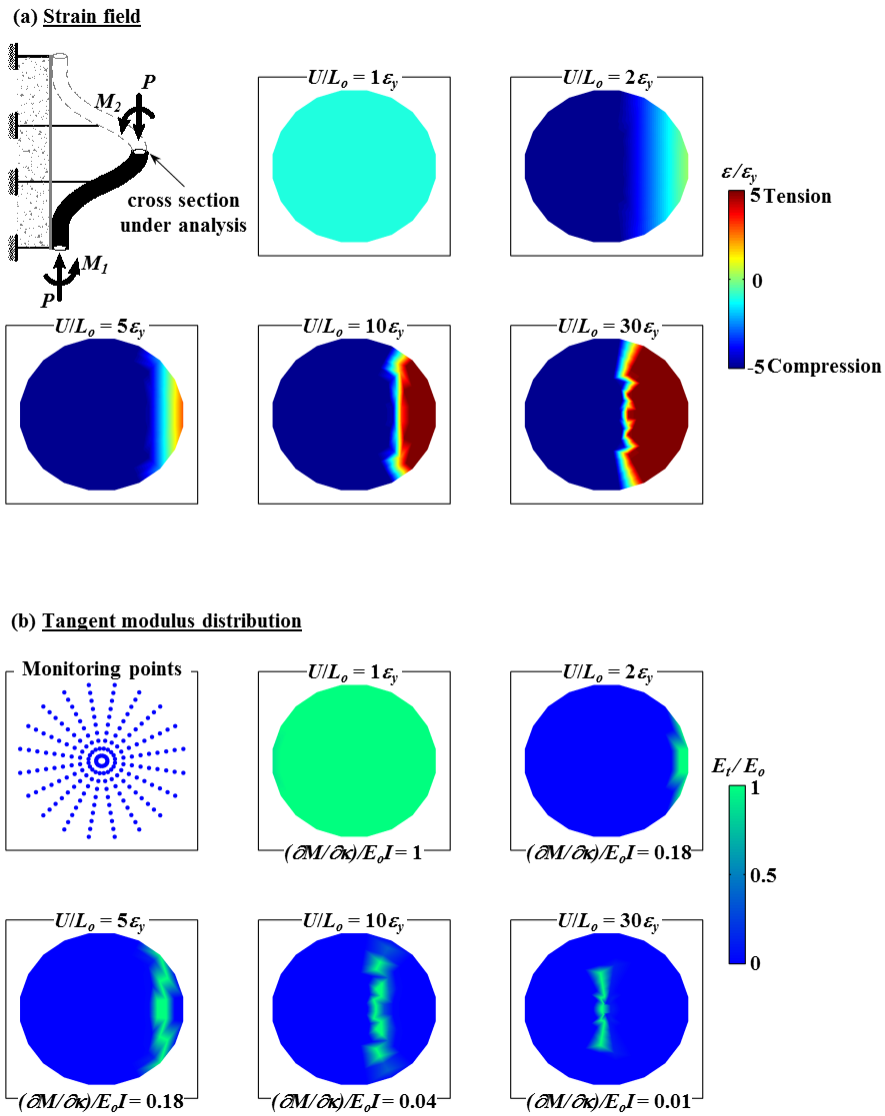


Figure B.2.2 – Test 29: (a) strain field evolution; (b) tangent modulus distribution evolution.

dbt 3/8"

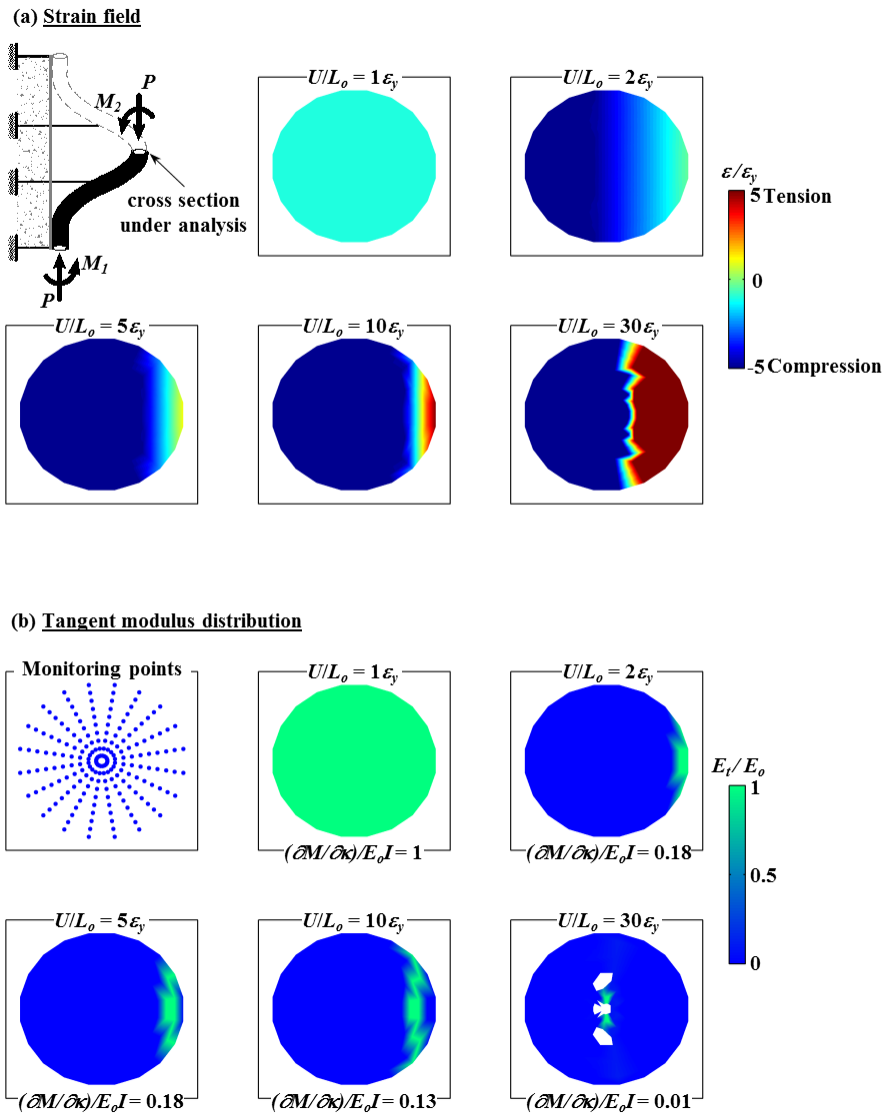


Figure B.2.3 – Test 30: (a) strain field evolution; (b) tangent modulus distribution evolution.

dbt 1/2"

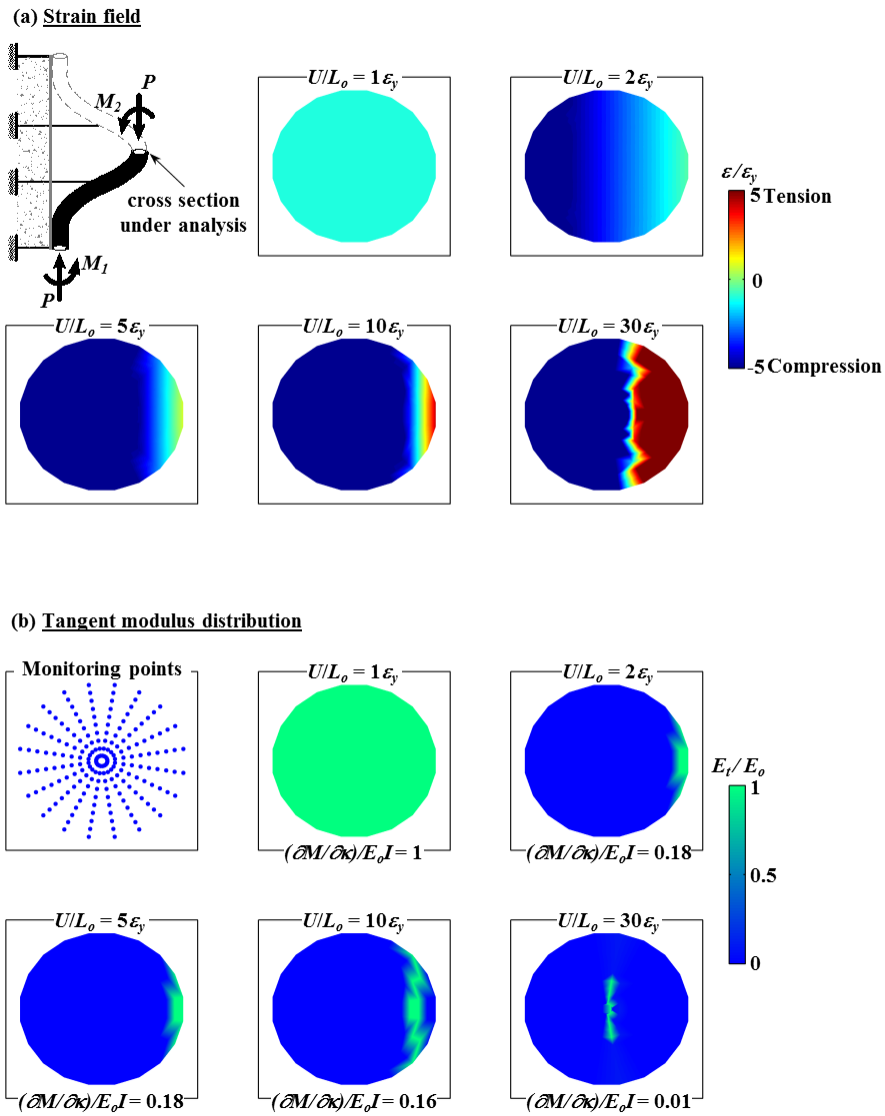
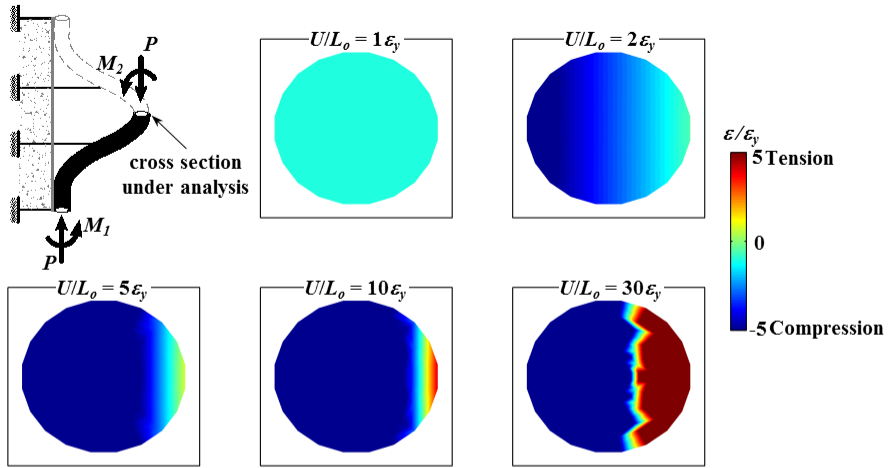


Figure B.2.4 – Test 31: (a) strain field evolution; (b) tangent modulus distribution evolution.

dbt 5/8"

(a) Strain field



(b) Tangent modulus distribution

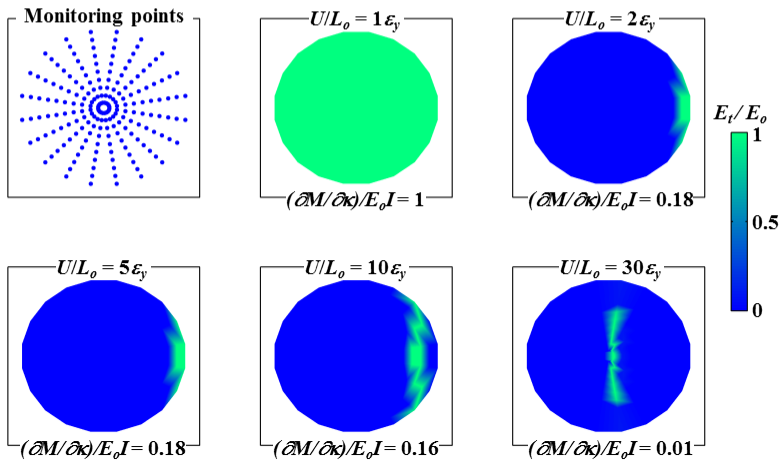


Figure B.2.5 – Test 32: (a) strain field evolution; (b) tangent modulus distribution evolution.

dbt 3/4"

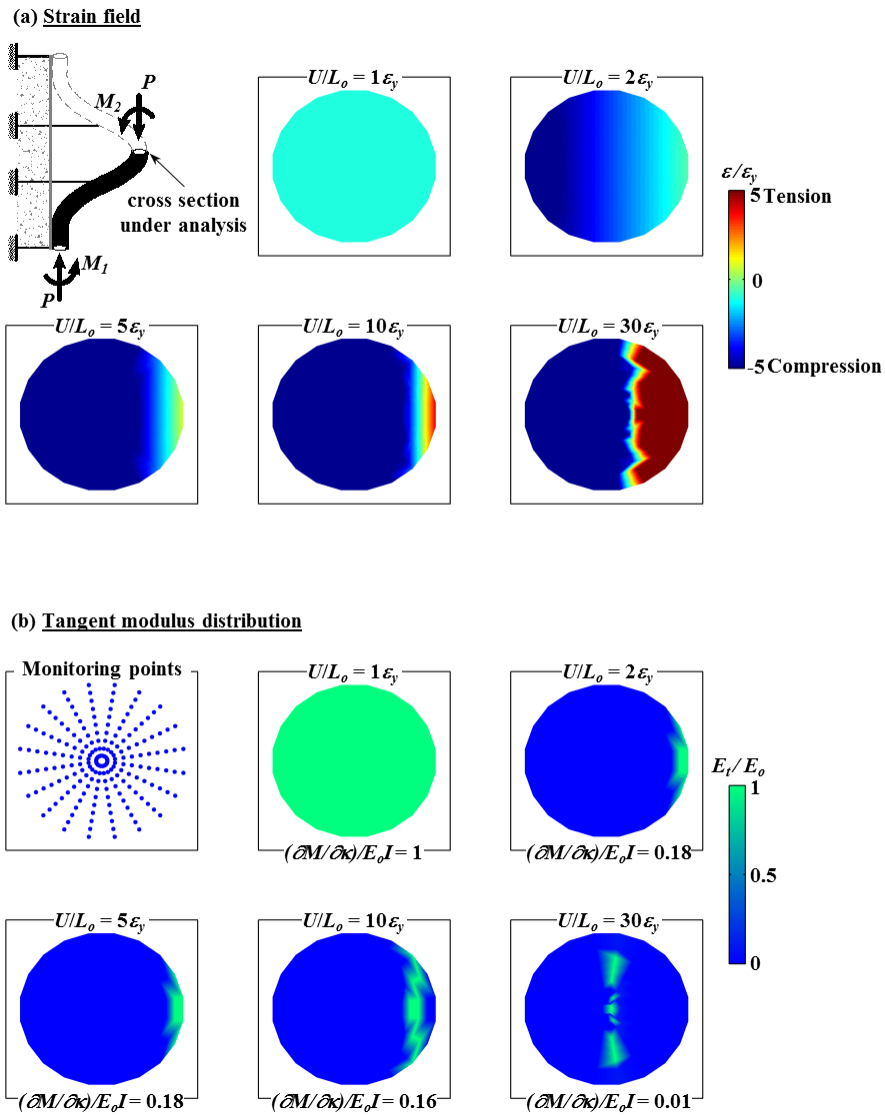


Figure B.2.6 – Test 33: (a) strain field evolution; (b) tangent modulus distribution evolution.

dbt 7/8"

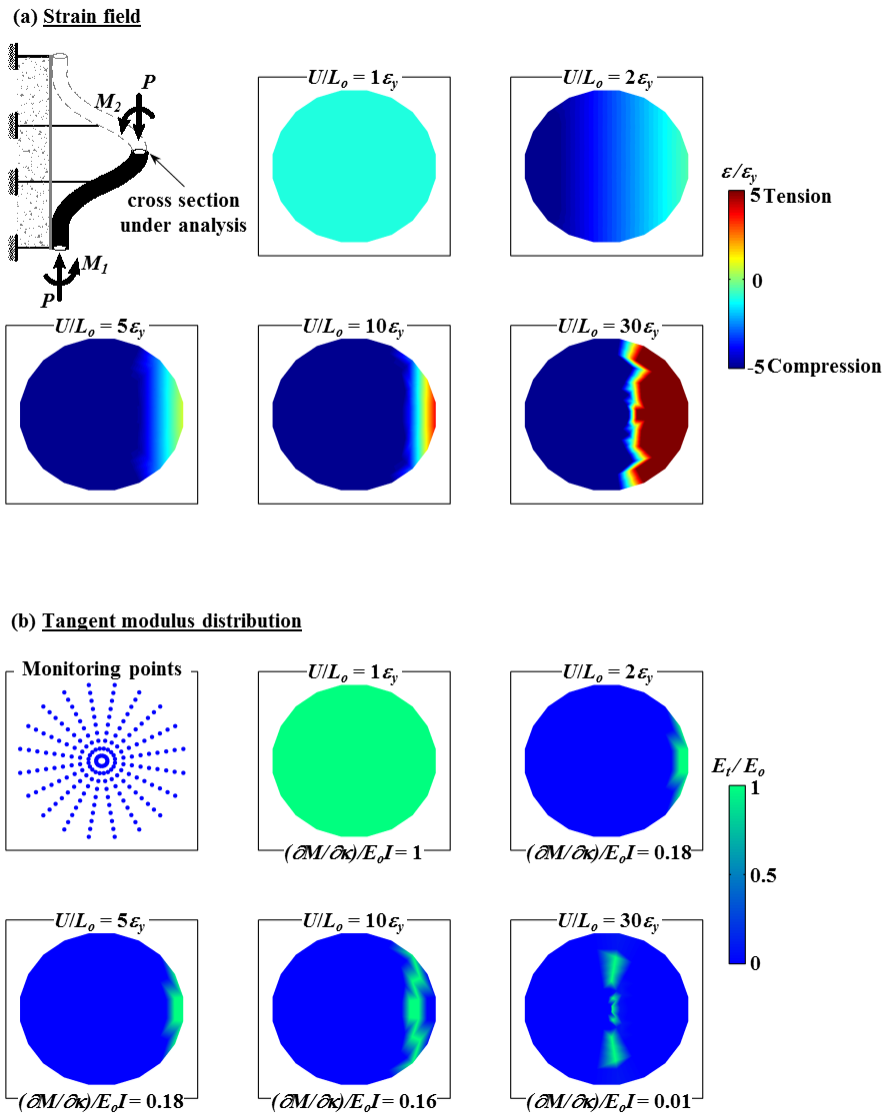


Figure B.2.7 – Test 34: (a) strain field evolution; (b) tangent modulus distribution evolution.

B.3 Stress-strain Evolution of the Discrete Fiber

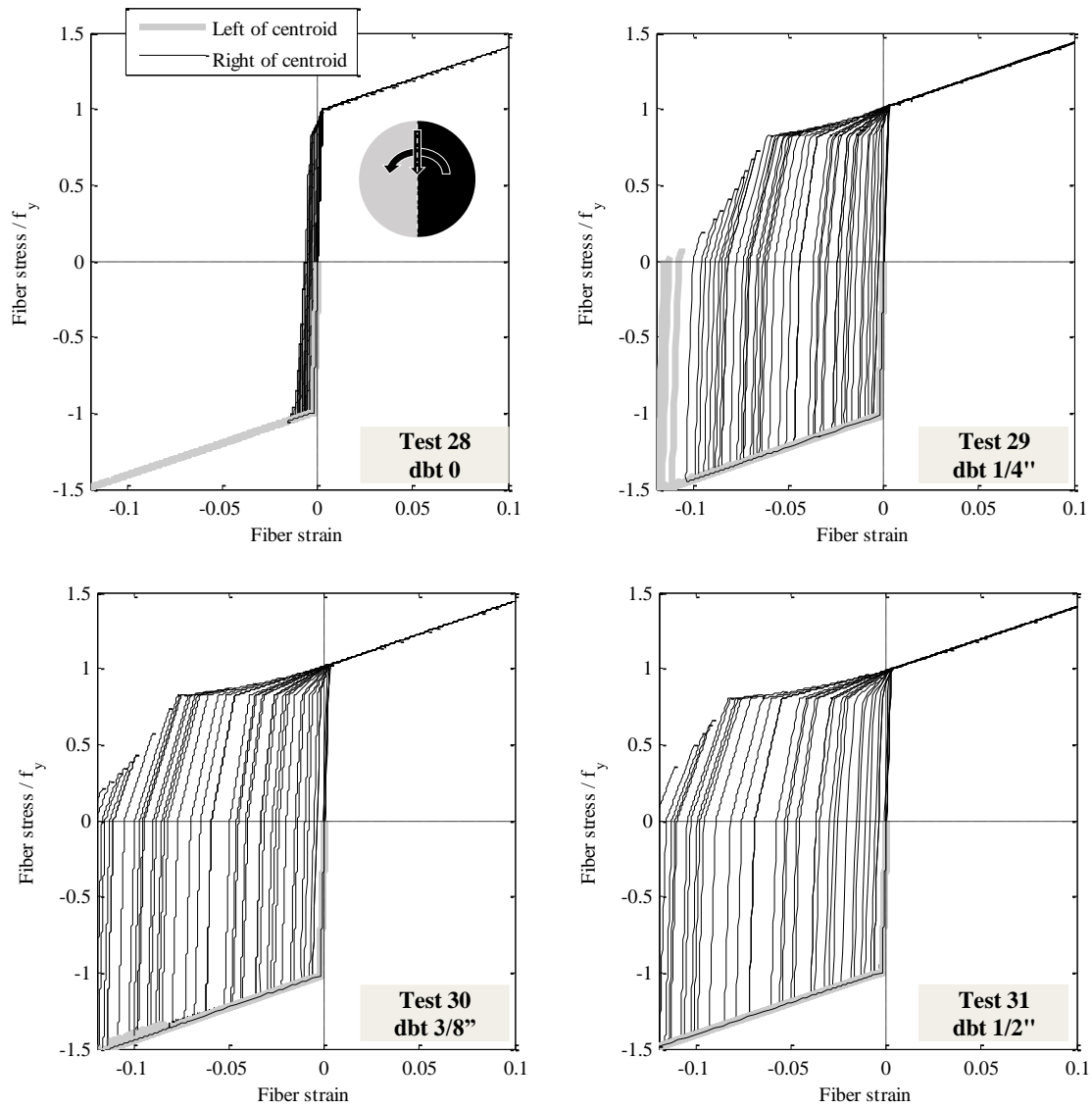


Figure B.3.1 – Tests 28 to 31: history of the fibers stress-strain relationship at the critical section, for different tie diameters.

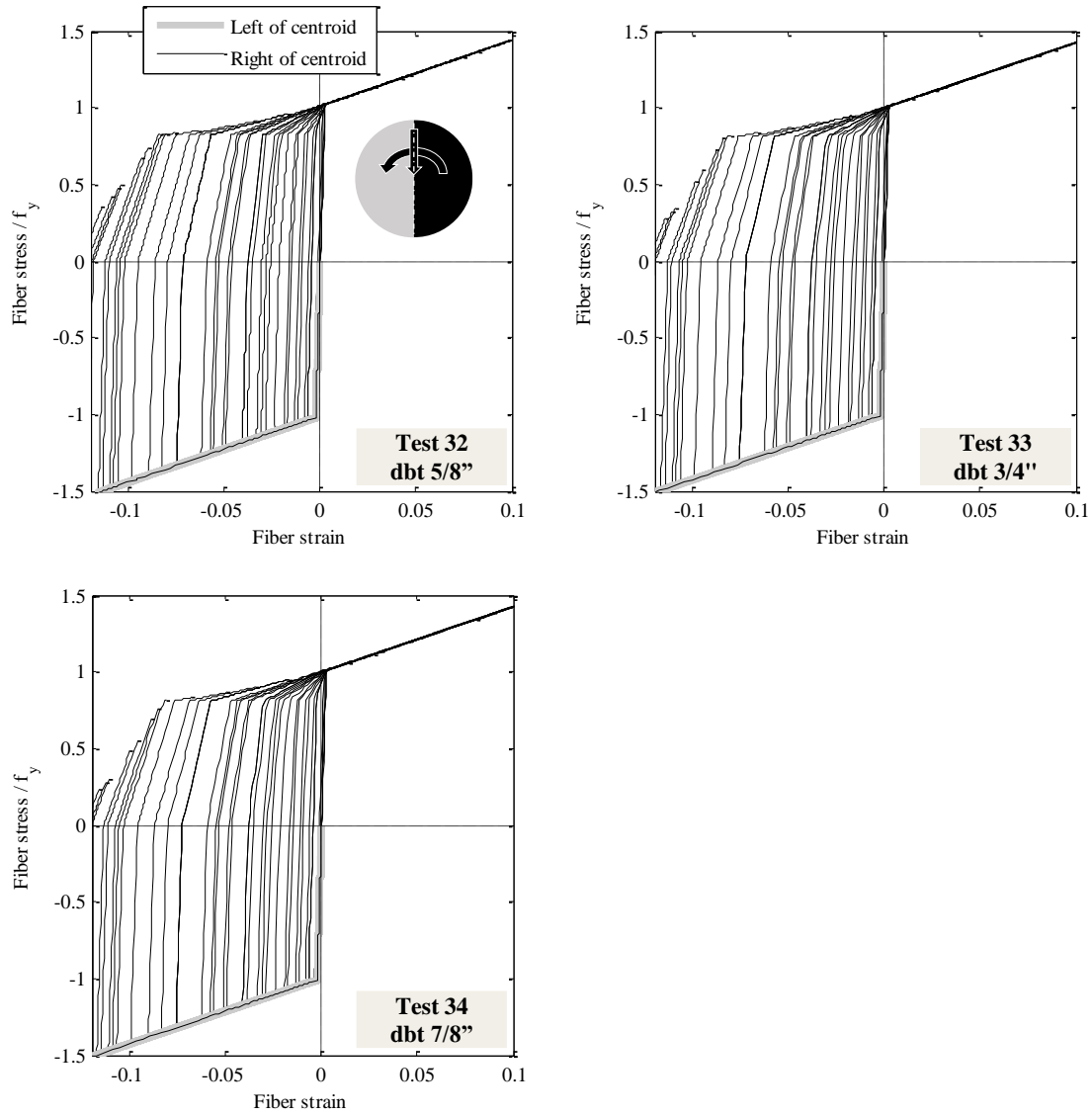


Figure B.3.2 – Tests 32 to 34: history of the fibers stress-strain relationship at the critical section, for different tie diameters.

B.4 Response of the Analytical Specimens of Bar Buckling Under Tie Setup 1 and 2.

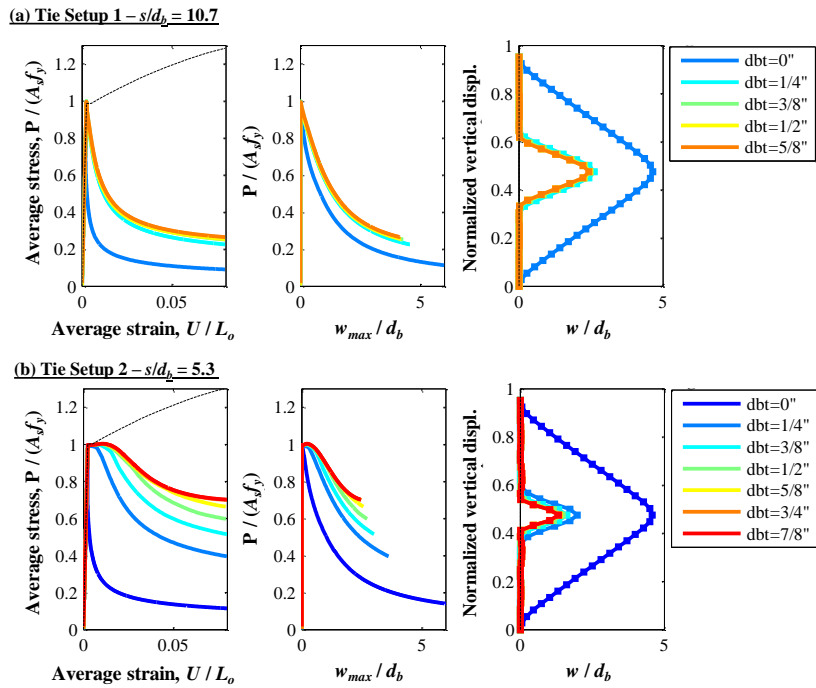


Figure B.4.1 – Response of Tests 1 to 5 and 21 to 27 ($d_b = 3/4$ in. [19 mm]).

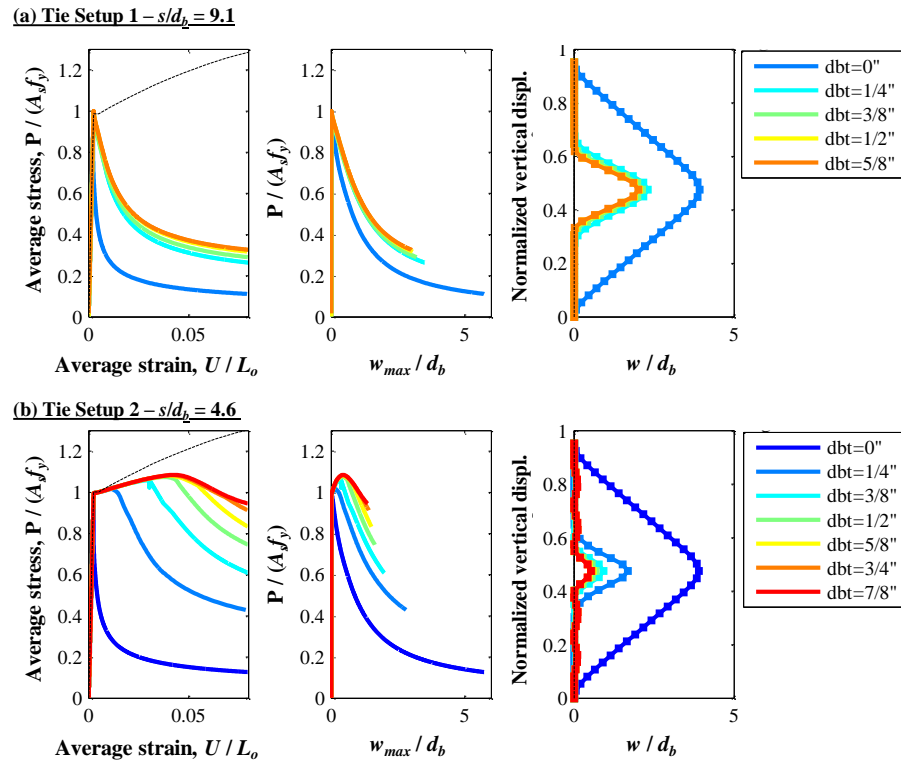


Figure B.4.2 – Response of Tests 6 to 10 and 28 to 34 ($d_b = 7/8$ in. [22 mm]).

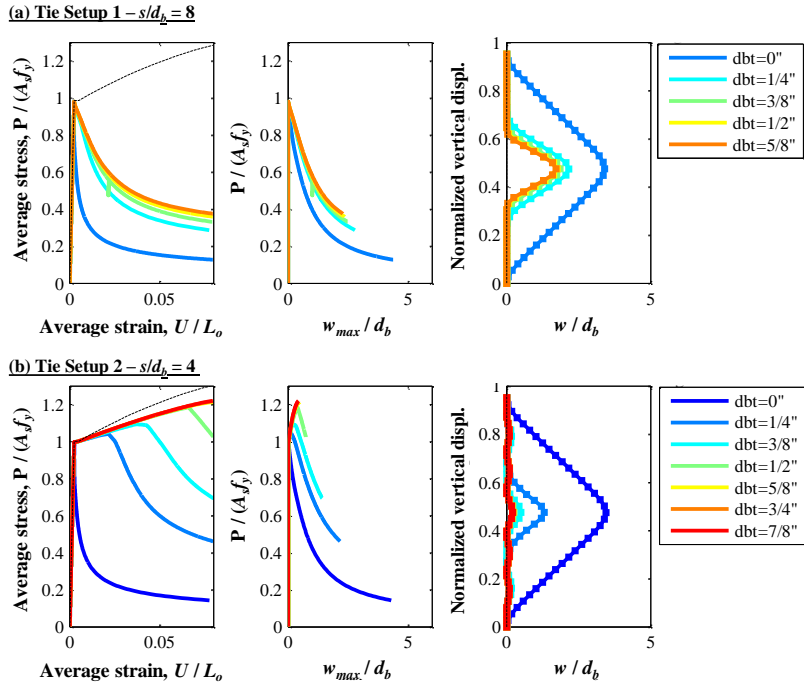


Figure B.4.3 – Response of Tests 11 to 15 and 35 to 41 ($d_b = 1$ in. [25 mm]).

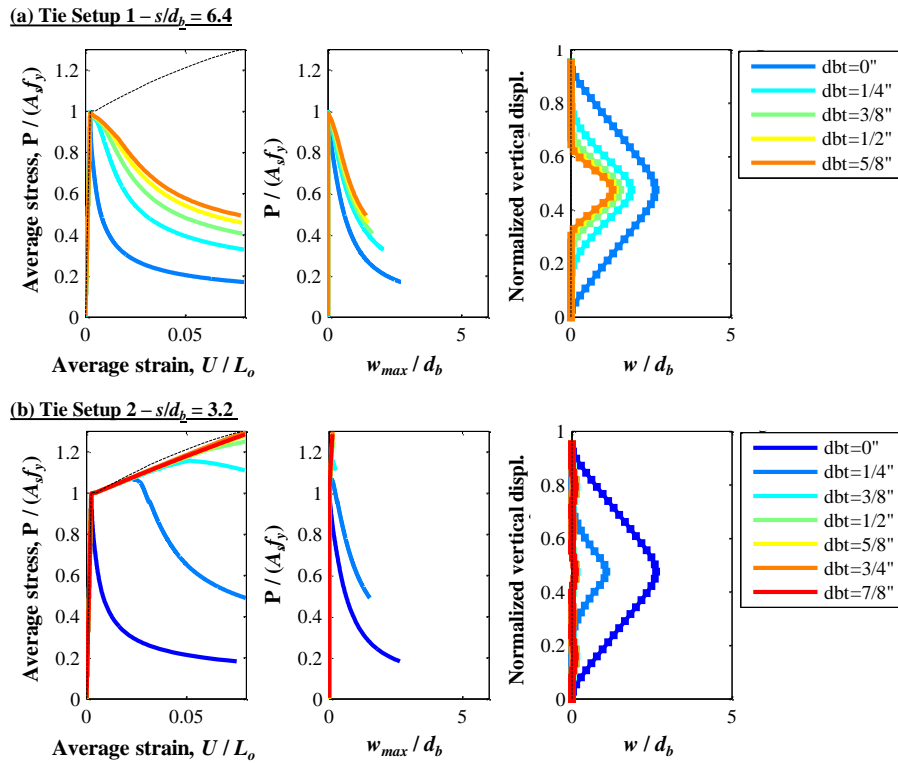


Figure B.4.4 – Response of Tests 16 to 20 and 42 to 48 ($d_b = 1 \frac{1}{4}$ in. [32 mm]).


```

33.0    33.0    19.2    9.8 3.8 1.0
];

%Bilinear interpolation process
r11=eb_eyT(yMark1,xMark1);
r21=eb_eyT(yMark1,xMark2);
r12=eb_eyT(yMark2,xMark1);
r22=eb_eyT(yMark2,xMark2);

b=[1 x1 y1 x1*y1; 1 x1 y2 x1*y2; 1 x2 y1 x2*y1; 1 x2 y2 x2*y2]^(-1)*([1;x;y;x*y]);
r=b(1)*r11+b(2)*r12+b(3)*r21+b(4)*r22;
eb_ey=r;
%%
%Post yield slope parameter
mhT=[0.00 0.00 0.00 0.00 0.00 0.00
0.74 0.47 0.40 0.22 0.00 0.00
0.76 0.58 0.52 0.23 0.00 0.00
0.78 0.63 0.53 0.25 0.00 0.00
0.80 0.68 0.54 0.26 0.00 0.00
0.82 0.69 0.54 0.27 0.03 0.00
0.82 0.69 0.54 0.28 0.06 0.00
0.82 0.69 0.54 0.29 0.09 0.00
0.82 0.69 0.54 0.29 0.09 0.00
0.82 0.69 0.54 0.29 0.09 0.00
0.82 0.69 0.54 0.29 0.09 0.00
0.82 0.69 0.54 0.29 0.09 0.00
0.82 0.69 0.54 0.29 0.09 0.00
0.82 0.69 0.54 0.29 0.09 0.00
]; %mh Table [%]

r11=mhT(yMark1,xMark1);
r21=mhT(yMark1,xMark2);
r12=mhT(yMark2,xMark1);
r22=mhT(yMark2,xMark2);

b=[1 x1 y1 x1*y1; 1 x1 y2 x1*y2; 1 x2 y1 x2*y1; 1 x2 y2 x2*y2]^(-1)*([1;x;y;x*y]);
r=b(1)*r11+b(2)*r12+b(3)*r21+b(4)*r22;
mh=r/100;
end
%%
fb_fy=1+mh*(eb_ey-1);
%%
yMark2=find(dbt2_db2T_y>=dbt2_db2,1);
xMark2=find(s_dbT2_x>=s_db,1);
yMark1=yMark2-1;
xMark1=xMark2-1;

x1=s_dbT2_x(xMark1);
x2=s_dbT2_x(xMark2);
y1=dbt2_db2T_y(yMark1);
y2=dbt2_db2T_y(yMark2);

%%
%Softening branch description
fr_ep001=[0.80 0.71 0.74 0.65 0.52
1.00 0.96 0.96 0.93 0.88
1.00 1.00 0.99 0.97 0.94
1.00 1.00 0.99 0.97 0.94
1.00 1.00 0.99 0.97 0.94
1.00 1.00 0.99 0.97 0.94
1.00 1.00 0.99 0.97 0.94
1.00 1.00 0.99 0.97 0.94
1.00 1.00 0.99 0.97 0.94
1.00 1.00 0.99 0.97 0.94
1.00 1.00 0.99 0.97 0.94
1.00 1.00 0.99 0.97 0.94
1.00 1.00 0.99 0.97 0.94
1.00 1.00 0.99 0.97 0.94
];

r11=fr_ep001(yMark1,xMark1);
r21=fr_ep001(yMark1,xMark2);
r12=fr_ep001(yMark2,xMark1);

```

```

r22=fr_ep001(yMark2,xMark2);

b=([1 x1 y1 x1*y1; 1 x1 y2 x1*y2; 1 x2 y1 x2*y1; 1 x2 y2 x2*y2]^-1)*([1;x;y;x*y]);
r=b(1)*r11+b(2)*r12+b(3)*r21+b(4)*r22;
fr_ep0_001=r;
%%
fr_ep0025=[0.60 0.55 0.57 0.48 0.40
1.00 0.91 0.91 0.85 0.77
1.00 0.99 0.97 0.92 0.86
1.00 0.99 0.98 0.92 0.86
1.00 1.00 0.98 0.93 0.86
1.00 1.00 0.98 0.92 0.86
1.00 1.00 0.98 0.92 0.86
1.00 1.00 0.98 0.92 0.86
1.00 1.00 0.98 0.92 0.86
1.00 1.00 0.98 0.92 0.86
1.00 1.00 0.98 0.92 0.86
1.00 1.00 0.98 0.92 0.86
1.00 1.00 0.98 0.92 0.86
1.00 1.00 0.98 0.92 0.86
1.00 1.00 0.98 0.92 0.86
];

r11=fr_ep0025(yMark1,xMark1);
r21=fr_ep0025(yMark1,xMark2);
r12=fr_ep0025(yMark2,xMark1);
r22=fr_ep0025(yMark2,xMark2);

b=([1 x1 y1 x1*y1; 1 x1 y2 x1*y2; 1 x2 y1 x2*y1; 1 x2 y2 x2*y2]^-1)*([1;x;y;x*y]);
r=b(1)*r11+b(2)*r12+b(3)*r21+b(4)*r22;
fr_ep0_0025=r;
%%
fr_ep005=[0.50 0.43 0.43 0.38 0.32
0.97 0.83 0.84 0.75 0.64
1.00 0.96 0.93 0.84 0.74
1.00 0.97 0.95 0.85 0.75
1.00 0.98 0.95 0.86 0.75
1.00 0.99 0.96 0.86 0.75
1.00 0.99 0.96 0.86 0.75
1.00 0.99 0.96 0.86 0.75
1.00 0.99 0.96 0.86 0.75
1.00 0.99 0.96 0.86 0.75
1.00 0.99 0.96 0.86 0.75
1.00 0.99 0.96 0.86 0.75
1.00 0.99 0.96 0.86 0.75
1.00 0.99 0.96 0.86 0.75
1.00 0.99 0.96 0.86 0.75
];

r11=fr_ep005(yMark1,xMark1);
r21=fr_ep005(yMark1,xMark2);
r12=fr_ep005(yMark2,xMark1);
r22=fr_ep005(yMark2,xMark2);

b=([1 x1 y1 x1*y1; 1 x1 y2 x1*y2; 1 x2 y1 x2*y1; 1 x2 y2 x2*y2]^-1)*([1;x;y;x*y]);
r=b(1)*r11+b(2)*r12+b(3)*r21+b(4)*r22;
fr_ep0_005=r;
%%
fr_ep0075=[0.41 0.38 0.37 0.33 0.27
0.92 0.77 0.78 0.67 0.57
1.00 0.93 0.90 0.77 0.65
1.00 0.95 0.91 0.79 0.66
1.00 0.96 0.92 0.80 0.67
1.00 0.97 0.93 0.80 0.67
1.00 0.97 0.93 0.80 0.67
1.00 0.97 0.93 0.80 0.67
1.00 0.98 0.93 0.80 0.67
1.00 0.98 0.93 0.80 0.67
1.00 0.98 0.93 0.80 0.67
1.00 0.98 0.93 0.80 0.67
1.00 0.98 0.93 0.80 0.67
1.00 0.98 0.93 0.80 0.67
1.00 0.98 0.93 0.80 0.67
];

r11=fr_ep0075(yMark1,xMark1);
r21=fr_ep0075(yMark1,xMark2);

```



```

r12=fr_ep0075(yMark2,xMark1);
r22=fr_ep0075(yMark2,xMark2);

b=([1 x1 y1 x1*y1; 1 x1 y2 x1*y2; 1 x2 y1 x2*y1; 1 x2 y2 x2*y2]^(-1))*([1;x;y;x*y]);
r=b(1)*r11+b(2)*r12+b(3)*r21+b(4)*r22;
fr_ep0_0075=r;
%%
fr_ep01=[0.38 0.34 0.32 0.30 0.24
0.87 0.72 0.73 0.61 0.51
0.99 0.90 0.86 0.71 0.59
1.00 0.92 0.88 0.74 0.60
1.00 0.93 0.90 0.75 0.61
1.00 0.95 0.90 0.75 0.61
1.00 0.95 0.90 0.75 0.61
1.00 0.95 0.90 0.75 0.61
1.00 0.96 0.90 0.75 0.61
1.00 0.96 0.90 0.75 0.61
1.00 0.96 0.90 0.75 0.61
1.00 0.96 0.90 0.75 0.61
1.00 0.96 0.90 0.75 0.61
1.00 0.96 0.90 0.75 0.61
];

r11=fr_ep01(yMark1,xMark1);
r21=fr_ep01(yMark1,xMark2);
r12=fr_ep01(yMark2,xMark1);
r22=fr_ep01(yMark2,xMark2);

b=([1 x1 y1 x1*y1; 1 x1 y2 x1*y2; 1 x2 y1 x2*y1; 1 x2 y2 x2*y2]^(-1))*([1;x;y;x*y]);
r=b(1)*r11+b(2)*r12+b(3)*r21+b(4)*r22;
fr_ep0_01=r;
%%
fr_ep015=[0.32 0.30 0.28 0.26 0.20
0.79 0.64 0.64 0.52 0.43
0.96 0.83 0.80 0.62 0.49
1.00 0.85 0.82 0.65 0.51
1.00 0.87 0.84 0.67 0.52
1.00 0.89 0.84 0.67 0.52
1.00 0.90 0.84 0.67 0.52
1.00 0.91 0.84 0.67 0.52
1.00 0.91 0.84 0.67 0.52
1.00 0.92 0.84 0.67 0.52
1.00 0.92 0.84 0.67 0.52
1.00 0.92 0.84 0.67 0.52
1.00 0.92 0.84 0.67 0.52
1.00 0.92 0.84 0.67 0.52
];

r11=fr_ep015(yMark1,xMark1);
r21=fr_ep015(yMark1,xMark2);
r12=fr_ep015(yMark2,xMark1);
r22=fr_ep015(yMark2,xMark2);

b=([1 x1 y1 x1*y1; 1 x1 y2 x1*y2; 1 x2 y1 x2*y1; 1 x2 y2 x2*y2]^(-1))*([1;x;y;x*y]);
r=b(1)*r11+b(2)*r12+b(3)*r21+b(4)*r22;
fr_ep0_015=r;
%%
fr_ep015=[0.32 0.30 0.28 0.26 0.20
0.79 0.64 0.64 0.52 0.43
0.96 0.83 0.80 0.62 0.49
1.00 0.85 0.82 0.65 0.51
1.00 0.87 0.84 0.67 0.52
1.00 0.89 0.84 0.67 0.52
1.00 0.90 0.84 0.67 0.52
1.00 0.91 0.84 0.67 0.52
1.00 0.91 0.84 0.67 0.52
1.00 0.92 0.84 0.67 0.52
1.00 0.92 0.84 0.67 0.52
1.00 0.92 0.84 0.67 0.52
1.00 0.92 0.84 0.67 0.52
1.00 0.92 0.84 0.67 0.52
];

r11=fr_ep015(yMark1,xMark1);

```

```

r21=fr_ep015(yMark1,xMark2);
r12=fr_ep015(yMark2,xMark1);
r22=fr_ep015(yMark2,xMark2);

b=([1 x1 y1 x1*y1; 1 x1 y2 x1*y2; 1 x2 y1 x2*y1; 1 x2 y2 x2*y2]^-1)*([1;x;y;x*y]);
r=b(1)*r11+b(2)*r12+b(3)*r21+b(4)*r22;
fr_ep0_015=r;
%%
fr_ep02=[0.29 0.27 0.25 0.23 0.18
0.71 0.58 0.58 0.47 0.39
0.93 0.76 0.74 0.56 0.44
1.00 0.79 0.76 0.59 0.46
1.00 0.82 0.78 0.60 0.47
1.00 0.84 0.79 0.61 0.47
1.00 0.85 0.79 0.61 0.47
1.00 0.86 0.79 0.61 0.47
1.00 0.87 0.79 0.61 0.47
1.00 0.88 0.79 0.61 0.47
1.00 0.88 0.79 0.61 0.47
1.00 0.88 0.79 0.61 0.47
];

r11=fr_ep02(yMark1,xMark1);
r21=fr_ep02(yMark1,xMark2);
r12=fr_ep02(yMark2,xMark1);
r22=fr_ep02(yMark2,xMark2);

b=([1 x1 y1 x1*y1; 1 x1 y2 x1*y2; 1 x2 y1 x2*y1; 1 x2 y2 x2*y2]^-1)*([1;x;y;x*y]);
r=b(1)*r11+b(2)*r12+b(3)*r21+b(4)*r22;
fr_ep0_02=r;
%%
fr_ep025=[0.27 0.24 0.23 0.21 0.16
0.66 0.53 0.53 0.42 0.35
0.90 0.71 0.68 0.50 0.40
1.00 0.74 0.70 0.54 0.42
1.00 0.76 0.73 0.55 0.43
1.00 0.79 0.73 0.56 0.43
1.00 0.80 0.73 0.56 0.43
1.00 0.82 0.73 0.56 0.43
1.00 0.83 0.73 0.56 0.43
1.00 0.84 0.73 0.56 0.43
1.00 0.85 0.73 0.56 0.43
1.00 0.86 0.73 0.56 0.43
1.00 0.86 0.73 0.56 0.43
];

r11=fr_ep025(yMark1,xMark1);
r21=fr_ep025(yMark1,xMark2);
r12=fr_ep025(yMark2,xMark1);
r22=fr_ep025(yMark2,xMark2);

b=([1 x1 y1 x1*y1; 1 x1 y2 x1*y2; 1 x2 y1 x2*y1; 1 x2 y2 x2*y2]^-1)*([1;x;y;x*y]);
r=b(1)*r11+b(2)*r12+b(3)*r21+b(4)*r22;
fr_ep0_025=r;
%%
fr_ep03=[0.25 0.23 0.22 0.19 0.15
0.61 0.49 0.49 0.39 0.32
0.88 0.66 0.63 0.46 0.38
1.00 0.69 0.66 0.50 0.40
1.00 0.72 0.68 0.51 0.41
1.00 0.75 0.69 0.52 0.41
1.00 0.77 0.69 0.52 0.41
1.00 0.79 0.69 0.52 0.41
1.00 0.80 0.69 0.52 0.41
1.00 0.82 0.69 0.52 0.41
1.00 0.83 0.69 0.52 0.41
1.00 0.83 0.69 0.52 0.41
1.00 0.84 0.69 0.52 0.41
];

```

```

r11=fr_ep03(yMark1,xMark1);
r21=fr_ep03(yMark1,xMark2);
r12=fr_ep03(yMark2,xMark1);
r22=fr_ep03(yMark2,xMark2);

b=( [1 x1 y1 x1*y1; 1 x1 y2 x1*y2; 1 x2 y1 x2*y1; 1 x2 y2 x2*y2]^-1)*([1;x;y;x*y]);
r=b(1)*r11+b(2)*r12+b(3)*r21+b(4)*r22;
fr_ep0_03=r;
%%
fr_ep04=[0.23    0.20    0.20    0.16    0.14
0.54    0.44    0.44    0.34    0.29
0.83    0.59    0.56    0.40    0.34
1.00    0.63    0.59    0.44    0.36
1.00    0.66    0.61    0.46    0.37
1.00    0.69    0.62    0.46    0.37
1.00    0.71    0.62    0.46    0.37
1.00    0.75    0.62    0.46    0.37
1.00    0.78    0.62    0.46    0.37
1.00    0.79    0.62    0.46    0.37
1.00    0.81    0.62    0.46    0.37
1.00    0.82    0.62    0.46    0.37
1.00    0.82    0.62    0.46    0.37
];

r11=fr_ep04(yMark1,xMark1);
r21=fr_ep04(yMark1,xMark2);
r12=fr_ep04(yMark2,xMark1);
r22=fr_ep04(yMark2,xMark2);

b=( [1 x1 y1 x1*y1; 1 x1 y2 x1*y2; 1 x2 y1 x2*y1; 1 x2 y2 x2*y2]^-1)*([1;x;y;x*y]);
r=b(1)*r11+b(2)*r12+b(3)*r21+b(4)*r22;
fr_ep0_04=r;
%%
fr_ep05=[0.22    0.18    0.18    0.14    0.13
0.49    0.40    0.40    0.31    0.26
0.79    0.55    0.50    0.37    0.32
1.00    0.59    0.54    0.40    0.33
1.00    0.62    0.56    0.42    0.34
1.00    0.66    0.57    0.43    0.34
1.00    0.70    0.57    0.43    0.34
1.00    0.74    0.57    0.43    0.34
1.00    0.77    0.57    0.43    0.34
1.00    0.79    0.57    0.43    0.34
1.00    0.81    0.57    0.43    0.34
1.00    0.82    0.57    0.43    0.34
1.00    0.82    0.57    0.43    0.34
];

r11=fr_ep05(yMark1,xMark1);
r21=fr_ep05(yMark1,xMark2);
r12=fr_ep05(yMark2,xMark1);
r22=fr_ep05(yMark2,xMark2);

b=( [1 x1 y1 x1*y1; 1 x1 y2 x1*y2; 1 x2 y1 x2*y1; 1 x2 y2 x2*y2]^-1)*([1;x;y;x*y]);
r=b(1)*r11+b(2)*r12+b(3)*r21+b(4)*r22;
fr_ep0_05=r;
%%
fr_ep06=[0.21    0.16    0.17    0.13    0.11
0.46    0.37    0.37    0.28    0.24
0.76    0.51    0.47    0.35    0.29
1.00    0.55    0.51    0.37    0.31
1.00    0.59    0.54    0.40    0.32
1.00    0.63    0.54    0.41    0.32
1.00    0.67    0.54    0.41    0.32
1.00    0.71    0.54    0.41    0.32
1.00    0.76    0.54    0.41    0.32
1.00    0.79    0.54    0.41    0.32
1.00    0.81    0.54    0.41    0.32
1.00    0.82    0.54    0.41    0.32
1.00    0.82    0.54    0.41    0.32
];

```

```
r11=fr_ep06(yMark1,xMark1);
r21=fr_ep06(yMark1,xMark2);
r12=fr_ep06(yMark2,xMark1);
r22=fr_ep06(yMark2,xMark2);

b=([1 x1 y1 x1*y1; 1 x1 y2 x1*y2; 1 x2 y1 x2*y1; 1 x2 y2 x2*y2]^-1)*([1;x;y;x*y]);
r=b(1)*r11+b(2)*r12+b(3)*r21+b(4)*r22;
fr_ep0_06=r;
end
```

Appendix C - Grading Ground Motion Modification Procedures for Structural Analysis Based on Conditional Scenario Spectra

Ground motion selection and modification procedures have grown in number and complexity in the last ten years. This is in part, because once-intricate nonlinear dynamic analyses are now routine practice in structural engineering offices, hence increasing the demand for accelerograms with particular time-series properties. The primary reason for scaling and modifying these time series is to attain specific intensity and/or frequency content characteristics that allow running a small suite of recordings over a structural model while still gathering meaningful values and ranges of engineering demand parameters. This appendix presents the comparison between two ground-motion-modification procedures for structural analysis. The modification methods presented herein are based on matching a target spectrum where a Uniform Hazard Spectrum is used as target. Of the two ground motion modification methods used, one matches the target spectra tightly at all periods of interest, while the other does it in a weak manner by matching the target on the average while allowing for some variability in the spectra of the individual ground motions around the target. Suites of ground motions selected and modified with the methods in discussion were used to perform nonlinear dynamic analyses of a code-compliant reinforced concrete multistory frame with special detailing. The two methods were graded on the basis of the resulting risk of a set of structural engineering demand parameters. Results show that while both methods yield the same median response with known dispersion in the elastic domain, as represented by the response of elastic single-degree-of-freedom systems (e.g. pseudo acceleration for a given damping ratio at different periods), the response of nonlinear inelastic systems subjected to the ground-motion suites corresponding to both modification methods vary in the median level (e.g. differ in risk) as well as in dispersion. It is shown that the ground motions of the tightly matched set produce median responses that are closer to their expected risk level.

C.1 Motivation

Selection and modification of earthquake ground motion records for geotechnical and structural response history analyses (RHA) is a subject of ongoing research (Baker, 2011; Baker & Cornell, 2006; Hancock et al., 2008; Huang et al., 2011; Jayaram et al., 2011; Lin, Haselton, et al., 2013; Watson-Lamprey & Abrahamson, 2006). The primary reason for scaling and modifying these time series is to attain specific intensity and/or frequency content characteristics that allow running a small suite of recordings over a structural model while still gathering meaningful values and ranges of engineering demand parameters. For structural analyses one of the most renowned methods make use of a Conditional Mean Spectrum (CMS) (Baker, 2011) that serves as target to selected times series that follow a similar spectral shape. The target CMS matches a Uniform Hazard Spectrum (UHS) for a specific hazard level at one structural period, typically the fundamental one. One of the shortcomings of CMS as target at a single period is that

structures undergoing seismic shaking of high intensity might experience fundamental period lengthening and depending on their configuration, higher mode participation might have an important effect on several structural responses. To account for the latter, structural engineers sometimes face the problem of having to perform structural analyses runs with more than one set of ground motions corresponding to selections based on more than one CMS to account for the different relevant structural periods. Other methods for ground motion selection, which satisfy structural engineering desire to perform as few runs as possible, are focused on modifying time series in order to match an UHS. Theoretically, this is over conservative because no single ground motion response spectrum has as high spectral coordinates at all periods but with by using this method, the problem of having to run analyses with many ground motion sets is minimized.

In this appendix, another application of the Conditional Scenario Spectra (CSS) methodology presented in **Section 5.1.3** is used for the objective comparison between two ground-motion-modification procedures for structural analysis. The modification methods presented herein are based on matching a target UHS with a selected return period (or hazard level). Of the two ground motion modification methods used, one matches the target spectra tightly at all periods of interest, while the other does it in a weak manner by matching the target on the average, while allowing for some variability in the spectra of the individual ground motions around the target. Suites of ground motions selected and modified with the methods in discussion were used to perform nonlinear dynamic analyses of a code-compliant reinforced concrete multistory frame with special detailing. The two methods were graded on the basis of the resulting risk of the maximum roof displacement and the base shear force. This risk is calculated by comparing responses from the modification method sets to those from the CSS.

C.2 Structural Design and Inelastic Modeling

An 8-story reinforced concrete building was selected as the object of study to analyze the impact of two different ground motion selection methods in the response of the structures. **Figure C.2.1** depicts the general geometric properties of the structure of analysis. Plan dimensions are 117 ft x 97 ft and total height is 96 ft. The structural system comprises circular gravity load columns and external special moment resistant frames (SMF) to resist lateral loads due to seismic demand. Analyses for combined gravity and lateral seismic loads followed ASCE-7. A three-dimensional, linear structural model of the buildings was implemented in the computer software ETABS (CSI, 2011). The model accounted for degraded stiffness of the structural elements due to seismic loading. The effective inertia of the beams was set to 35% of the gross inertia and those of the columns were set in the range 50% to 70% according to their gravitational axial loading. A response modification factor $R = 8$ was selected. Concrete was assumed normal weight ($\gamma_c = 150$ lb/ft³) with nominal strength $f'_c = 6$ ksi for beams and columns of the SMFs. The elastic modulus of the reinforced concrete structural elements was computed as $57000\sqrt{f'_c}$ [psi]. Reinforcing steel was assumed ASTM A706 with nominal yielding strength of $f_y = 60$ ksi.

Seismic load effects on the structural members were calculated by means of the Equivalent Lateral Force Analysis described in ASCE 7. The design spectrum depicted in **Figure 5.1** was used as the seismic demand after reducing it by R . A modal analysis was performed over the structure to calculate its dynamic properties. Since the nonlinear modeling was performed over a 2D-model representative of half the structure in the EW direction, in the following, the

mentioned values will only refer to that direction of analysis. The fundamental period was $T_{1EW-Dir} = 1.75s$ and second and third translational modal periods were 0.53s and 0.27s respectively. Design base shears including response modification factor $R=8$ were $V_{bEW} = 721.5$ kN ($V_{bEW} / W = 4.8\%$). Maximum inter-story drift ratio was 1.61% which is below the maximum allowed of 2%. Design of the reinforced concrete structural elements (beams and columns) was performed in accordance with provision for special moment frames in ACI-318 (2011). Columns were 32 x 32 in. with minimum longitudinal steel ratios (total area of steel to gross area ratio) $\rho_{min} = 1.00\%$ and transverse steel ratio with $A_v / bs > 0.87\%$, where A_v is the total area of transverse reinforcement within distance s of two adjacent layers and b is the core dimension of column. Beams were 22 x 32 in. with longitudinal steel ratios (area of tension reinforcement divided by web width and effective depth) ranging from $\rho = 0.39$ to 0.54% and transverse steel ratios $A_v / bs > 0.63\%$. The slab was 8 in. thick at all floors.

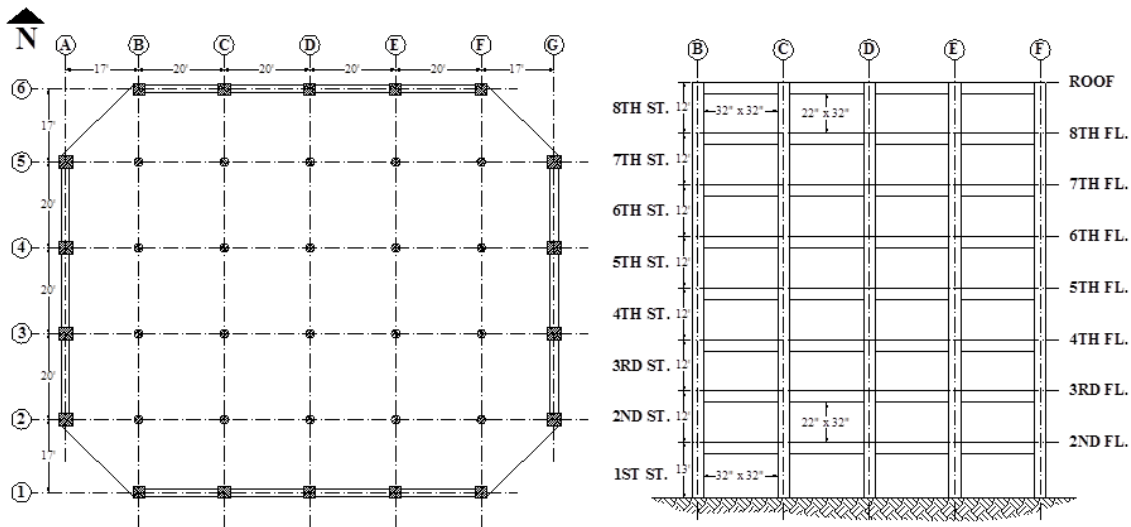


Figure C.2.1 – General layout of structural elements: (a) plan; (b) elevation of Frame 1.

To account for epistemic uncertainty in modeling, two planar inelastic mathematical models, representative of half the structure in the EW-direction, were constructed: (i) *LC Model* and (ii) *NLC Model*. The LC Model (leaning column model) accounts for P-Delta effects due to high axial load in the gravity load resisting system through a so-called leaning column which is a mathematical artifact that effectively reduces the tangent stiffness of the system at large displacements. NLC Model only accounts for P-Delta effect due to axial loading of the SMF. The software package OpenSees (McKenna et al., 2000) was selected as the modeling tool because its nonlinear analysis capabilities allow conducting a large number of simulations and its efficacy has been validated by the research community for many years. Static nonlinear analyses (“pushover”) and dynamic nonlinear analyses were performed on the structures.

Force-based nonlinear beam-column elements with concentrated plasticity at the ends were used to model all structural elements (M. H. Scott & Fenves, 2006). Fiber sections assigned to the plastic hinge regions simulate material nonlinearities while accounting for moment-axial load interaction. For nonlinear dynamic analyses, mass and stiffness-proportional Rayleigh damping was used to simulate the energy dissipation characteristics of the building that is not accounted for by the nonlinear behavior of the structural elements. The Rayleigh damping

coefficients were established to achieve a damping ratio of $\zeta = 2.5\%$ at periods corresponding to the first and third translational vibration modes of the linear model. Calculated periods for the nonlinear models were obtained after applying the vertical load, therefore some initial service level cracking is accounted for. The first, second and third periods of the nonlinear model are: $T_{1EW-NL} = 1.73s$, $T_{2EW-NL} = 0.54s$ and $T_{3EW-NL} = 0.29s$, which closely match those of the elastic model with cracked sections. **Figure C.2.2** shows pushover curves for the two OpenSees models. The influence of P-Delta effects is apparent on the LC Model. The design base shear and yielding base shear, from displacement based analysis (“by hand”) of the designed structure, are also presented. The minimum overstrength factor, defined as the ratio between the maximum base shear of LC Model and the design base shear is, approximately 1.12; the maximum overstrength factor, defined as the ratio between the maximum base shear of the NLC Model and the design base shear is, approximately 1.57.

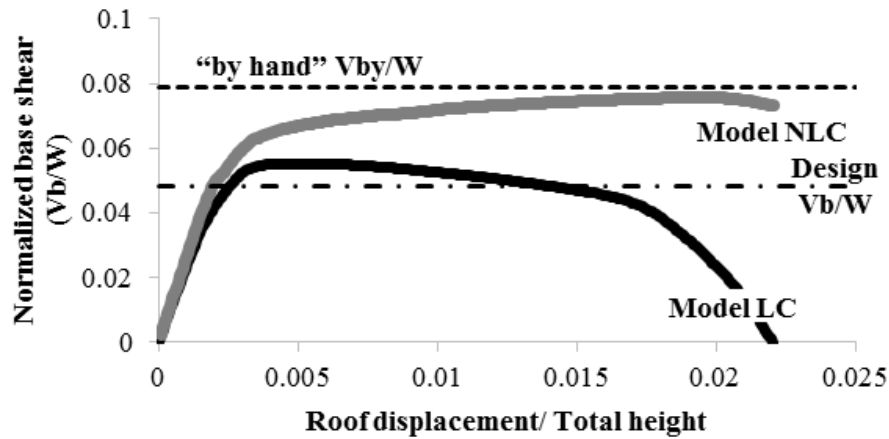


Figure C.2.2 – Pushover curves.

C.3 Ground Motion Selection and Modification Procedures

Structural systems subjected to high intensity shaking undergo relatively large displacements and their period of vibration shifts toward larger values, product of stiffness degradation of the structural elements. For the system shown in **Figure C.2.1**, the expected lengthening is, on average, approximately 1.5 times the elastic period of vibration. This suggests that to estimate the response of this inelastic multi-degree-of-freedom system (MDOFS) properly, the frequency content of the selected ground motions must be rich enough to properly excite the structural vibration modes that most contribute to the response. For the building in discussion, at least the first and second elastic modes should be excited with enough energy and the expected degraded period should also be covered by the frequency content range of the times series used as the uniform excitation at the base. The building code achieves this by requiring that the average spectrum of the ground motions does not fall below the target design spectrum for the site in a period range between 0.2 and 1.5 times the fundamental elastic period of the structure being analyzed.

Loose Mean-Spectrum match (LM) set

The LM set comprises twenty ground motions that were selected, scaled and their frequency content was modified such that their average spectrum matches the 4,000-year return period

UHS for the site (**Figure C.3.1a**). This method of ground-motion modification allows for the variability around the mean which tight spectral matching removes (Mazzoni et al., 2012). In addition, the frequency-content modification removes the higher-mode amplification effects that results when records are simply scaled and not modified.

Tight Component-Spectrum match (TM) set

The TM set also comprises twenty ground motions as shown in (**Figure C.3.1b**). The frequency content of these records, however, was modified such that the response spectrum of each component matched the target UHS for the site. This method is used in many structural-engineering project because of it meets the design code requirements and is easy to implement and use.

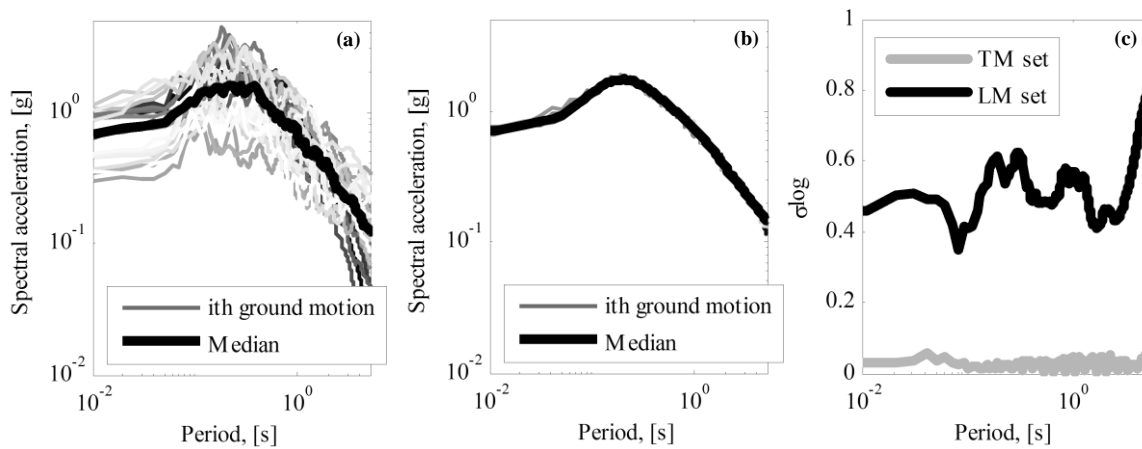


Figure C.3.1 – Selected ground motion set and their variability: (a) LM set, with variability around the median; (b) TM set, without much variability; (c) variability (in log units) of the LM and TM sets for different periods.

C.4 Structural Responses

The inelastic mathematical models of the building were subjected to simulated seismic shaking using the two sets of ground motions described above. Excluding collapses, **Figure C.4.1** show two engineering demand parameters (EDP) for each run: (a) maximum roof drift ratio (RDR), defined as the lateral displacement of the roof divided by the total height of the building, versus the elastic spectral displacement at the elastic fundamental period ($Sd_{(T1)}$); and (b) maximum base shear normalized by the weight of the building versus spectral acceleration at the fundamental period ($Sa_{(T1)}$). Under each set of ground motions, the response of both mathematical models of the building (i.e. NLC and LC model) is included. It is apparent how both ground motion sets differ in dispersion of the elastic ground motion parameters (i.e. spectral coordinates of pseudo acceleration or displacement are concentrated around a single value for the TM set), while the structural response dispersion difference is not as obvious.

Median values and dispersion estimates of the EDPs of interest are depicted in the boxplots of **Figure C.4.2**. Median values, product of the TM set runs, are 3% to 13% larger than those from the LM set. The structural responses reported here follow a logNormal distribution with unbounded values on the upper tail of the distribution due to structural collapses. To

overcome the latter, the dispersion of the EDPs is calculated with a standard deviation estimate according to **Equation ((C.1))**:

$$\sigma_{log} \approx \frac{\ln Ri_{p84} - \ln Ri_{p16}}{2} \quad (C.1)$$

where $\ln Ri_{p16}$ and $\ln Ri_{p84}$ are, respectively, the 16th and 84th percentile of the natural logarithm of the response of interest. The dispersion from the runs corresponding to the LM set is 2.3 to 2.9 times larger than those from the TM set. For analyses under the TM set, it is important to notice how the response of the inelastic MDOFS dispersion is not as low as the dispersion of the input ground motions, represented by their elastic response spectra. This result supports the hypothesis that spectral shape is not the only relevant parameter of the input ground motions that drives the response of inelastic MDOFS.

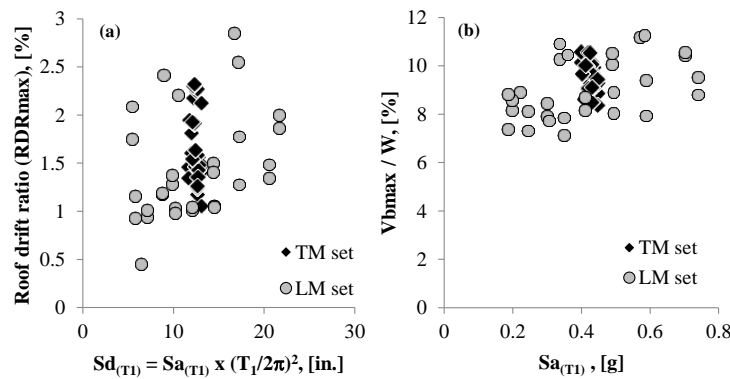


Figure C.4.1 – Structural response under each set of ground motions: (a) maximum roof drift ratio versus elastic spectral displacement at the fundamental period; (b) normalized maximum base shear versus spectral acceleration at the fundamental period.

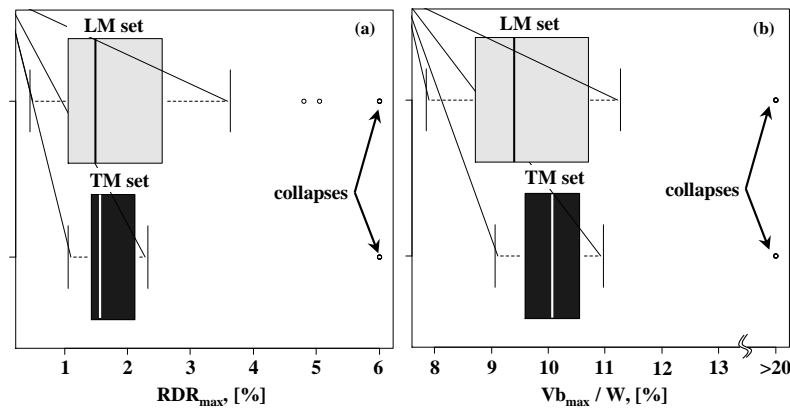


Figure C.4.2 – Boxplots of the structural responses.

C.5 EDP risk curves from CSS

Figure C.5.1 shows EDPs estimated using the inelastic NLC model and the ground motion set associated with the CS described above. The same type of data was estimated with the LC model and the results were averaged with equal weights for each model. It is interesting to

notice that one of the depicted EDPs is bounded by the strength of the building while the other is practically unbounded and is related to the displacement of the framing system. It is also worth mentioning, that the CSS ground motion set covers low and very high levels of intensity that may drive the inelastic model into the collapse range.

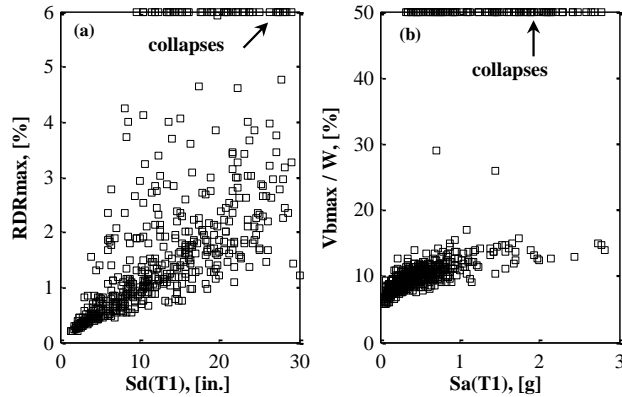


Figure C.5.1 – Engineering demand parameter response from CS runs on the NLC model: (a) maximum roof drift ratio versus elastic spectral displacement at the fundamental period; (b) normalized maximum base shear versus spectral acceleration at the fundamental period.

To construct an objective ground for comparison of the EDPs estimated with the LM and TM ground motion sets, product of the modification methods in study, the EDPs from the CSS set, along with the assigned rates of each time series, can be used to estimate a risk curves for EDPs using the formulation in **Section 5.1.3.1** (see **Equation (5.11)**). Boxes (a) and (b) of **Figure C.5.2** and **Figure C.5.3** show risk curves for the maximum RDR and the normalized maximum base shear. Also shown are the responses from the TM and LM set runs, which are placed at the expected abscissa of 4,000 years return period (rate of 2.5×10^{-4}). To compare the adequacy of the response estimates from both sets of ground motions, **Figure C.5.2c** and **Figure C.5.3c** depict the median values of the EDPs of interest and their interpolated rate of being exceeded. It is observed that the interpolated rates for the TM set medians are closer to the expected hazard of 1/4,000 years. Furthermore, the median value of the normalized maximum base shear estimated with the TM set is almost on top the risk curve for return period 4,000 years. On the other hand, due to the steep behavior of the aforementioned EDP, the rate of the median response from the LM set is deemed unconservative at 1/850 years approximately.

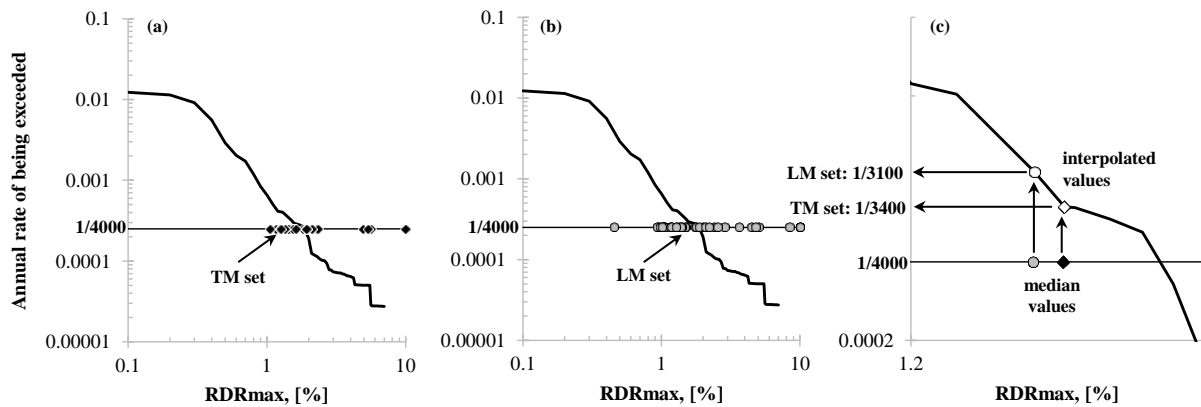


Figure C.5.2 – Hazard curves for maximum roof drift ratio: (a) with responses from the TM set; (b) with responses from the LM set; (c) interpolated rates for median values from runs with the TM and LM set.

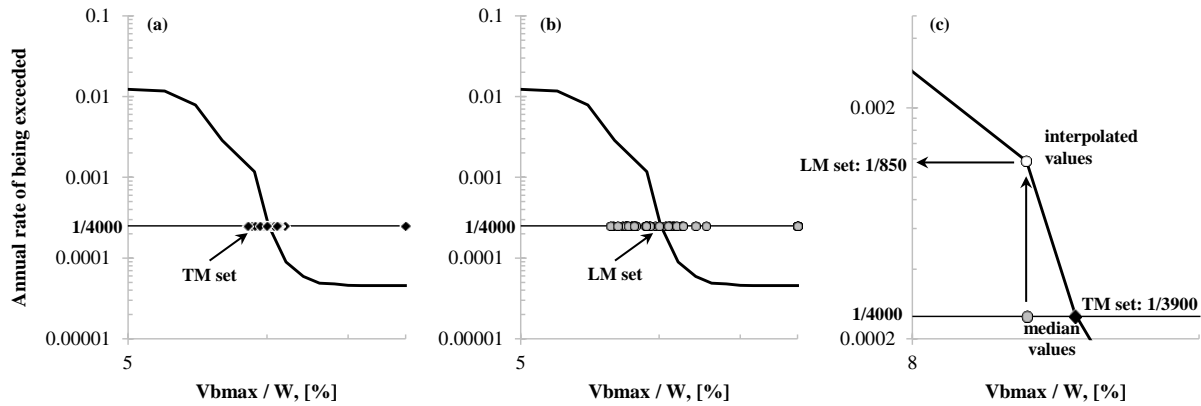


Figure C.5.3 – Hazard curves for normalized base shear: (a) with responses from the TM set; (b) with responses from the LM set; (c) interpolated rates for median values from runs with the TM and LM set.

C.6 Final comments

An application was presented in which Conditional Scenario Spectra (CSS) are utilized to construct risk curves for engineering demand parameters (EDPs). The rates of these demand parameters serve as basis to grade the adequacy of two sets of ground motions, product of two different modification procedures. The two sets are similar in that their mean response spectrum approximately matches a target UHS with return period 4,000 years. The two sets differ in that one had variability around the mean spectrum while the other is a set comprised of spectrally matched time series with low variability.

The estimated median EDPs of each procedure are graded by interpolating their rate of being exceeded within their risk curves from the CSS. It was observed that median inelastic responses from the low variability ground motion set have rates closer to their matched target UHS. In addition to the value of the results of this comparison, the methodology used in this appendix is a valuable tool in evaluating any set of ground motions.

Appendix D - Conditional Scenario Spectra Metadata

D.1 CSS Metadata

Metadata related to the selected 402 ground motions used for the construction of the CSS in **Chapter 5** is present in **Table D.1.1**. Additionally, rate versus EDP scatter plot for the DuM model are shown in .

Table D.1.1 – Metadata of Conditional Scenario Spectra set.

ID per Scenario	Original Index	Hazard Level	RSN	EqID	Mag M_w	Rrup [km]	Vs30 [m/s]	Scale Factor	Rate
1	2	1	126	31	6.2	4.1	288.8	0.23	6.98E-04
2	14	1	139	42	5.5	17.7	659.6	0.61	7.23E-04
3	16	1	162	49	5.9	13.3	338.6	0.74	3.73E-04
4	9	1	171	50	6.5	15.2	659.6	0.24	3.43E-04
5	18	1	312	68	6.9	10.8	1000	1.95	2.11E-04
6	10	1	457	90	6.2	3.3	488.8	1.17	6.99E-04
7	6	1	741	116	6.5	18.2	192.1	0.45	8.29E-05
8	8	1	767	118	6.9	24.6	239.7	0.40	7.75E-04
9	13	1	983	125	7.3	23.6	353.6	0.22	8.58E-05
10	19	1	1013	127	6.7	22.2	446	0.25	4.06E-05
11	3	1	1039	127	6.7	5.4	525.8	0.68	5.47E-04
12	4	1	1091	127	6.7	7	2016.1	1.10	3.85E-05
13	17	1	1176	129	6.9	0.9	1043	0.26	1.62E-04
14	1	1	1528	137	7.6	19	401.3	0.42	#####
15	7	1	1532	137	7.6	0.9	573	0.56	3.06E-04
16	5	1	1549	137	7.6	6.1	494.1	0.33	2.04E-03
17	11	1	2628	171	5.9	15.4	443	0.54	2.74E-04
18	15	1	6886	175	6.3	24.7	433.6	0.72	6.31E-05
19	12	1	8142	175	6.3	24.8	664.4	1.63	1.64E-04
1	21	2	126	31	6.2	4.1	288.8	0.36	3.11E-04
2	40	2	139	42	5.5	17.7	659.6	0.95	1.22E-04
3	44	2	162	49	5.9	13.3	338.6	1.15	8.96E-05
4	22	2	165	50	6.5	2.7	223	0.81	3.32E-07
5	20	2	178	50	6.5	21.7	237.3	0.86	1.26E-04
6	43	2	212	50	6.5	7.7	202.9	1.53	3.34E-04
7	34	2	292	64	6.3	7.3	274.5	0.53	7.88E-05
8	33	2	457	90	6.2	3.3	488.8	1.82	5.80E-04
9	25	2	729	113	6	18.5	308.6	0.71	2.03E-07
10	38	2	730	113	6	16.3	308.6	1.40	1.02E-07
11	30	2	741	116	6.5	18.2	192.1	0.71	2.76E-06
12	32	2	767	118	6.9	24.6	239.7	0.62	4.75E-04
13	39	2	983	125	7.3	23.6	353.6	0.34	4.94E-05

ID per Scenario	Original Index	Hazard Level	RSN	EqID	Mag M_w	Rrup [km]	Vs30 [m/s]	Scale Factor	Rate
14	41	2	995	127	6.7	17.1	355.8	0.87	8.96E-05
15	26	2	1091	127	6.7	7	2016.1	1.71	1.12E-04
16	23	2	1197	129	6.9	0.3	312	0.41	2.40E-05
17	31	2	1510	137	7.6	10.5	440.2	0.66	9.59E-05
18	29	2	1512	137	7.6	17.1	230.3	0.58	2.04E-07
19	28	2	1521	137	7.6	0.6	433.6	0.70	1.32E-04
20	27	2	1549	137	7.6	6.1	494.1	0.51	6.40E-04
21	37	2	1550	137	7.6	12.9	543.8	0.92	2.70E-05
22	45	2	1611	137	7.6	11.6	212.7	1.40	1.69E-04
23	24	2	1752	145	5.6	13.2	370.8	1.02	4.36E-05
24	35	2	2628	171	5.9	15.4	443	0.84	7.21E-05
25	42	2	6886	175	6.3	24.7	433.6	1.12	5.14E-05
26	36	2	8142	175	6.3	24.8	664.4	2.54	1.02E-07
1	46	3	95	30	6.6	22.6	670.8	1.43	3.59E-05
2	48	3	126	31	6.2	4.1	288.8	0.53	5.59E-05
3	68	3	139	42	5.5	17.7	659.6	1.39	5.47E-05
4	71	3	162	49	5.9	13.3	338.6	1.68	6.12E-08
5	47	3	178	50	6.5	21.7	237.3	1.26	1.02E-04
6	70	3	212	50	6.5	7.7	202.9	2.22	3.52E-05
7	61	3	457	90	6.2	3.3	488.8	2.64	6.12E-05
8	51	3	729	113	6	18.5	308.6	1.03	1.74E-05
9	56	3	741	116	6.5	18.2	192.1	1.03	1.02E-05
10	60	3	767	118	6.9	24.6	239.7	0.90	1.52E-04
11	66	3	983	125	7.3	23.6	353.6	0.49	9.48E-05
12	49	3	1039	127	6.7	5.4	525.8	1.54	2.26E-05
13	62	3	1048	127	6.7	24	316.5	0.63	1.35E-05
14	52	3	1091	127	6.7	7	2016.1	2.49	1.75E-05
15	74	3	1113	127	6.7	5.3	440.5	2.04	2.64E-05
16	72	3	1141	129	6.9	11.3	256	0.78	8.93E-06
17	57	3	1510	137	7.6	10.5	440.2	0.96	1.05E-06
18	59	3	1511	137	7.6	11.8	479.3	0.79	5.22E-05
19	55	3	1512	137	7.6	17.1	230.3	0.84	3.42E-05
20	54	3	1549	137	7.6	6.1	494.1	0.74	1.86E-04
21	65	3	1550	137	7.6	12.9	543.8	1.34	9.82E-06
22	73	3	1611	137	7.6	11.6	212.7	2.04	1.73E-05
23	63	3	2628	171	5.9	15.4	443	1.23	5.91E-05
24	50	3	2699	172	6.2	22.5	468.1	3.53	8.21E-06
25	58	3	2893	172	6.2	7.6	443	2.76	1.40E-05
26	67	3	4098	173	6.2	19.7	427.7	1.00	9.06E-05
27	53	3	4117	173	6.2	17.7	542.6	1.57	4.18E-06
28	69	3	6886	175	6.3	24.7	433.6	1.64	3.99E-06
29	64	3	8142	175	6.3	24.8	664.4	3.69	8.01E-05
1	106	4	97	30	6.6	1.8	2016.1	4.54	4.29E-05

ID per Scenario	Original Index	Hazard Level	RSN	EqID	Mag M_w	Rrup [km]	Vs30 [m/s]	Scale Factor	Rate
2	77	4	126	31	6.2	4.1	288.8	0.69	2.99E-05
3	100	4	139	42	5.5	17.7	659.6	1.82	3.22E-05
4	110	4	161	49	5.9	4.6	659.6	1.58	3.86E-05
5	104	4	162	49	5.9	13.3	338.6	2.20	1.07E-05
6	75	4	178	50	6.5	21.7	237.3	1.65	3.06E-05
7	86	4	182	50	6.5	22	249.9	0.76	2.75E-08
8	103	4	212	50	6.5	7.7	202.9	2.92	9.12E-05
9	76	4	284	61	5.9	12.4	338.5	6.09	1.09E-04
10	111	4	286	61	5.9	16	345.4	2.57	2.39E-05
11	94	4	292	64	6.3	7.3	274.5	1.00	1.99E-05
12	93	4	457	90	6.2	3.3	488.8	3.47	2.82E-05
13	80	4	553	102	5.8	24.5	338.5	4.58	5.11E-05
14	83	4	729	113	6	18.5	308.6	1.35	7.09E-06
15	98	4	730	113	6	16.3	308.6	2.68	1.25E-05
16	88	4	741	116	6.5	18.2	192.1	1.35	5.18E-06
17	92	4	767	118	6.9	24.6	239.7	1.18	8.28E-05
18	78	4	850	118	6.9	14.7	671.8	1.96	4.60E-06
19	101	4	995	127	6.7	17.1	355.8	1.66	3.46E-05
20	79	4	1039	127	6.7	5.4	525.8	2.02	1.20E-06
21	84	4	1091	127	6.7	7	2016.1	3.27	2.42E-06
22	109	4	1113	127	6.7	5.3	440.5	2.68	5.73E-06
23	105	4	1116	127	6.7	22.3	376.1	1.35	9.03E-06
24	81	4	1197	129	6.9	0.3	312	0.79	2.02E-06
25	89	4	1510	137	7.6	10.5	440.2	1.25	7.54E-06
26	91	4	1511	137	7.6	11.8	479.3	1.04	3.07E-06
27	107	4	1530	137	7.6	7	468.1	1.57	1.79E-05
28	87	4	1549	137	7.6	6.1	494.1	0.97	6.16E-05
29	97	4	1550	137	7.6	12.9	543.8	1.76	7.10E-06
30	108	4	1611	137	7.6	11.6	212.7	2.68	4.14E-05
31	82	4	1752	145	5.6	13.2	370.8	1.94	3.34E-05
32	95	4	2628	171	5.9	15.4	443	1.61	5.69E-06
33	112	4	2650	171	5.9	23.4	680	1.37	1.18E-05
34	90	4	2893	172	6.2	7.6	443	3.63	2.48E-05
35	99	4	4098	173	6.2	19.7	427.7	1.32	1.04E-05
36	85	4	4117	173	6.2	17.7	542.6	2.07	6.92E-06
37	102	4	6886	175	6.3	24.7	433.6	2.15	3.99E-06
38	96	4	8142	175	6.3	24.8	664.4	4.85	1.11E-06
1	114	5	95	30	6.6	22.6	670.8	2.99	3.42E-07
2	153	5	97	30	6.6	1.8	2016.1	7.25	2.68E-06
3	118	5	126	31	6.2	4.1	288.8	1.10	1.11E-06
4	151	5	162	49	5.9	13.3	338.6	3.52	7.71E-06
5	138	5	171	50	6.5	15.2	659.6	1.12	4.87E-06
6	116	5	175	50	6.5	7.3	192.1	3.58	4.66E-08

ID per Scenario	Original Index	Hazard Level	RSN	EqID	Mag M_w	Rrup [km]	Vs30 [m/s]	Scale Factor	Rate
7	115	5	178	50	6.5	21.7	237.3	2.63	8.10E-06
8	150	5	212	50	6.5	7.7	202.9	4.66	1.78E-05
9	139	5	266	60	5.7	15.9	345.4	2.77	2.87E-08
10	117	5	284	61	5.9	12.4	338.5	9.72	2.29E-05
11	160	5	286	61	5.9	16	345.4	4.10	3.73E-06
12	157	5	312	68	6.9	10.8	1000	9.25	6.70E-07
13	140	5	457	90	6.2	3.3	488.8	5.55	5.82E-06
14	137	5	544	101	6.1	4	345.4	5.61	3.08E-07
15	121	5	553	102	5.8	24.5	338.5	7.32	4.80E-06
16	136	5	554	102	5.8	6.4	271.4	5.78	4.04E-05
17	127	5	729	113	6	18.5	308.6	2.16	4.42E-06
18	154	5	740	116	6.5	17	208.7	4.53	5.16E-06
19	133	5	741	116	6.5	18.2	192.1	2.16	2.42E-07
20	135	5	767	118	6.9	24.6	239.7	1.89	7.88E-06
21	158	5	802	118	6.9	20.3	597.1	1.42	2.38E-08
22	164	5	827	118	6.9	22.7	333.9	3.62	2.81E-06
23	123	5	949	118	6.9	17.5	376.1	2.00	5.09E-06
24	146	5	983	125	7.3	23.6	353.6	1.02	3.75E-06
25	148	5	995	127	6.7	17.1	355.8	2.65	3.10E-06
26	119	5	1039	127	6.7	5.4	525.8	3.23	7.25E-07
27	141	5	1048	127	6.7	24	316.5	1.33	3.11E-06
28	120	5	1082	127	6.7	24.8	405.2	1.96	1.86E-06
29	128	5	1091	127	6.7	7	2016.1	5.22	3.71E-06
30	161	5	1106	127	6.7	13.4	557.4	0.85	5.76E-07
31	159	5	1113	127	6.7	5.3	440.5	4.28	7.21E-06
32	167	5	1114	127	6.7	15.6	257.2	0.72	6.48E-09
33	163	5	1165	129	6.9	22.5	312	2.28	1.09E-07
34	145	5	1182	129	6.9	7.1	609	1.29	5.82E-06
35	122	5	1197	129	6.9	0.3	312	1.26	1.75E-07
36	147	5	1491	137	7.6	24.1	442.2	2.18	1.03E-06
37	156	5	1493	137	7.6	10.8	553.4	3.14	1.75E-06
38	162	5	1503	137	7.6	3.8	487.3	0.64	5.52E-06
39	152	5	1505	137	7.6	7.7	467.5	0.68	7.77E-06
40	134	5	1508	137	7.6	5.3	460.7	1.19	6.86E-07
41	132	5	1512	137	7.6	17.1	230.3	1.77	1.31E-06
42	131	5	1521	137	7.6	0.6	433.6	2.13	4.82E-08
43	113	5	1528	137	7.6	19	401.3	2.01	1.22E-07
44	166	5	1536	137	7.6	5.2	472.8	1.02	1.08E-06
45	130	5	1549	137	7.6	6.1	494.1	1.55	1.20E-05
46	144	5	1550	137	7.6	12.9	543.8	2.80	7.40E-07
47	155	5	1611	137	7.6	11.6	212.7	4.28	5.06E-06
48	126	5	1752	145	5.6	13.2	370.8	3.10	2.18E-06
49	165	5	2114	145	5.6	10.4	821.7	0.86	1.07E-05

ID per Scenario	Original Index	Hazard Level	RSN	EqID	Mag M_w	Rrup [km]	Vs30 [m/s]	Scale Factor	Rate
50	125	5	2461	152	5.7	24.7	659.6	3.16	8.86E-07
51	142	5	2628	171	5.9	15.4	443	2.58	1.77E-06
52	124	5	2699	172	6.2	22.5	468.1	7.40	2.66E-06
53	129	5	4117	173	6.2	17.7	542.6	3.30	7.92E-07
54	149	5	6886	175	6.3	24.7	433.6	3.43	3.08E-06
55	143	5	8142	175	6.3	24.8	664.4	7.75	3.74E-06
1	168	6	95	30	6.6	22.6	670.8	3.92	2.44E-07
2	172	6	126	31	6.2	4.1	288.8	1.45	2.98E-09
3	204	6	139	42	5.5	17.7	659.6	3.80	6.04E-07
4	216	6	161	49	5.9	4.6	659.6	3.30	1.94E-06
5	170	6	175	50	6.5	7.3	192.1	4.69	9.46E-09
6	169	6	178	50	6.5	21.7	237.3	3.45	3.93E-06
7	207	6	212	50	6.5	7.7	202.9	6.10	3.83E-06
8	193	6	266	60	5.7	15.9	345.4	3.63	8.08E-09
9	171	6	284	61	5.9	12.4	338.5	12.73	1.61E-05
10	217	6	286	61	5.9	16	345.4	5.37	2.79E-06
11	196	6	292	64	6.3	7.3	274.5	2.10	2.12E-07
12	200	6	313	69	6.2	19.6	1000	2.71	4.09E-08
13	192	6	544	101	6.1	4	345.4	7.34	2.43E-06
14	175	6	553	102	5.8	24.5	338.5	9.58	2.05E-08
15	191	6	554	102	5.8	6.4	271.4	7.57	9.59E-06
16	182	6	558	103	6.2	21.9	271.4	2.13	2.54E-08
17	194	6	568	103	6.2	21.1	345.4	1.64	1.15E-06
18	219	6	721	113	6	17.3	370.8	2.16	2.28E-09
19	179	6	729	113	6	18.5	308.6	2.83	2.20E-08
20	199	6	730	113	6	16.3	308.6	5.61	8.35E-07
21	210	6	740	116	6.5	17	208.7	5.93	8.21E-06
22	185	6	741	116	6.5	18.2	192.1	2.83	1.97E-07
23	190	6	767	118	6.9	24.6	239.7	2.47	1.58E-06
24	213	6	802	118	6.9	20.3	597.1	1.86	4.11E-09
25	206	6	821	118	6.9	14.3	221.8	1.18	9.17E-07
26	173	6	850	118	6.9	14.7	671.8	4.10	2.00E-08
27	212	6	864	118	6.9	8.5	370.8	2.09	9.23E-07
28	177	6	949	118	6.9	17.5	376.1	2.62	1.19E-08
29	202	6	983	125	7.3	23.6	353.6	1.34	7.07E-08
30	205	6	995	127	6.7	17.1	355.8	3.47	1.42E-06
31	220	6	1013	127	6.7	22.2	446	1.56	6.10E-08
32	184	6	1044	127	6.7	23.4	278	1.08	2.70E-08
33	195	6	1048	127	6.7	24	316.5	1.74	4.05E-07
34	174	6	1082	127	6.7	24.8	405.2	2.57	3.75E-06
35	201	6	1086	127	6.7	12.1	280.9	0.96	4.11E-09
36	215	6	1113	127	6.7	5.3	440.5	5.60	6.52E-07
37	214	6	1119	127	6.7	23.6	996.4	0.91	2.72E-09

ID per Scenario	Original Index	Hazard Level	RSN	EqID	Mag M_w	Rrup [km]	Vs30 [m/s]	Scale Factor	Rate
38	208	6	1141	129	6.9	11.3	256	2.14	6.17E-07
39	209	6	1176	129	6.9	0.9	1043	1.59	2.68E-07
40	176	6	1197	129	6.9	0.3	312	1.65	1.76E-07
41	186	6	1510	137	7.6	10.5	440.2	2.62	9.81E-07
42	189	6	1511	137	7.6	11.8	479.3	2.18	4.09E-09
43	183	6	1521	137	7.6	0.6	433.6	2.78	1.58E-06
44	188	6	1532	137	7.6	0.9	573	3.49	8.33E-07
45	181	6	1549	137	7.6	6.1	494.1	2.03	2.73E-06
46	211	6	1611	137	7.6	11.6	212.7	5.60	4.46E-07
47	221	6	2114	145	5.6	10.4	821.7	1.13	1.26E-06
48	197	6	2628	171	5.9	15.4	443	3.37	4.34E-07
49	178	6	2699	172	6.2	22.5	468.1	9.69	2.87E-06
50	187	6	2893	172	6.2	7.6	443	7.59	3.24E-06
51	203	6	4098	173	6.2	19.7	427.7	2.75	1.48E-06
52	180	6	4117	173	6.2	17.7	542.6	4.32	5.17E-06
53	218	6	6969	175	6.3	11.5	443	2.95	6.41E-07
54	198	6	8142	175	6.3	24.8	664.4	10.15	8.90E-07
1	273	7	97	30	6.6	1.8	2016.1	12.25	8.29E-07
2	225	7	126	31	6.2	4.1	288.8	1.86	1.82E-07
3	267	7	130	41	6.8	5.5	659.6	8.52	1.71E-09
4	261	7	139	42	5.5	17.7	659.6	4.91	1.52E-07
5	287	7	161	49	5.9	4.6	659.6	4.26	3.47E-09
6	269	7	162	49	5.9	13.3	338.6	5.95	1.27E-06
7	227	7	165	50	6.5	2.7	223	4.19	3.51E-07
8	223	7	175	50	6.5	7.3	192.1	6.05	8.25E-09
9	222	7	178	50	6.5	21.7	237.3	4.45	8.70E-07
10	237	7	182	50	6.5	22	249.9	2.05	1.77E-09
11	268	7	212	50	6.5	7.7	202.9	7.87	5.73E-07
12	224	7	284	61	5.9	12.4	338.5	16.42	6.46E-06
13	288	7	286	61	5.9	16	345.4	6.93	4.35E-07
14	255	7	292	64	6.3	7.3	274.5	2.71	5.33E-07
15	283	7	312	68	6.9	10.8	1000	15.63	6.09E-07
16	272	7	316	69	6.2	22.7	530	3.90	8.01E-09
17	253	7	457	90	6.2	3.3	488.8	9.37	1.76E-09
18	251	7	544	101	6.1	4	345.4	9.48	3.52E-09
19	230	7	553	102	5.8	24.5	338.5	12.36	4.44E-06
20	250	7	554	102	5.8	6.4	271.4	9.77	4.95E-06
21	239	7	558	103	6.2	21.9	271.4	2.75	4.69E-07
22	252	7	568	103	6.2	21.1	345.4	2.12	3.13E-08
23	281	7	722	113	6	18.1	969.1	4.50	5.26E-09
24	285	7	723	113	6	17.3	370.8	1.16	3.14E-06
25	234	7	729	113	6	18.5	308.6	3.65	8.42E-07
26	259	7	730	113	6	16.3	308.6	7.23	2.25E-08

ID per Scenario	Original Index	Hazard Level	RSN	EqID	Mag M_w	Rrup [km]	Vs30 [m/s]	Scale Factor	Rate
27	278	7	740	116	6.5	17	208.7	7.65	7.81E-07
28	292	7	766	117	6.8	24	274.5	1.83	3.49E-09
29	248	7	767	118	6.9	24.6	239.7	3.19	1.26E-07
30	284	7	802	118	6.9	20.3	597.1	2.40	4.13E-09
31	289	7	803	118	6.9	10	729.7	2.15	5.24E-09
32	265	7	821	118	6.9	14.3	221.8	1.52	6.89E-09
33	226	7	850	118	6.9	14.7	671.8	5.29	7.06E-09
34	280	7	864	118	6.9	8.5	370.8	2.69	3.34E-07
35	260	7	959	125	7.3	19.7	271.4	2.17	3.34E-07
36	274	7	986	126	6.5	8.3	338.5	4.29	4.15E-09
37	249	7	989	127	6.7	18.4	545.7	4.65	5.96E-07
38	264	7	995	127	6.7	17.1	355.8	4.48	1.08E-07
39	293	7	1045	127	6.7	20.5	740.1	1.38	8.79E-09
40	254	7	1048	127	6.7	24	316.5	2.24	5.12E-08
41	235	7	1091	127	6.7	7	2016.1	8.83	2.36E-07
42	286	7	1119	127	6.7	23.6	996.4	1.18	1.72E-09
43	228	7	1120	128	5.9	12.8	345.4	0.72	9.23E-09
44	295	7	1165	129	6.9	22.5	312	3.85	5.66E-07
45	277	7	1176	129	6.9	0.9	1043	2.05	3.52E-09
46	231	7	1197	129	6.9	0.3	312	2.13	1.47E-07
47	245	7	1208	136	7.5	10.9	792	5.09	8.23E-09
48	263	7	1491	137	7.6	24.1	442.2	3.68	8.09E-09
49	300	7	1492	137	7.6	24.1	291.9	0.89	4.60E-09
50	297	7	1494	137	7.6	2.7	680	3.47	4.06E-09
51	294	7	1503	137	7.6	3.8	487.3	1.08	4.20E-09
52	270	7	1505	137	7.6	7.7	467.5	1.15	5.22E-07
53	242	7	1508	137	7.6	5.3	460.7	2.01	4.99E-07
54	243	7	1510	137	7.6	10.5	440.2	3.38	3.62E-08
55	247	7	1511	137	7.6	11.8	479.3	2.81	4.02E-09
56	241	7	1512	137	7.6	17.1	230.3	2.98	4.58E-07
57	240	7	1521	137	7.6	0.6	433.6	3.59	1.75E-07
58	275	7	1530	137	7.6	7	468.1	4.24	7.59E-08
59	246	7	1532	137	7.6	0.9	573	4.50	1.24E-08
60	301	7	1536	137	7.6	5.2	472.8	1.72	1.73E-09
61	238	7	1549	137	7.6	6.1	494.1	2.61	1.62E-07
62	258	7	1550	137	7.6	12.9	543.8	4.74	1.65E-07
63	282	7	1551	137	7.6	17.2	575.5	2.87	1.79E-06
64	229	7	1605	137	7.6	13.1	424.2	2.00	1.69E-07
65	279	7	1611	137	7.6	11.6	212.7	7.23	2.56E-06
66	233	7	1752	145	5.6	13.2	370.8	5.24	8.58E-09
67	276	7	1787	145	5.6	22	684.9	2.35	3.52E-09
68	299	7	2495	153	5.9	24.1	274.5	1.91	6.31E-07
69	256	7	2628	171	5.9	15.4	443	4.35	8.29E-08

ID per Scenario	Original Index	Hazard Level	RSN	EqID	Mag M_w	Rrup [km]	Vs30 [m/s]	Scale Factor	Rate
70	298	7	2650	171	5.9	23.4	680	3.69	3.45E-09
71	262	7	2654	172	6.2	19.6	427.7	6.95	4.83E-09
72	296	7	2661	172	6.2	16.5	624.9	4.30	1.76E-09
73	232	7	2699	172	6.2	22.5	468.1	12.50	6.38E-08
74	291	7	2734	172	6.2	16.6	549.4	2.64	1.78E-09
75	244	7	2893	172	6.2	7.6	443	9.79	2.52E-06
76	271	7	3548	172	6.2	12.8	664.4	1.56	6.94E-09
77	236	7	4117	173	6.2	17.7	542.6	5.57	2.84E-07
78	266	7	6886	175	6.3	24.7	433.6	5.80	4.56E-07
79	290	7	6969	175	6.3	11.5	443	3.81	3.39E-07
80	257	7	8142	175	6.3	24.8	664.4	13.09	1.47E-07
1	304	8	126	31	6.2	4.1	288.8	2.90	9.91E-08
2	335	8	139	42	5.5	17.7	659.6	7.65	1.94E-07
3	352	8	161	49	5.9	4.6	659.6	6.64	2.99E-07
4	305	8	165	50	6.5	2.7	223	6.52	1.23E-07
5	323	8	171	50	6.5	15.2	659.6	2.95	7.92E-08
6	302	8	178	50	6.5	21.7	237.3	6.93	1.42E-07
7	324	8	266	60	5.7	15.9	345.4	7.30	3.47E-09
8	303	8	284	61	5.9	12.4	338.5	25.58	7.99E-08
9	341	8	285	61	5.9	12.4	338.5	5.28	7.94E-10
10	327	8	292	64	6.3	7.3	274.5	4.22	3.21E-08
11	339	8	316	69	6.2	22.7	530	6.07	3.49E-09
12	326	8	457	90	6.2	3.3	488.8	14.59	1.22E-07
13	322	8	554	102	5.8	6.4	271.4	15.21	1.16E-06
14	325	8	568	103	6.2	21.1	345.4	3.30	2.27E-09
15	333	8	569	103	6.2	21.1	345.4	3.44	1.38E-07
16	346	8	722	113	6	18.1	969.1	7.01	7.45E-07
17	348	8	723	113	6	17.3	370.8	1.81	6.75E-10
18	311	8	729	113	6	18.5	308.6	5.69	2.67E-07
19	330	8	730	113	6	16.3	308.6	11.27	5.83E-10
20	343	8	740	116	6.5	17	208.7	11.91	4.65E-07
21	321	8	767	118	6.9	24.6	239.7	4.96	1.26E-07
22	320	8	779	118	6.9	3.8	462.2	1.78	2.52E-09
23	337	8	821	118	6.9	14.3	221.8	2.37	1.11E-08
24	355	8	827	118	6.9	22.7	333.9	9.52	5.84E-10
25	345	8	864	118	6.9	8.5	370.8	4.19	6.66E-10
26	308	8	949	118	6.9	17.5	376.1	5.26	1.55E-08
27	316	8	1044	127	6.7	23.4	278	2.16	1.93E-09
28	356	8	1045	127	6.7	20.5	740.1	2.15	4.18E-10
29	332	8	1086	127	6.7	12.1	280.9	1.93	2.03E-07
30	312	8	1091	127	6.7	7	2016.1	13.75	4.80E-08
31	351	8	1113	127	6.7	5.3	440.5	11.25	9.53E-08
32	340	8	1116	127	6.7	22.3	376.1	5.68	3.49E-09

ID per Scenario	Original Index	Hazard Level	RSN	EqID	Mag M_w	Rrup [km]	Vs30 [m/s]	Scale Factor	Rate
33	349	8	1119	127	6.7	23.6	996.4	1.84	4.67E-08
34	306	8	1120	128	5.9	12.8	345.4	1.12	1.25E-07
35	342	8	1141	129	6.9	11.3	256	4.31	1.44E-08
36	331	8	1182	129	6.9	7.1	609	3.39	4.83E-08
37	313	8	1198	129	6.9	1.5	256	6.50	2.65E-08
38	350	8	1227	136	7.5	4.8	297	4.73	2.12E-09
39	317	8	1231	137	7.6	25	235.1	1.65	9.12E-08
40	336	8	1491	137	7.6	24.1	442.2	5.73	6.86E-10
41	360	8	1492	137	7.6	24.1	291.9	1.39	1.56E-07
42	347	8	1493	137	7.6	10.8	553.4	8.25	4.09E-08
43	357	8	1494	137	7.6	2.7	680	5.40	4.64E-09
44	307	8	1495	137	7.6	22.7	253.7	4.65	1.99E-10
45	354	8	1503	137	7.6	3.8	487.3	1.69	1.87E-08
46	318	8	1510	137	7.6	10.5	440.2	5.27	1.81E-07
47	315	8	1512	137	7.6	17.1	230.3	4.64	8.20E-08
48	314	8	1521	137	7.6	0.6	433.6	5.59	6.42E-08
49	361	8	1536	137	7.6	5.2	472.8	2.67	2.33E-10
50	353	8	1541	137	7.6	18.2	680	4.19	1.66E-09
51	329	8	1550	137	7.6	12.9	543.8	7.38	6.54E-09
52	344	8	1611	137	7.6	11.6	212.7	11.26	4.10E-07
53	358	8	2114	145	5.6	10.4	821.7	2.27	1.38E-08
54	310	8	2461	152	5.7	24.7	659.6	8.32	2.50E-07
55	359	8	2650	171	5.9	23.4	680	5.74	4.76E-07
56	309	8	2699	172	6.2	22.5	468.1	19.47	1.10E-08
57	319	8	2893	172	6.2	7.6	443	15.25	2.08E-08
58	338	8	3548	172	6.2	12.8	664.4	2.43	2.69E-07
59	334	8	4098	173	6.2	19.7	427.7	5.53	1.99E-10
60	328	8	8142	175	6.3	24.8	664.4	20.40	7.52E-09
1	362	9	175	50	6.5	7.3	192.1	13.79	1.56E-08
2	384	9	212	50	6.5	7.7	202.9	17.94	5.32E-11
3	386	9	285	61	5.9	12.4	338.5	7.73	4.84E-07
4	393	9	286	61	5.9	16	345.4	15.79	4.22E-09
5	377	9	292	64	6.3	7.3	274.5	6.17	4.38E-08
6	399	9	297	68	6.9	8.2	1000	22.39	5.26E-11
7	378	9	313	69	6.2	19.6	1000	7.98	2.61E-08
8	385	9	316	69	6.2	22.7	530	8.88	5.06E-08
9	375	9	544	101	6.1	4	345.4	21.59	9.98E-11
10	363	9	553	102	5.8	24.5	338.5	28.17	4.88E-09
11	374	9	554	102	5.8	6.4	271.4	22.25	1.26E-07
12	376	9	568	103	6.2	21.1	345.4	4.83	5.20E-11
13	395	9	721	113	6	17.3	370.8	6.36	1.69E-08
14	389	9	722	113	6	18.1	969.1	10.25	1.01E-07
15	390	9	724	113	6	17.3	370.8	11.99	1.06E-10

ID per Scenario	Original Index	Hazard Level	RSN	EqID	Mag M_w	Rrup [km]	Vs30 [m/s]	Scale Factor	Rate
16	391	9	778	118	6.9	15.2	288.6	7.38	2.15E-10
17	383	9	821	118	6.9	14.3	221.8	3.47	2.18E-09
18	388	9	864	118	6.9	8.5	370.8	6.13	1.74E-09
19	380	9	959	125	7.3	19.7	271.4	4.94	5.38E-11
20	381	9	983	125	7.3	23.6	353.6	3.94	5.12E-11
21	373	9	989	127	6.7	18.4	545.7	10.60	5.34E-11
22	379	9	1086	127	6.7	12.1	280.9	2.83	5.24E-11
23	392	9	1113	127	6.7	5.3	440.5	16.45	7.11E-08
24	397	9	1165	129	6.9	22.5	312	8.76	8.36E-08
25	372	9	1208	136	7.5	10.9	792	11.60	1.04E-10
26	369	9	1231	137	7.6	25	235.1	2.42	5.15E-11
27	382	9	1491	137	7.6	24.1	442.2	8.38	2.32E-08
28	402	9	1492	137	7.6	24.1	291.9	2.03	1.82E-10
29	396	9	1503	137	7.6	3.8	487.3	2.47	2.86E-09
30	401	9	1504	137	7.6	9.5	470.7	3.34	5.20E-09
31	368	9	1508	137	7.6	5.3	460.7	4.58	1.85E-08
32	370	9	1510	137	7.6	10.5	440.2	7.71	1.96E-08
33	367	9	1517	137	7.6	9.8	476.1	1.88	3.18E-10
34	365	9	1752	145	5.6	13.2	370.8	11.94	5.29E-11
35	387	9	1787	145	5.6	22	684.9	5.36	1.10E-10
36	400	9	2650	171	5.9	23.4	680	8.40	1.24E-10
37	398	9	2661	172	6.2	16.5	624.9	9.80	3.21E-08
38	364	9	2699	172	6.2	22.5	468.1	28.48	1.02E-08
39	394	9	2734	172	6.2	16.6	549.4	6.02	4.61E-10
40	371	9	2893	172	6.2	7.6	443	22.30	5.26E-11
41	366	9	4117	173	6.2	17.7	542.6	12.70	2.16E-08

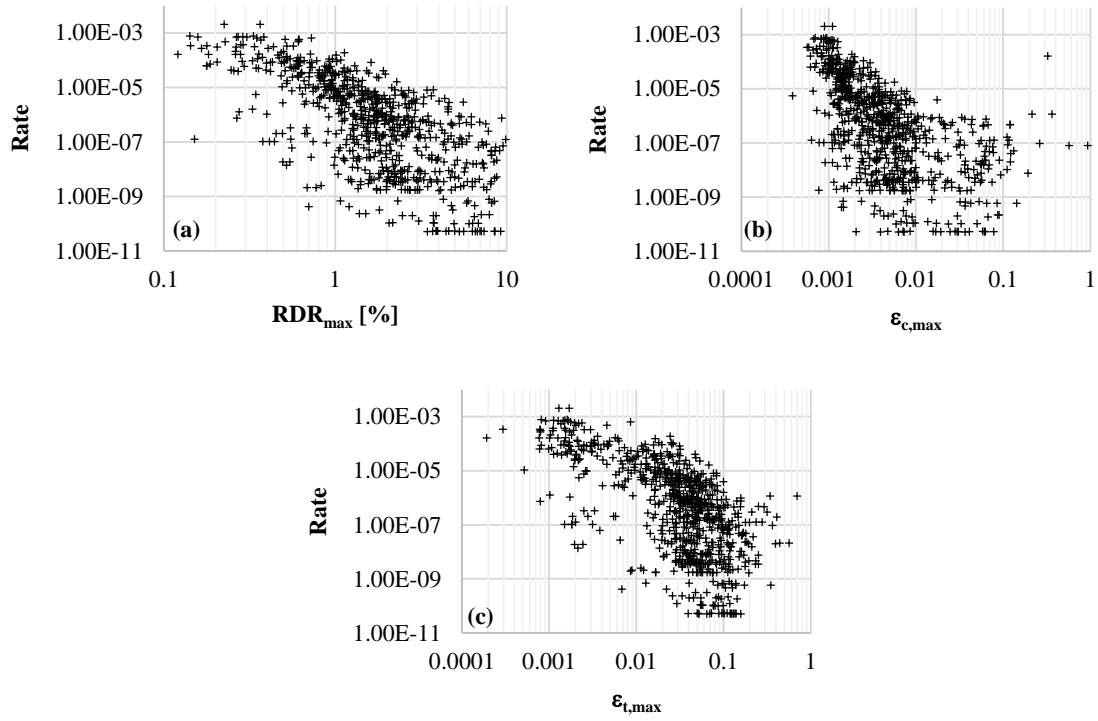


Figure D.1.1 – Rate versus EDP level, DuM model: (a) rates of occurrence for maximum roof drift ratio; (b) rates of occurrence for maximum compressive strain in the stem SBE; (c) rates of occurrence for maximum tensile strain in the stem SBE.